UNCLASSIFIED

AD 296 544

Reproduced
by the

ARMED SERVICES TECHNICAL INFORMATION AGENCY
ARLINGTON HALL STATION
ARLINGTON 12, VIRGINIA

UNCLASSIFIED

NOTICE: When government or other drawings, specifications or other data are used for any purpose other than in connection with a definitely related government procurement operation, the U. S. Government thereby incurs no responsibility, nor any obligation whatsoever; and the fact that the Government may have formulated, furnished, or in any way supplied the said drawings, specifications, or other data is not to be regarded by implication or otherwise as in any manner licensing the holder or any other person or corporation, or conveying any rights or permission to manufacture, use or sell any patented invention that may in any way be related thereto.

63-2-4

1

Belv/Sym 10/24-26/61

296544

296 544

DEPARTMENT OF THE ARMY
CORPS OF ENGINEERS

PROCEEDINGS OF THE TENTH BASIC RESEARCH GROUP CONTRACTORS' CONFERENCE and SYMPOSIUM

24 - 26 October 1961

ASTIA
FEB 25 1963
TISIA

U. S. Army Engineer Research And Development Laboratories

PROPERTY OF
[illegible]
TECHNICAL LIBRARY

$19.75

FORT BELVOIR, VIRGINIA

PROCEEDINGS OF THE
TENTH BASIC RESEARCH GROUP
CONTRACTORS' CONFERENCE
and
SYMPOSIUM

24 - 26 October 1961

U. S. Army Engineer Research and Development Laboratories
Fort Belvoir, Virginia

Sponsored by

Project 8X99-25-001-40A
U. S. Army Engineer Research and Development Laboratories
Fort Belvoir, Virginia

Prepared by Hyman Rosenwasser, USAERDL

INTRODUCTION

The Tenth Basic Research Group Contractors' Conference and Symposium was held on 24-26 October 1961 at USAERDL, Fort Belvoir, Virginia. Papers by contractors and staff members of the Basic Research Group were presented as well as invited papers by guests of the symposium.

In order to allow more time for discussion fewer papers were presented at this conference in comparison with previous years. It was felt that considerable gain by informal discussion was achieved.

Since the proceedings of the Ninth Basic Research Group Contractors' Conference and Symposium were enthusiastically received, not only by the contractors, but also by organizations and individuals working in the field, the Tenth Contractors' Conference and Symposium is herewith also covered by printed proceedings.

We wish to extend our thanks to all the authors and to those who contributed to the several discussions. They were responsible for the success of the symposium and for this impressive volume. To the authors of the invited papers special thanks should be given because their contributions considerably increased the value of the symposium.

Some authors preferred to publish the papers they gave at this conference elsewhere. For this reason only the abstracts of their papers appear in the main body of the proceedings. Authors who did not submit their manuscripts will find that only the abstracts appear in this volume.

As in the past year, an informal expression of opinion was solicited from all participants of this conference as to the desirability of continuing annual conferences of this nature. The result of this canvass was so encouraging that it was decided to hold an eleventh contractors' conference and symposium next year. Tentatively, this eleventh conference will be held again at USAERDL, Fort Belvoir, Virginia, sometime in the Fall of 1962. Any suggestions for improving the conference will be appreciated.

Z. V. HARVALIK
Director
Basic Research Group

PROGRAM

Tuesday, 24 October 1961

Presiding:	H. Rosenwasser (Chairman)
0900 - 0915	O. F. Kezer, Jr., Basic Research Group: "A Study of the Thermal Profile of Solutions."
0925 - 0945	W. C. McCrone, McCrone Associates: "Growing of Azide Crystals."
0955 - 1005	INTERMISSION
1005 - 1025	B. Krause, Basic Research Group: "Order-Disorder Phenomena in Thallium Azide."
1035 - 1055	E. L. Hendricks and B. Krause, Basic Research Group: "X-Ray Radiation Damage of Alkali Azides."
1105 - 1135	I. J. Solomon, Armour Research Foundation: "Metal Ozonides."
1145 - 1300	LUNCH
1300 - 1330	J. H. Boyer, American Chemical Society: "Intramolecular Changes Initiated by Electrophilic Attack on Alkyl Azides."
1340 - 1410	E. Lieber and J. Dodd, Roosevelt University: "The Nature of the Bent State of the Azide Group."
1420 - 1430	INTERMISSION
1430 - 1510	P. W. M. Jacobs, F. C. Tompkins, and V. R. Pai-Verneker, Imperial College: "The Photochemical Decomposition of Barium Azide."
1520 - 1550	J. A. Joebstl and H. J. Mueller, Basic Research Group: "On the Applicability of Hahn's Emanation Method for Decomposition Studies of Inorganic Azides."

Wednesday, 25 October 1961

Presiding:	Donald P. Easter
0900 - 0945	F. F. Carlson, G. J. King, R. C. McMillan, and B. Miller, Basic Research Group: "A Study of Radiation-Induced Defects in Sodium Azide." "Electron Spin Resonance Experiments on Alpha Lead Azide."

0955 - 1025	R. B. Horst, J. H. Anderson, University of Pittsburgh, and D. E. Milligan, Mellon Institute: "Paramagnetic Resonance Centers in Potassium Azide Irradiated at 77° K."
1035 - 1045	INTERMISSION
1045 - 1115	H. J. Mueller, Basic Research Group: "Exo-electron Emission and Related Electron-emissions from Solids."
1125 - 1140	D. Mergerian and S. A. Marshall, Armour Research Foundation: "Irradiation Produced Paramagnetic Defect Centers in Single Crystal Potassium Azide."
1150 - 1310	LUNCH
1310 - 1340	K. Torkar and H. Krischner, Technischen Hochschule, Graz: "Studies of Preparation and Properties of Alkali Azides and Effects of this Activity on Thermodynamic and Thermochemical Data."
1350 - 1415	J. I. Bryant, Basic Research Group, and G. C. Turrell, Howard University: "Infrared Spectra of the Azide Ion in Alkali Halide Lattices."
1425 - 1435	INTERMISSION
1435 - 1505	M. C. Cook, L. A. Head, R. T. Keyes, and R. A. Rollins, University of Utah: "Electron Micrographs, Photoconductivity and the Mechanism of Thermal Decomposition of Lead Azide."
1515 - 1545	W. C. McCrone, McCrone Associates: "Structure and Sensitivity Determinations of Alpha and Beta Lead Azides."

Thursday, 26 October 1961

Presiding:	James I. Bryant
0900 - 0930	H. Egghart, Basic Research Group: "Studies on the Thermal Decomposition of Molten KN_3 in the Presence of Metals and Metal Oxides."
0940 - 1010	J. Dodd, Roosevelt University: "Theoretical Studies on the Thermal Decomposition of Lead Azide."

1020 - 1030	INTERMISSION
1030 - 1100	S. K. Deb, National Research Council, Ottawa, Canada: "Optical and Electrical Properties of Alkali Azides."
1110 - 1140	D. S. Ling, Jr., PEC Corporation: "A Statistical Theory of Initiation."
1150 - 1300	LUNCH
1300 - 1330	E. Lieber, Roosevelt University: "The Synthesis and Properties of Tetravalent Lead Azides."
1340 - 1400	H. Rosenwasser, Basic Research Group: "Basic Rare Earth Azides."
1410	ADJOURN

ATTENDANCE LIST

Altman, Peter	Naval Weapons Laboratory	Dahlgren, Va
Anderson, John H	Department of Physics, University of Pittsburgh	Pittsburgh, Pa
Anderson, Roger	Lawrence Radiation Laboratory	Livermore, Calif
Boyer, J H	American Chemical Society	Washington, D C
Bryant, James I	USAERDL	Fort Belvoir, Va
Burton, James S	Howard University	Washington, D C
Carlson, Fred F	USAERDL	Fort Belvoir, Va
Chang, Marguerite	U S Naval Propellant Plant	Indian Head, Md
Clift, G	Army Chemical Center	Maryland
Cohn, E M	Army Research Office	Washington, D C
Coleman, Amos J	USAERDL	Fort Belvoir, Va
Cook, Charles J	Stanford Research Institute	Menlo Park, Calif
Cook, M A	University of Utah	Salt Lake City, Utah
Davenport, D E	Stanford Research Institute	Menlo Park, Calif
Davis, V	USAERDL	Fort Belvoir, Va
Deb, S K	National Research Council	Ottawa, Canada
Dibeler, Vernon H	National Bureau of Standards	Washington, D C
Dickinson, Neil K	USAERDL	Fort Belvoir, Va
Dodd, Jack	Roosevelt University	Chicago, Ill
Mueller, Herbert J	USAERDL	Fort Belvoir, Va
Easter, Donald P	USAERDL	Fort Belvoir, Va
Egghart, Heinrich	USAERDL	Fort Belvoir, Va
Fair, Harry D, Lt	Picatinny Arsenal	Dover, N J
Fisher, Howard	Aerojet General Corporation	Downey, Calif
Fredericks, W F	Stanford Research Institute	Menlo Park, Calif
Ghirardelli, R G	U S Army Research Office (DURHAM)	Durham, N C
Gould, Don F	American Chemical Society	Washington, D C
Harvalik, Zaboj V	USAERDL	Fort Belvoir, Va
Hendricks, Ernest L	USAERDL	Fort Belvoir, Va
Herzfeld, K F	Catholic University	Washington, D C
Hickox, George W	USAERDL	Fort Belvoir, Va
Hook, Arthur B	USAERDL	Fort Belvoir, Va
Joebstl, Johann A	USAERDL	Fort Belvoir, Va
Keyes, R T	University of Utah	Salt Lake City, Utah
Kezer, Osman F	USAERDL	Fort Belvoir, Va
King, Gerard J	USAERDL	Fort Belvoir, Va
Kraus, Olen	National Bureau of Standards	Washington, D C
Krause, Brigitte H	USAERDL	Fort Belvoir, Va
Krischner, Harald	Technischen Hochschule	Graz, Austria
Lieber, Eugene	Roosevelt University	Chicago, Ill
Ling, D S	PEC Corporation	Boulder, Colo
McCrone, Walter	McCrone Associates	Chicago, Ill
MacDiarmid, A G	University of Pennsylvania	Philadelphia, Pa
Mergerian, Dickron	Armour Research Foundation	Chicago, Ill

Mapes, J E	Brookhaven National Laboratory	Upton, Long Island, New York
Marshall, Sam A	Armour Research Foundation	Chicago, Ill
Mason, Ernest	U S Naval Weapons Station	Yorktown, Va
Mason, Richard M	Office Chief of Engineers	Washington, D C
Meikle, Bill	Sandia Base	Albuquerque, N M
Miller, Brian S	USAERDL	Fort Belvoir, Va
Naeser, C R	George Washington University	Washington, D C
O'Dell, Mylous S Jr	USAERDL	Fort Belvoir, Va
Otto, Fred	University of Connecticut	Storrs, Conn
Pai-Verneker, V R	Imperial College	London, England
Pitt, C H	University of Utah	Salt Lake City, Utah
Radell, Jack	Frankford Arsenal	Philadelphia, Pa
Roecker, George W	Naval Propellant Plant	Indian Head, Md
Rollefson, Ragnar O	University of Wisconsin	Madison, Wisc
Rosenwasser, Hyman	USAERDL	Fort Belvoir, Va
Silverstein, M S	Frankford Arsenal	Philadelphia, Pa
Smoluchowski, R	Princeton University	Princeton, N J
Solomon, I J	Armour Research Foundation	Chicago, Ill
Taylor, James L	USAERDL	Fort Belvoir, Va
Turrell, G C	Howard University	Washington, D C
Vandersluis, H J Jr	USAERDL	Fort Belvoir, Va
Weida, Frank M	USAERDL	Fort Belvoir, Va

CONTENTS

Page

Kezer
"A Study of the Thermal Profile of Solutions" 1

Krause
"Order-Disorder Phenomena in Thallium Azide" 3

Hendricks and Krause
"X-Ray Radiation Damage of Alkali Azides" 17

Solomon
"Inorganic Ozonides" 23

Boyer
"Intramolecular Changes Initiated by Electrophilic Attack on Alkyl Azides" 25

Lieber and Dodd
"The Nature of the Bent State of the Azide Group" 37

Jacobs, Tompkins, and Verneker
"The Photochemical Decomposition of Barium Azide" 55

Joebstl and Mueller
"On the Applicability of Hahn's Emanation Method for Decomposition Studies of Inorganic Azides" 73

Carlson, King, McMillan, and Miller
"A Study of Radiation-Induced Defects in Sodium Azide" 85

King, McMillan, Miller, and Carlson
"Electron Spin Resonance Experiments on Alpha Lead Azide" 111

Horst, Anderson, and Milligan
"Paramagnetic Resonance in Potassium Azide Irradiated at 77° K" 117

Mueller
"Exo-Electron Emission and Related Electron-Emissions from Solids" 135

Mergerian and Marshall
"Irradiation Produced Paramagnetic Defect Centers in Single Crystal Potassium Azide" 145

Page

Torkar and Krischner
"Studies of Preparation and Properties of Alkali Azides and Effects of This Activity on Thermodynamic and Thermochemical Data" 147

Bryant and Turrell
"Infrared Spectra of the Azide Ion in Alkali Halide Lattices" 155

Cook, Head, Keyes, and Rollins
"Photoconductivity, Electron Micrographs and the Mechanism of Thermal Decomposition of Lead Azide" 183

Egghart
"Studies on the Thermal Decomposition of Molten KN_3 in the Presence of Metals and Metal Oxides" 241

Dodd
"Theoretical Studies on the Thermal Decomposition of Lead Azide" 253

Deb
"Optical and Electrical Properties of Alkali Metal Azides" 277

Ling
"A Statistical Theory of Initiation" 289

Lieber
"The Synthesis and Properties of Tetravalent Lead Azides" 299

Rosenwasser
"Basic Rare Earth Azides" 317

A STUDY OF THE THERMAL PROFILE OF SOLUTIONS

by

O. F. Kezer, Jr.
Basic Research Group
U. S. Army Engineer Research and Development Laboratories
Fort Belvoir, Virginia

The background information necessary for the growth of good crystals of any compound comes from a wide variety of sources. It is believed that a great deal of this information may be derived from a study of the physical and thermal chracteristics of the crystal growing solution. This study of the saturated and unsaturated solutions should give the experimenter a better understanding as to the nature of the compound. It was observed during purification and saturation studies made in connection with the growth of NaN_3 crystals that there was a marked difference between the temperature at the surface of the solution and at the surface of the undissolved solute. It was observed that this difference in temperature was related to the formation of crystallizing nuclei and their subsequent growth into good crystals. This temperature difference being in the form of a thermal gradient allows the use of standard laboratory equipment for its measurements. If these measurements are handled with care, thereby decreasing the possibility of contamination, this allows the solution to be used for future crystal growth.

The preliminary thermal profile studies were carried out on large containers of NaN_3 solutions. Similar studies were also carried out on distilled water and these results used as a reference for the NaN_3 work. The temperature measurement was carried out by use of thermocouples and an L. & N. Galvanometer. This instrumentation was later refined such that the original thermocouples were replaced by special calibrated thermocouple probes and the galvanometer was replaced by a multi-channel strip recorder. This arrangement allows for continuous recording of the data and eliminates to a large extent the error introduced by the human element. The heat source remained the same as before, a 14" x 21" laboratory heater. A total of 16 of the precision thermocouple probes were arranged throughout the container such that the temperature at various horizontal and vertical positions could be measured during an experimental run. On the basis of this physical arrangement of the thermocouples, the recorded data was considered as a series of cylindrical shells oriented both vertically and horizontally. In addition the data was also treated as an ellipsoid of revolution oriented vertically in the container.

During the heating and cooling cycles a series of concentration zones are visible in the solution. As the temperature increases these zones migrate toward the surface in conjunction with their associated temperature zones, and are replaced by zones of greater concentration and temperature. By measuring the vertical distance between the top of the solute and these zones it is possible to determine their respective concentrations. In addition, by observing the relationships of these zones to the zones where crystallizing nuclei form and subsequent growth of crystals result, one may determine a crude representation of the solubility curve for the respective compound under study. In most instances the resultant curve will be sufficiently accurate for crystal growth work. It is also possible on the basis of this information to empirically determine the concentration of the zones present in the crystal growth container merely by knowing the thermal gradient present. Since temperature is not the only critical factor in crystal growth, the influence of other factors on the growing solution must be considered. These considerations must be made in view of their relationships to the thermal environment such that by one temperature measurement the localized properties of the growing solution will be known. As a result of the correct interpretation of the thermal profile data, information may be derived on the pH, concentration and numerous other thermally related factors at any point in the crystal growing solution relative to time.

After the maximum temperature is achieved and the source of heat is removed the next phase of the profile work comes into being. As the solution cools thermal gradients are set up in the solution such that at the point where the most perfect thermal gradient for the compound under study is achieved, crystal nuclei will form. If conditions remain suitable the nuclei will attach themselves to the tip of the nearest thermocouple and continue to grow in place rather than settle to the bottom of the container which, in all probability, will be a less suitable environment for continued growth. A good example of the importance of the thermal gradient can be observed in NaN_3 solutions.

It has been observed that as the thermal gradient decreases a point is reached where good crystals are no longer produced and simple twinning becomes prevalent. A further decline in the thermal gradient results in the formation of overgrowths, complex twinning, and an excess of solute precipitated on the bottom of the growing container.

Summation. On the basis of the thermal profile studies the crystal growth environment most suitable for the compound and perfection of crystals required may be derived. It then becomes necessary to duplicate this growth environment on a larger scale by the use of suitable instrumentation.

ORDER-DISORDER PHENOMENA IN THALLIUM AZIDE

by

B. Krause
Basic Research Group
U. S. Army Engineer Research and Development Laboratories
Fort Belvoir, Virginia

As is well known, x-rays are diffracted by crystals in a manner similar to optical light by 3-dimensional optical gratings. In the case of parallel, monochromatic x-ray radiation and perfect crystals, one would expect sharp diffraction peaks at well defined angles with very rapidly diminishing intensity in the vicinity of these angles. A broadened intensity distribution around the diffraction angle allows conclusions about disorder phenomena within the crystal. These may be of differing nature, such as distortion of the unit cells of the crystal, mosaic character of the crystal with only small regions of coherent scattering, stacking faults, or other statistical deviations from the 3-dimensional translation periodicity. In order to decide between these possibilities, one has to consider the mathematical character of the whole intensity distribution around the diffraction peak angle. We will refer to this angle-intensity-distribution as a line profile. The efforts described below were dedicated to measuring these line profiles accurately enough to make theoretical interpretation possible at a later time.

Line profile studies on TlN_3 were carried out at different stages of irradiation with soft x-rays and at different stages of annealing. The experimental arrangement consisted of a copper x-ray target operated at 35Kv, 39 ma., wide angle goniometer with scintillation counter, pulse height discriminator, and counting rate computer as shown in Fig. 1. The sample in the center of the goniometer was in the form of a powder. A nickel filter between the x-ray source and sample served as a partial monochromator. This arrangement provides neither ideal geometrical conditions nor perfectly monochromatic radiation, resulting in an additional broadening of the diffraction line profiles. A distinction between "instrument" broadening and crystal disorder broadening, however, is possible by mathematical procedures developed by Stokes[1].

One of the reasons for studying line profiles was to obtain quantitatively accurate results of relative lattice constant changes caused by x-rays. In the case of the alkali-halides, for instance, the knowledge of density changes measured by x-ray methods, as compared with density measurements by other methods, would be valuable in order to decide between different types of lattice defects (such as Schottky and Frenkel type defects)[2]. The density changes,

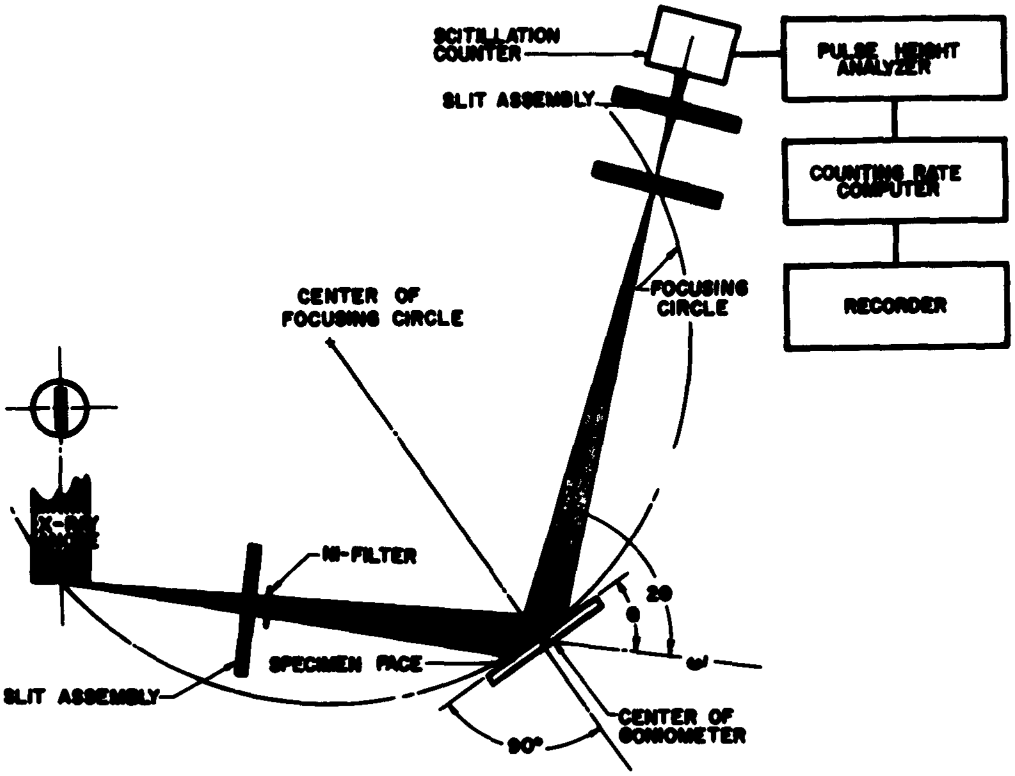
SCITILLATION COUNTER
SLIT ASSEMBLY
PULSE HEIGHT ANALYZER
COUNTING RATE COMPUTER
RECORDER
CENTER OF FOCUSING CIRCLE
FOCUSING CIRCLE
X-RAY TUBE
Ni-FILTER
2θ
θ
ω
SPECIMEN FACE
SLIT ASSEMBLY
CENTER OF GONIOMETER
90°

EXPERIMENTAL ARRANGEMENT

Figure 1

however, are very small, in the order of magnitude of 10^{-4} per hour. Besides, the changes occur continuously even within the measurement of a single line profile, which make any evaluation very time consuming. In order to relate a measured line profile to a certain time, intensity-time interpolations for each angle increment as demonstrated in Fig. 2 were made. The plotting of those interpolated intensities versus the diffraction angle then gives the desired line profiles. From Fig. 2a and 2b of the left and right side of the diffraction peak, it can be easily visualized that the line profile as a whole shifts towards smaller angles. Another effect is the profile broadening as demonstrated by decreasing resolution for consecutive angle increments. Most of the changes occur during the first 30-40 hours. Figure 3a and 3b show similar plots for the (200) diffraction line. It is evident that no appreciable line shifts occur and that also the line broadening is much smaller than for the (002) peak discussed before. This is even more evident in Fig. 4 and Fig. 5 where line profile changes for various reflections are shown. Reflections mainly determined by the crystallographic c-direction show strong line profile shifts and changes;

INTENSITY CHANGES FOR VARIOUS 2-θ INCREMENTS

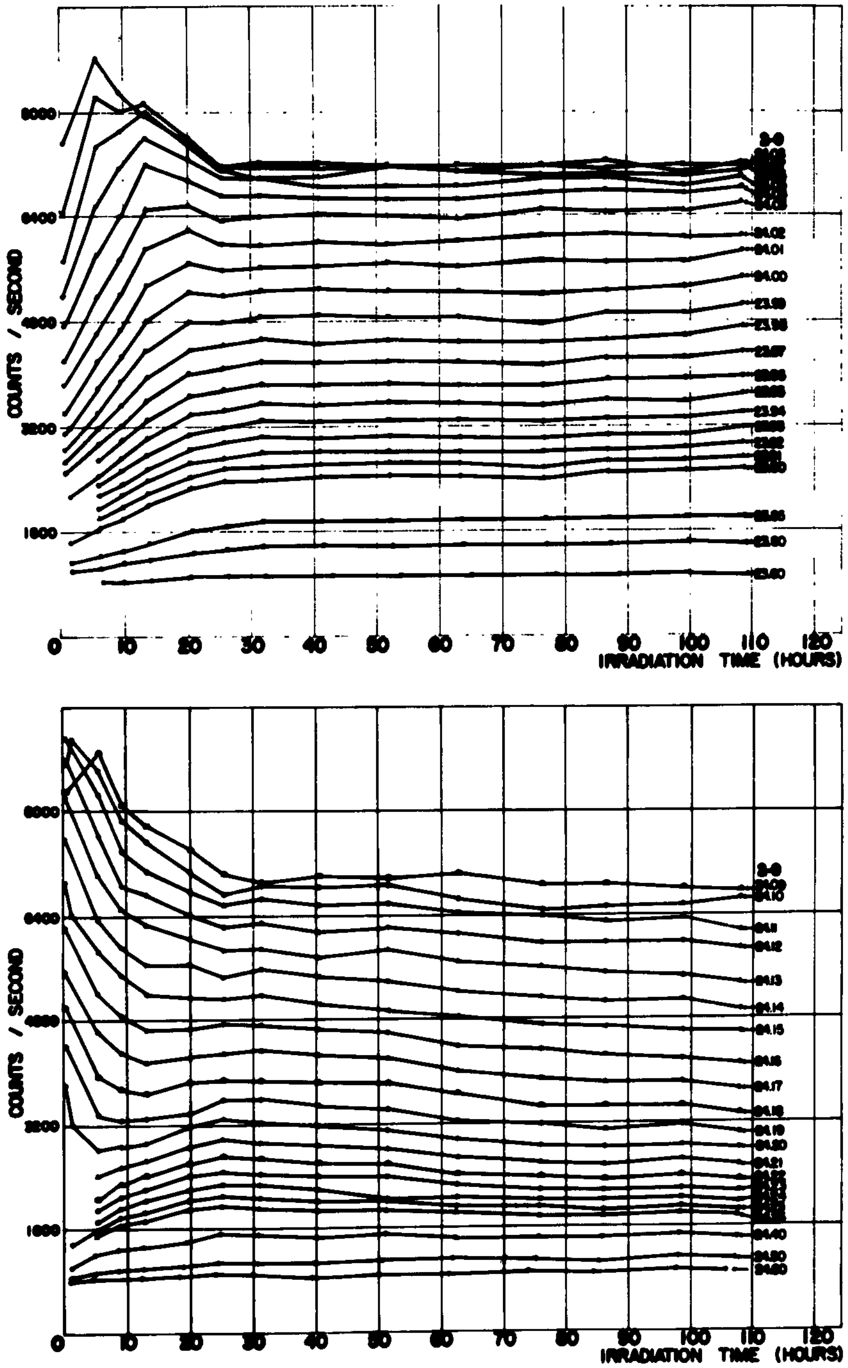

Figure 2

INTENSITY CHANGES FOR VARIOUS 2-θ INCREMENTS

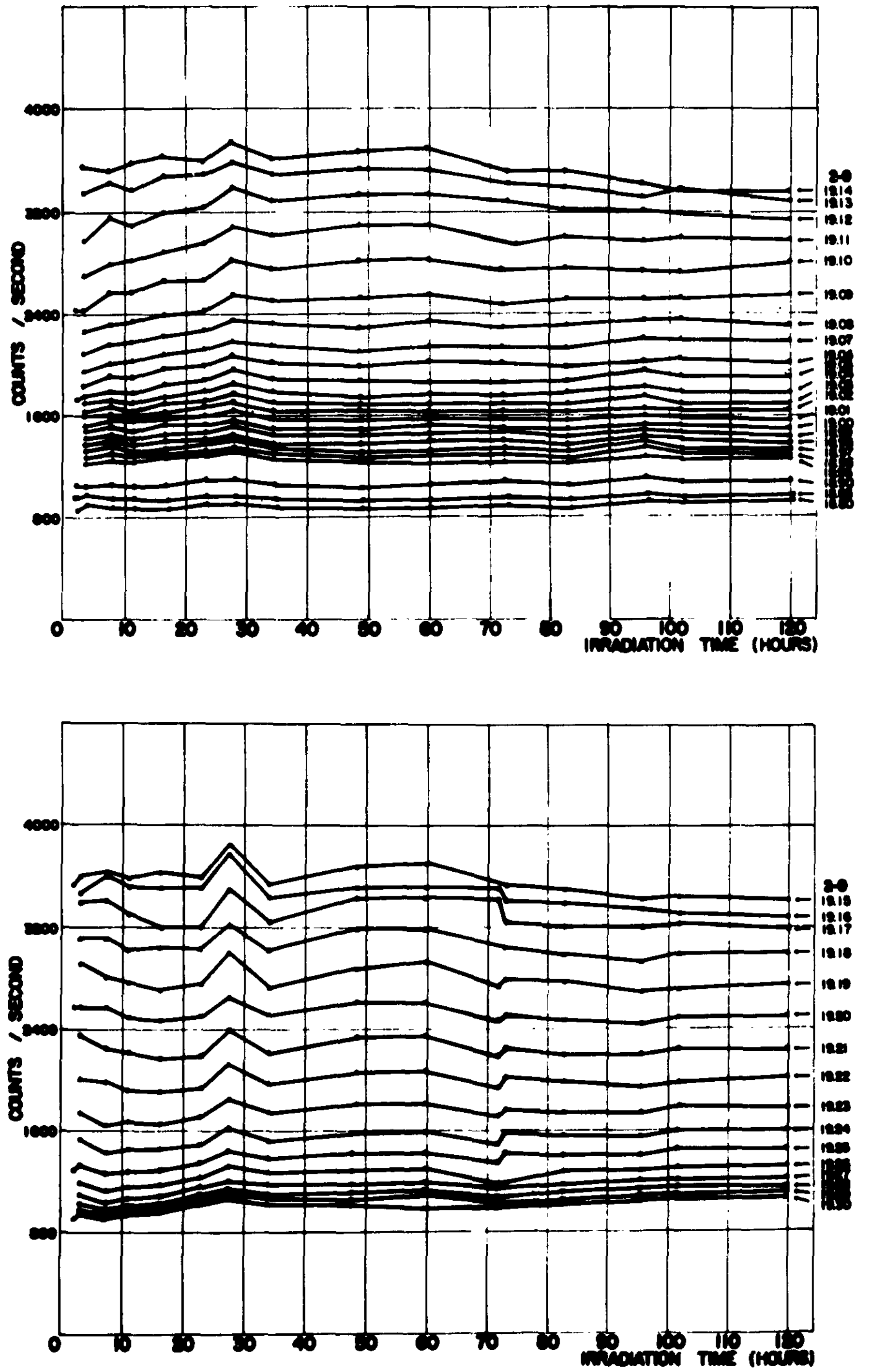

Figure 3

VARIOUS LINE PROFILES FOR TLH_3

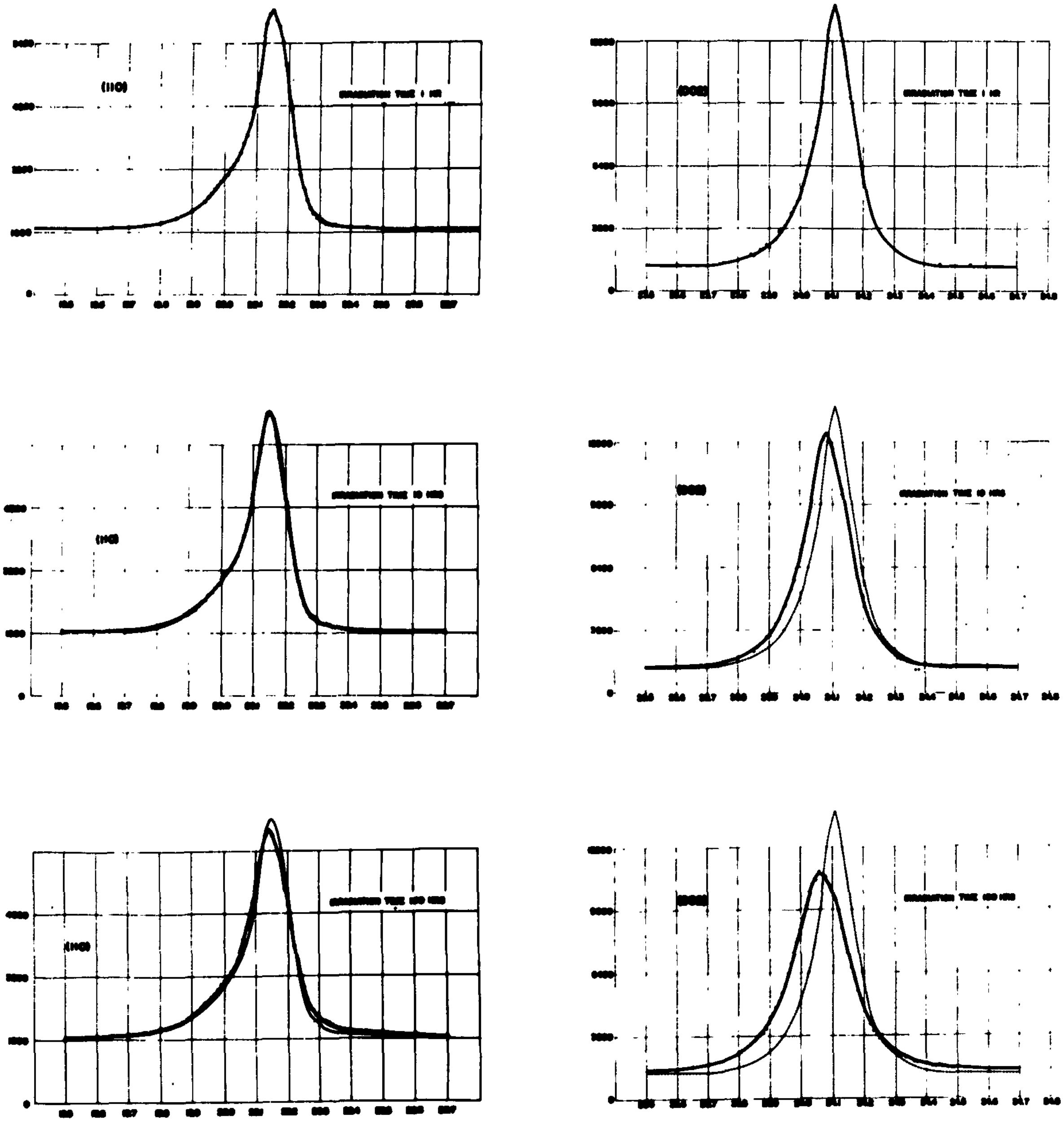

Figure 4

VARIOUS LINE PROFILES FOR TLH_3

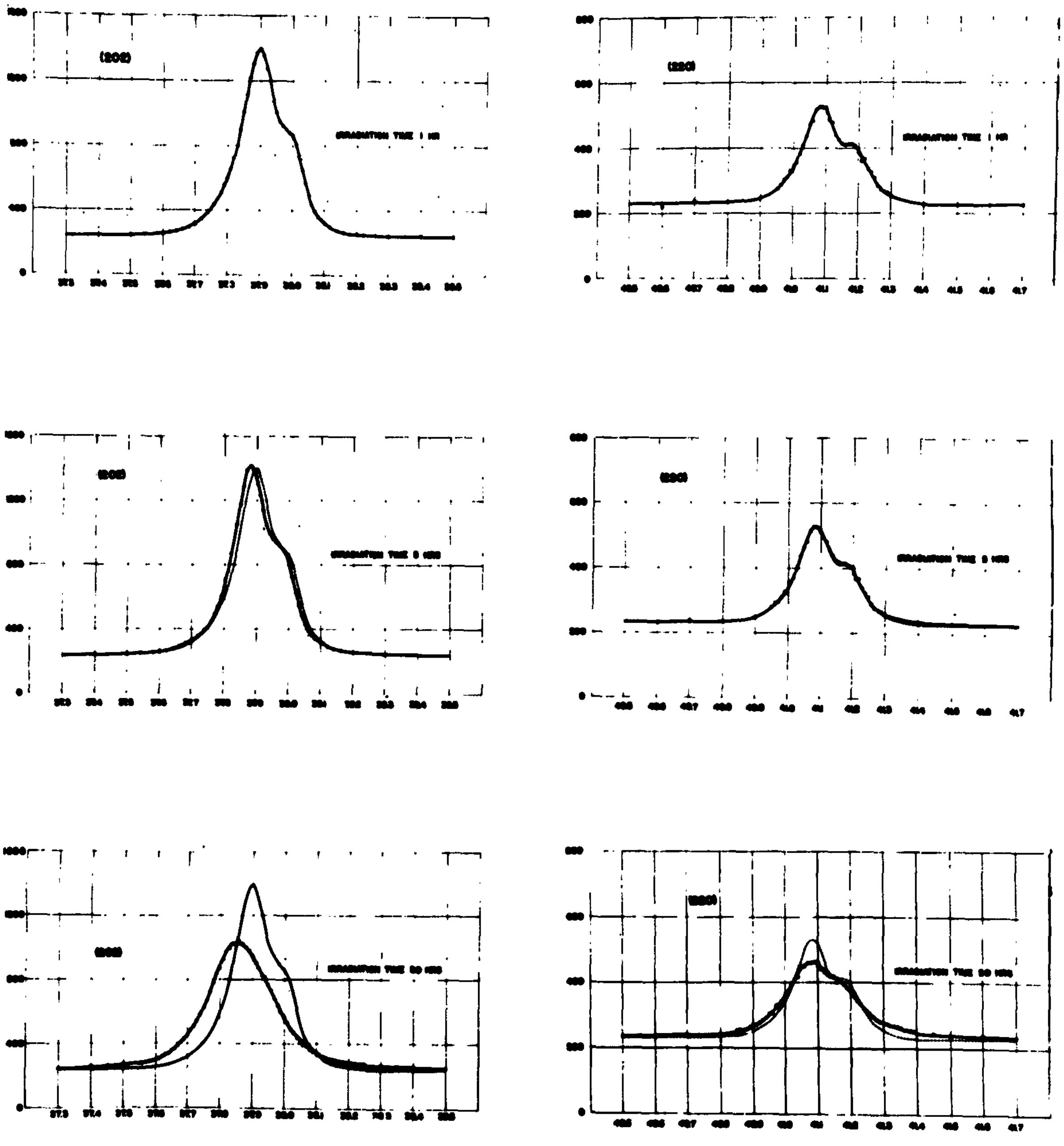

Figure 5

reflections determined by the a and b direction remain relatively unchanged.

Quantitative evaluations were done by calculation of the abscissae of the center of gravity for each line profile and by using this value as the diffraction angle 2Θ in the Bragg formula for lattice constant determination. Since the tails of the line profiles were rather inaccurate we used the Ladell[3] method which considers only the main part of a line profile and cuts off the tails with a line drawn parallel to the background in a theoretically well defined way. But even with this cut-off method, the results become less reliable as the lines become broader and for advanced irradiation times no quantitatively reliable values can be obtained. Figure 6 shows relative lattice constant changes for a and c. c was calculated from the 202 reflection by assuming a to be constant, an assumption that undoubtedly introduces some errors into the result. Some changes, although much smaller than in the c-direction, undoubtedly take place for a also. They may be either

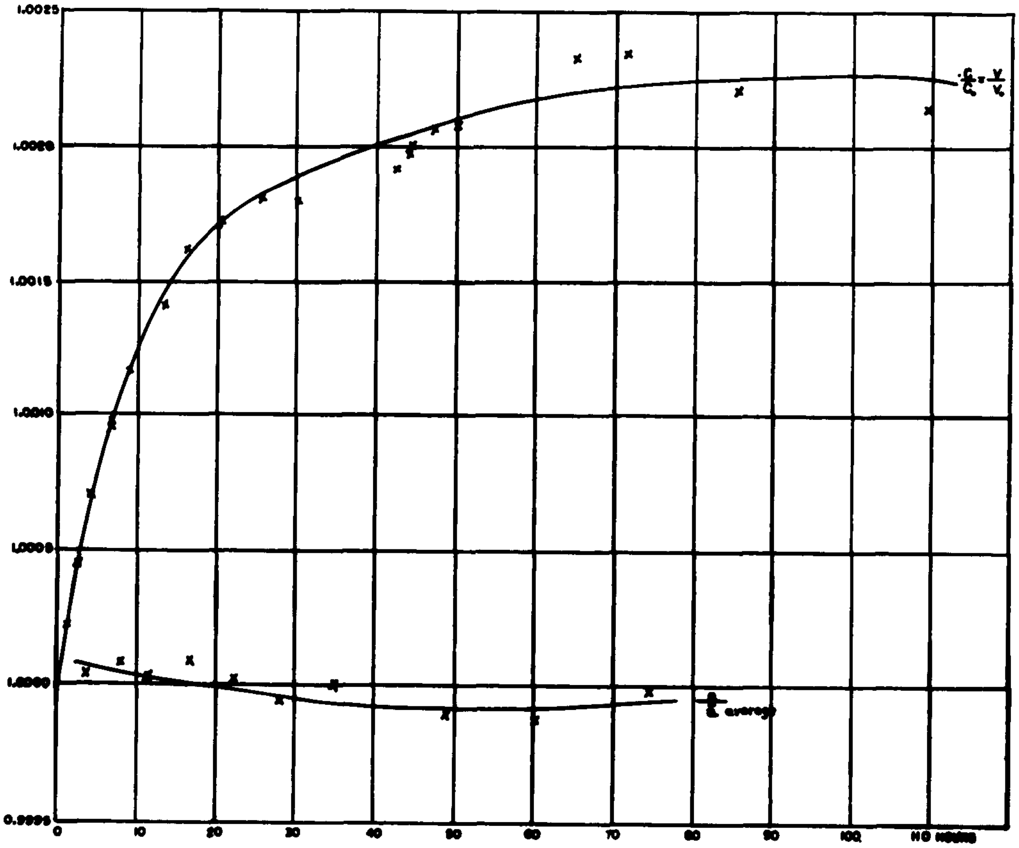

RELATIVE LATTICE CONSTANT CHANGES VERSUS IRRADIATION TIME

Figure 6

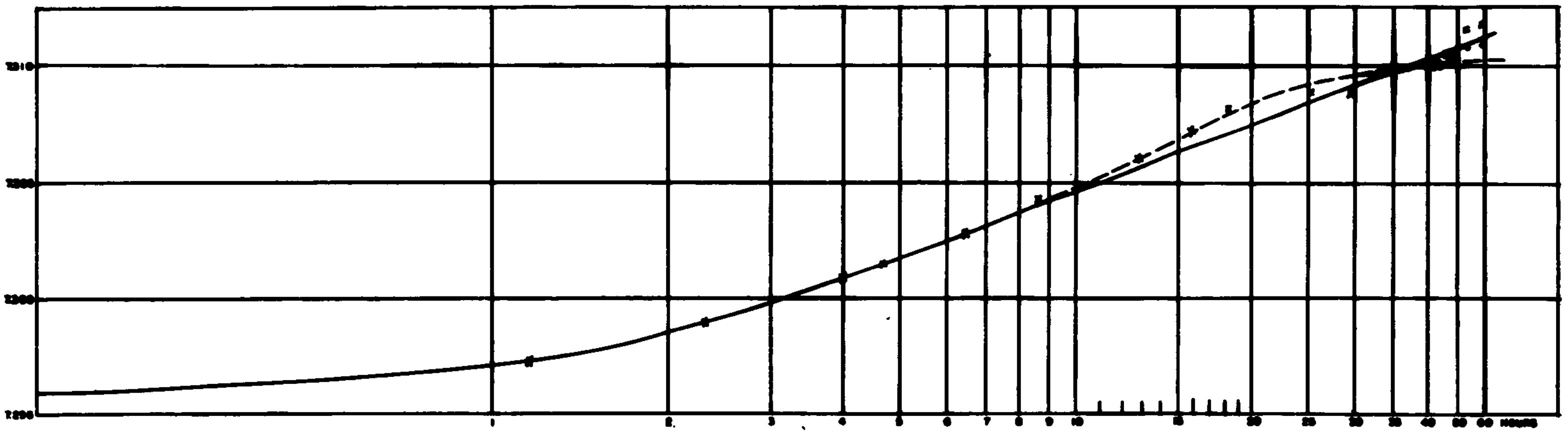

LATTICE CONSTANT "C" CHANGE
VERSUS LOGARITHM OF THE IRRADIATION TIME

Figure 7

lattice contraction as shown in Fig. 6 or lattice expansion, different for different samples. A plot of c versus the logarithm of the irradiation time (Fig. 7) shows a rather linear region between 2 and 200 hours. An extrapolation of the time to zero is rather difficult since the changes are most pronounced at the beginning of an experiment.

The lattice constant changes can be reversed by annealing the sample as shown in Fig. 8, and the line qualities can also be improved. However, at the beginning of the annealing process the line profile becomes even broader than at the end of the previous

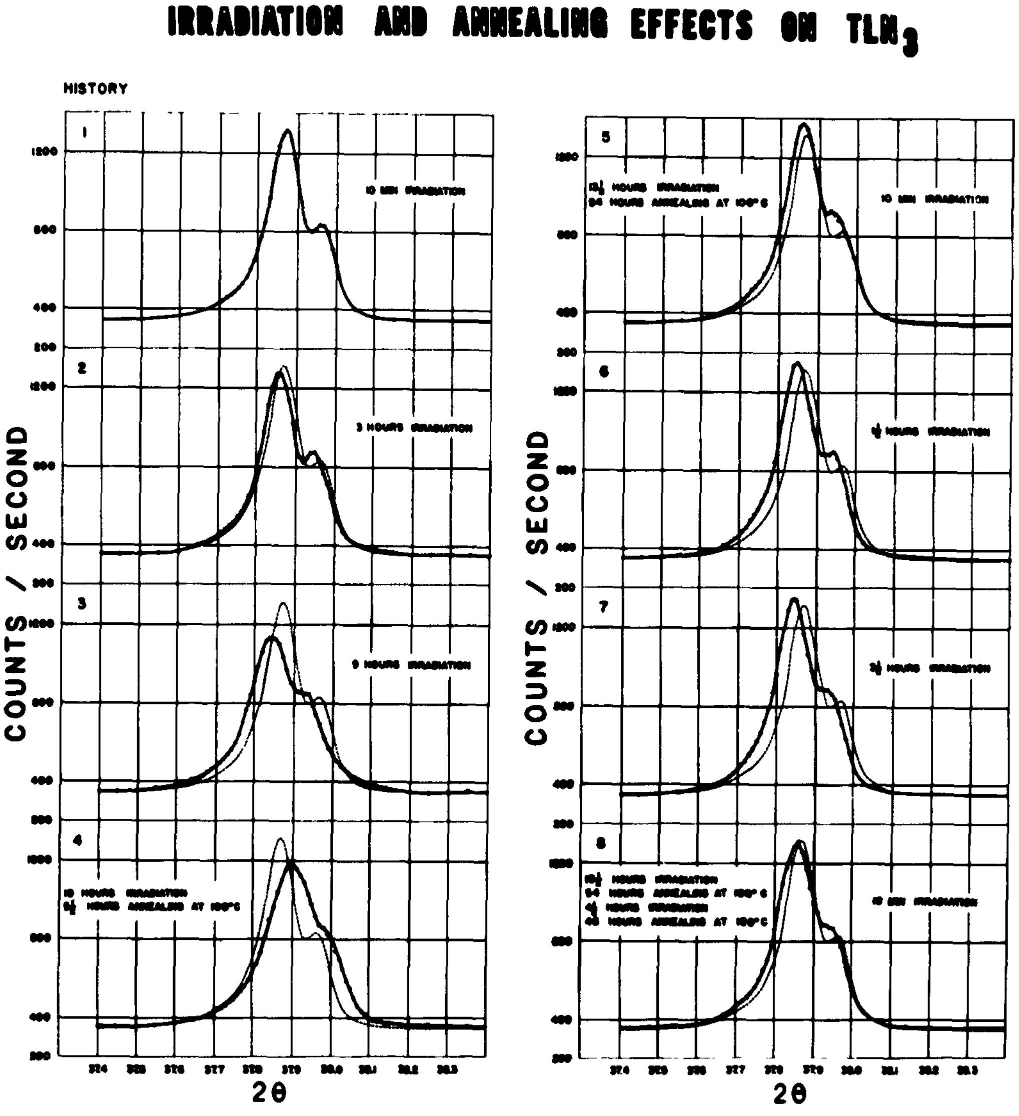

Figure 8

irradiation period. The peak, on the contrary, is shifted towards even smaller angles than at the beginning of the experiment. The annealing time of 54 hours at 100° C after only 13½ hours of irradiation does not seem sufficient to restore the original crystal quality nor does a 46 hour annealing after 3½ more hours of irradiation. It may be noted at the beginning of each irradiation that during the first hour the peak quality seems to improve as observed by the better resolution of the α and α_2 peaks. An appreciable line profile change occurs only after about 3 hours while line shifts take place immediately and are strongest at the beginning. The lattice constant changes, corresponding to Fig. 8, are shown in Fig. 9. Whether or not the stronger changes are typical after the first annealing cannot yet be decided. Annealing effects can also be observed at room temperature; Fig. 10, which shows the intensities for angle increments to the right of the diffraction peak, is similar to Fig. 2b, except that the irradiation was interrupted twice. The two effects of this incomplete annealing are a change in the line profile and an increased rate of change upon renewed irradiation. More data have to be gathered in order to explain the annealing mechanism.

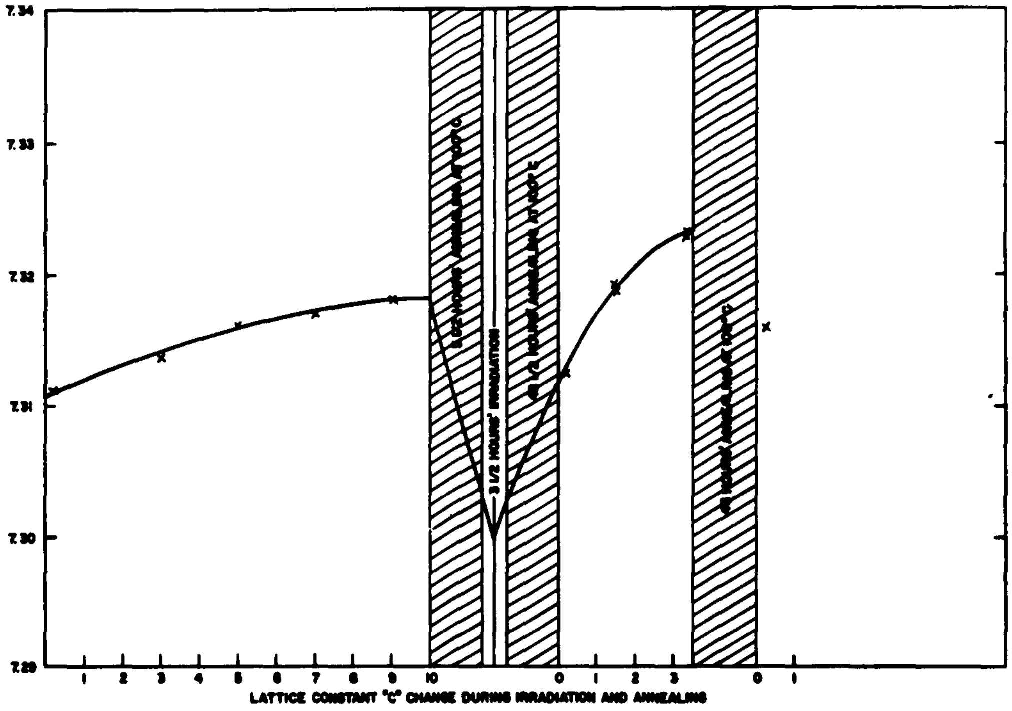

Figure 9

As mentioned above, the x-ray irradiation not only causes line shifts but also line profile changes. In order to evaluate those, one has to eliminate the effects of the "instrument broadening".

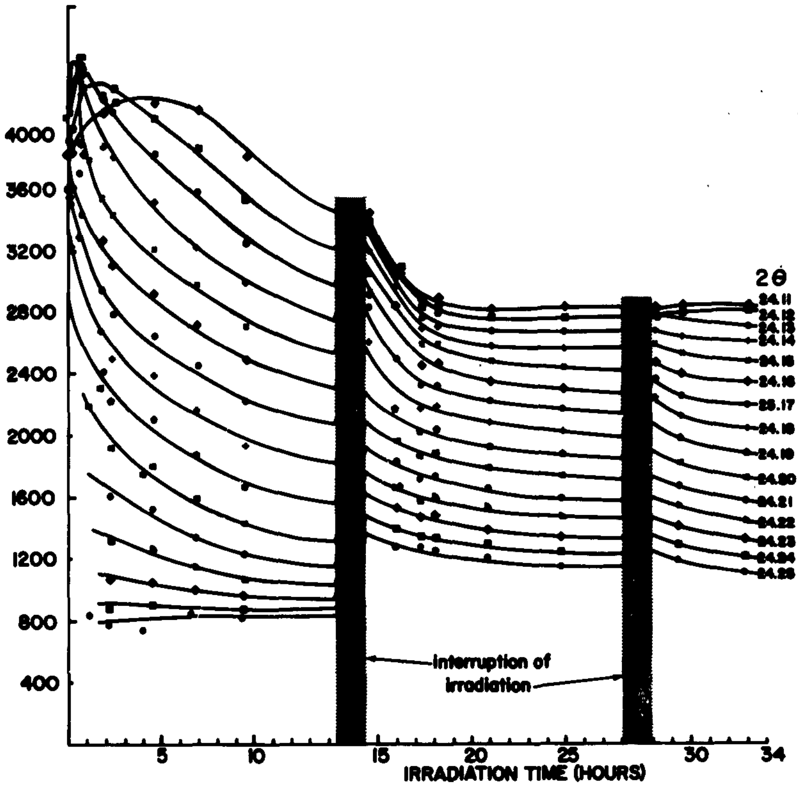

IRRADIATION AND ANNEALING EFFECTS AT ROOM TEMPERATURE

Figure 10

This is possible by mathematical unfolding procedures, presuming one knows the diffraction line profile of perfect crystals diffracting at the same angle and under the same experimental conditions as the sample in question. We tried to obtain this required function g(x) from curves such as in Fig. 2 by extrapolation to irradiation time zero. The required line profile f(x) due to radiation broadening only is obtained by unfolding the measured broadened profile h(x);[6]

$$h(x) = \int_{-\infty}^{+\infty} f(y)g(x-y)dy.$$ (The variable in this case is in units of angular displacement of a point from the theoretical scattering angle 2θ.) This is achieved by Fourier procedures and the desired function f(y) can also be obtained in the form of a Fourier series. A computer program for these lengthy computations was available[4]. The unfolding results for a special line profile are shown in Fig. 11. The broadening of the line profiles with increasing irradiation time becomes evident from Fig. 12. The Fourier coefficients A_n of

the series $f(y) = \sum_{-\infty}^{\pm\infty} A_n \cos(2\pi n h_3)$ allow conclusions as to the character of the line broadenings. However, the results of this approach will be discussed at a later time. The only evident result from Fig. 13, showing plots of A_n versus n for different irradiation times, is the following: as in the case of the lattice constant shifts, strong changes occur mainly at the beginning of the irradiation period and slow down later on. It is possible that the starting time of this process does not coincide with the beginning of irradiation, but may occur one to three hours later.

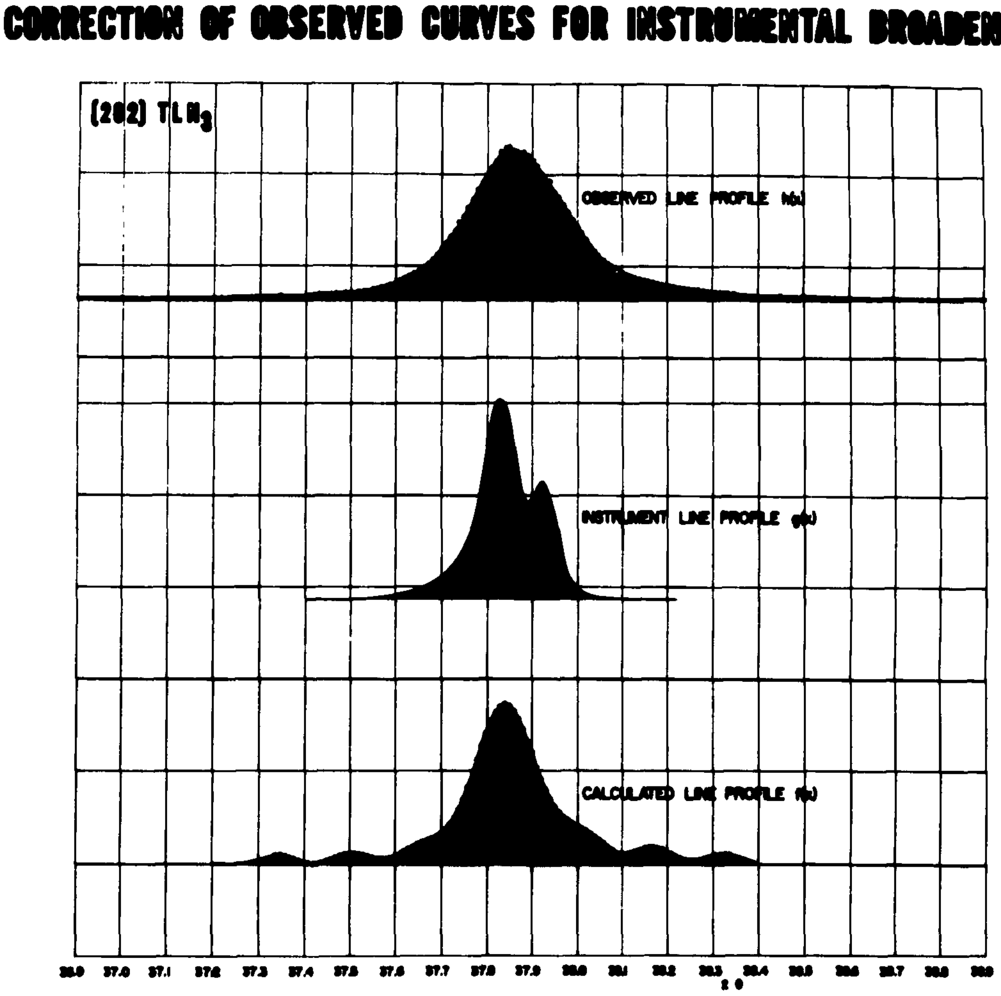

Figure 11

CALCULATED LINE PROFILES FOR THE 202 REFLECTION OF TLN_3

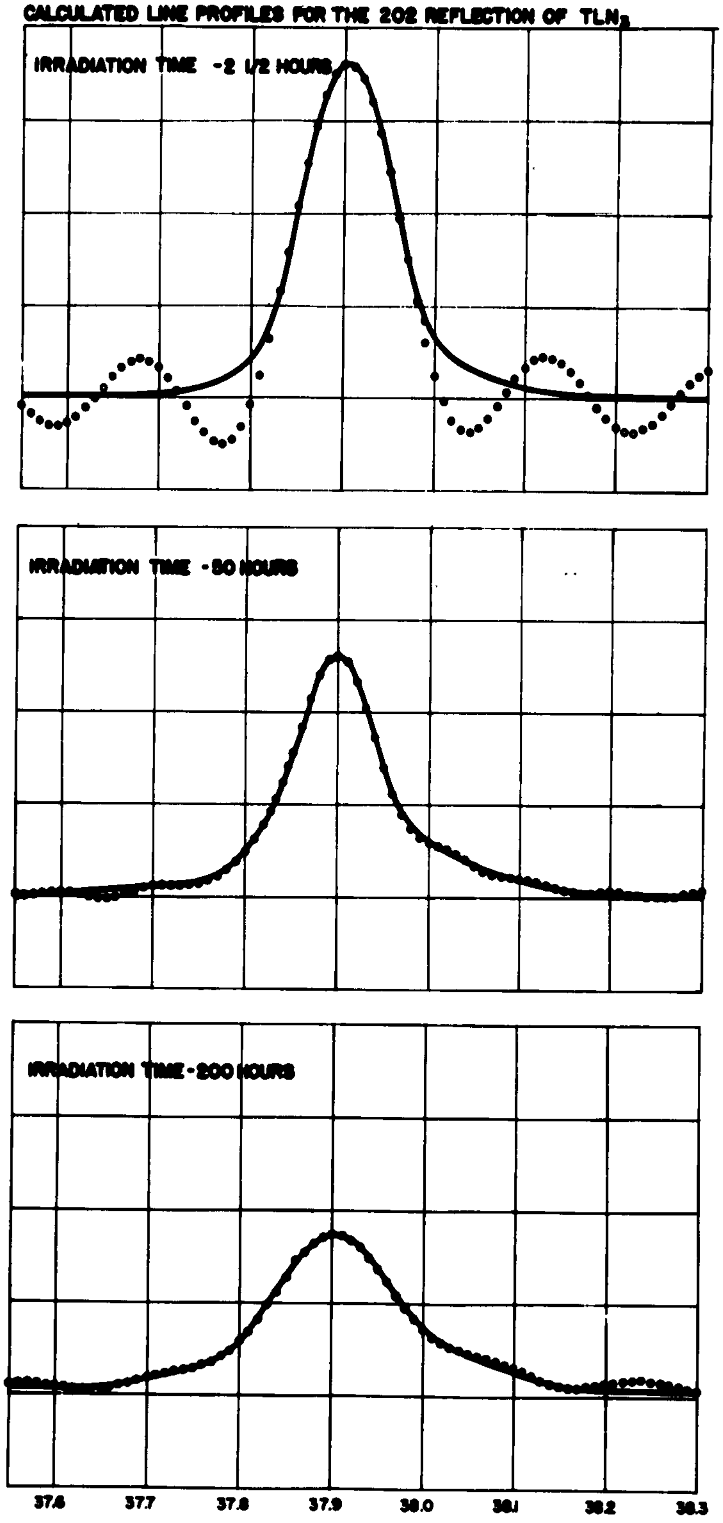

Figure 12

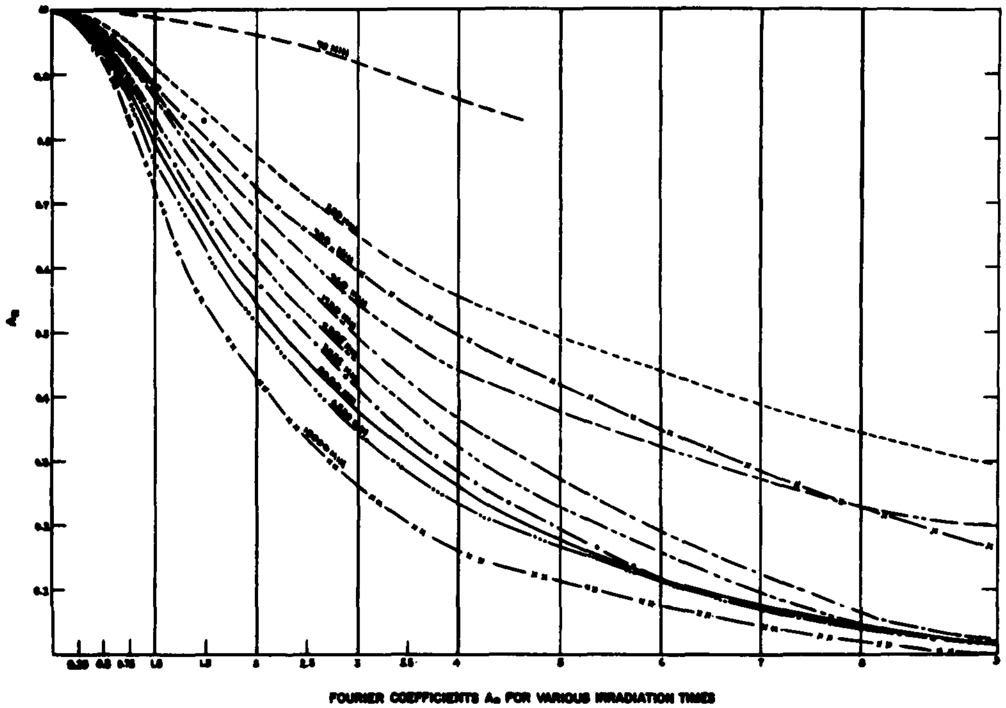

Figure 13

ACKNOWLEDGMENTS

We wish to thank the Computer Section, especially Mr. Harold H. Smith and Mrs. Barbara M. O'Carroll for the many computations required in this work, Dr. E. R. Boyko, Westinghouse, for his IBM 650 program for Fourier analysis of line shapes, and Mr. H. Rosenwasser for preparing the TlN_3 crystals.

REFERENCES

1. A. R. Jones, Proc. Roy. Soc. (London), Ser. A, 190, 382 (1947).

2. Douglas S. Billington and James H. Crawford, Jr., "Radiation Damage in Solids," Princeton University Press, page 286.

3. J. Ladell, W. Parrish, and J. Taylor, Acta Cryst, 12, 561 (1959).

4. E. R. Boyko and G. J. Mohn, Westinghouse Rpt, WAPD-T-885 (Nov 1958).

5. B. E. Warren and B. L. Averbach, J. Applied Phys. 21, 595 (1950).

6. A. R. Stokes, Proc. Phy. Soc. 61, 382 (1948).

X-RAY RADIATION DAMAGE OF ALKALI AZIDES

by

E. L. Hendricks and B. Krause
Basic Research Group
U. S. Army Engineer Research and Development Laboratories
Fort Belvoir, Virginia

The work presented here is an addition to the results, presented at the last Contractors' Conference, on anisotropic lattice constant changes in x-ray irradiated azides. These changes were calculated from x-ray powder diffraction data. The azides studied were all of similar structure, namely, either a regular or slightly distorted KN_3 structure[1,2,3,4] (Fig. 1). This structure is

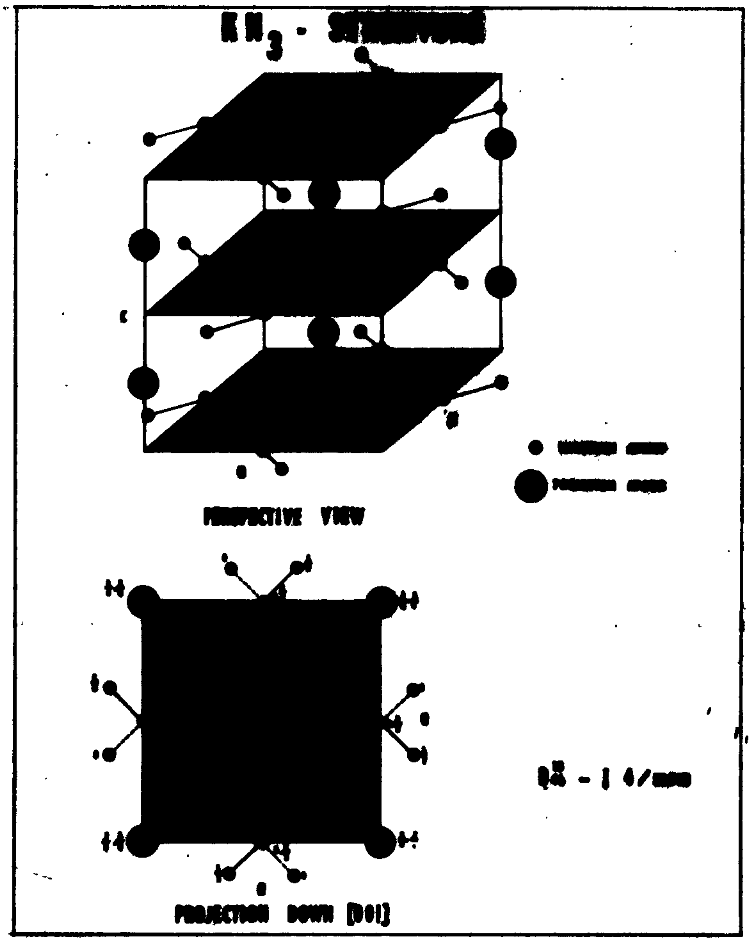

Figure 1

tetragonal and resembles the cubic CsCl structure. The lower point symmetry of the N_3^- ion as compared with the Cl^- ion gives rise to the tetragonal dimensions of KN_3, RbN_3, CsN_3, and TlN_3. AgN_3 being partly covalent is reduced still more to an orthorhombic structure. The additional work was done to determine if the similarities of decomposition observed were coincidence or a typical reaction for this type structure.

Last year data on AgN_3 and TlN_3 were presented showing lattice changes with irradiation. Both showed relatively strong expansions in the crystallographic "c" direction. The "a" direction for TlN_3 showed practically no change.

An investigation of RbN_3 has been made using peak position data only. An expansion in the "c" direction as with other samples was observed while the "a" direction remained unchanged. This expansion is of the same order of magnitude as that for TlN_3 (Fig. 2).

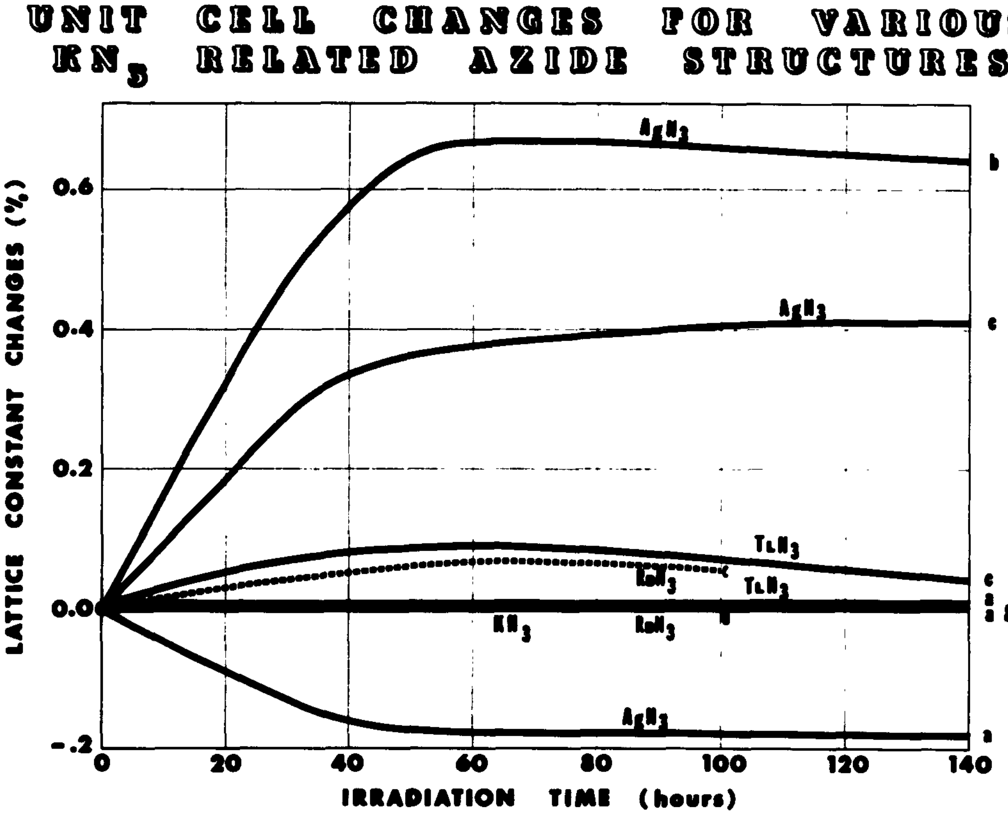

Figure 2

It was observed that where a lattice constant expansion was observed, it was accompanied by a broadening of the line profile of

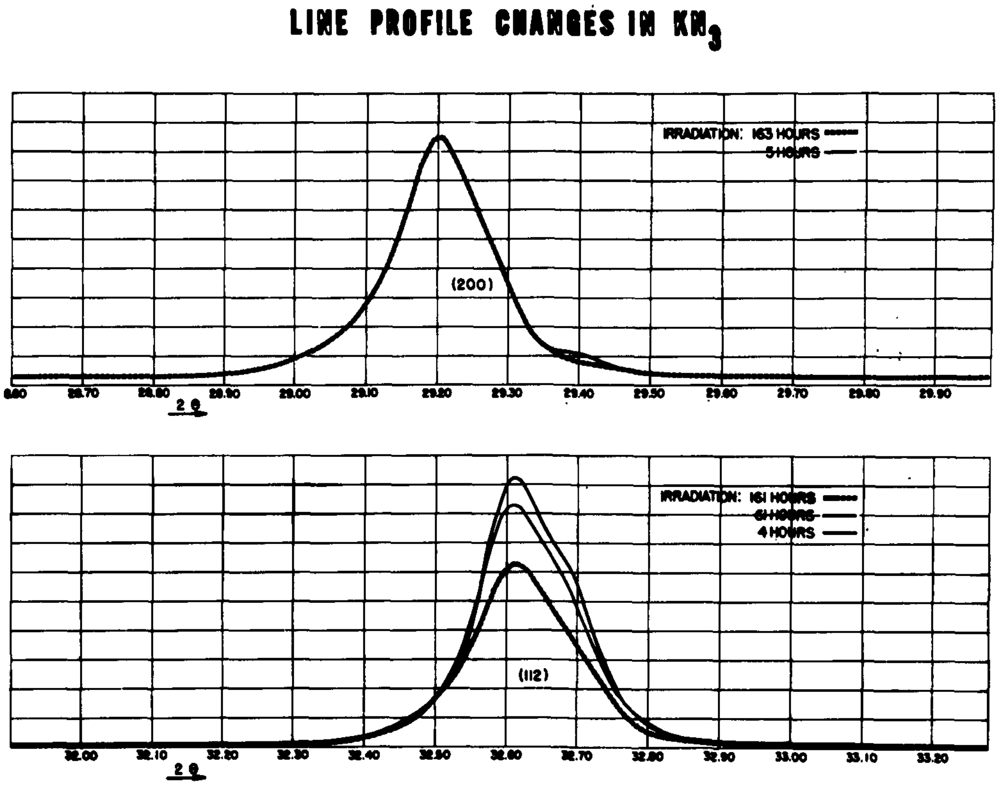

Figure 3

the reflection. If the converse of this were to hold true a change in KN_3 should occur, though it was not observed last year within the accuracy of the measurements (Fig. 3). Consequently, this profile data was reevaluated. The center of gravity instead of peak position was used for determining the diffraction angle thus getting a smaller statistical error. The results indicated an expansion in the "c" direction while the "a" direction was unchanged (Fig. 4).

If it is possible to draw conclusions from the few samples studied, the data indicates that lattice constant changes are much less in predominantly ionic than in partly covalent compounds. In all cases observed there was a comparatively strong expansion perpendicular to the plane of the nitrogen chains. The reflections which show the lattice constant expansions also show the most broadening which indicates the highest degree of disorder. Small lattice constant contractions on the contrary, as observed by us in the "a" direction of AgN_3 cause little disorder.

Keating[5] exposed NaN_3 to pile irradiation and found the "c" direction contracting slightly and reported no change in "a", whereas we observed changes in the "c" direction with "a" nearly

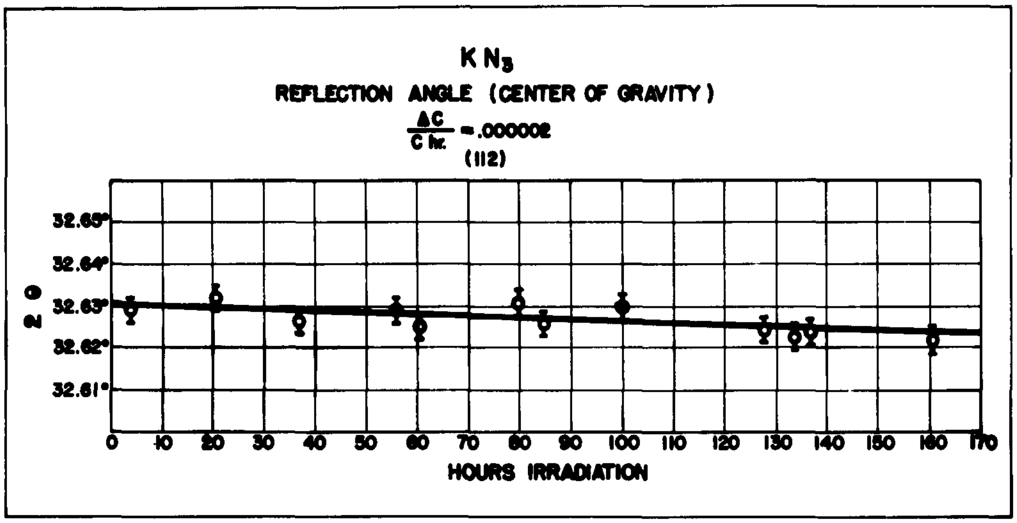

Figure 4

constant in the above mentioned azides. Along with this he observed that the (009) reflection was not much broadened while the (110) reflection was. This is no contradiction to our results if we take into account the different structure. In NaN_3 the nitrogen chains are perpendicular to the a-b planes instead of horizontal as in the above mentioned azides. We suspected that the strong line broadening of the (110) peak was coupled with a lattice constant expansion perpendicular to the nitrogen chains.

We tested a NaN_3 sample and found that this expansion was present and in the same order of magnitude as for KN_3. This expansion cannot be explained by stacking fault theory as applied by Keating, which predicts lattice constant shifts for reflections where the equation $h\text{-}k = 3M\pm 1$ (h, k - Miller indices, M - natural number) holds. The shifts required by stacking fault theory could not be detected by Keating. He did, however, report a contraction in the "c" direction (direction of the nitrogen chains) which would correspond to the lattice constant contraction of "a" in AgN_3. Since different mechanisms of decomposition may be present, the lattice expansions observed by us do not preclude the possibility of stacking faults being present.

If the rule that a major disorder occurs in planes perpendicular to the plane of the nitrogen chains holds true, it should be a valuable aid in determining the structure of α-lead azide. α-lead azide shows an expansion in the "a" direction indicating that the nitrogen chains should be parallel to the (b-c) planes.

ACKNOWLEDGMENTS

The authors would like to thank the Computer Section, especially Mrs. O'Carroll, for performing the many calculations related to this research, and Mr. Rosenwasser for preparing the Ag, Tl, and Rb azides.

REFERENCES

1. Gunther, Porger, and Rosebaud, Z. Physik. Chem. Abt. B, 6, 459 (1930). (C. A. 24:2930).
2. Hendricks and Pauling, J. Am. Chem. Soc. 47, 2904 (1925).
3. Groth, "Chemische Krystallographie", Engelmann, Leipzig, 1908, Vol. 1, p. 204.
4. Wyckoff, R. W. G., "Crystal Structures", Vol. II, Chap. 6, Table p. 7, (Interscience, New York, 1952).
5. Keating, D. T., J. Phys. Chem. Solids, 20, 150 (1961).

INORGANIC OZONIDES

by

Irvine J. Solomon
Armour Research Foundation
Chicago, Illinois

Alkali metal ozonides, except lithium ozonide, may be prepared by the reaction of either the metal hydroxide or superoxide with dilute gaseous ozone. All of these compounds are red, paramagnetic solids that are soluble in liquid ammonia; their stability increases as the size of the cation increases.

Sodium ozonide appears to exist in two forms; one is soluble in liquid ammonia and unstable at room temperature, and the other is insoluble and stable.

Ammonium ozonide has been prepared by the low temperature ozonization of ammonia, and has been characterized by electron paramagnetic resonance and visible spectroscopy. Its visible spectrum has the characteristic five-peaked ozonide structure which shows a maximum in the vicinity of 450 mμ. The compound is thermally unstable and starts to decompose above -120° C. Its decomposition products are ammonium nitrate, oxygen, and water.

Tetramethylammonium ozonide has been prepared and characterized. Electron paramagnetic resonance measurements show that the compound is a free radical with one unpaired electron. Its visible spectrum is very similar to those of the alkali metal ozonides, which have wavelength maximums near 450 mμ. The solubility of tetramethylammonium ozonide at -63° C is 1.3 ± 0.1 g per 100 g of liquid ammonia. The heat of formation of the pure material was found to be 49.5 ± 4.2 kcal per mole.

The structure of potassium ozonide has been calculated from x-ray diffraction powder data.

INTRAMOLECULAR CHANGES INITIATED BY ELECTROPHILIC ATTACK ON ALKYL AZIDES

by

J. H. Boyer
American Chemical Society
Washington, D. C.

A measure of the base strength of hydrogen azide (pKa for $H_2N_3^+ = -6.21$)[1] suggests that simple alkyl azides will be qualitatively comparable to simple aromatic ketones in base strength (pKa for $C_6H_5C(=\overset{+}{O}H)CH_3 = -6.03$ and p-$CH_3C_6H_4C(=\overset{+}{O}H)\ CH_3 = -5.35$).[2] Each terminal nitrogen of the azido group may be attacked by the proton, and presumably by other electron deficient reagents; however, our present information is most reasonably satisfied with the assumption that protonation occurs at the substituted nitrogen.

$$RN{=}\overset{+}{N}{=}NH \rightleftharpoons RN_3 + H^+ \rightleftharpoons RNH\overset{+}{N}{\equiv}N$$

Reversible dissociation of the conjugate acid of an alkyl azide generally favors the formation of the proton and an alkyl azide rather than a carbonium ion and hydrogen azide. Resonance stabilization of the triphenylmethyl cation accounts for the exceptional dissociation of the conjugate acid of triphenylmethyl azide in concentrated sulfuric acid at 150°.[3]

Irreversible dissociation of nitrogen from the conjugate acid apparently occurs at measurable rates in weaker acid environments but may occur explosively fast in the presence of strong acid. Apparently rearrangement is synchronous with loss of nitrogen.[4] It is assumed that the same conjugate acid may result either from an alkyl azide in strong acid or from the corresponding carbinol and hydrogen azide in strong acid. This is demonstrated in the formation of piperidine and cyclopentanone from cyclopentyl azide and from cyclopentanol.[3]

These reversible and irreverisble reactions represent general acid catalysis of simple alkyl azides.

In an acid catalyzed reaction of α-azidophenylacetic acid, phenyl migrates in preference to hydrogen to bring about the formation of the assumed intermediate anil of glyoxylic acid.[5] Dimerization of the anil with the formation of o,o'-diamino stilbenedicarboxylic acid is not understood. The same product was previously obtained from the anil of glyoxylic acid in acetic acid and from aniline and dichloroacetic acid in the presence of sodium acetate.[6]

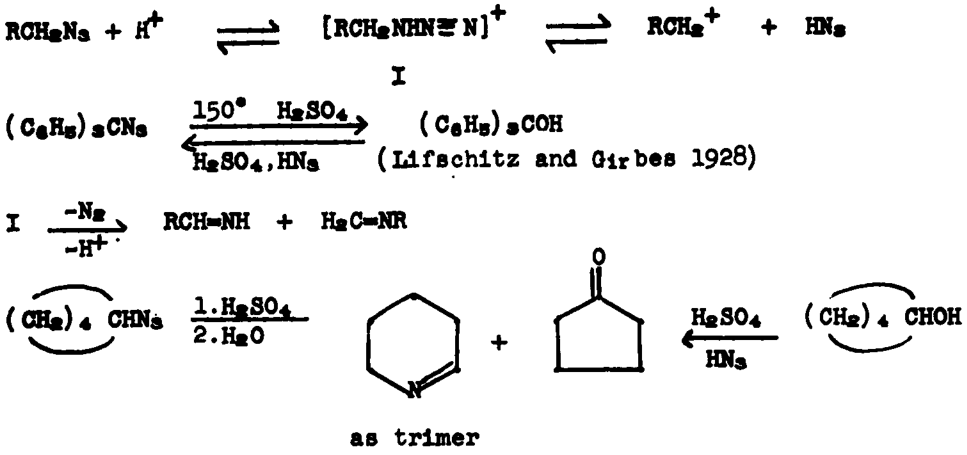
RCH₂N₃ + H⁺ ⇌ [RCH₂NHN≡N]⁺ ⇌ RCH₂⁺ + HN₃
I
(C₆H₅)₃CN₃
150° H₂SO₄
H₂SO₄, HN₃
(C₆H₅)₃COH
(Lifschitz and Girbes 1928)
I
-N₂
-H⁺
RCH=NH + H₂C=NR
(CH₂)₄ CHN₃
1. H₂SO₄
2. H₂O
N
O
H₂SO₄
HN₃
(CH₂)₄ CHOH
as trimer

Boyer, Canter, Hamer and Putney 1955, 1956.

Figure 1

$$C_6H_5CH(N_3)CO_2H \xrightarrow[-N_2]{H_2SO_4} [C_6H_5N{=}CHCO_2H]$$

I

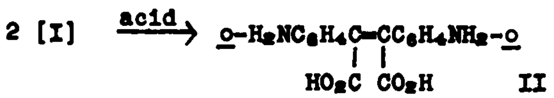

$$2\,[I] \xrightarrow{acid} \underline{o}\text{-}H_2NC_6H_4\underset{HO_2C}{C}{=}\underset{CO_2H}{C}C_6H_4NH_2\text{-}\underline{o} \qquad II$$

Boyer and Stocker 1956.

$$C_6H_5NH_2 + Cl_2CHCO_2H \xrightarrow{AcONa} II \xleftarrow{AcOH} I$$

Heller 1910

Figure 2

Acid catalysis of simple alkyl azides promotes the migration of hydrogen, in preference to alkyl, from carbon to nitrogen; however, the products required from both rearrangements are detected.[3,7] It appears that smaller alkyl groups migrate more readily than larger ones.

In earlier investigations it was anticipated that acid catalysis of ethylene azidohydrin in the presence of benzaldehyde would produce aminoacetaldehyde *in situ* and that subsequent condensations would lead to a new synthesis of isoquinoline. This did not occur. The products formed in good yield were N-β-hydroxyethyl-benzamide and its dehydration product 2-phenyl-Δ^2-oxazoline.[8]

$$[RCH_2NHN_2]^+ \longrightarrow \underset{I}{RCH{=}NH} + \underset{II}{H_2C{=}NR}$$

$$I \xrightarrow{H_2O} RCHO + NH_3 \qquad II \xrightarrow{H_2O} H_2CO + RNH_2$$

R	RCHO(%)	
n-C_3H_7	40	(H_2CO, 12%; n-$C_3H_7NH_2$, 6%; NH_3, detected)
n-C_5H_{11}	73	
n-C_7H_{15}	60	Boyer, Canter, Hamer, Putney 1956.
n-$C_{11}H_{23}$	88	Boyer, Porter, Unpublished results.

Figure 3

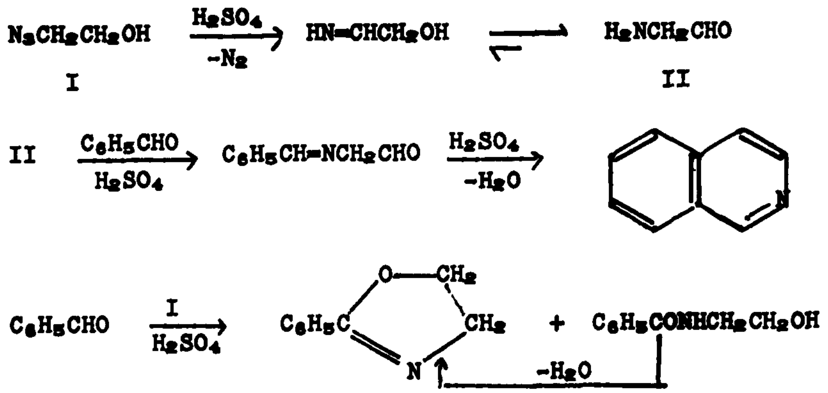
N₃CH₂CH₂OH
H₂SO₄
-N₂
HN=CHCH₂OH
H₂NCH₂CHO
I
II
II
C₆H₅CHO
H₂SO₄
C₆H₅CH=NCH₂CHO
H₂SO₄
-H₂O
N
C₆H₅CHO
I
H₂SO₄
O
CH₂
C₆H₅C
CH₂
N
+ C₆H₅CONHCH₂CH₂OH
-H₂O

Boyer, Hamer 1955.

Figure 4

Apparently the competition for the azide favored the conjugate acid of benzaldehyde over the proton. This was unexpected since earlier reports indicated that no reaction occurred between methylazide and either benzoic acid[9] or acetophenone[10] in sulfuric acid. The new reaction was immediately reminiscent of the Schmidt reaction between benzaldehyde and hydrogen azide in sulfuric acid leading to the formation of benzamide, formanilide, benzonitrile and phenyl isocyanide. The generally accepted explanation for the Schmidt reaction[10,11] accounts for these products.

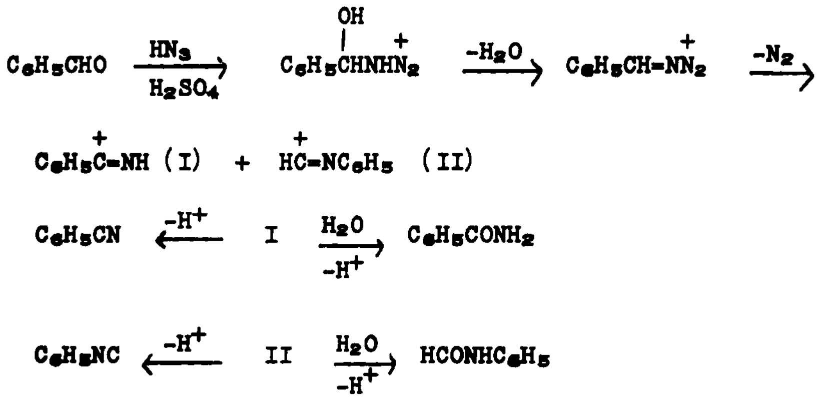

$$C_6H_5CHO \xrightarrow[H_2SO_4]{HN_3} C_6H_5\overset{OH}{\overset{|}{C}}HNH\overset{+}{N}_2 \xrightarrow{-H_2O} C_6H_5CH{=}N\overset{+}{N}_2 \xrightarrow{-N_2}$$

$$C_6H_5\overset{+}{C}{=}NH\ (I) + H\overset{+}{C}{=}NC_6H_5\ (II)$$

$$C_6H_5CN \xleftarrow{-H^+} I \xrightarrow[-H^+]{H_2O} C_6H_5CONH_2$$

$$C_6H_5NC \xleftarrow{-H^+} II \xrightarrow[-H^+]{H_2O} HCONHC_6H_5$$

Smith (1948); Newman (1947).

Figure 5

A similar argument suggests four products from benzaldehyde and an alkyl azide in sulfuric acid. Two of these are not diagnostic since they are also produced by general acid catalysis of the acid. The other two, an N-alkylaniline and an N-alkylbenzamide, have each been obtained in several examples.

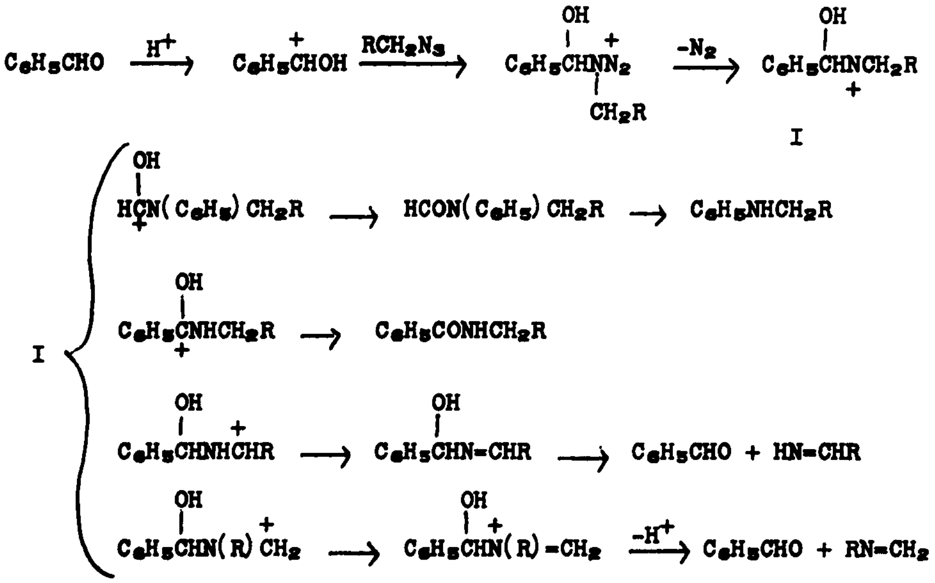

$$C_6H_5CHO \xrightarrow{H^+} C_6H_5\overset{+}{C}HOH \xrightarrow{RCH_2N_3} C_6H_5\overset{OH}{\overset{|}{C}}H\underset{CH_2R}{\underset{|}{N}}\overset{+}{N}_2 \xrightarrow{-N_2} C_6H_5\overset{OH}{\overset{|}{C}}H\overset{}{\underset{+}{N}}CH_2R \quad I$$

$$I \begin{cases} H\overset{OH}{\overset{|}{\underset{+}{C}}}N(C_6H_5)CH_2R \longrightarrow HCON(C_6H_5)CH_2R \longrightarrow C_6H_5NHCH_2R \\ C_6H_5\overset{OH}{\overset{|}{\underset{+}{C}}}NHCH_2R \longrightarrow C_6H_5CONHCH_2R \\ C_6H_5\overset{OH}{\overset{|}{C}}HNH\overset{+}{C}HR \longrightarrow C_6H_5\overset{OH}{\overset{|}{C}}HN{=}CHR \longrightarrow C_6H_5CHO + HN{=}CHR \\ C_6H_5\overset{OH}{\overset{|}{C}}HN(R)\overset{+}{C}H_2 \longrightarrow C_6H_5\overset{OH}{\overset{|}{C}}H\overset{+}{N}(R){=}CH_2 \xrightarrow{-H^+} C_6H_5CHO + RN{=}CH_2 \end{cases}$$

Figure 6

The reaction carried out in benzene as solvent affords an N-alkyl aniline with no detectable amounts of an N-alkylbenzamide. On the other hand the reaction with excess benzaldehyde serving as solvent affords N-alkylbenzamides without N-alkylanilines. Perhaps aldehyde solvation of intermediates represses the migration of aryl groups from carbon to nitrogen.[8,12] The presence of strong electron releasing groups in positions ortho or para to the carbonyl carbon atom inhibits a reaction between aldehydes and azides probably as a result of a decrease in the acidity of the corresponding aldehyde conjugate acids. Electron attracting ring substituents, e.g., nitro, may inhibit the reaction at the earlier stage in which protonation of the aldehyde is required.

$$C_6H_5CHO + RN_3 \xrightarrow[\substack{H_2SO_4 \\ -N_2}]{C_6H_6} \xrightarrow{H_2O} C_6H_5NHR$$

R	Amine (%)	Unreactive benzaldehydes
n-Butyl	22	p-methoxy
n-Hexyl	25	p-nitro
n-Octyl	18	m-nitro
Phenyl	10	

$$p\text{-}CH_3C_6H_4CHO \xrightarrow[\substack{H_2SO_4 \\ C_6H_6}]{m\text{-}C_4H_9N_3} p\text{-}CH_3C_6H_4NHC_4H_9 \quad (21\%)$$

$$C_6H_5CHO + C_6H_5CH_2CH_2N_3 \xrightarrow{H_2SO_4} C_6H_5CONHCH_2CH_2C_6H_5 \quad (10\%)$$

Boyer, Hamer 1955. Boyer, Morgan, 1959.

Figure 7

In the formation of Δ^2 - oxazolines from aryl aldehydes and ethylene azidohydrins the effect of electron releasing groups as ring substituents in the aldehyde accounts for certain low yields but the effect of electron attracting substituents appears to be negligible. Similar results are observed in the formation of Δ^2 - dihydroöxazines from aryl aldehydes and trimethylene azidohydrin.[3,8]

The earlier observations that methyl azide did not react with benzoic acid[9] or acetophenone[10] were in agreement with the argument[10] for intermediate dehydration in the Schmidt reaction. With an alkyl group at nigrogen this is inhibited.

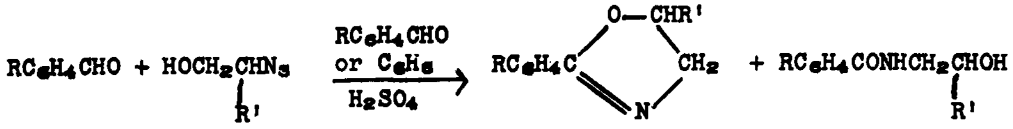

R	R'	Oxazoline (%)
H	H	77 (plus amide)
2-OH	H	15
4-OH	H	25
4-Cl	H	75
4-(CH$_3$)$_2$N	H	10
4-NO$_2$	H	70
3-NO$_2$	H	73 (or amide 63%)
H	CH$_3$	80
3-NO$_2$	CH$_3$	56
4-NO$_2$	CH$_3$	53

Boyer, Hamer 1956

Figure 8

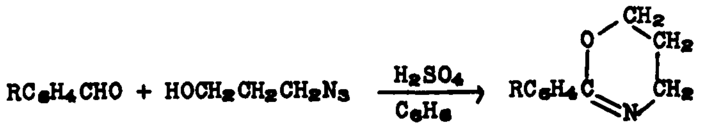

R	oxazine (%)
H	72
3-NO$_2$	82
4-NO$_2$	70

Boyer, Hamer 1955

Figure 9

Nevertheless we have found that a reaction does occur between certain aromatic ketones and alkyl azides in concentrated sulfuric acid.[13] Aromatic ketones of the type $C_6H_5COCH_2R$ in an inert solvent containing concentrated sulfuric acid are transformed by certain alkyl azides into benzaldehyde and an aldehyde corresponding to the alkyl group (RCH_2). The best yields (70-85%) of benzaldehyde are obtained from acetophenone. Alkyl azides are reduced to corresponding primary amines in 50-65% yields. A probable explanation requires (1) a Lewis acid-base reaction between the ketone conjugate

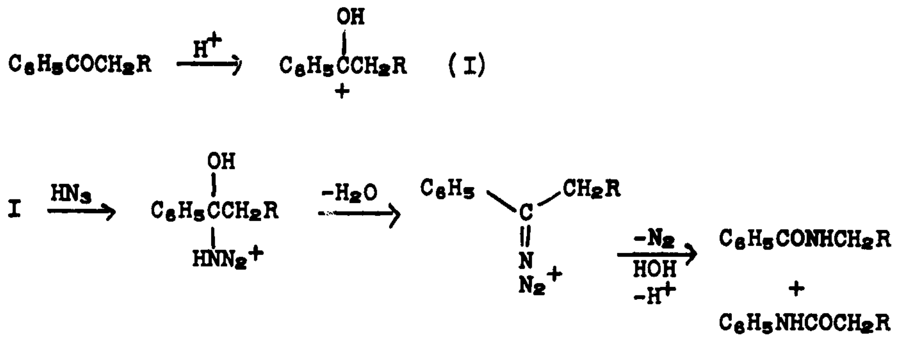

$C_6H_5COCH_3 \xrightarrow[H_2SO_4]{CH_3N_3} C_6H_5NHCOCH_3$ (2%)

Smith 1948.

$C_6H_5CO_2H \xrightarrow[H_2SO_4]{CH_3N_3}$ No product identified

Briggs, DeAth and Ellis 1942.

Figure 10

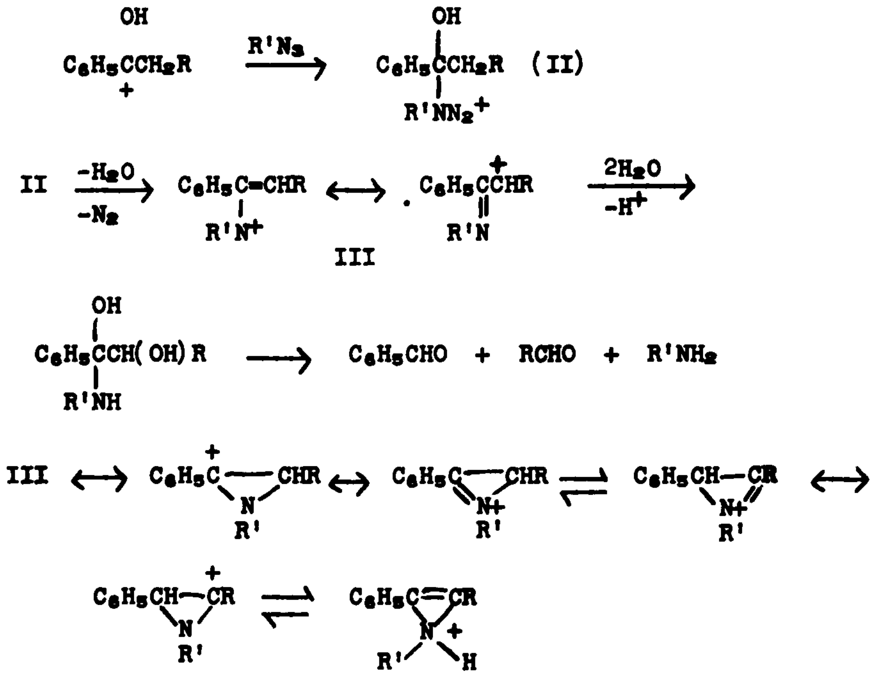

Boyer, Morgan 1959

Figure 11

acid and an alkyl azide, (2) dehydration and elimination of nitrogen and (3) recombination with water followed by proton elimination and breakdown of a proposed intermediate adduct of an α-ketoalcohol and a primary amine. The last step (3) apparently occurs only after dilution with water and is supported by the acid-catalyzed breakdown of phenacyl alcohol into benzaldehyde and formaldehyde.

$$C_6H_5COCH_2R + R'N_3 \xrightarrow[\substack{H_2SO_4 \\ -N_2}]{C_6H_6} C_6H_5CHO + RCHO + R'NH_2$$

R	R'	Benzaldehyde (%)	Other aldehyde (%)	Amine (%)
H	$\underline{n}$-C_4H_9	70	86	61
H	$\underline{n}$-C_6H_{13}	80	80	65
H	Cyclo-C_6H_{11}	85	- -	50
H	$\underline{n}$-C_8H_{17}	70	- -	52
CH_3[a]	$\underline{n}$-C_4H_9	62	50	- -
C_6H_5[b]	$\underline{n}$-C_4H_9	19	- -	- -

[a] Reaction at 90-91° in toluene
[b] Reaction at 135-138° in nitrobenzene

Boyer, Morgan 1959.

Figure 12

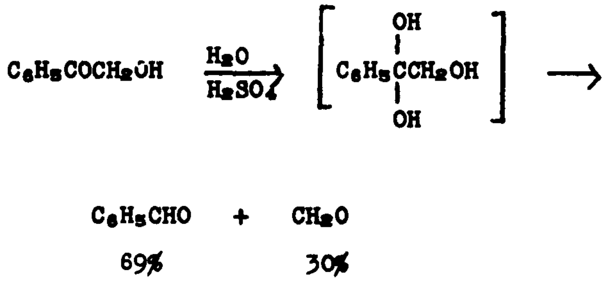

$$C_6H_5COCH_2OH \xrightarrow[H_2SO_4]{H_2O} \left[C_6H_5\overset{OH}{\underset{OH}{C}}CH_2OH \right] \longrightarrow \underset{69\%}{C_6H_5CHO} + \underset{30\%}{CH_2O}$$

Boyer, Morgan 1959.

Figure 13

Attempts to find another effective acid catalyst for the reaction between acetophenone and n- dodecyl azide have been unsuccessful.[7]

EFFECT OF ACIDS ON EQUIMOLAR COMBINATIONS OF ACETOPHENONE AND n-DODECYL AZIDE

Acid	Recovered Ketone (%)	Lauraldehyde(%)	Reaction Conditions
$BF_3 \cdot Et_2O$	80	61	C_6H_6, 75°
$BF_3 \cdot Et_2O$	30	57*	$CH_3C_6H_5$, 110°
$BF_3 \cdot C_6H_5OH$	90	55	C_6H_6,75° or C_7H_8, 110°
$AlCl_3$	90	50	C_6H_6,75° or C_7H_8, 110°
p-$CH_3C_6H_4SO_3H$	90	65	C_6H_6,75° or C_7H_8, 110°
HCl (anhydrous)	90	60	C_6H_6,75° or C_7H_8, 110°
F_3CCO_2H	85	8	C_6H_6, 70-75°
F_3CCO_2H	83	67	F_3CCO_2H, 70-72°
Cl_3CCO_2H	95	5	Cl_3CCO_2H, 60-70°
H_3PO_4 (85%)	95	5	C_6H_6, 75° or C_7H_8,110°

*C_6H_5CHO, 7%; CH_2O, 7%; $C_{12}H_{25}NH_2$, 7%.

Boyer, Porter Unpublished results.

Figure 14

It has also been unsuccessful to extend the reaction to aliphatic ketones, to isobutyrophenone,[13] to naphthyl ketones and to p- methylacetophenone.[7] The last example is of unusual interest because p- methylbenzaldehyde does enter into an acid catalyzed reaction with an alkyl azide (Fig. 7).

EFFECT OF ACIDS ON EQUIMOLAR COMBINATIONS OF A KETONE AND AN ALKYL AZIDE IN BENZENE AT 75°

Ketone	Acid	Azide	Recovered Ketone (%)	Aldehyde (%)
$CH_3COC(CH_3)_3$	H_2SO_4	n-C_8H_{17}	37	n-$C_7H_{15}CHO$ (27)
$CH_3COC(CH_3)_3$	$BF_3 \cdot Et_2O$	n-C_8H_{17}	50	n-$C_7H_{15}CHO$ (28)
$CH_3COC(CH_3)_3$	p-$CH_3C_6H_4SO_3H$	n-C_8H_{17}	50	n-$C_7H_{15}CHO$ (20)
$CH_3COCH(CH_3)_2$	H_2SO_4	n-C_8H_{17}	85	n-$C_7H_{15}CHO$ (30)
α-$CH_3COC_{10}H_7$	H_2SO_4	n-C_8H_{17}	44	n-$C_7H_{15}CHO$ (34)
β-$CH_3COC_{10}H_7$	H_2SO_4	n-C_8H_{17}	79	n-$C_7H_{15}CHO$ (40)
β-$CH_3COC_{10}H_7$	$AlCl_3$	n-C_8H_{17}	75	n-$C_7H_{15}CHO$ (29)
p-$CH_3C_6H_4COCH_3$	H_2SO_4	n-C_6H_{13}	91	n-$C_5H_{11}CHO$ (44)
p-$CH_3C_6H_4COCH_3$[a]	H_2SO_4	n-C_6H_{13}	85	n-$C_5H_{11}CHO$ (32)
p-$CH_3C_6H_4COCH_3$[b]	H_2SO_4	n-C_6H_{13}	50	n-$C_5H_{11}CHO$ (20)

[a]Reaction in C_7H_8 at 110°. [b]Reaction in $C_6H_5NO_2$ at 140°

Boyer, Porter Unpublished Results.

Figure 15

In at least one example the ketone undergoes self-condensation in preference to a reaction with an azide. *o*-Acetobenzoic acid in concentrated sulfuric acid gives the expected *o*,*o*'-dicarboxyldypnone, isolated as its anhydride, a *bis*-lactone.[14]

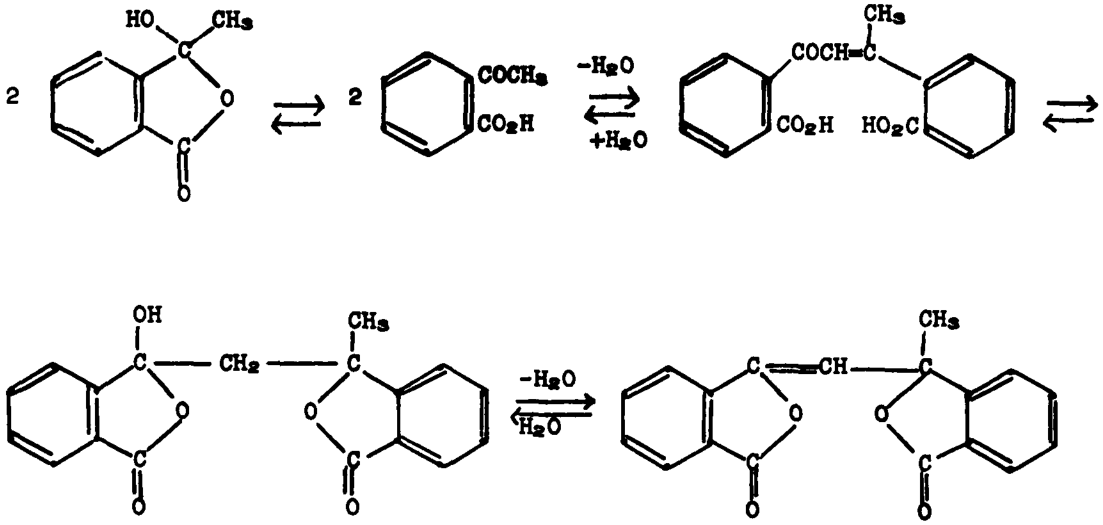
2
HO
CH₃
C
O
C
O
2
COCH₃
CO₂H
-H₂O
+H₂O
CH₃
COCH=C
CO₂H
HO₂C
OH
C
CH₂
CH₃
C
O
C
O
-H₂O
H₂O
C
CH
CH₃
C
O
C
O

Boyer, Darre Unpublished results

Figure 16

REFERENCES

1. T. A. Bak and E. L. Prestgaard, Acta Chem. Scand. 11, 901 (1957). C. A. 52, 13381 (1958).

2. L. A. Flexser, L. P. Hammett and A. Dingwald, J. Am. Chem. Soc. 57, 2103 (1935).

3. J. H. Boyer, F. C. Canter, J. Hamer and R. K. Putney, J. Am. Chem. Soc. 78, 325 (1956).

4. P. A. S. Smith, private communication. Earlier data reported by C. H. Gudmundsen and W. E. McEwen, J. Am. Chem. Soc. 79 329 (1957) interpreted in terms of a nonsynchronous process is reviewed.

5. J. H. Boyer and J. Stocker, J. Org. Chem. 21, 1030 (1956).

6. G. Heller, Ann. 332, 268 (1904); 358, 354 (1907); 375, 266 (1910).

7. J. H. Boyer and M. J. Porter, Unpublished results.

8. J. H. Boyer and J. Hamer, J. Am. Chem. Soc. 77, 951 (1955).

9. L. H. Briggs, G. G. De Ath and S. R. Ellis, J. Chem. Soc. 61 (1942).

10. P. A. S. Smith, J. Am. Chem. Soc. 70, 320 (1948).

11. M. S. Newman and H. L. Gildenhorn, Organic Symposium, Boston, Mass., June 12, 1947; J. Am. Chem. Soc. 70, 317 (1948).

12. J. H. Boyer and L. R. Morgan, Jr., J. Org. Chem. 24, 561 (1959).

13. J. H. Boyer and L. R. Morgan, Jr., J. Am. Chem. Soc. 81, 3369 (1959).

14. J. H. Boyer and B. Darre, Unpublished results.

THE NATURE OF THE BENT STATE OF THE AZIDE GROUP

by

Eugene Lieber and Jack G. Dodd
Roosevelt University
Chicago, Illinois

Abstract

Professor Lieber has hypothesized a "bent" configuration of the azido group in order to satisfactorily explain the proclivity with which that group reacts with a variety of reagents to form cyclic structures. A summary of this theory is given in a Progress Report, dated September 30, 1957 (ENG-3242) where its application to the properties of lead (II) azide is speculated upon. Important verifications for this theory are now available. The existence of a bent ground state of the azide group in certain organic azides is shown to be indicated by the splitting of the asymmetric stretching frequency and from the amplitude and distribution of these sidebands, estimates of the angular deformation of the equilibrium state and of the height of the potential barrier between the two bent equilibrium states are made from several azides which exhibit this splitting. The application of molecular orbital theory is shown to lead to correct qualitative predictions of the behavior of the observed splitting as a function of electronegativity of attached groups. It is concluded that, while the ground state of the azide group is linear in general for either the strictly covalent or strictly ionic cases, intermediate cases exist in which the linearity may be violated; and in any case, there will very likely exist bent excited states of low energy which may be responsible for the tendency of azides to cyclize.

INTRODUCTION

In a discussion (superscripts refer to section on references) on the nature of the reactive intermediate state of the azide group, Lieber[1] pointed out the necessity of postulating a "bent" state for that group in order to account for its proclivity to enter into reaction to form five-membered cyclic structures. The following reactions[2,3,4,5] proceed with remarkable ease at relatively low temperatures and with high yields:

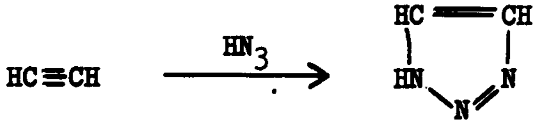

(1)

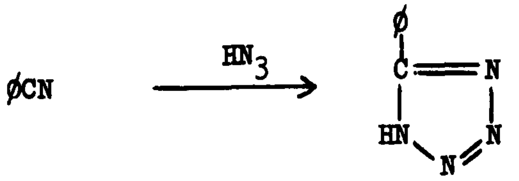

(2)

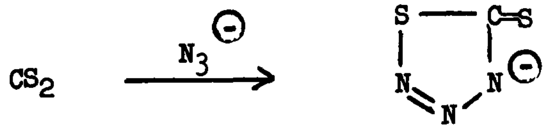

(3)

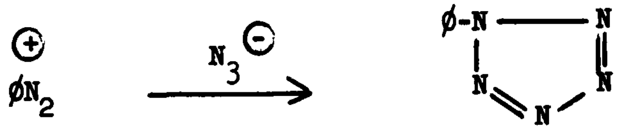

(4)

A large number of additional examples can be cited and the reader is referred to the discussions by Lieber^{1,6} on this subject. Reaction (4) is worthy of attention in this respect. The reaction takes place smoothly at -40° C and the existence of the pentazole ring has been unequivocally demonstrated. The necessity for the "bent" state of the azide group is readily epitomized for the entire field by asking the question for this specific case; viz, "how is the pentazole ring produced?" The initial condensation (at -40° C) is pictured in Chart I. Assuming a rigid azide ion, the valency direction requirements of the nitrogen atoms produce the two stereo structures (A) and (B) (Chart I). Structures (A) and (B) are interconvertible by rotation about the axis of the bond between nitrogen atoms 2 and 3. In either case, the basic question to be asked is "how do the starred (N*) nitrogen atoms in structure (A) or (B) in Chart I form a bond to produce the very compact pentazole ring as shown in reaction (4) above. Lieber^{6} has offered two explanations to account for this. First, it is obvious that structure (B) (Chart I) is more favorably arranged in space than form (A). Starting then with structure (B) in Chart II, neutralization of the positive charge on nitrogen atom 4 and subsequent "bending" about atoms 3, 4 and 5 to form the (normal) angle of about 108° brings atoms 1 and 5 within bond forming distance (shown by the dotted line). Subsequent rearrangement of charges produces the pentazole structure (D). The second theory suggests that nature really tends to follow the "simplest path." Thus, the pentazole ring can be

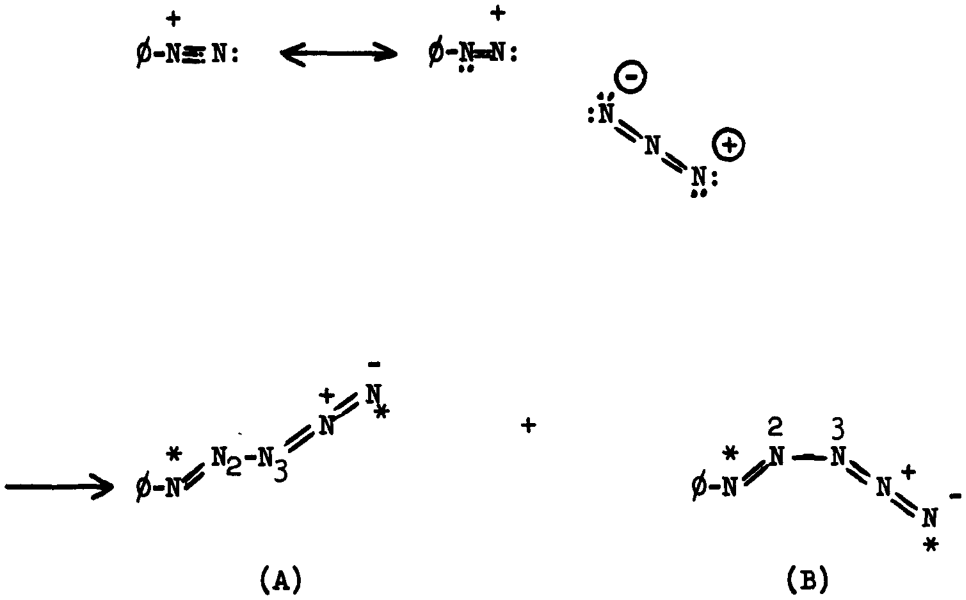

Chart I: Initial condensation in formation of pentazole ring

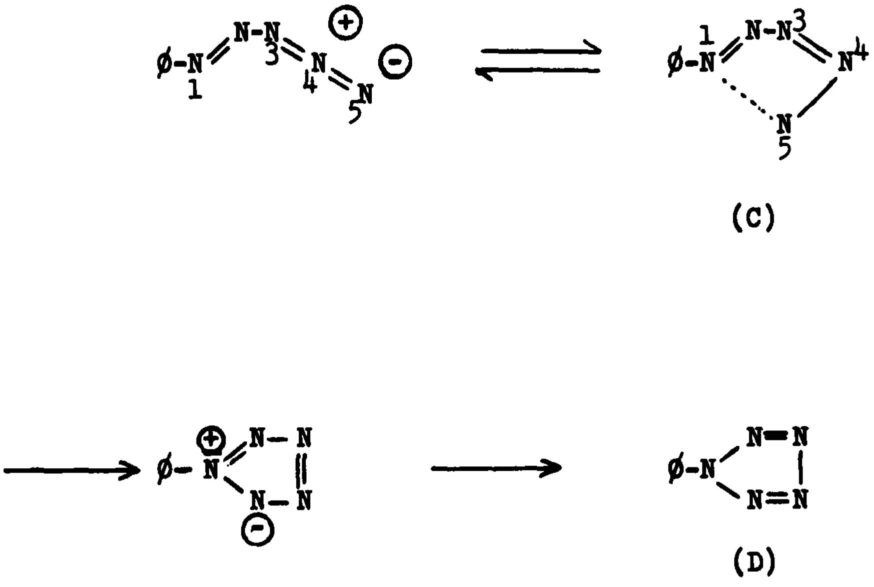

Chart II: Formation of the pentazole ring considered to be produced simply by a neutralization of charges as follows:

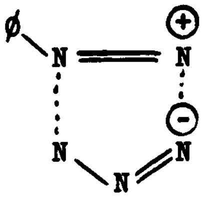

In order to produce the "bent" form of the azide group from the usually accepted[1] rigid linear structure of the azide ion, Lieber[1] assumed that the activation process produced the following reaction:

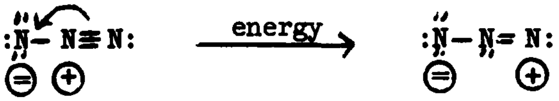

the separation of the charges accounting for the absorbed energy. The "high energy" form then bends to form the shape:

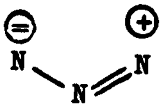

necessary for the formation of cyclic structures. Dodd[7] has calculated that about 4.47 ev would be required for this process which would correspond to the usually observed absorption peak at about 2760 Å in sodium azide[8]. These calculations were based upon the classical concept of a rigid linear azide structure for the ground state of that group.

In 1959, Lieber[9] discovered that the asymmetric N_3 stretching frequency of organic acid azides of the structure appeared as a doublet.

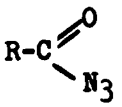

This is shown in Figures Number 1 and 2 for benzoyl azide (A) and para-nitrobenzoyl azide (B), respectively.

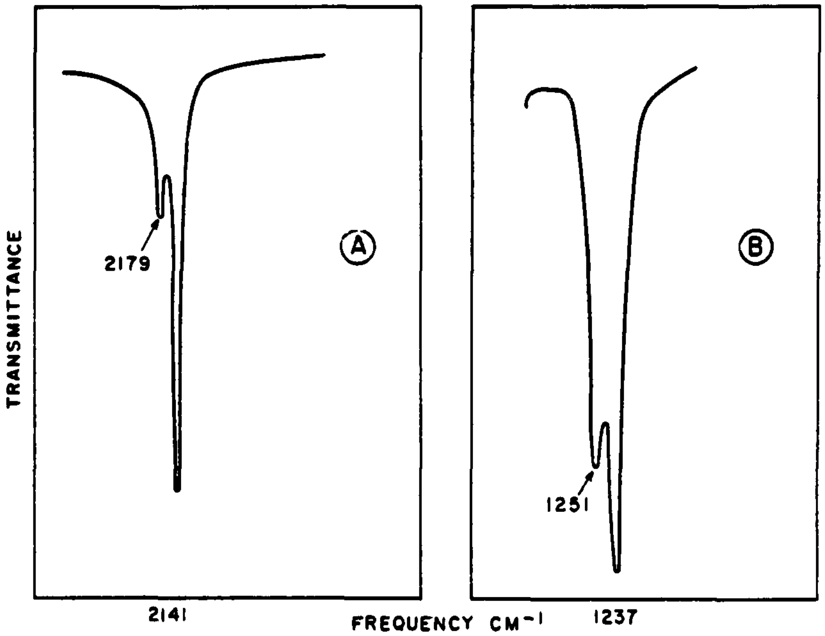

Figure 1. The asymmetric and symmetric N_3 stretching vibration absorption frequencies for benzazide showing a doublet in each case.

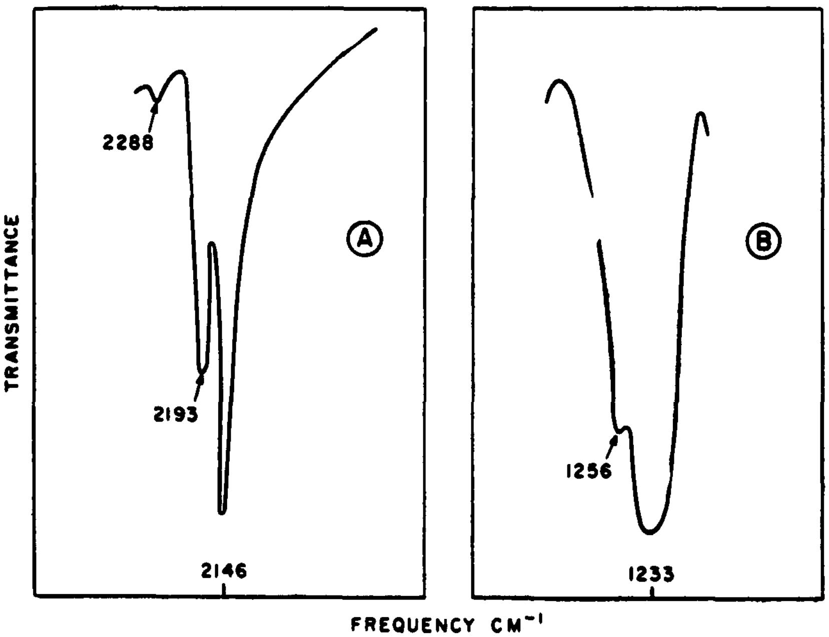

Figure 2. The N_3 infrared absorptions for para-nitrobenzazide showing shoulder in symmetric vibration and trace of p-nitrophenylisocyanate as an impurity.

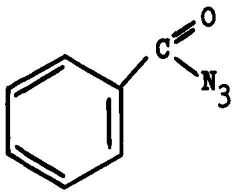

(A) Benzoyl Azide

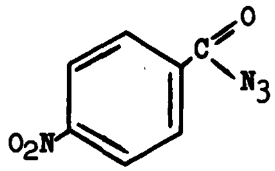

(B) Para-Nitrobenzoyl Azide

The isocyanate group, -N=C=O shows absorptions at about 2250 cm^{-1}, however, it was demonstrated that the lower intensity side bands (2179 cm^{-1} in Figure No. 1 and 2193 cm^{-1} in Figure No. 2) are not due to the presence of isocyanate which could occur due to the reaction:

$$R\text{-}C(O)N_3 \longrightarrow R\text{-}N{=}C{=}O \quad + \quad N_2$$

Actually, the spectrum between 2500 to 2000 cm-1 serves as a powerful method for establishing the purity of acid azides and the presence or absence of isocyanates. In subsequent papers[10,11], Lieber investigated the structural factors affecting the infrared spectra of acid azides and the effects of oxygen, sulfur and nitrogen alpha to azido groups.

Recently, Fahr[12] and Yates[13] have investigated the infrared absorption spectra of aliphatic diazo compounds. The aliphatic diazo group is isoelectronic to the azide group and is characterized by a single intense band which falls around 2080 cm^{-1}. Both Fahr[12] and Yates[13] have observed that a single carbonyl group (CO) alpha to the aliphatic diazo group produces only a single band; however, Fahr[12] has pointed out that in some cases a weak absorption, at slightly lower wave length, can sometimes be observed. In those cases in which two carbonyl groups are alpha to the diazo group, two bands are observed very similar in character to the splitting noted in the organic acid azides. This is shown in Figure No. 3 taken from the paper by Fahr[12]. Fahr[12] attributed these effects to an additional electronic interaction of the diazo-group over the two fold pi (π) electrons of the adjacent carbonyl groups:

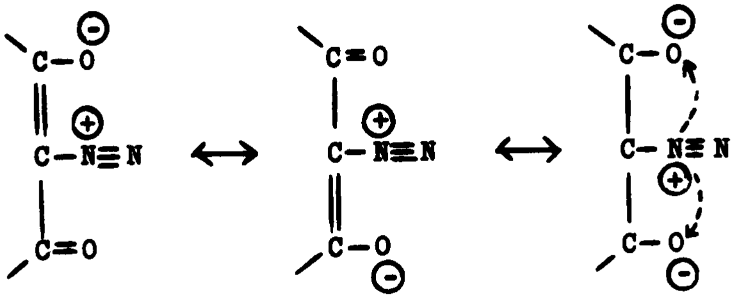

A single carbonyl group adjacent to the diazo group markedly reduces this effect as shown in the spectra for 1,7-bis-diazo-heptandion-2,6 (right hand portion of Figure No. 3). The application of this to the present problem is discussed below.

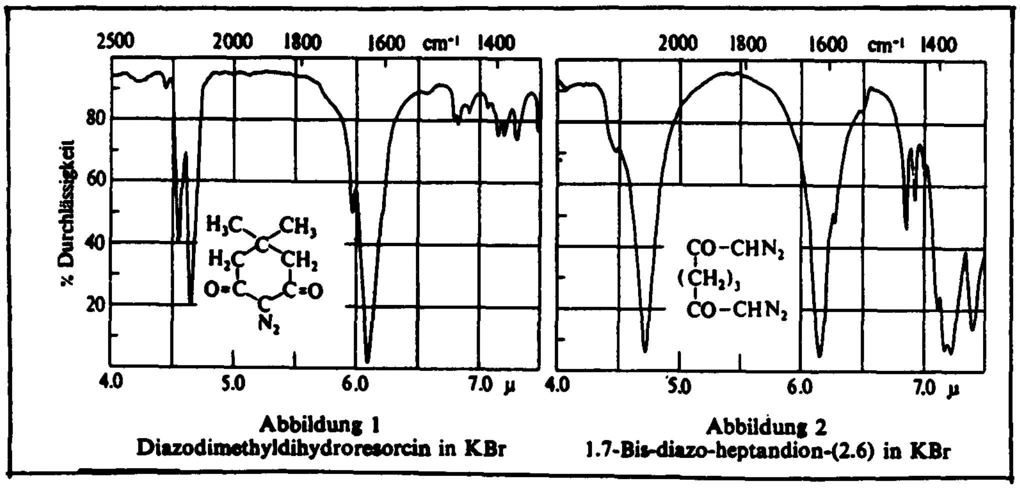

Figure 3. Infrared absorption spectra of diazodimethyldihydroresorcin and 1,7-bis-diazo-heptandion-2,6. Taken from the paper by Fahr[12].

In examining the effects of oxygen, sulfur and nitrogen alpha to the azide group, in which splitting of the asymmetric stretching vibration of N_3 was observed in several cases, Lieber[11] suggested a dipolar field effect, however, initiated by a charge separation in the azido moiety:

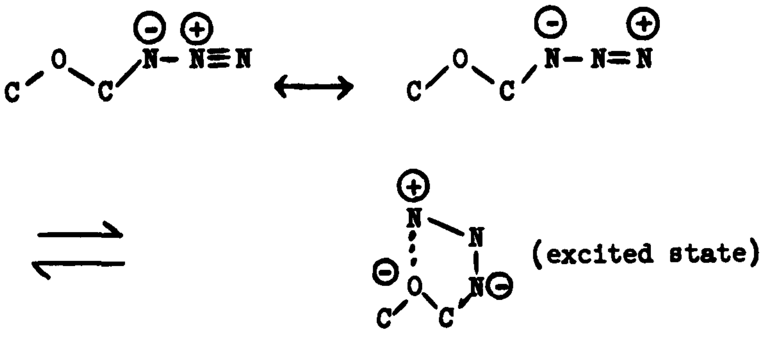

in which the two peaks represent the asymmetric stretching modes of the excited and normal states.

THEORETICAL CONSIDERATIONS

The circumstantial evidence, discussed above, seems very strong for the existence of a bent excited state of the azide group. The observations[9,10,11] of a splitting of the asymmetric stretching frequency in certain compounds offers an unusual insight into the hypothesis of the bent state.

The insight arises from the kind of difficulties encountered in attempts to explain the splitting. Since the asymmetric stretching frequency of the linear triatomic form is non-degenerate, it is quite clear that the two peaks observed must arise from two distinct molecular species, or possibly from a single species in association with one or the other of two distinct environments. The latter explanation is adequate for the splitting observed in the azide asymmetric stretching frequency in barium azide[14] and the alkali metal azides[15] since it is quite possible that the two azide groups might see different environments. However, in the case of organic acid azides, $RC(O)N_3$, it is difficult to envision that the two distinct species, or that two distinct environments, can exist.

Two clues are offered by the studies[9,10,11] on structural factors in relation to the asymmetric band split. For example, in the case of the alpha-azido ethers:

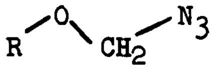

the splitting becomes less pronounced the higher the molecular weight of the group R (e.g., methyl to ethyl). Azidomethylethyl ether:

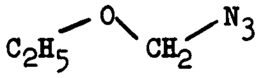

exhibits only weak shoulders rather than a distinct splitting of the asymmetric N_3 frequency. In the case of the organic acid azide, the interposition of a saturated group appears to eliminate the splitting. This was observed for the structures (C) and (D):

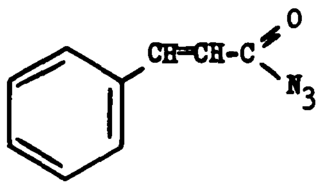

(C) : Cinnamic Acid Azide

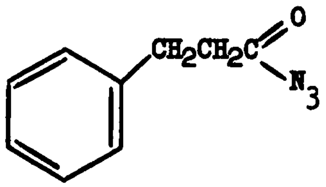

(D) : Dihydrocinnamic Acid Azide

Structure (C) exhibits a strong splitting while structure (D) exhibits only a slight broadening.

On the basis of the above observations, several possibilities can be eliminated immediately. Since the doublet is observed for benzoyl azide (structure (A) above), in which the ethylenic bridge, CH=CH, is absent, the effect is not due to cis and trans geometric isomerism about an ethylenic bond. The additional resonance interaction of an azido group attached to a carbonyl group:

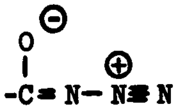

$$-\overset{\overset{O^{\ominus}}{|}}{C}=N-\overset{\oplus}{N}\equiv N$$

can be ruled out since the isolated $-C(O)N_3$ grouping exhibits only a single band. Further, oxytriazole formation:

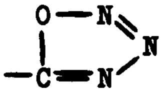

can also be eliminated since it would mean the disappearance of all azide absorption frequencies. A proposal that appeared reasonable[10,11] suggested an interaction similar to that of carbonyl groups alpha to a diazo group[12]. Electronic interaction takes place between the carbonyl azide group ($C(O)N_3$), the alpha-situated conjugated unsaturation, and the pi (π) electrons of the carbonyl group. For cinnamic acid azide (structure (C) above) this can be diagrammed as follows:

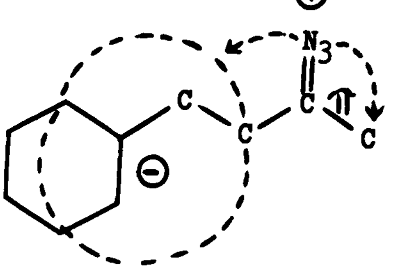

Such interactions, as depicted above, are absent when the carbonyl azide group is attached to a saturated system. Bellamy[16] has termed these interactions "dipolar field effects." This effect distorts the azide bonding distances and, hence, shifts the asymmetric stretching frequency. If at this point it can be assumed that the absorption of (infrared) energy during measurement generates the excited state of the azide group (which may be bent), then two distinct species would exist, with separate asymmetric stretching frequencies. This proposition fails only because such a bent state ought to be generated regardless of structural environment. The more serious objection to this hypothesis are the energy requirements[7]. The amount of band splitting is small, approximately 25 cm^{-1}; since the absorption peaks occur in the neighborhood of 2000 cm^{-1} the equivalent energy of this radiation is about 0.247 ev, whereas the energy required to excite the azide group is greater by a factor of at least 300. Radiation of sufficient energy would have a wavelength of about 320 mμ (maximum). There is further the question as to whether this excitation can occur by means of radiation by a consideration of spin conservation[7].

LINEAR TRIATOMIC MOLECULES PERTURBATION THEORY

Recently, a paper by Thorson and Nakagwa[17] has appeared on "quasi-linear triatomic molecules" which predicts the kind of phenomena described above. Thorson and Nakagwa[17] develop the effects which arise from a small but significant deviation from linearity of a triatomic system. The discussion which follows is an application of their principles to the azide system.

It is assumed that, under certain conditions as outlined below, the azide group may, in the *ground state*, be bent. Then, instead of a simple harmonic bending potential, such as in Figure No. 4 (A), which could apply for a linear system, one would have the potential shown in part (B) of Figure No. 4. The potential barrier at Θ is equal to zero. This system is bistable in that there are *two configurations* of equal energy. For the azide group, this can be represented by structures (E) and (F):

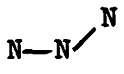

and

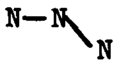

(E) (F)

The system is thus doubly degenerate and the height of the potential barrier (as shown in Figure No. 4) is simply the energy to "snap" configuration (E) to configuration (F). The concern here is the effect that this additional degeneration has upon the asymmetric stretching frequency of the system.

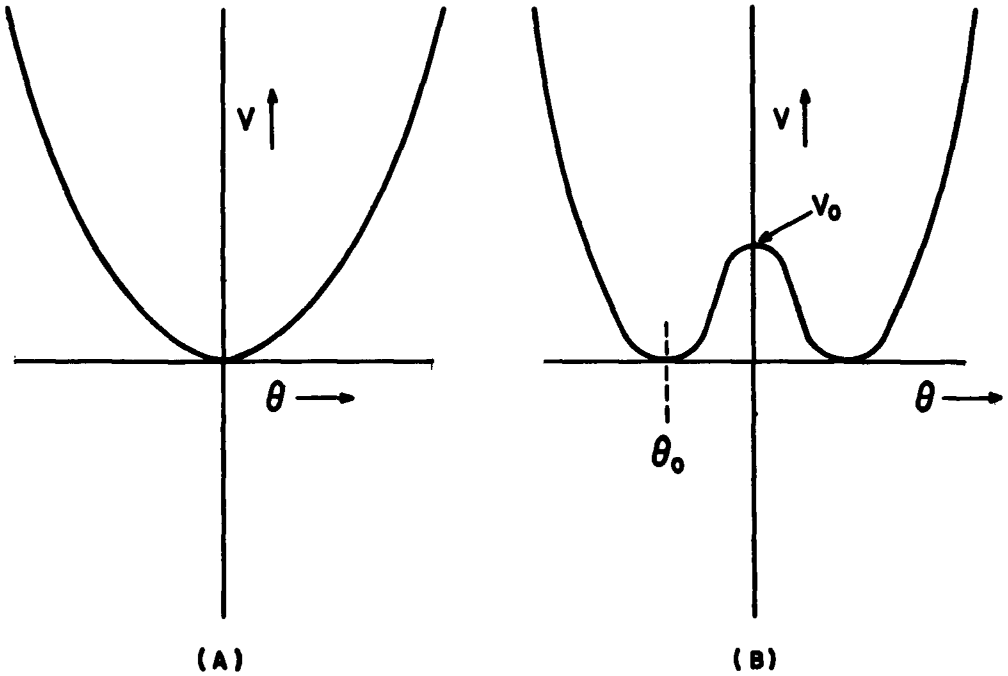

Figure 4. Bending Potentials For Deviations From Linearity.

Through the use of perturbation theory, Thorson and Nakagwa[17] show that coupling terms appear between the bending and stretching modes which, in the case of a low potential barrier between the two equilibrium positions result in a simple and structureless broadening of the asymmetric line; however, in the case of a potential barrier approximately equal to the lowest vibrational quantum of the system, this produces a series of side bands on either side of the principal line. If the barrier is still higher, e.g., two or three vibrational quanta, a single side band will appear. It may show up on either side of the principal frequency and will have a magnitude depending upon the amplitude of bending necessary to go from one of the bistable states to the other.

On the basis of the above principle, it now becomes possible to classify the nature of the ground state of the azide group by an examination of the asymmetric stretching frequency of the N_3 in its compounds.

From the studies of Lieber[9,10,11] on a wide variety of organic azides, the compounds can be depicted as occupying a kind of "linearity space." This is illustrated in Figure No. 5 which qualitatively locates several compounds according to the barrier heights and equilibrium angle of their azide groups as deduced from the criteria of Thorson and Nakagwa[17]. Figure No. 5 indicates that most of the organic azides depart from a strictly linear azide group. It is evident that the hypothesis of a "bent excited state" of the azide group can be readily made and, in many cases, it can also be assumed that even the ground state is bent.

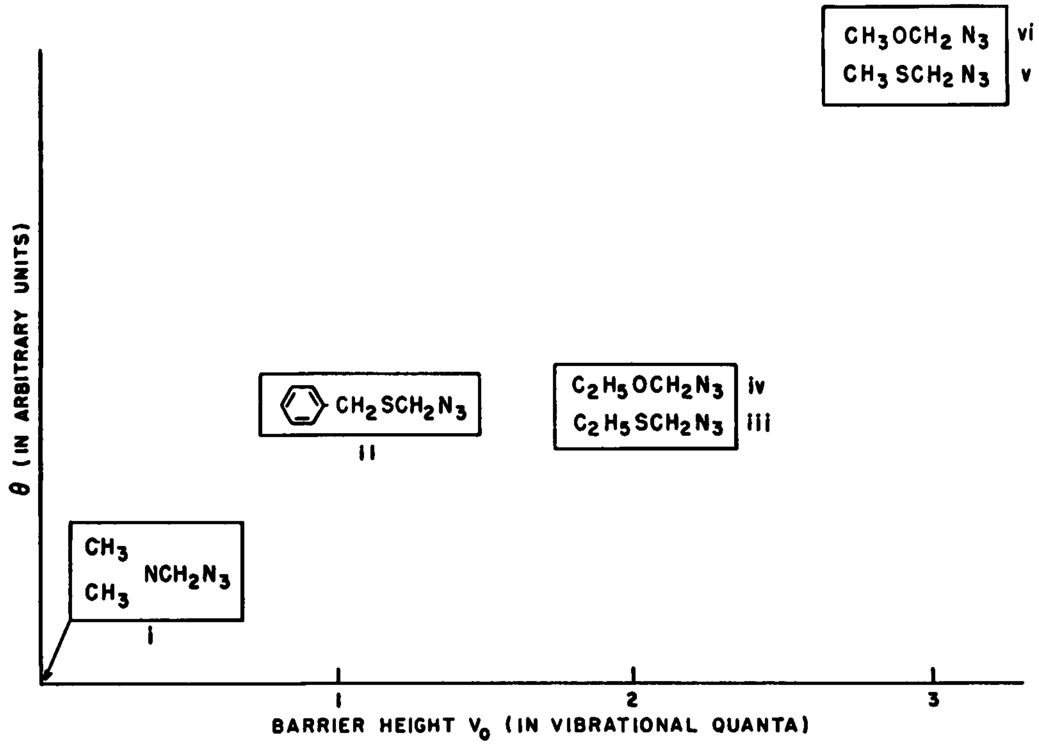

Figure 5. "Linearity Space" location, in qualitative fashion, of organic azides according to barrier height and equilibrium angle of azide group: (i) N-azidomethyl dimethylamine; (ii) azidomethyl benzyl sulfide; (iii) azidomethyl ethyl ether; (iv) azidomethyl ethyl sulfide; (v) azidomethyl methyl sulfide; (vi) azidomethyl methyl ether.

APPLICATION OF MOLECULAR ORBITAL THEORY[18]

It was of some importance and of considerable interest to attempt a qualitative application of molecular orbital theory to the bound azide group. Although some of the reasoning presented below is "ad hoc," it is shown that the hypothesis of a bent ground state for the azide group, as developed through the principle of Thorson and Nakagwa[17], is not at variance with the observed perturbations produced by introducing various groups into azido-compounds. The discussion which follows is to be considered as a preliminary one for the azide group.

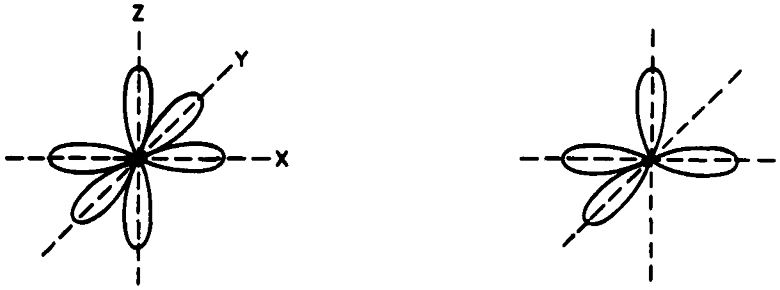

(a) p-ORBITALS

(b) COMPLETE sp HYBRIDIZATION

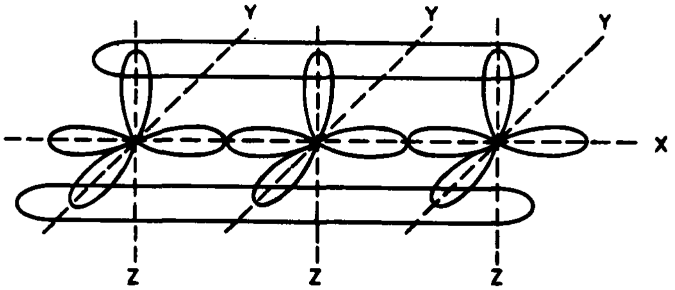

(c) SET OF THREE (b) PLUS ONE ELECTRON

Figure 6. Application of Molecular Orbital Theory to Nitrogen and Azide Group.

Nitrogen has five electrons in the (bonding) outer ring[18]. Three of these are in the p state, and two in the s state. The p-bonding directions are mutually perpendicular along three Cartesian directions (Figure 6 (a)). Nitrogen only rarely (really, only in N_2) can be described solely in terms of these electrons; generally, and specifically in the azide structure, these p-electron bonds are "hydridized" with the s-electrons to form asymmetric bond patterns. Figure 6 (b) shows the result of complete "sp" hybridization. The bond angles remain at 90°. Figure No. 6 (c) shows the result of combining three sp-hybrids plus one electron. The "in-line" unhybridized p-orbitals form linear bonds (localized σ-(sigma) bonds) and the sp-hybrid orbitals (aimed along the y and z directions) "couple" over the whole length of the group to form "de-localized bonds." The significance of such delocalization is that an electron "belonging" to the z-directed bond of the first atom, e.g., cannot tell whether it is the property of that atom, or either of the others. Thus it may, with equal probability be considered the property of any (or all) of the atoms. This "delocalization" is the molecular orbital counterpart of resonance, and increases molecular stability (resonance energy). The configuration represented by Figure No. 6 (c) is thought to be the ion (N_3^-) structure.

In order to bond the configuration represented by Figure No. 6 (c) covalently it is necessary to "use" one electron from one of the delocalized π bonds (if this electron be considered as removed then the 15-electron nitrogen radical results). To do this we must break one of the π bonds. This places one of the terminal nitrogens in a state of "sp^2-hybridization": (i.e., instead of forming orbitals by pairing "p" and "s" electrons, they are formed by "p-p-s" triples). The resultant structure (Figure No. 7 (a)) is different in two ways; one of the π bonds does not now extend over all three of the atoms; and the sp^2-hybridized N atom no longer exhibits 90° bond angles for all bonds. The unaffected orbitals (there are two along the Z and X axes) are still mutually perpendicular, hence, the configuration is still linear; but now the lone electron pair and the group bonding pair, both in "sp-hybridization" are not mutually

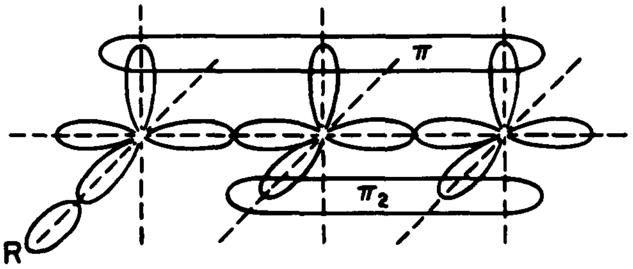

(a) RESULT OF sp^2 HYBRIDIZATION OF TERMINAL N

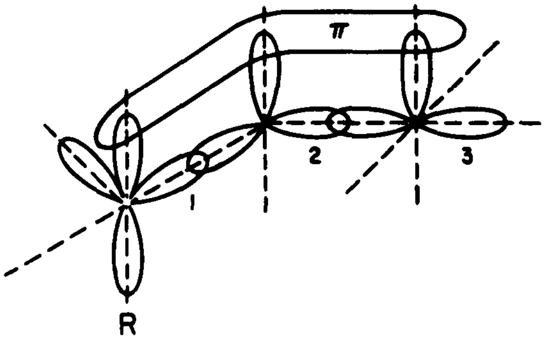

(b) EXCITED "BENT" BONDED N_3 GROUP

Figure 7. Molecular Orbital Configurations of Covalently Bonded Azide In Linear and Excited "Bent" Configurations.

perpendicular. The question is "how can a bent configuration be achieved?" What states resulting in departure from linearity are possible?

DeHeer[19] has suggested one method for doing this. The two right-hand nitrogen (Figure No. 7 (b)) atoms change into "sp^2-hybridization." The upper π bond is still retained but the two bonding angles are changed. The bonding axis is now "bend" and because the y-orbitals of the right hand nitrogen pair (Figure No. 7 (b)) are no longer parallel, they cannot form a π_2 bond as shown in Figure No. 7 (a). This loss of "delocalization" should increase the bond distance between nitrogen atoms 2 and 3 (Figure No. 7 (b)) in the "excited" group over the ground state. The "sp^2-hybridization" suggested in Figure No. 7 (b) should change the bonding angle from 180° (as shown in Figure No. 7 (a)) to that of 120° (Figure No. 7 (b)).

Thus we see that to explain how the azide group might seem non-linear in some molecules, it could be assumed that some perturbing field changes the bonding orbital state within the azide group from "sp-hybridization" to something between sp and sp^2 hybridization. From the molecular orbital analysis it seems that the normal ionic state of the azide group is linear as is the strictly covalently bonded group. But what of the intermediate states? It is reasonable to assume that it is possible that intermediate states between the completely covalent case and the completely ionic case might exist in which the group deviates from linearity. If this were, indeed, the case, then we would expect a correlation between (in certain types of azido-compounds) the deviation from linearity and the deviation from pure covalency. This latter deviation from pure covalency should be a function of the electron affinity of the parent compound, and indeed, a "splitting" (of the asymmetric stretching mode of N_3-type compounds) occurs in just those cases in which R (the substituent in Figure No. 7) is an electron donor group. Interposition of saturated "bridges" insulates the azide group from the electron pressure. However, this insulation does not appear to offer complete protection; appreciable broadening of the asymmetric N_3 stretching mode with some evidence of "shoulders" attests to the fact that the azido-group in the particular molecular constellation under observation is not linear.

The exact nature of these postulated intermediate states cannot be qualitatively deduced with any certainty since molecular orbital theory deals with a highly idealized model of molecular bonds and while this ideal model has proved spectacularly successful in a wide variety of cases, it is in no sense an exact treatment. Shortcomings of treatment is in exactly that area of greatest interest, i.e., between pure covalent and pure ionic compounds. Thus, it may not be entirely possible from molecular orbital calculations alone to determine, in a given case, whether the linearity or the bend form is in the ground state. Considerably more work has to be done by this approach.

A recent quantitative study by Roberts[20] of the energy difference between the linear and the bent state of the azide group support the above theoretical discussions in detail. Roberts[20] reports, from his calculations based on simplified molecular orbital treatment, that the energy difference between the linear and bent states of the bonded azide group is very small, indeed, less than the probable error of calculation.

CONCLUSION

From the above discussion it can be concluded that the hypothesis of Lieber[1,9,10,11] concerning the bent excited state in cyclization reactions and Dodd's[21] treatment of the splitting of the N_3 asymmetric stretching frequency rests on a firm footing. Further, in all reactions involving azides the consequences of a bent state for that group must be considered.

REFERENCES

1. Lieber, E., Second Letter Progress Report For Period September 1-30, 1957, ERDL Contract ENG-3242.

2. Dimroth, O. and Fester, G., Ber., 43, 2222 (1910).

3. Mihina, J. S. and Herbst, R. M., J. Org. Chem., 15, 1082 (1950); Finnegan, W. G., Henry, R. A. and Loquist, R., J. Org. Chem., 80, 3908 (1958).

4. Lieber, E., et. al., J. Org. Chem., 22, 1750 (1957).

5. Huisgen, R. and Ugi, I., Chem. Ber., 90, 2914 (1957); 91, 531 (1958).

6. Lieber, E., Final Technical Report dated December 1, 1959, ERDL Contract ENG-3728.

7. Dodd, J. G., Second Interim Technical Report, ERDL, Contract ENG-3773 for period 10 March 1959 to 9 June 1959. First Letter Progress Report on Theoretical Studies, ERDL, Contract ENG-4142 dated December 28, 1960.

8. Dodd, J. G., Final Technical Report, ERDL, Contract ENG-3427 for period 10 December 1957 to 9 December 1958, Section IV, Figure 2.

9. Lieber, E., Final Technical Report, ERDL Contract ENG-3242, dated February 10, 1959; J. Org. Chem., 24, 1014 (1959).

10. Lieber, E. and Oftedahl, E., Approved for publication by BRG, ERDL and submitted (August, 1961) for publication to Spectrochimica Acta.

11. Lieber, E., Roosevelt University Technical Report (31 January 1961), ERDL Contract ENG-4142. A paper on this subject has been accepted for publication in "Applied Spectroscopy".

12. Fahr, E., Ann., 617, 11 (1958).

13. Yates, P., et. al., J. Am. Chem. Soc., 79, 5756 (1957).

14. Evans, Yoffe and Gray, Chem. Revs., 59, 539 (1959).

15. Papazian, H. A., J. Chem. Physics, 34, 1614 (1961).

16. Bellamy, L. J., "The Infrared Spectra of Complex Molecules," Methuen and Co., Ltd., London, 1958.

17. Thorson and Nakagwa, J. Chem. Physics, 33 (4), 994 (1960).

18. Coulson, "Valence," Clarendon Press, 1952.

19. DeHeer, Proceedings of Contractors' Conference, Boulder, Colorado (1959).

20. Roberts, J. D., Chem. Ber., 94, 273 (1961).

21. Lieber, E. and Dodd, J. G., Final Technical Report, ERDL Contract ENG-4142, dated July 1, 1961.

THE PHOTOCHEMICAL DECOMPOSITION OF BARIUM AZIDE

by

P. W. M. Jacobs, F. C. Tompkins
and V. R. Pai Verneker
Department of Chemistry
Imperial College
London, S.W.7.

The kinetics of nitrogen evolution from barium azide irradiated with ultra-violet light from low and high pressure mercury arcs has been investigated as a function of intensity, temperature and time of irradiation. These results emphasize the important role played in the reaction by the barium product formed as a result of photolysis. Two mechanisms of the photodecomposition which are consistent with these detailed kinetic results are proposed and discussed in the light of our present knowledge of the physical properties of azide crystals. The first of these, which occurs chiefly in fresh salt, is the formation of barium atoms (pre-nuclei) at kink sites; the second is the thermal production of positive holes by the transfer of electrons to barium pre-nuclei which have become ionised by photomission of an electron into the conduction band. The significance of a purely thermal contribution to the photolytic rate is also assessed.

There have been several previous investigations of the effects of radiation on barium azide. Irradiation with soft X-rays[1] produces barium nitride and nitrogen. Pre-irradiation of barium azide with α-particles[2] or ultra-violet light[3] accelerates the rate of subsequent thermal decomposition. Irradiation with ultra-violet light[4] evolves nitrogen at a rate proportional to the square of the intensity and with a temperature-dependence corresponding to an energy of activation of 5 kcal/mole. Mott[5] proposed that the mechanism of photolysis involved four steps:

(i) irradiation with ultra-violet light produces electrons and positive holes (N_3 radicals);

(ii) the mobile positive holes diffuse to the surface and combine bimolecularly to produce gaseous nitrogen;

(iii) the electrons migrate through the conduction band of the azide until trapped by specks of barium metal;

(iv) interstitial barium ions diffuse to the negatively charged specks and combine with them.

However, the failure to detect photoconductivity[6] seemed to imply either that the primary effect of the radiation was the production of excitons[4] rather than that of holes and electrons, or that the latter were not mobile. It must be emphasized that, owing to the difficulty of producing crystals of suitable size, the photoconductivity experiments were performed using compressed pellets. Nevertheless, a detailed kinetic analysis[4] established that exciton production was more likely for the primary process.

Furthermore, the low ionic conductivity of barium azide makes unlikely a mechanism of reaction based on ionic transport.

Recent investigations[7] have shown that the mechanism of photolysis must be more complicated than the bimolecular decomposition of excitons at traps[4]. In particular, the rate of photolysis under irradiation with a high pressure lamp at first decreased and then increased again, finally attaining a constant value. The intensity-dependence appeared to be complicated, the exponent n in the equation $R = CI^n$, varying from 0.5 to 2. This work, though valuable in pointing to the role of the metallic product in photochemical as well as thermal decompositions, was unsatisfactory in that the temperature dependence was not examined and also because insufficient account was taken of the effects of the 'dark rate' in determining the value of n. Consequently, the kinetics of nitrogen evolution under ultra-violet irradiation has been re-examined in some detail and the results of this investigation are recorded below.

EXPERIMENTAL

Barium azide was prepared by neutralization of an approximately 5% solution of hydrazoic acid with barium hydroxide of A.R. quality. The solution was maintained neutral to phenolphthalein during evaporation on a water bath to incipient crystallization and the azide was then precipitated by addition of absolute alcohol. The fine white precipitate was filtered off, re-dissolved in the minimum amount of distilled water made slightly acidic with hydrazoic acid and the barium azide obtained either by addition of absolute alcohol or by slow evaporation of the acidic solution. The former method yields a white amorphous powder, the latter a mass of tiny crystals. The azide was dehydrated over phosphorous pentoxide in a desiccator. The hydrazoic acid was obtained by two methods: (i) by dropping sulphuric acid onto a solution of sodium azide and sodium hydroxide and distilling off the hydrazoic acid into water and (ii) by passing a 10% solution of sodium azide through a cation exchanger in the hydrogen form. No differences were observed in the behaviour of products obtained by these slight variations in technique.

The azide was contained in a transparent silica cell with a flat window, connected via a B.14 standard joint to the vacuum line. This consisted, in sequence, of a trap immersed in liquid nitrogen, a standard volume, a pirani gauge (P_1) a cut off (C_1), a diffusion pump (D_1), a second trap, a second pirani gauge (P_2), a McLeod gauge, and a second cut off (C_2) which separated the line from the second diffusion pump (D_2) and the backing pump. The object of this arrangement was so that the rate of nitrogen evolution could be measured either on P_1 with C_1 raised (the accumulatory method) or on P_2 with C_1 lowered and C_2 raised. In the accumulatory method the azide is in continual contact with the nitrogen evolved which may reach a pressure of several microns. In the second method (referred to as 'pumping') the diffusion pump D_1 maintains a pressure of $<10^{-5}$ mm Hg over the salt during photolysis. The volumes of the two measuring systems were determined by calibration with nitrogen and it was also confirmed that the effective volume of the second system was independent of the pressure in it (which of course backs the first diffusion pump D_1) up to the limit tested (20 μ).

The temperature of the salt was measured with a calibrated copper-constantin thermocouple. The intensity of irradiation of the low pressure arc was varied by controlling the voltage to the primary of the lamp transformer; because the intensity distribution of the high pressure arc varies with temperature, its intensity was varied by varying the distance of the lamp from the photolysis cell. Both lamps were calibrated by replacing the cell by a Kipp thermopile; intensities are recorded in terms of the e.m.f. registered by the thermopile as the intensity distribution for the high pressure arc is not accurately known and the number of quanta received by the azide cannot therefore be calculated. The emission spectra of the two arcs have been reproduced in another paper[7]. A water filter was always used in conjunction with the high pressure arc to remove infra-red components.

RESULTS

The rate of nitrogen evolution from barium azide irradiated with the low pressure arc is shown in Fig. 1 as a function of time. For fresh salt (a,b,c) the rate at first decreases with time (for about 100 min at the higher intensity) then remains more or less constant, then increases again and finally, after about 5 hr, attains a constant rate which is maintained over very long irradiations. If the shutter between the lamp and cell is replaced, the rate of evolution of gas decreases steadily until it becomes equal to the original outgassing rate of the system. The rate of gas evolution after the shutter is replaced, we term the 'dark rate'.

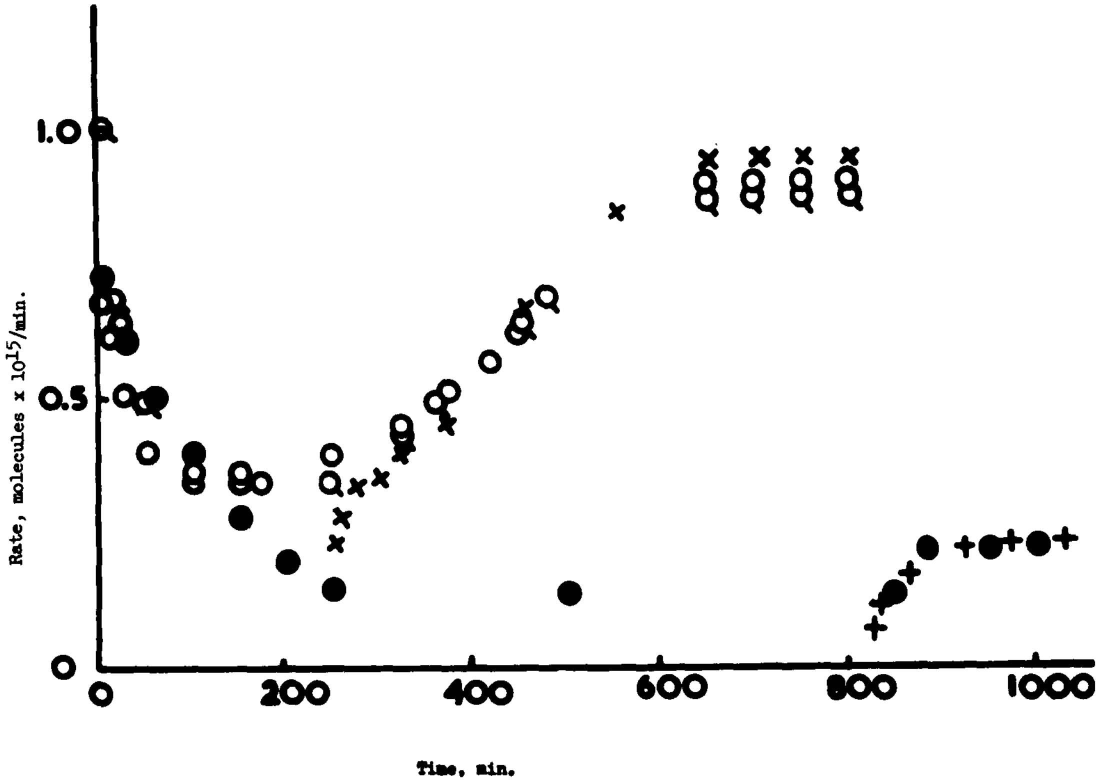

Figure 1. Rate of photolysis of barium azide, expressed in molecules x 10^{15}/min, as a function of time. (a) O, fresh salt, pumped; (b) Q, fresh salt, accumulatory; (c) ●, fresh salt, pumped, at half the intensity used for (a); (d) X, annealed azide, pumped, at same intensity as (a); (e) +, annealed azide, pumped, at same intensity as (c). Time scales for (d) and (e) have been adjusted to match the acceleratory periods of (a) and (c), respectively.

It is apparent from Fig. 1 that there is no difference in the behaviour of the salt whether the accumulatory technique is used or whether it is pumped during irradiation (cf. a and b). The somewhat higher initial rate for b is probably not significant for it could be due to other causes such as a difference in particle size or the distribution of material in the cell. When salt which has been irradiated for at least 5 h., is left overnight connected to the pumps and then re-irradiated, the rate is at first slightly lower than the minimum found for that intensity using fresh salt (curve d) but it rapidly increases until it coincides with the value at the beginning of the acceleratory region, after which it follows precisely the behaviour of the fresh salt. The changes which take place during the intervals between successive irradiations, we refer to as 'annealing'. The same type of behaviour is observed when irradiation of lower intensity (curves d, e) is used, the initial fall in rate to the minimum taking longer, the minimum being much flatter and the acceleration to a final constant rate being longer delayed and smaller in magnitude. The previous experimental results[4] with low pressure arcs were obtained using short irradiation times over which the variations found here during much longer irradiations would not normally be observed, although Thomas and Tompkins[4] did note a decreasing rate on a long irradiation of fresh salt.

Salt irradiated with the high pressure arc behaves in precisely the same way as depicted in Fig. 1 and again there is no dependence on the pressure of nitrogen in the reaction vessel. The dependence of the final constant rate on intensity is shown by the data plotted in Fig. 2 to be $R \propto I^2$, a result that is independent of whether the reaction cell is pumped during photolysis or whether the accumulatory

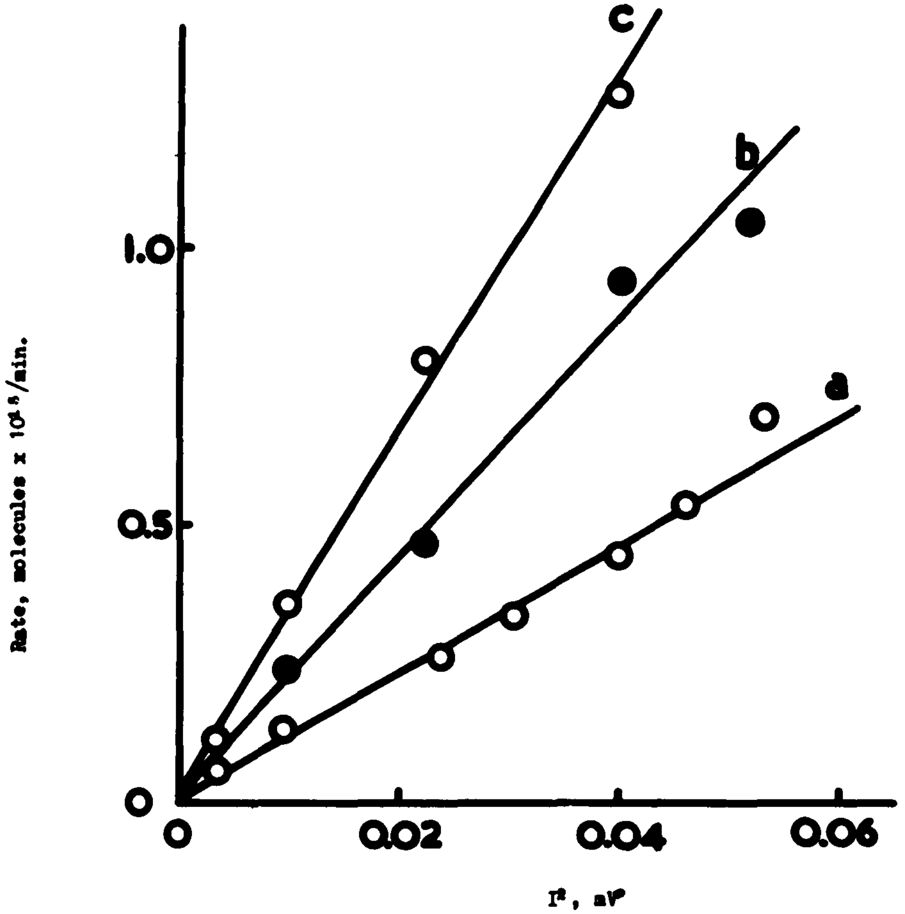

Figure 2. Dependence of the rate of photolysis on intensity of the low pressure arc (given in terms of the thermopile e.m.f.). (a) during the acceleratory period, after 60 min irradiation, (b) in constant rate period, pumping, (c) in constant rate period, accumulatory.

method is used. The dark rate is practically zero for fresh salt and increases steadily with the amount of decomposition, reaching a maximum in the constant rate period. The dark rate also depends on the intensity during irradiation, the relationship being $R_d \propto I^2$. This dependence of both the light and dark rates on the square of the intensity holds not only during the final constant rate period but also during the acceleratory period.

The temperature coefficient of the photolytic reaction was measured at various stages of the reaction and the corresponding activation energies calculated. These results are shown in Table I.

Table I.

Activation energy (in kcal/mole) for the photochemical decomposition of barium azide at various stages of the reaction

source	initial process	at the minimum	constant rate period	'dark' reaction
low pressure arc	4.4	9.3	20.1	19.8
high pressure arc	4.7	11.5	19.4	20.2
high pressure arc + OX7 filter	-	-	19.3	-
high pressure arc + OY10 filter	5.1	19.7	37.4	-

The radiation from the low pressure arc is predominantly the 2537 Å resonance line. That from the high pressure arc is more or less continuous, with the principle mercury lines superimposed. On interposing the filter, Chance OY10, radiation shorter than wavelength of 3500 Å is totally excluded (50% transmission at 3690 Å). If the filter, Chance OX7, is used, radiation between 2400 and 4200 Å is passed, with >50% transmission between 2550 Å and 3890 Å. For brevity, we shall refer to the two wavelength regions as 'short' and 'long'.

There are three main differences in the photolytic behaviour of short and long wavelengths. The high pressure lamp filtered by OX7 behaves like the low pressure lamp: the rate of photolysis goes through the same variations with time, it varies with the second power of the intensity of the radiation (Fig. 3) and the activation energy (Table I) shows the same variations. In contrast, with long wavelengths, the rate of photolysis of salt (pre-irradiated with the full arc into the constant rate period), varies as the first power of I (Fig. 3) and the activation energy is 37 kcal/mole. The dependence of photolysis rate on time for fresh salt is also quite different. Surprisingly, fresh salt does photolyse at a reasonable rate (2 x 10^{14} molecules/min) but the rate decreases steadily to 1/5th of the initial value over a period of about 13 h, after which is remains constant (Fig. 4) at a rate equal to about 1/20th of the constant rate obtained with the unfiltered arc.

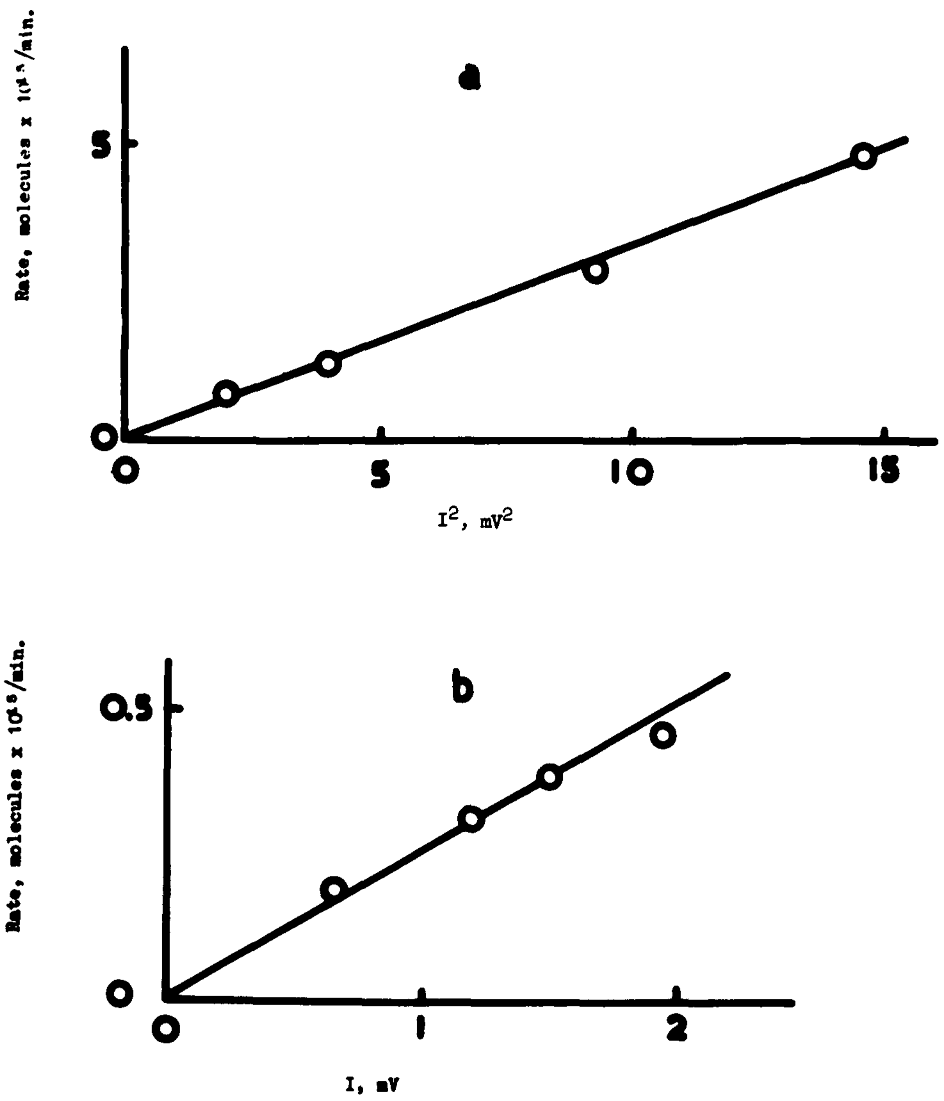

Figure 3. Dependence of the rate of photolysis on intensity of the high pressure arc (a) filtered through OX7, (b) filtered through OY10.

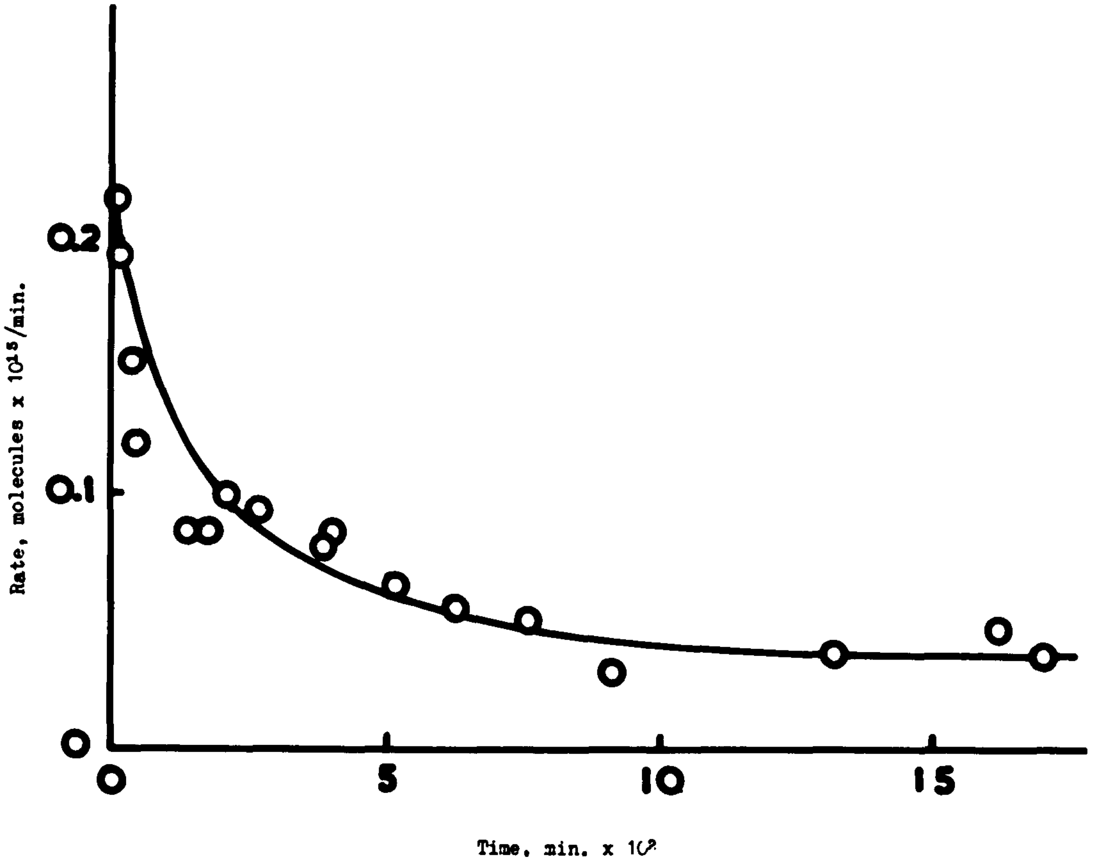

Figure 4. Dependence of the rate of photolysis of fresh barium azide on time when irradiated with the high pressure arc filtered through OY10.

It seems clear that the acceleratory period is due to the presence of barium formed during the photolysis. This was confirmed by two experiments. First irradiated salt was exposed to the atmosphere for several days. The brown salt gradually went white with this treatment and, on subsequent irradiation, showed the deceleratory period associated with fresh salt (Fig. 5). The initial rate was lower than for fresh salt and the minimum rate more rapidly attained as though the barium had been partly but not completely oxidised by this treatment. The effect of intensity on the rate versus time curve is again clearly shown in Fig. 5.

In the second experiment fresh salt was decomposed thermally to various stages and the photolytic rate determined at each stage. The fractional decomposition α could be calculated from the amount of gas evolved and in Fig. 6, the photolytic rate is plotted against α. Also shown is the photolytic rate versus α for a run in which the salt was decomposed entirely photochemically.

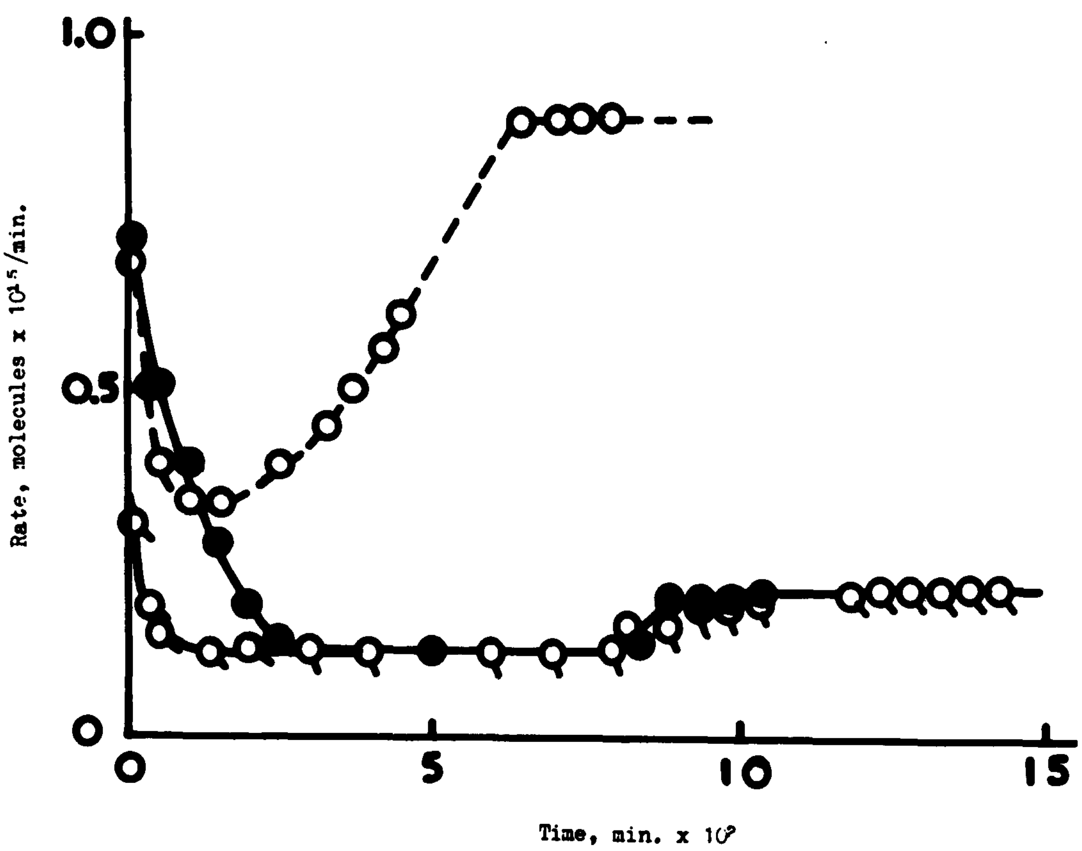

Figure 5. Effect of exposing annealed salt to the atmosphere. (a) O, fresh salt; (b) ●, fresh salt, at half the intensity used for (a); (c) Q, salt used for (a) after exposure to the atmosphere, same intensity as (b). (Compare Fig. 1.)

Figure 7 shows the rate, time curves for barium azide which has been irradiated until the constant rate is reached and then annealed. Curve 1 shows the normal behaviour on irradiation after a 12 h anneal. The constant rate is attained after 4 h. Curve 2 shows the photolytic rate after thermal decomposition (to the extent required to give the same constant rate) followed by a 5 min anneal. Curve 3 shows the behaviour in a similar experiment but after a 12 h anneal while for curve 4 (identical with 1) the annealing time was 24 h. Thus, again, in the acceleratory period, the photolytic rate depends only on the extent of the previous decomposition and not on whether it is performed thermally or photochemically, except that the annealing process is somewhat slower after thermal decomposition than after photochemical decomposition (cf. curves 3 and 1).

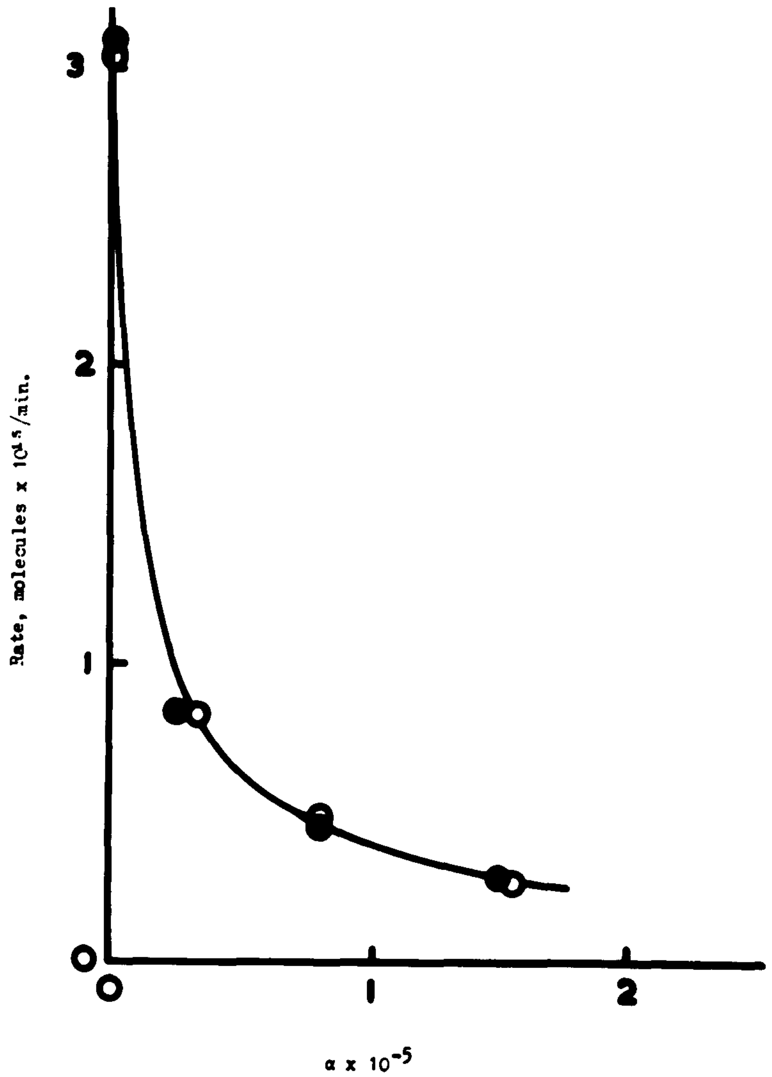

Figure 6. Rate of decomposition of fresh salt as a function of the fractional decomposition α. O, photolytic rate, after thermal decomposition; ●, photolytic rate after photochemical decomposition.

In an attempt to elucidate whether or not more than one mechanism for the production of nitrogen exists, a fresh sample of BaN_6 was irradiated for $\frac{1}{2}$ h at -70° C at which temperature the rate of nitrogen evolution is zero. The dewar was then lowered and the salt allowed to warm up without further irradiation and the temperature of the salt and gas pressure noted at suitable time intervals. The rate of gas evolution is plotted in Fig. 8 as a function of salt temperature. This experiment must be regarded as only a qualitative one, but in spite of this, certain conclusions can be drawn. Two

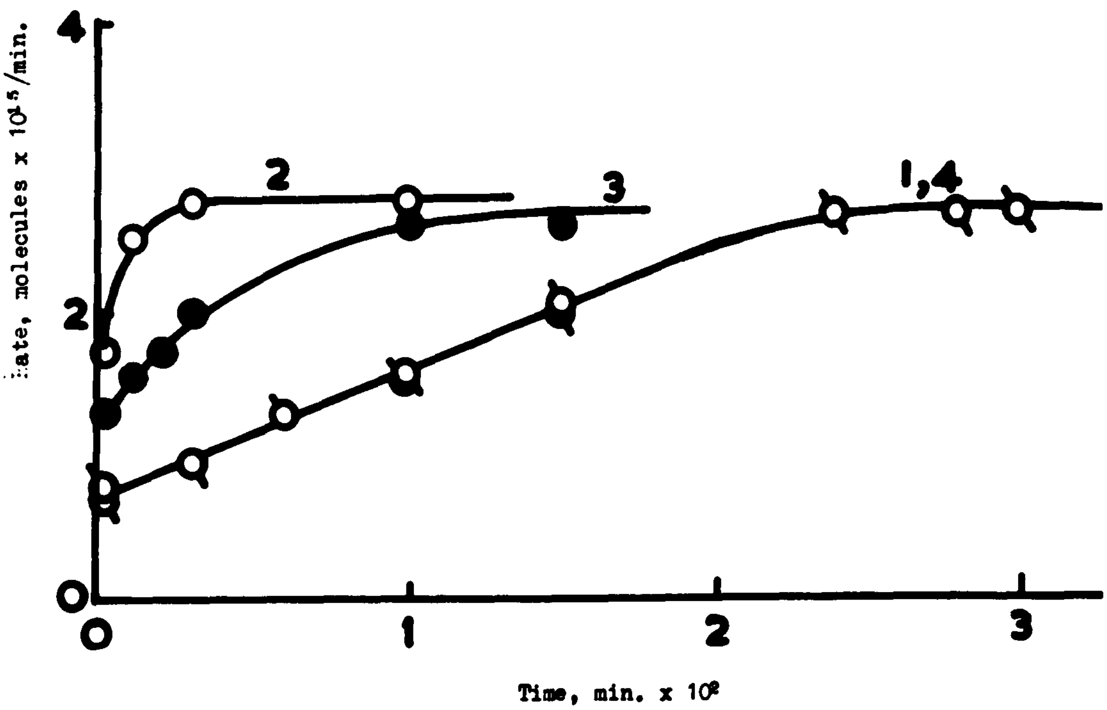

Figure 7. Rate of photochemical decomposition of barium azide after thermal decomposition and annealing. For details, see text.

peaks, centred at about -35° and -5° are observed. (In the first run, the heating was carried out too rapidly so that the first peak is merged with the second one.) The peak heights decrease in successive runs, in agreement with the usual behaviour in photolysis at higher temperatures, but possible variations in the rates of the peak heights could not be established.

Significant colour changes were noticed during these experiments. When fresh salt is irradiated at -70° C there is no colour change but on warming to -35° C the salt shows a violet coloration, which disappears at -5°, when the salt turns white again. This cycle of changes was repeated with the second irradiation, but on the third cycle, the salt appeared greenish after warming to -5° C and thereafter turned gradually brown, the usual colour observed on prolonged photolysis. Nevertheless the appearance of a violet colour at -35° when the first gas evolution takes place was still observable. These observations imply the formation of some unstable intermediate (with the evolution of N_2) from the primary result of the irradiation, at -35° C, and the decomposition of this intermediate at -5° C with further nitrogen evolution.

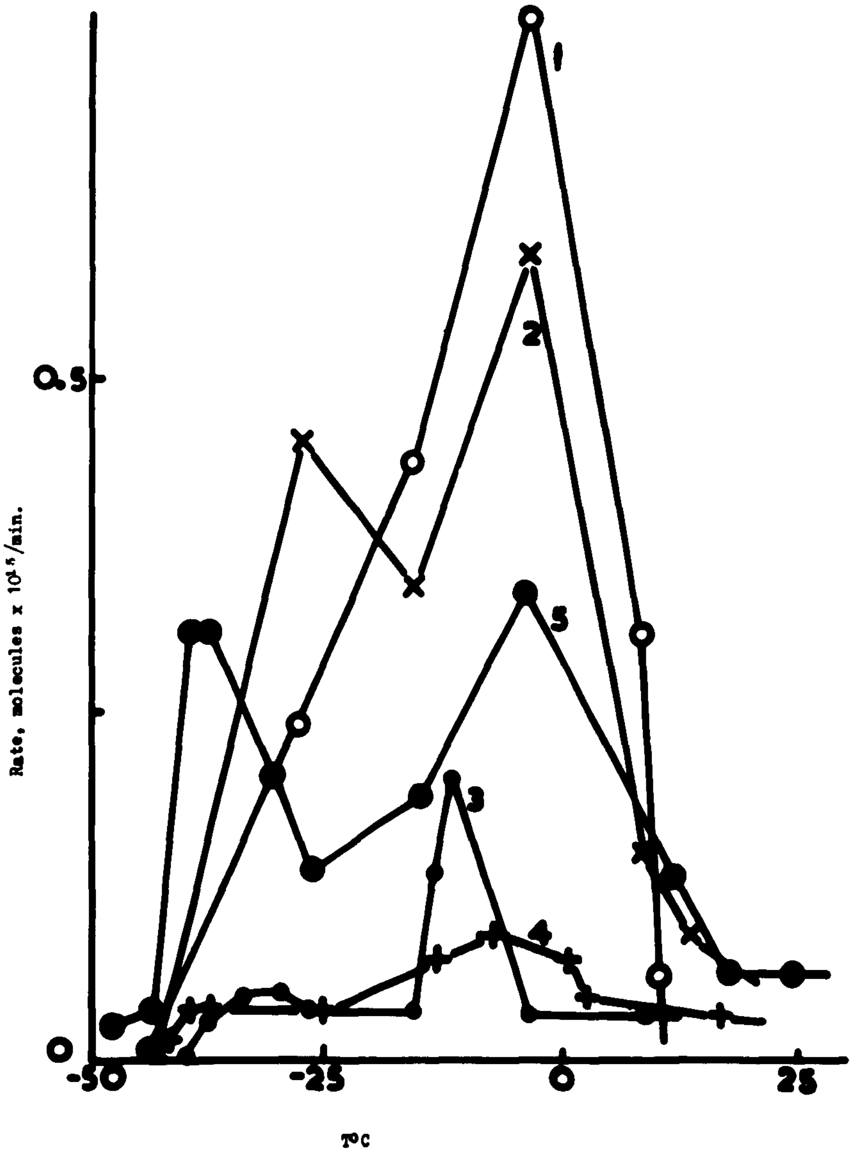

Figure 8. Rate of gas evolution as a function of temperature from barium azide irradiated at -70° C. 1, 2, 3, 4 indicate successive irradiations of $\frac{1}{2}$ h each. The time of irradiation for curve 5 was 3 h.

DISCUSSION

The experimental results reported in this paper indicated that there must be at least two photolytic mechanisms for the production of nitrogen when barium azide is irradiated with ultra-violet light.

By considering the results for the dependence of the rate of photolysis on time (Fig. 1) temperature (Table I) and source (Fig. 4 and Table I) we may conclude that fresh salt is decomposed by ultraviolet light of wavelength in the region of 2537 Å at a rate which (i) decreases steadily with increasing amount of decomposition, (ii) varies as the square of the intensity of the radiation and (iii) is associated with an activation energy of about 5 kcal/mole. These results, while more detailed, are in substantial agreement with the earlier investigation by Thomas and Tompkins[4]. In contrast the rate of photolysis of fresh salt with light of long wavelength ($>$ 3500 Å) is about 5 times smaller, and an acceleratory period was not observed. We are, however, not inclined to regard this result as indicating a new mode of photolysis but believe rather that it simply reflects reduced probability of reaction for light of long wavelength as compared with ultra-violet light. The whole scale of events is therefore altered (cf. the effect of intensity shown in Fig. 1).

When irradiation of fresh salt with the low or high pressure arc, or with the latter using an OX7 filter, is prolonged beyond about 300 min, an increase in the rate of photolysis is observed. This definitely indicates the onset of a new mechanism for although the rates are throughout proportional to I^2, the activation energy increases from 9-10 at the minimum to 20 kcal/mole during the constant rate period. We interpret these results as indicating that the second mechanism, characterised by a thermal activation energy of around 20 kcal/mole can only set in once substantial photolysis has occurred and that the apparent activation energy of 9-10 kcal is due to both processes occurring concurrently.

We accordingly propose the following model for the decomposition of barium azide. Light of short wavelength, i.e. around 2537 Å, is absorbed within the tail of the first absorption band. Previously[7], this had been tentatively identified with an exciton transition: however, the remarkable constancy of the position of this band in sodium, potassium, rubidium and caesium azides[8,9,10] and the recent identification of exciton bands at much shorter wavelengths[11] makes it likely that the band in the 2400-2600 Å region of the alkali azides corresponds to an internal transition[11] on the azide ion. This excitation then will be the primary photochemical process on irradiation and it seems reasonable to presume that this statement is also true of barium azide, the absorption edge of which has been placed by reflectance measurements[6] at around 2600 Å.

The decreasing rate of photolysis of fresh salt with time (Fig. 1) indicates that the reaction proceeds at centres which are gradually consumed. These centres seem likely to be either impurity ions or crystal imperfections, namely anion vacancies or jogs in dislocations. Each of these three species possesses the necessary property of being able to function as an electron acceptor. In perfect, pure crystal, the excited azide ion N_3^{-*} has no option but to decay to the normal ground state, N_3^-, after the appropriate lifetime, but adjacent to an electron acceptor it may become stabilized by partial or total charge transfer of the excited electron to the 'trap', T. Formally, then

perfect crystal: $$N_3^- \overset{h\nu}{\rightleftharpoons} N_3^{-*} \qquad (1)$$

special sites: $$N_3^-T \overset{h\nu}{\rightleftharpoons} N_3^{-*}T \rightleftharpoons \left[N_3\ T\right]^- \qquad (2)$$

Repetition of (2) within the (relatively long) lifetime of $[N_3T]^-$ gives two adjacent excited azide ions,

$$N_3^- \left[N_3\ T\right]^- \overset{h\nu}{\rightleftharpoons} N_3^{-*} \left[N_3\ T\right]^- \rightleftharpoons \left[N_3TN_3\right]^= \qquad (3)$$

which can either revert to the ground state with the emission of phonons or undergo chemical decomposition:

$$[N_3T\ N_3]^= + Ba^{++} \longrightarrow 3N_2 + T\ Ba \qquad (4)$$

The latter process involves the transfer of the two excited electrons to an adjacent Ba^{++} ion and the evolution of nitrogen. As the reaction proceeds, the crystal clearly assumes different properties in the locality of T, and the rate of reaction thus decreases due to the falling number of sites which can function as traps. The possibility that T is an anion vacancy ought not to be excluded because the production of anion vacancies by (4) would not regenerate the trap, since it would leave an aggregate of three vacancies in place of the original single one. It is noteworthy that the final steady rate of this process is not zero (Fig. 1); possibly more than one type of trap is involved. On balance, we favour the hypothesis that the traps are kink sites in dislocations, as is evidently true in silver bromide[11]. Since the reaction involves two activated species, the rate will depend on the second power of the intensity, as observed. The low activation energy of 5 kcal is associated with (4) since neither (2) nor (3) should require thermal energy. The much lower rates observed with long wavelengths are due to the very low efficiency of the excitation of the internal transition.

The result of this first reaction is the production of barium atoms at kink sites or other special positions in the lattice. Since the first ionization potential of barium is 5 eV, these atoms can, under irradiation, emit electrons into the conduction band of the crystal. This does not give a normal lattice barium ion but a Ba^+ ion which is not part of the lattice. An electron is then transferred thermally from an adjacent azide ion giving a positive hole. Simultaneously irradiation is producing excited azide ions and these react with each other (as in the first process) and with the positive holes. There will also be some bimolecular decomposition of holes but this is likely to be less probable than the reaction of holes and excited ions. The second process is then:

$$Ba \underset{}{\overset{h\nu}{\rightleftharpoons}} Ba^+ + e^- \qquad (5)$$

$$Ba^+ + N_3^- \xrightarrow{E} Ba + N_3 \qquad (6)$$

$$N_3^- \overset{h\nu}{\rightleftharpoons} N_3^{-*} \qquad (1)$$

$$N_3^{-*} + N_3 \longrightarrow 3N_2 + e^- \qquad (7)$$

$$2N_3 \longrightarrow 3N_2 \qquad (8)$$

$$Ba + Ba^{2+} + 2e^- \longrightarrow Ba_2 \qquad (9)$$

With $R_7 > R_8$. This mechanism explains the increasing rate, since sites are produced by the first process and regenerated by the second one (Eq. 9). The activation energy for (6) should be about 1 eV since this is the dominant thermal process in the constant rate period. The apparent activation energies of 0.45 at the minimum and 0.9 eV in the constant rate period are 'averages' of the two simultaneous photochemical processes, the second are becoming more important over the acceleratory period. This second process will continue in a self-propagatory manner as long as the barium produced can be regarded as 'atomic', i.e. single atoms or small groups of atoms. At some state which we are not in a position to specify precisely, these pre-nuclei will become large enough to recrystallize and form metal specks. When they do so, their energy levels become those characteristic of bulk metal and can no longer participate in this reaction. An approximate energy level diagram is given in Fig. 9.

On closer inspection, it appears that the second process, summarised in equations (5)-(9), can proceed by a purely thermal mechanism. A barium atom traps an adjacent barium ion (cf. 12)

$$Ba + Ba^{2+} \longrightarrow (Ba_2)^{2+} \qquad (10)$$

Electrons are then transferred from azide ions to the positively charged barium and the positive holes react together. This cycle of events can continue until the pre-nuclei all grow into large specks of barium. This mechanism is consistent with the known facts about the dark rate. With fresh salt the dark rate is zero, but it steadily increases up to a maximum in the constant rate period. The pre-nuclei are destroyed by this reaction so consequently the initial

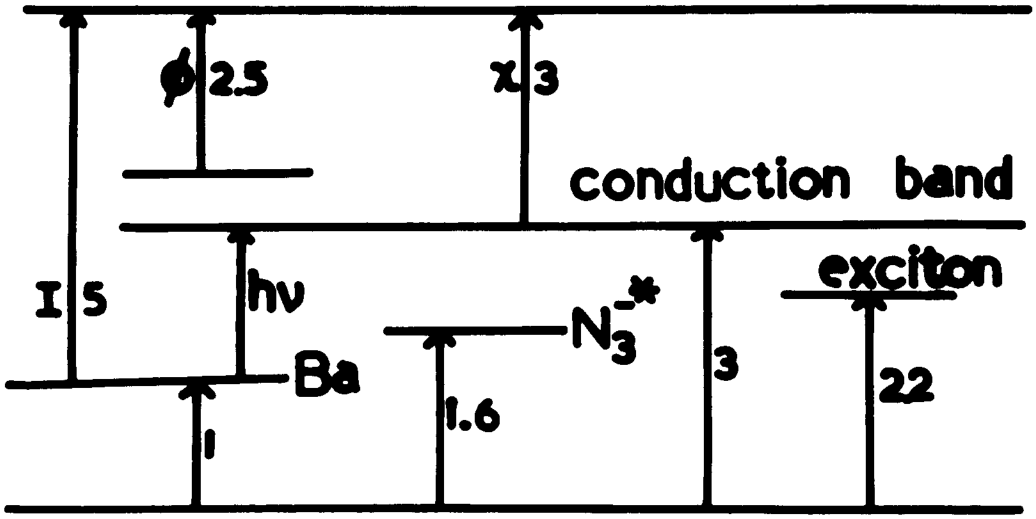

Figure 9. Approximate energy level diagram for barium azide. All energy values are in eV; with the exception of I and ϕ these have been roughly estimated by analogy with other azides.

photo-rate is low (below the minimum) on recommencing irradiation. The annealing process is thus the growth of barium atoms and pre-nuclei into metal specks by thermal decomposition of the azide.

With light of long wavelength (>3500 Å) the first process (bimolecular decomposition of excited azide ions) occurs but with low efficiency. Once some decomposition has occurred, i.e. on the flat region of Fig. 4, the activation energy is 20 kcal/mole because the second process

$$N_3 + N_3^{-*} \longrightarrow 3N_2 + e^- \qquad (7)$$

is dominant. However, if the salt is first decomposed into the constant rate period, so that more barium pre-nuclei are available, then positive holes are produced at a faster rate than excited ions because the photo ionization of Ba is more efficient than excitation of the internal transition, with light of long wavelength. The rate of supply of N_3^{-*} then becomes the limiting factor and the activation becomes that for the thermal value of this excitation. This can be estimated as roughly the optical value divided by the dielectric constant ratio i.e. 4.8/3 or 1.6 eV. This is in accord with the experimental value. Moreover, the rate depends on the first power of the intensity, as it should since only the concentration of holes is proportional to the intensity.

Finally, the results of the 'warm-up' experiments shown in Fig. 8 allow us to be a little more specific about the nitrogen evolution reaction. This apparently goes in two steps: a possible sequence is

$$\left[N_3T\ N_3\right]^{=} \longrightarrow N_4^- + N_2 + e^-$$

at -35° C, followed by-

$$N_4^- \longrightarrow N_3^- + N$$

$$N + N \longrightarrow N_2$$

at -5° C. The species N_4^- has been identified in irradiated KN_3 by electron spin resonance[13].

We are indebted to the Corps of Engineers, U. S. Army for financial support under contract DA-44-009.ENG.4187.

References

1. P. Gunter, Lepin and Andreew, Z. Elektrochem., 36, 218 (1930).
2. W. E. Garner and C. H. Moon, Nature, 131, 513 (1933).
3. W. E. Garner and J. Maggs, Proc. Roy. Soc. A, 172, 299 (1939).
4. J. G. N. Thomas and F. C. Tompkins, Proc. Roy. Soc., A, 209, 550 (1951); A, 210, 111 (1951).
5. N. F. Mott, Proc. Roy. Soc., A, 172, 325 (1939).
6. P. W. M. Jacobs and F. C. Tompkins, Proc. Roy. Soc. A, 215, 254 (1952); A, 215, 265 (1952).
7. P. W. M. Jacobs, F. C. Tompkins and D. A. Young, Discuss. Faraday Soc., 28, 234 (1959).
8. J. Cunningham and F. C. Tompkins, Proc. Roy. Soc., A, 251, 27 (1959).
9. H. G. Heal and J. P. S. Pringle, J. Phys. Chem. Solids, 15, 261 (1960).
10. H. A. Papazian, J. Chem. Physics, in the press.
11. S. K. Deb, J. Chem. Physics, in the press.

12. J. W. Mitchell, Rep. Prog. Physics, 20, 433 (1957).

13. Shuskus, Young, Gilliam and Levy, J. Chem. Phys., 33, 622 (1960).

ON THE APPLICABILITY OF HAHN'S EMANATION METHOD FOR DECOMPOSITION STUDIES OF INORGANIC AZIDES

by

J. A. Joebstl and H. J. Mueller
Basic Research Group
U. S. Army Engineer Research and Development Laboratories
Fort Belvoir, Virginia

Introduction:

The emanation method was introduced by Otto Hahn(1,2) 30 years ago as a technique for the examination of transformations and reactions in the solid state. In the thirties the theoretical interpretation of the emanation process in solids was given by Fluegge(3) and Zimens(4,5,6) which laid the basis for a quantitative evaluation of emanating power data.

The basic principle of the emanation method is the following: A radioactive parent which will produce an isotope of radon by its radioactive decay is incorporated homogeneously into the solid to be investigated. Thus the radioactive parent acts as a constant source of emanation in the interior of the latter. Because of its short half-life, only a part of the emanation produced can escape from the solid by diffusion or recoil. The ratio between the rate at which emanation escapes from the solid and the rate at which it is being produced by the radioactive decay is called the emanating power E of the sample. The emanating power consists of two components: the recoil component E_R and the diffusion component E_D (Fig. 1). The emanation atom ejected during the α-decay of the parent is able to penetrate some hundreds of Å of the solid due to its recoil impulse. If the surface lies within the recoil range R of the parent, the emanation will escape from the surface and can be carried along by a carrier gas to an α-detector. This case is demonstrated by A in Fig. 1. The emanating power due to recoil is relatively small, independent of temperature and proportional to the surface of the sample. For the majority of the emanation atoms, however, the recoil track terminates in the interior of the solid. Nevertheless, the emanation atoms can still escape by diffusion and, thus, contribute to the total emanation power. This is demonstrated by B in Fig. 1. The emanating power due to diffusion is strongly dependent on the temperature, i.e., it increases with increasing temperature. For large grains (with dimensions of 10^{-4} cm and above) the components of the emanating power are given by the following equations:

$$E_R = \frac{Rps}{4m} \qquad (1)$$

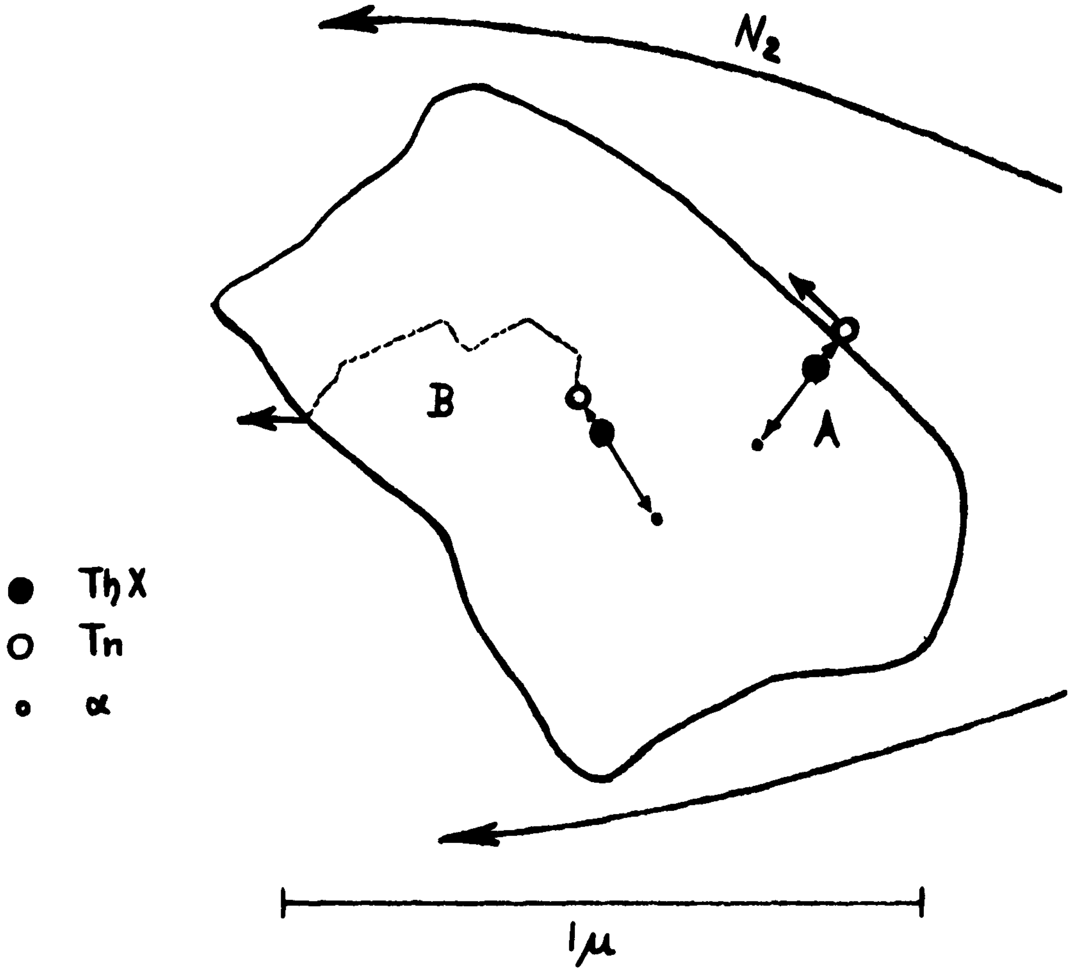

A ··· Emanating power due to recoil (E_R)
B ··· Emanating power due to diffusion (E_D)

$$E = E_D + E_R$$

$$\text{Emanating power} = \frac{\text{escaping emanation} \times 100}{\text{produced emanation}}$$

Figure 1. Scheme of the emanating power of a solid.

$$E_D = \sqrt{\frac{D}{\lambda}} \cdot \frac{ps}{m} \qquad (2)$$

R is the recoil range, p the density of the solid, s and m are surface and mass, respectively, λ is the decay constant and D the diffusion coefficient. The total emanating power of a large grain is obtained by addition of these two equations:

$$E = E_R + E_D = \left(\frac{R}{4} + \sqrt{\frac{D}{\lambda}}\right) \frac{ps}{m} \qquad (3)$$

From this equation both the specific surface $\frac{s}{m}$ and the diffusion coefficient D may be calculated, provided the total emanating power can be resolved into the recoil and diffusion components.

Measurement of the emanating power E:

As defined, the emanating power is the ratio between the rate of escape of the emanation and the rate of its formation. If the rate of escape of short-lived emanations (e.g. thoron or actinon) is to be measured, the flow method is usually employed. In this method an inert carrier gas is used to sweep the emanation from the sample into an ionization chamber or another α-detector. There an activity is measured which is due to α-particles emitted by the emanation and its immediate daughters, decaying in the measuring chamber. This activity is proportional to the rate of escape of the emanation from the preparation. The apparatus used for the flow measurements is shown in Figs. 2 and 3. The flow rate and dryness of the inert carrier gas is controlled in the first section (Fig. 2) of the apparatus, which is similar to that used by Gregory(7). The gas comes from a cylinder A, which is equipped with a standard reducing valve, and passes through a small needle valve B at low pressure. A by-pass in the cylinder C under a constant pressure head of water (h) regulates the pressure in the apparatus. A volume (flask D) and a capillary resistance (E) are introduced in the circuit to compensate the slight oscillations of the pressure, resulting from the bubbling in the by-pass. The rate of flow is controlled by means of a needle valve at the other end of the flow apparatus (I in Fig. 3). The flow rate is measured by the flow meter F. After the flow meter the carrier gas passes through a silica gel drying column G and a cooling trap H. Figure 3 shows the second section of the flow apparatus. The carrier gas enters at A, passes in the quartz tube over the sample and carries the escaping emanation to the chamber B where the activity is measured by means of a scintillation counter. A scaler or a ratemeter with recorder are connected with the scintillation counter for measuring the activity. The temperature of the sample is measured by means of a thermocouple which is likewise connected

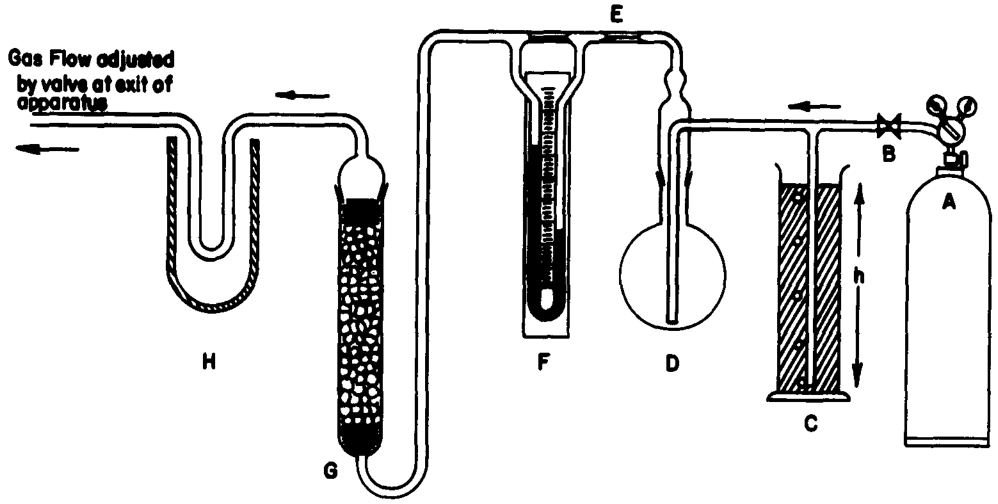
Gas Flow adjusted by valve at exit of apparatus
E
B
A
h
H
F
D
C
G

Figure 2. Apparatus for flow measurement of an emanation: Control and purification of the carrier gas.

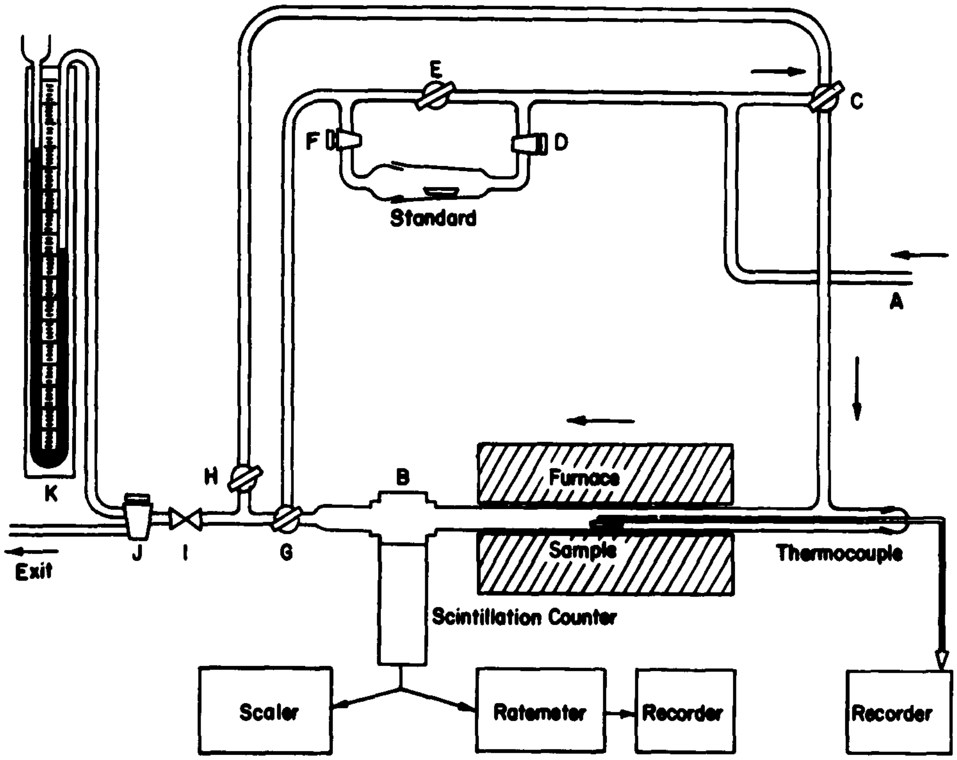
E
C
F
D
Standard
A
K
H
B
Furnace
Sample
Thermocouple
Exit
J
I
G
Scintillation Counter
Scaler
Ratemeter
Recorder
Recorder

Figure 3. Apparatus for flow measurement of an emanation: Collection and measurement of the emanation.

with a recorder. The furnace is of a multiple unit type: it may be opened and removed quickly for the purpose of abrupt cooling of the sample. A standard preparation is placed in an alternate circuit of this apparatus. It can be switched into the circuit whenever calibration is required. The flow of the carrier gas can be reversed in order to measure the background activity in the chamber B. The background activity increases slowly during an experiment because of the radioactivity decay products of the emanation and has to be subtracted from the measured total activity. By means of the three-way stopcock J, the manometer K can be connected to the apparatus for the purpose of leak testing.

The activity measured by means of the flow method may be standardized in terms of absolute emanating power. The absolute emanating power of the sample can be obtained by comparison of its α and β activities with those of a standard preparation of known absolute emanating power (so-called "β-determined" standard).

Discussions of emanating power versus temperature (EP/T) curves:

Usually the emanating power is either measured at slowly increasing temperature or isothermally. Let us consider at first the

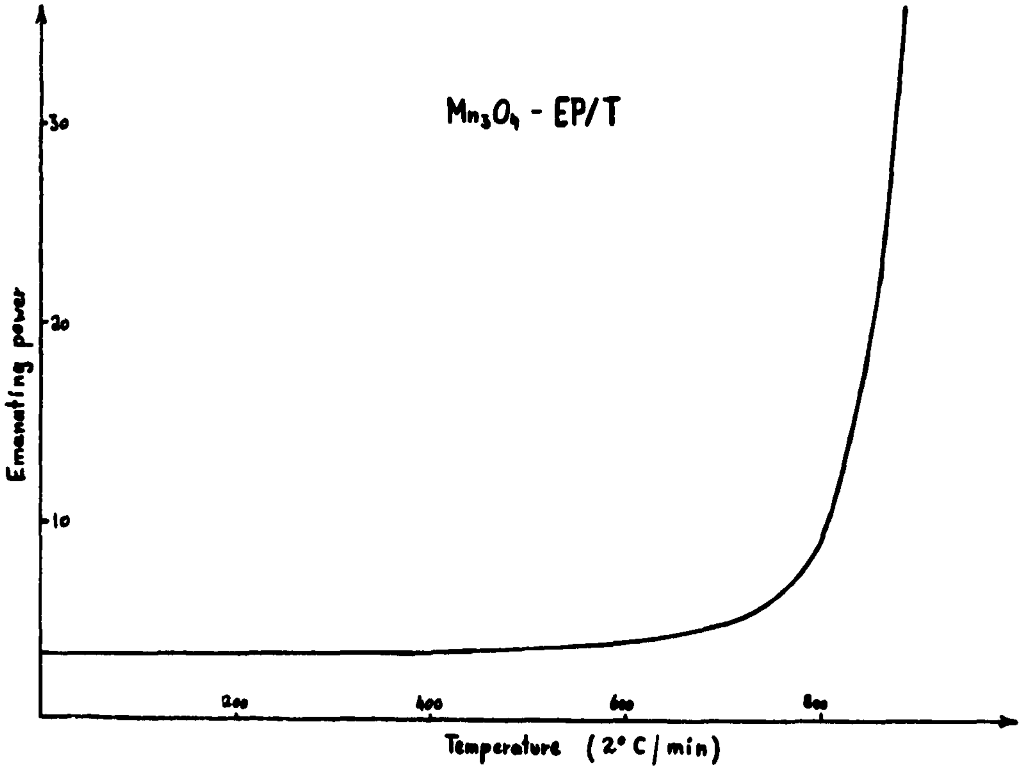

Figure 4. Emanating power vs. temperature curve of Mn_3O_4.

characteristic emanating power vs. temperature diagram of a chemically stable, solid substance (Fig. 4). The substance in question is hausmannite (Mn_3O_4) with incorporated RdTh. In accordance with Jagitsch(8) the following interpretation of this diagram can be given: The emanating power of Mn_3O_4 is relatively low at room temperature and stays nearly constant for several hundred degrees Celsius since at ordinary temperature the emanation is practically unable to diffuse out of a closely packed, inorganic crystal lattice. In this case the emanating power at room temperature consists only of the emanating power due to recoil and is proportional to the external and internal surface of the solid. The emanating power due to recoil also stays constant if the temperature increases, provided there is no change in the surfaces of the solid. However, a continuous increase of the total emanating power of hausmannite can be observed at elevated temperatures which is caused by the rise of the emanating power due to diffusion (E_D) at higher temperatures. If we now plot logarithmically the differences between the emanating power at higher temperatures and the emanating power at room temperature ($EV - EV_0$) against the reciprocal of the absolute temperature 1/T, then we recognize two discontinuities in the slope of the curve (Fig. 5). The first change of the slope occurs at 686° C. This is

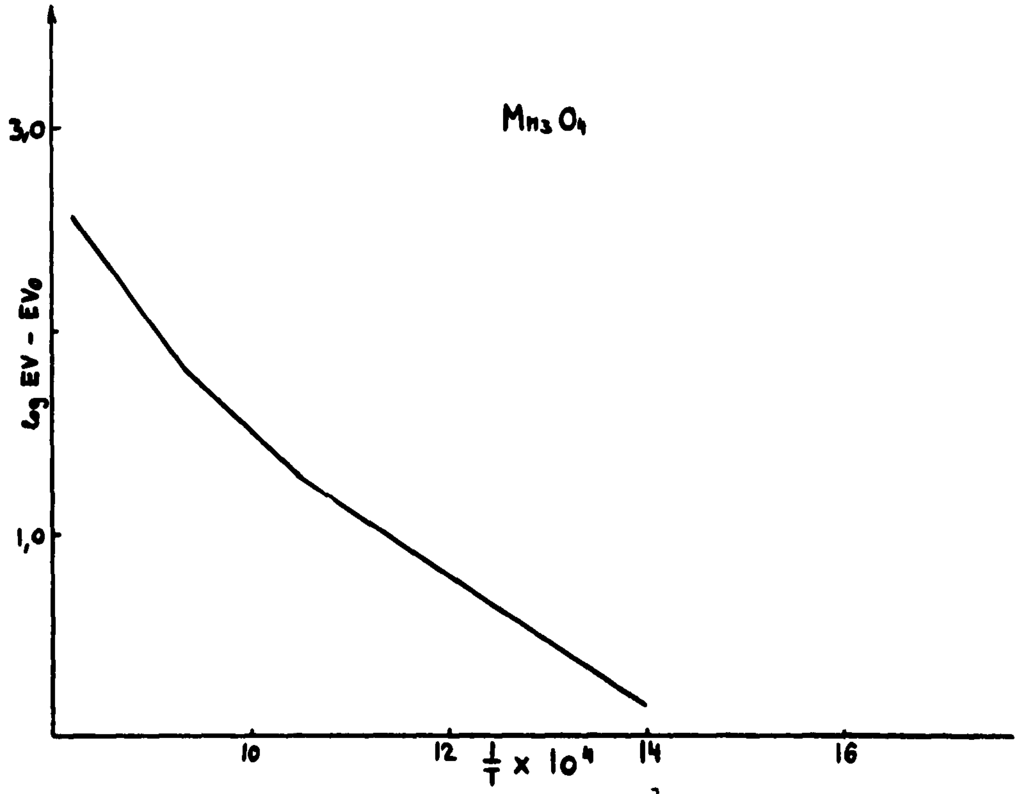

Figure 5. log $EV - EV_0$ vs. $\frac{1}{T}$ of Mn_3O_4.

0.5 times that of the absolute melting temperature of hausmannite. The second change appears at 800° C and this is 0.5 times that of the absolute melting temperature of manganous monoxide (MnO) which compound was contained as an impurity in the hausmannite used in this investigation.

Similar results have been obtained on many other compounds: the temperature at which the enhancement of the emanating power of stable solids starts is always between 0.5 and 0.6 times that of the absolute melting temperature of the solids. According to Tammann(9) this is also the temperature at which the lattice begins to "loosen", and reactions in the solid state become possible since the mobility of the lattice components has become sufficiently high. It is for this reason that the escape of emanation atoms from the interior of the solid begins to accelerate in the same temperature range and will increase rapidly as the temperature rises. Both discontinuities in the diagram of Mn_3O_4 can therefore be correlated to an increasing lattice diffusion of the emanation in the solid caused by the loosening of the lattice at this temperature. This demonstrates the high dependency of the emanating power due to diffusion (E_D) on changes of the condition of diffusion in the solid. Hence, one may reasonably expect that other structural changes in a solid (like phase transformations, decompositions, etc.) can also be detected and followed by means of the emanation method.

We shall consider now the EP/T diagram of a chemically metastable solid, BaN_6, as established by our own measurements. BaN_6 has been chosen because the thermal decomposition and the photolysis of this compound were well examined in the past. We prepared BaN_6 in the usual way from $Ba(OH)_2$ and HN_3 by precipitation with alcohol and then incorporated about 1 µC of RdTh (Fig. 6) per gram of BaN_6. The EP/T curve of BaN_6 is shown in Fig. 7. The temperature increase during the measurement was 3° C/min and nitrogen was used as carrier gas. On the ordinate the activity is given in counts per minute per milligram. The solid curve was obtained on heating, the dashed one on cooling. The sample at room temperature already showed a relatively high emanating power which increased slowly up to a temperature of 120° C. Beyond this temperature, however, the emanating power rapidly increased, passed a maximum, and then decreased again. During cooling the emanating power gradually approached the original room temperature value. BaN_6 is being prepared by dehydration of the monohydrate and this fact may be responsible for the relatively high activity observed at room temperature. Obviously the structure of BaN_6 became defective due to the dehydration process. We ascribe the strong increase of the emanating power starting at 120° C to the breakdown of the lattice during the decomposition process as a result of which practically all emanation produced in the interior of the sample can escape. The decrease of the emanating power observed after completion of the decomposition probably coincided with the

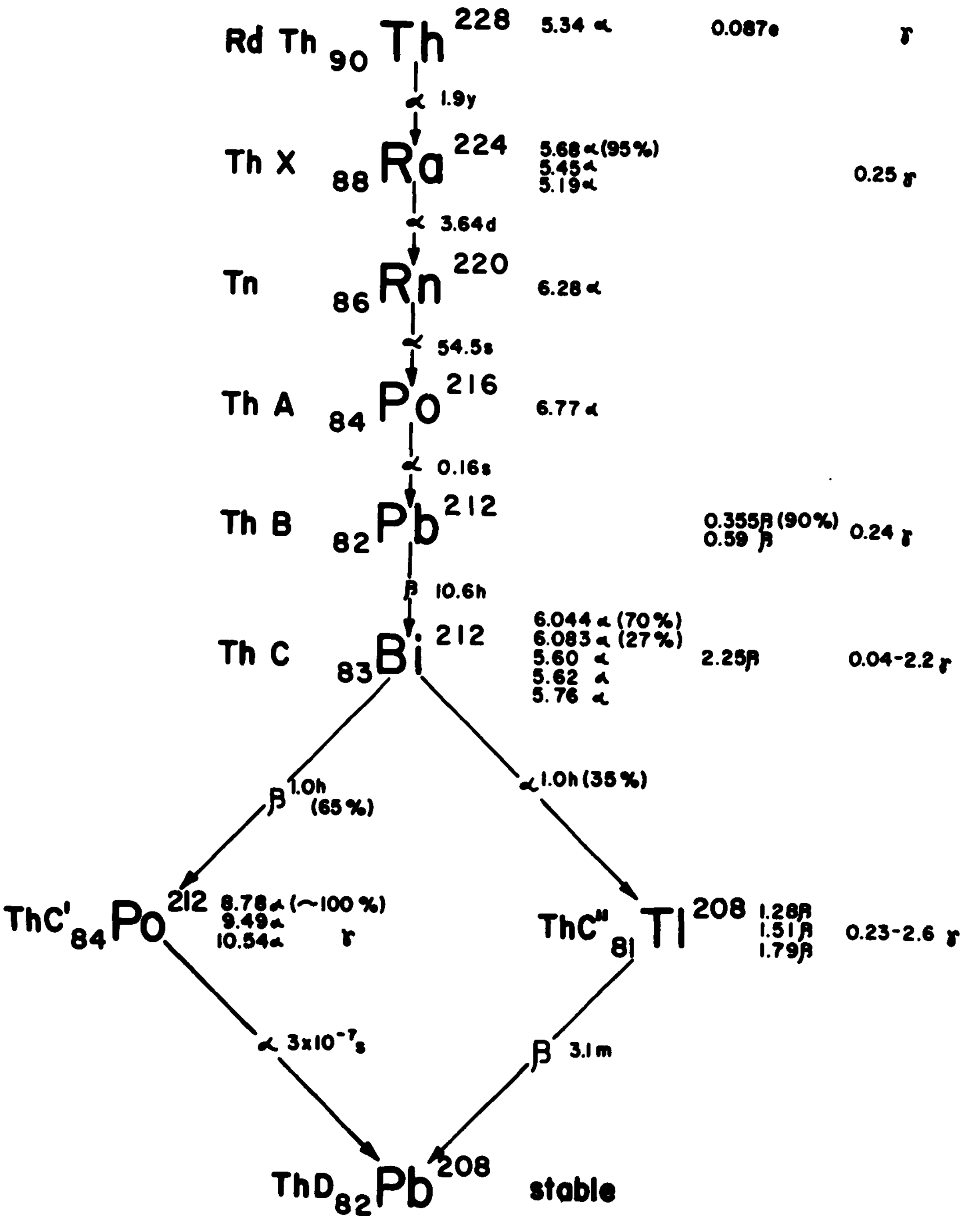
Rd Th 90 Th 228
5.34 α
0.087e
γ
α 1.9y
Th X 88 Ra 224
5.68 α (95%)
5.45 α
5.19 α
0.25 γ
α 3.64d
Tn 86 Rn 220
6.28 α
α 54.5s
Th A 84 Po 216
6.77 α
α 0.16s
Th B 82 Pb 212
0.355 β (90%)
0.59 β
0.24 γ
β 10.6h
Th C 83 Bi 212
6.044 α (70%)
6.083 α (27%)
5.60 α
5.62 α
5.76 α
2.25 β
0.04-2.2 γ
β 1.0h (65%)
α 1.0h (35%)
ThC' 84 Po 212
8.78 α (~100%)
9.49 α
10.54 α
γ
ThC" 81 Tl 208
1.28 β
1.51 β
1.79 β
0.23-2.6 γ
α 3x10⁻⁷s
β 3.1m
ThD 82 Pb 208
stable

Figure 6. RdTh and its decay products.

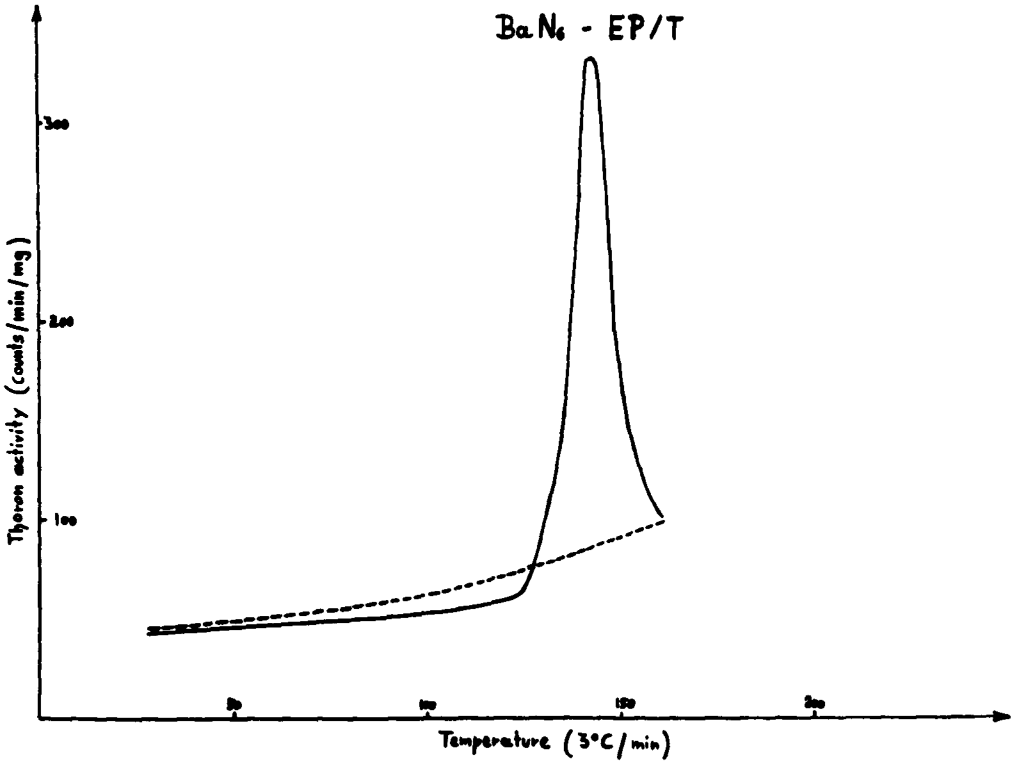

Figure 7. Activity vs. temperature curve of BaN_6.

growth of the decomposition products (in this case Ba and Ba_3N_2) and thus might be related to it. The peak of the emanating power was slightly displaced to lower temperatures when the heat treatment was undertaken after preheating or preirradiation with ultraviolet light. The use of argon as carrier gas showed a much sharper outburst of the emanation during the decomposition. Figure 8 shows isotherms which were taken with the same preparations. These curves demonstrate how the emanating power reflects the pattern of decomposition at different temperatures. Figure 9 illustrates the effect of quenching of the sample: The solid line shows the increase of the emanating power at rising temperature, the dashed line shows the changes of the emanating power during the cooling process and the dotted line represents the increase of the emanating power during the re-warming of the sample. After the beginning of the decomposition we cooled the preparation as fast as possible with dry ice. At first the emanating power increases further during the cooling process. The emanation obviously still had the opportunity to escape from the interior of the lattice during a certain time after cooling. The BaN_6 was only partly decomposed when the heating was interrupted as a re-warming curve proved (Fig. 10). The results obtained so far are preliminary and we shall not evaluate them quantitatively until

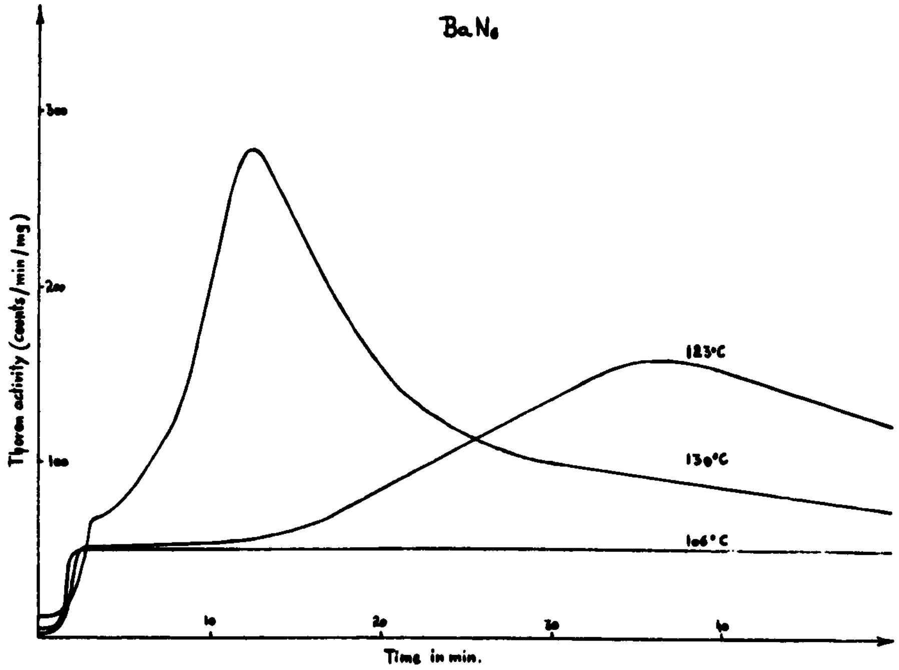

Figure 8. Isotherms of BaN_6.

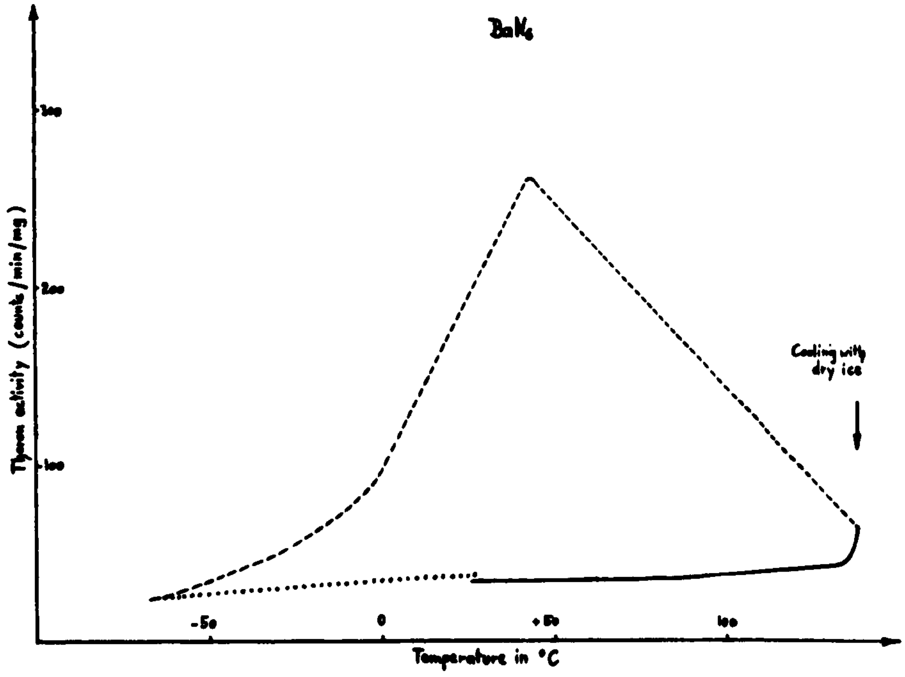

Figure 9. Effect of quenching on BaN_6.

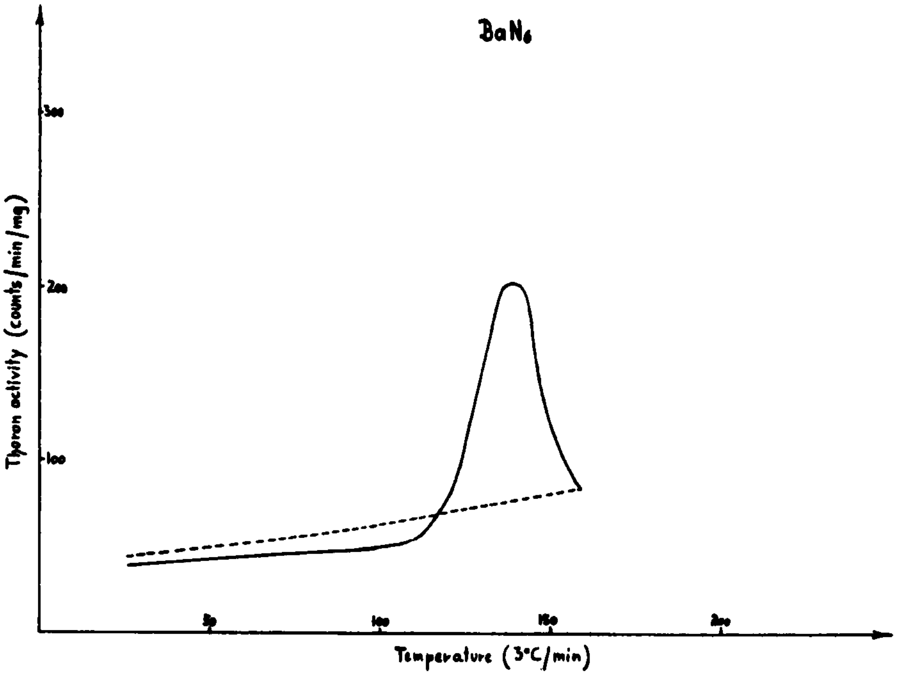

Figure 10. Reheating curve of BaN_6.

we are able to observe simultaneously the nitrogen evolution and the emanating power. An apparatus for such examinations is being designed.

Aforementioned experiments show that it is possible to follow the course of a decomposition by measuring the emanation which escapes from the metastable solid. At room temperature the emanating power is a characteristic value of a solid. If preparations of the same chemical constitution exhibit a different emanating power at ordinary temperature, one can assume that they will also differ with regards to their internal and external surface and the degree of perfection of the lattice, and thus the emanating power is closely related to the chemical activity of a solid.

The emanation technique may be successfully used, therefore, for the characterization of a metastable compound and for the examination of its decomposition pattern.

References

1. O. Hahn, Z. Elektrochemie 29, 189 (1923).
2. O. Hahn, Applied Radio-Chemistry, Cornell University (1936), p. 191.
3. S. Fluegge and K. E. Zimens, Z. Physik Chem. 42, 179 (1939).
4. K. E. Zimens, Z. Physik. Chem. 191, 1, (1942).
5. K. E. Zimens, Z. Physik. Chem. 191, 95, (1942).
6. K. E. Zimens, Z. Physik. Chem. 192, 1, (1943).
7. J. N. Gregory, AERE-CR-460.
8. R. Jagitsch, Z. Physik Chem. 44, 209, (1939).
9. G. Tammann and W. Pape, Z. Angew. Chem. 39, 869 (1926).

A STUDY OF RADIATION-INDUCED DEFECTS IN SODIUM AZIDE*

by

F. F. Carlson, G. J. King,
R. C. McMillan, and B. S. Miller
Basic Research Group
U. S. Army Engineer Research and Development Laboratories
Fort Belvoir, Virginia

ABSTRACT

Optical absorption and electron spin paramagnetic resonance, ESPR, experiments on ultraviolet irradiated NaN_3 have revealed a number of color centers. A series of interrelated thermal and optical bleaching experiments are described which allow one to correlate the optical absorption bands with the ESPR data. The experiments are interpreted by analogy with the well known work on alkali halides, in terms of the DeBoer model of the F center and the Seitz models of the F_2 and F_2^+ centers. A reassignment of the optical absorption bands to the appropriate centers is made. Calculations of band energies based on the continuum models for these centers are found to be in excellent agreement with the data. Besides the vacancy centers formed by the ultraviolet light, x-irradiation at 77° K causes an additional defect which appears as a power sensitive three-line ESPR signal. This spectrum is interpreted as N^{14} atoms trapped in the crystal lattice. Upon warming, the signal rapidly disappears and the sample glows. The implications of all of the above experiments upon the chemical kinetics of vacancy formation and crystal decomposition will be discussed.

I. INTRODUCTION

Sodium azide in its available pure state is a white microcrystalline powder. Clear, colorless crystalline platelets of the material may be grown, with some difficulty, from aqueous solution. The compound is an insulator, is diamagnetic,(1) and is highly ionic. It differs in thermal properties from alkali halide materials in that it decomposes(2) easily at temperatures well below its melting point (~598° K). Sodium azide is also photosensitive(3) and decomposes under uv irradiation according to the highly exothermic bimolecular

---

* Most of this report appeared as "Solid State Photochemical Processes in Sodium Azide," by G. J. King, B. S. Miller, F. F. Carlson, and R. C. McMillan in J. CHEM. PHYS., 35, No. 4, 1422 (Oct. 1961).

chemical reaction $2N_3^- \dashrightarrow 3N_2+2e$, which creates an energy surplus of approximately 9 ev(4). This reaction can also be produced by irradiation with x rays,(3,5) gamma rays,(6) and also by neutrons(6).

Irradiation by the mercury 2537-A line at ~77° K produces a deep optical absorption band at 6100 A and a smaller band on the long wavelength shoulder at 7300 A. By analogy with the alkali halides,(7) these bands have been previously termed the F band and the R band, respectively. No band corresponding to the V band in alkali halides is observed when irradiation is performed with the 2537-A mercury line at ~77° K(3). The optical bands at 6100 A and 7300 A become thermally unstable below ~298° K.

Electron spin resonances produced in sodium azide by uv irradiation have been reported previously(8,10). Irradiation for short periods with an unfiltered mercury lamp at 573° K produces sodium metal colloids in sodium azide. The electron spin paramagnetic resonance (ESPR) of the conduction electrons of the colloidal sodium is easily observed(8,9). Identification of the resonance as that from colloidal sodium has been corroborated by spectrophotometric means(8).

Irradiation of sodium azide with a mercury uv lamp at 77° K, however, produces an ESPR absorption identified as an F center with resolved nuclear hyperfine interactions(10). The difference in behavior of sodium azide at the two temperatures is attributed to the stability of photo-induced defect structure at 77° K. At the high temperature, which is only slightly below the melting point of sodium azide, thermal- and photo-decomposition produce large quantities of nitrogen gas and allow remaining sodium atoms to migrate and form colloids. The process of thermal aggregation of metallic sodium in photolysed azides has been compared to the development of photographic images.(11)

II. EXPERIMENTAL PROCEDURES

Microcrystalline standards of sodium azide powder of very high purity were prepared by direct reaction of gaseous hydrazoic acid and pure sodium metal. The hydrazoic acid used in this procedure was prepared by the method of Kemp(12) in order to avoid sulfate contamination introduced into the hydrazoic acid during its production. In this manner, dry iron-free sodium azide is produced which shows a diamagnetic susceptibility of 17×10^{-6} cgs units per mole. Normal, chemically pure samples of sodium azide contain iron as a result of their manufacture and commonly show paramagnetic behavior. The impurities can usually be eliminated by multiple recrystallization of the material.

The crystals of sodium azide which were used for all optical measurements were grown from saturated aqueous solution. Until very recently, crystals suitable for optical experiments were obtained only with great difficulty. After an extensive investigation of environmental growth conditions, Kezer(13) has determined the parameters needed for successful production of large quantities of crystals of optical quality. These crystals are in the form of thin platelets which typically are 6x6x0.1 mm in size. Careful selection procedures are required to avoid use of crystals exhibiting morphological disturbances such as twinning and stacking faults. These defects seriously interfere with optical measurements since the index of refraction of sodium azide is anisotropic. Occasionally a crystalline sample was crushed into a powder and its behavior compared to that of the pure dry powder in ESPR experiments.

The high purity microcrystalline sodium azide samples were prepared for ESPR measurements in such a manner as to prevent contamination by contact with air or water. The azide was placed in a fused silica tube and the tube then evacuated to a pressure of 2×10^{-5} mm Hg. The fused silica tube was then sealed off with a torch. No microwave resonances were detected when such untreated samples were examined in the ESPR spectrometer. In some cases, to improve thermal contact for low-temperature experiments, the sample tubes were filled with helium gas to a pressure of about 0.5 mm Hg.

During the torching off of the sample, the azide in the tube is subjected to irradiation from the hot fused silica. By comparison with other sealing methods, no effect traceable to this irradiation was found. A small amount of sodium azide also decomposes near the seal-off point giving deposited sodium metal and pure nitrogen gas. The part of the tube covered by the sodium metal does not enter the sensing volume of the microwave cavity but does, however, serve as an effective getter for any residual active gases such as oxygen.

Ultraviolet irradiation of the sealed sample through the fused silica tube was performed by using a Hanovia SH616A mercury vapor lamp placed approximately 5 cm from the sample. During the irradiation the sample was barely submerged in an open dewar of liquid nitrogen. This rather crude arrangement permits optimum aperture conditions, results in efficient sample cooling, and the gas from the boiling nitrogen provides an optical path which transmits short-wavelength uv light.

The sample tube was periodically shaken to obtain mixing of the powder to assure good irradiation coverage. Approximately one hour of this treatment was sufficient to color the sample deep blue.

Irradiation with uv light at 195° K was accomplished by pressing the sample tube into dry-ice powder in the dewar instead of liquid nitrogen. In cases where optical bleaching of color centers was attempted, a Sylvania Blue Top type 300T8-1/2 tungsten projection lamp was used in conjunction with water heat filters and various suitable Corning glass filters.

All of the ESPR measurements were performed at 77° K. After appropriate sample treatment at a desired temperature, speedy transfer to a quick-sealing low-temperature H_{102} cavity surrounded by a Styrofoam dewar completed the preparation without allowing significant temperature change of the sample. The cavity had a quick-sealing entry port which allowed approximately three-fourths of the fused silica sample tube to extend beyond the limits of the cavity proper. The sample tube was approximately one-fourth filled (1cc) with sodium azide. By proper mechanical treatment of the cavity the entire powdered sample could be shaken out of the sensitive volume of the cavity while the fused silica tube was held rigidly in its original position in the cavity. In this way, precise blank runs were obtained and any sample holder effects eliminated. Unless otherwise stated, in every case the optical and ESPR measurements were performed at 77° K.

The spectrometer used in these experiments consisted of a Varian type V4500 EPR spectrometer; a Varian regulated power supply type V2100A, and a 12-in. type 4012 high resolution NMR magnet. A simple X band magic tee bridge with the AFC locked on to the sample cavity was employed for the majority of the measurements. Air-cooled VA201B klystrons, which are low noise and stable, were used for the majority of the measurements. Some high-power experiments were performed using a Varian type V58 klystron. The field of the magnet was modulated at 200 cps in most of the experiments.

Klystron frequencies were measured by means of a Hewlett-Packard type 540B frequency counter system and magnetic field strengths were determined by a proton magnetometer designed by Singer and Johnson(14) This is an excellent instrument if moderate care is given to placement of components and shielding of the rf choke.

Optical measurements were performed using a Beckman DK-2 spectrophotometer which was equipped with liquid-helium cryostat(8). All optical measurements were transmission type, and thin crystalline platelets of NaN_3 were used.

III. CORRELATION OF OPTICAL AND ESPR ABSORPTION BANDS

Initial experiments served to correlate the optical bands with the corresponding ESPR bands produced by uv irradiation at 77° K. Several criteria were used for deciding that a particular optical band and ESPR absorption were produced by the same defect center. It was required that the particular optical absorption to be related to an ESPR absorption must first show identical thermal and optical bleaching properties and that these properties should be unique to both of the absorptions. Another criterion was that, once a correlation was made, the optical band and the ESPR absorption should have separate and independent justifications within their own disciplines or techniques. That is, the F optical band should fit some optical model explaining its center wavelength with respect to other bands. The ESPR absorption for an F center should fit the symmetry properties and other reasonable requirements of an F-center spin resonance.

In the initial ESPR experiments, microcrystalline samples of sodium azide were irradiated for one hour with uv light at 77° K and then examined in the ESPR spectrometer. At sufficiently high power, a strong symmetric resonance with resolved hyperfine structure (Fig. 1) was observed, which previously(10) was ascribed to an F-center resonance.

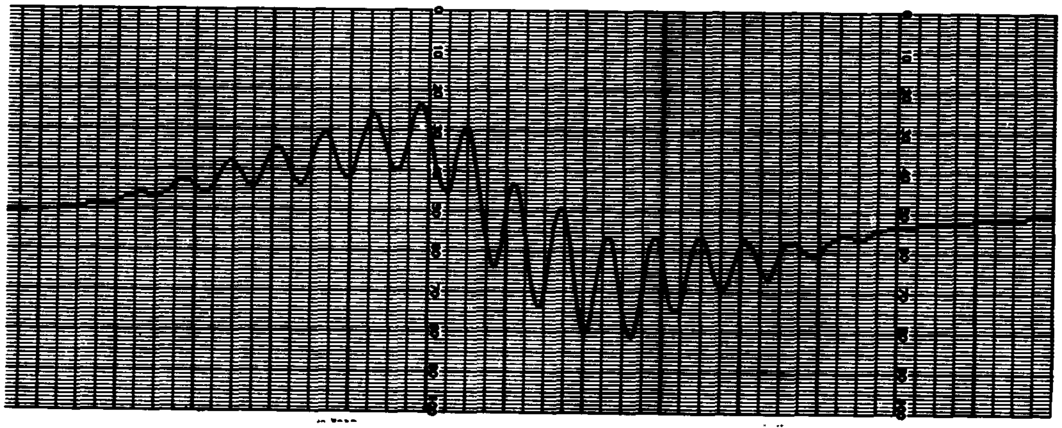

Figure 1. The slope d_{x}''/dH of the ESPR absorption in sodium azide powder at high power. The spectroscopic splitting factor g is given for three points. Field modulation is 3 gauss at 200 cps. Temperature is ~ 77° K.

Single crystal plates of sodium azide, given the same irradiation treatment and also kept at all times at 77° K, were found to

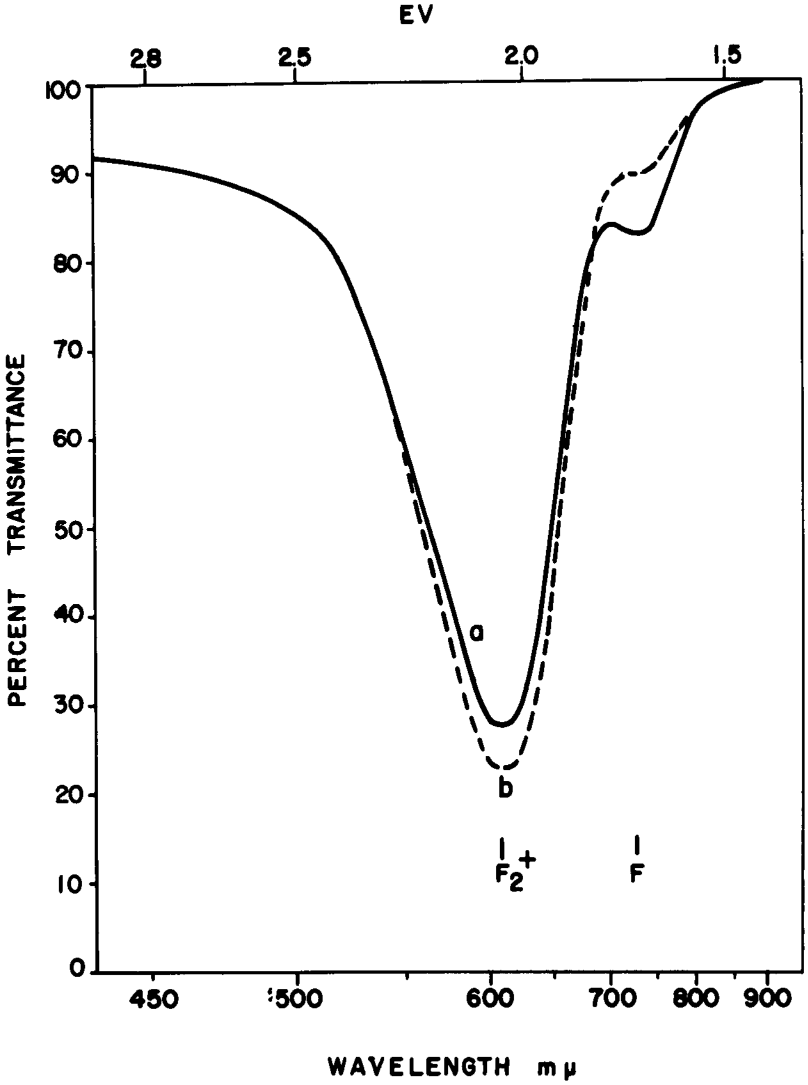

Figure 2. (a) NaN_3 exposed to Hg vapor lamp for 15 min at 77° K. (b) After exposure to F-band light. Both curves measured at 77° K. The crossover point at 680 mμ is a point of constant absorption for this bleaching process.

exhibit optical absorption band at 6100 A and 7300 A [Fig. 2(a)]. These two optical bands were the only two bands discernible after short-term (approx. 1 hour) irradiation at 77° K. Long duration (approx. 10 hours) uv irradiation at 77° K yielded other optical absorption bands which, however, were at least 100 times smaller than the 6100 A and 7300 A optical bands. These two optical bands were previously observed by Cunningham and Tompkins(3) in fresh crystals under the same general irradiation conditions. The ratio of the area of the 7300-A band to the area of the 6100-A band was found to be smaller in their experiment than in ours. This difference is possibly associated with the difference in the optical properties of the uv light sources used in the experiments. In our experiments it was found that the 7300-A optical band bleached rapidly at 195° K with the accompanying growth of the 6100-A band. The same thermal treatment given to the sample used in ESPR caused the F-center resonance to bleach and exposed a broad asymmetric absorption (Fig. 3) which was, in part, present before thermal bleaching (see below).

In addition to the thermal bleaching experiments, the 6100-A and 7300-A bands were irradiated with resonance radiation, as well as other wavelengths above the first absorption edge, in an attempt to bleach them optically. It was found, for irradiation with light within the 7300-A band alone, that the 7300-A band bleached and the 6100-A band grew. The 6100-A band did not bleach with light of any wavelength between 3000 A and 10000 A. The ESPR absorption curve for the F center (Fig. 1) was found to have the identical optical bleaching properties to the 7300-A band.

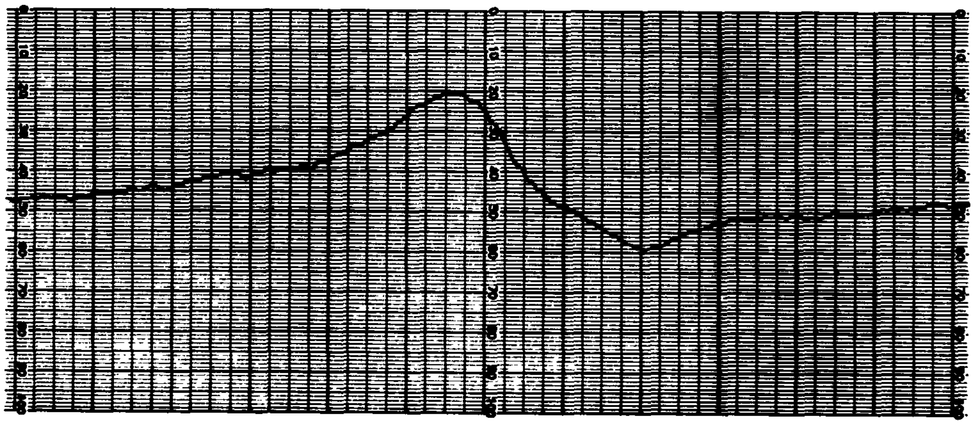

Figure 3. The slope $d\chi''/dH$ of the ESPR absorption in sodium azide powder after thermal bleaching of the F center at 195° K. Data taken at 77° K.

The possibility of the presence of a second ESPR band lying under the F-center ESPR signal (Fig. 1) was then investigated, since the simultaneous presence of two optical bands possibly indicated the simultaneous presence of two separate ESPR signals. It was found that when the microwave power was reduced at least 15 db the symmetric F-center signal (Fig. 1) became distorted on the low magnetic field side (Fig. 4). Further reduction in power (20 db) produced an assymmetric resonance signal very similar to the

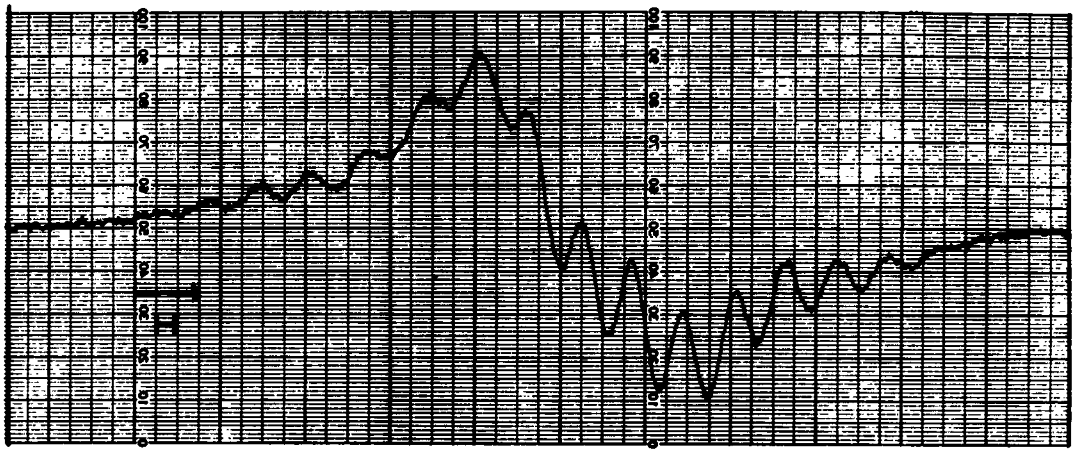

Figure 4. The slope $d\chi''/dH$ of the ESPR absorption in sodium azide powder at reduced power (15 db). Other conditions are the same as in Fig. 1.

bleached signal (Fig. 3). It was concluded that the sensitivity of shape to power is caused by the presence of a second ESPR center which saturates at less power than the F center and which is very asymmetric in its spin properties. Thus, a second center was found which was simultaneously present with the F center and which was asymmetric and possessed an unpaired spin. Further, by power desaturation it was demonstrated that the second ESPR center had the same ESPR character as the signal remaining after optical or thermal bleaching at 195° K. The ESPR powder data showed that the F-center resonance possessed a very large isotropic component since a large symmetric ESPR signal is observed in the powdered material. Questions concerning the actual mixing of the signals, e.g., how much of the envelope of the symmetric signal at high power actually belongs to the second more saturable asymmetric signal, could not be determined from the powder data. The reasons for this are that the spectrometer sensitivity to the individual signals is very much different because of linewidths and the non-isotropic behavior of the second center does not permit proper assessment of that center in the powdered material. Discussion of these aspects is deferred to Sec. VIII. For present purposes the ESPR information from powder samples is presumed to be sufficient.

One further correlation remained. The optical band at 6100 A bleached in the order of minutes at room temperature. The asymmetric ESPR band showed the same behavior and at the same time the blue color of the material disappeared. Optical bleaching could not be accomplished, as previously noted.

In summary, the 6100-A band (Fig. 2) is presumed to be caused by the same center which produces the broad ESPR signal (Fig. 3). The 7300-A band (Fig. 2) and the F-center resonance curve (Fig. 1) are presumed to be both produced by the F center.

IV. OTHER PROPERTIES OF THE BANDS

Irradiation at 77° K

The color centers produced by uv irradiation in NaN_3 at 77° K have some of the peculiarities of optical and thermal bleaching of color centers in alkali halides. The 7300-A F band is slightly unstable at 77° K, decaying roughly 20 percent in the first 24 hours. When bleached at 195° K, the process proceeds in several minutes to roughly 90 percent completion. The remaining F centers are "hard," a situation common to alkali halide F centers. These "hard" F centers can even tolerate several seconds of exposure to room temperature. Optical bleaching also presents the same behavior, some F centers showing "hard" behavior. The ESPR measurements agree in detail with all of the optical experiments in this connection.

It is presumed that outer surface effects may be responsible for some of the "hard" F-band behavior. At 77° K the first exciton absorption band is centered at 2400 A. All the output of our uv lamps which is effective in photolysis of NaN_3 is from 2537 A down to shorter wavelengths. The 50 percent transmission point in our crystals is approximately 2500 A. Thus, much of the short-wavelength incident light is absorbed on the surface. For this reason, proper comparison of the ESPR and optical data required running ESPR data on single crystals having the same approximate thickness as the optical samples. This work is included in Sec. VIII.

Optical bleaching of the 6100-A band does not occur, even after a three-hour irradiation with a filtered 1-kw tungsten projection lamp (see also Sec. III). This resistance to optical bleaching is typical of coagulation-type centers such as those responsible for the R and M bands in alkali halides.

During optical bleaching by F light at 77° K or thermal bleaching at 195° K, the 7300-A F band decreases and the 6100-A band increases. No other bands occur in crystals uv irradiated for one hour, and the bleaching process is entirely a two component system as is indicated by an isosbestic point. The ratio of area of growth of the 6100-A band to decrease of 7300-A band is roughly three. This permits the interpretations that the oscillator strength of the 6100-A band is greater than that of the 7300-A band or that one of the centers causing the 7300-A band decays into more than one of the centers causing the 6100-A band. A model which fits the optical observations (see Sec. VI) agrees with the former choice.

Irradiation at Helium Temperature

The optical bands at 6100 A and 7300 A were found to form with only slightly reduced efficiency at liquid-helium temperature. The optical bleaching of the 7300-A F band occurs readily at liquid-helium temperature also. While the optical bleach of the F band at 77° K is always accompanied by growth of the 6100-A band, at liquid-helium temperature, we found no growth at all of the 6100-A band when the F band was optically bleached. When the optically bleached sample was then raised to 77° K for 30 min and subsequently recooled to liquid-helium temperature, it was found that the 6100-A band had now grown (without any other changes in the absorption curve). The F band had not changed at all during the thermal treatment at 77° K.

A second, blank run, experiment was then performed which was identical in all respects to the previous experiment, except that no optical bleaching was attempted. In this case the band at 6100 A grew during thermal cyling at 77° K at the expense of the 7300-A band. Thus, the formation of the 6100-A band from the 7300-A band is primarily a thermal coagulation process. The optical bleaching at liquid-helium temperature removes an electron from the F-center vacancy but the liquid-helium temperature does not permit the vacancy to migrate. Apparently, the F center is definitely more stable at liquid-helium temperature than at 77° K, as is indicated by the thermal decay of the optical band. An important conclusion is, however, that coagulation of the F centers yields more of the centers responsible for the 6100-A band. Other conclusions are that some of the F centers formed at liquid-helium temperature are unstable at 77° K and the F vacancy is mobile at 77° K.

V. PRODUCTION OF ANION VACANCY TRAPS BY PHOTOCHEMICAL REACTIONS

In alkali halides, the production of an F band by uv light(15,16) may lead to the formation of auxiliary bands on the long wavelength side of the F band by coagulation of F centers or F-center vacancies. It appears that the formation of single vacancies in the initial stages of irradiation is favored since the F band is normally very much larger than R- or M-type bands. In sodium azide, assuming reasonable oscillator strengths, the formation of the F band as a primary band does not seem to occur since it is much smaller than the 6100-A band. This is in direct accord, however, with the chemical nature of the azide ion. A basic mode of photolytic decomposition available to sodium azide can be summarized by the bimolecular decomposition $2N_3 \dashrightarrow 3N_2$ which is exothermic in the amount of 9 ev(4). This reaction produces sodium metal as the other product. The unimolecular decomposition of an azide ion by a ground-state process into N_2 and N is not favored by conservation rules(4). In the event the excited state unimolecular interaction can be photolytically induced within the lattice, it is likely that the N atom or ion would interact with adjacent azide ions. This, in effect, accomplishes a bimolecular decomposition if the reaction $N+N_3^- \dashrightarrow 2N_2+e$ can then occur. If one assumes that adjacent azide ions in the lattice are induced to interact by the action of uv irradiation, then three N_2 gas molecules will be produced in the center of a considerable thermal spike. This process of interaction may be assisted by defects such as excitons, internal surfaces, and other imperfections. Since the N_2 molecule is small in comparison to the lattice dimensions of sodium azide, the probability is large that it will diffuse rapidly from the spike. This process requires that double anion vacancies be produced in preference to single anion vacancies. This agrees with a model adopted to fit the NaN_3 optical band structure, which assumes that the 6100-A band is formed by two vacancies with a trapped electron.

The occurrence of photo processes at low temperatures within the crystals is consistent with some previous studies(8,9) on sodium colloids but does not exclude external surface effects. The ESPR results are, however, primarily due to volume effects and not due to external surfaces.

VI. INTERPRETATION OF OPTICAL BANDS IN TERMS OF THE CONTINUUM MODEL

The location of the 6100-A band on the short wavelength side of the F optical band is the reverse of the usual behavior of the R-type bands in alkali halides. On the basis of a continuum model(17,18) modified to fit the wavelength of the F-center optical band(20), this behavior serves to point out the particular center responsible for the 6100-A band. The continuum model for R-type centers is based on the assumption that the optical transitions of the R-type centers in alkali halides can be interpreted in terms of the transitions of hydrogen molecules or molecule ions immersed in an effective dielectric continuum. According to this model, the only simple transition occurring on the short wavelength side of the F band is the $1s\sigma g \rightarrow 2p\pi_u$ transition of the hydrogen molecule ion, or in the notation of Seitz, the F_2^+ center. In order to compare theoretical and experimental values, the effective dielectric parameter was assumed to be that demanded by the continuum theory to fit the F-center optical band position, K=2.45.

The crystal structure of sodium azide is rhombohedral (Fig. 5) and there are two likely vacancy pairs which can produce F_2^+ centers. An azide ion in sodium azide has six nearest neighbor sodium ions at a distance of 3.28 A from the center of the azide ion. These sodium ions are symmetrically placed about the azide ion in a roughly isotropic manner. The next nearest spherical shell of ions about the azide ion consists of twelve azide ions, if one considers not the center-to-center distances of the ions but the distance of closest approach. Sodium azide has a layer structure which separates the sodium and azide ions into parallel planes to which the [111]

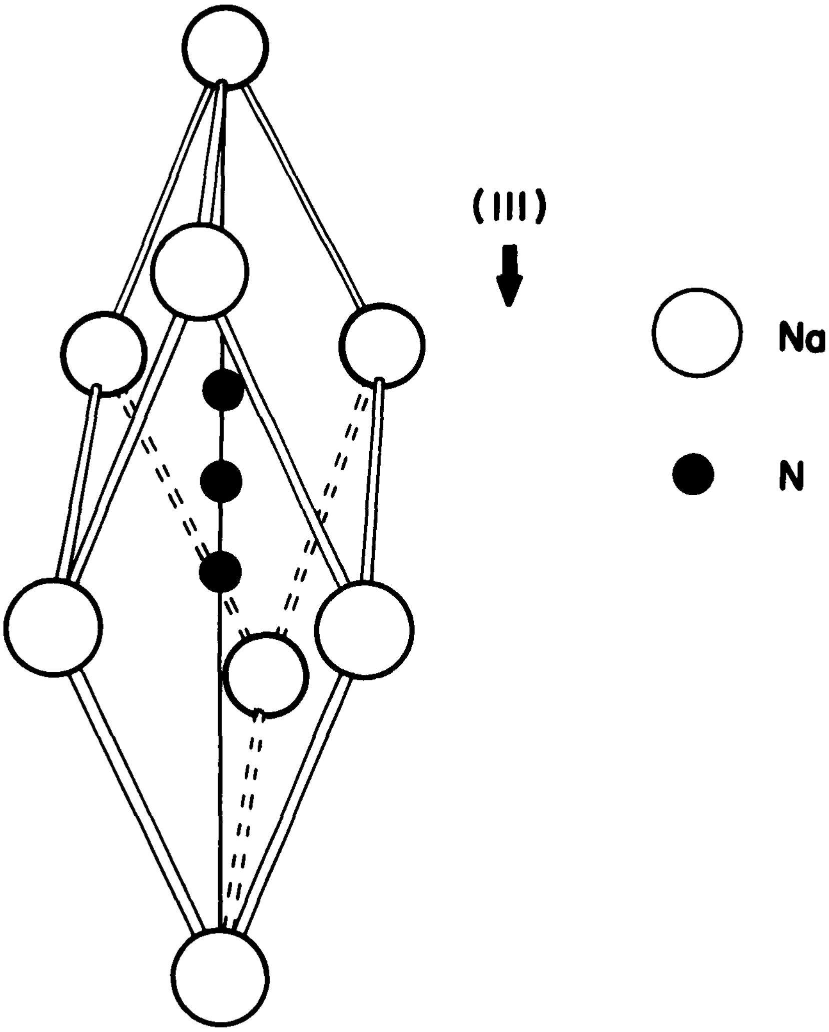

Figure 5. Rhombohedral unit cell of sodium azide [see S. B. Hendricks and L. Pauling, J. Am. Chem. Soc. 47, 2904 (1925)]. Magnetic field direction for ESPR single crystal measurements is shown. The light beam direction in optical measurements is also parallel to [111].

direction in the lattice is perpendicular. The separation of the center of each azide ion in the azide plane is 3.62 A, and since the internuclear axes of the ions are parallel, this is the minimum separation. The separation of the center of each azide ion from its nearest neighbor in the next azide plane is 5.46 A, but due to the length of the azide ions the actual minimum separation is only 3.42 A.

In forming adjacent anion vacancies in sodium azide, the chemical reaction may involve the transport of a single N atom from the decayed azide radical site to the nearest azide ion. While the center-to-center separation of one possible vacancy pair is much larger than that of the other, the actual transport distances are nearly the same. Thus, two types of F_2^+ centers are to be expected. The 6100-A band was carefully investigated for structure by bleaching techniques and the two F_2^+ bands were found. The standard method was used to form the 7300-A and 6100-A bands except the irradiation lasted for 18 hr and very deep bands were formed [Fig. 6(a)]. The sample was then bleached by rapidly warming to 298° K and then immediately recooling to 77° K. The optical absorption curve then showed five distinct bands in the space covered by the 6100-A and 7300-A bands [Fig. 6(b)]. By using photoemission techniques (see below) it has been possible to show that the 5470-A band and the 6250-A band grow in a unique manner and merge into one band having an apparent center at 6100 A.

Based on the assumption that the F-center band is at 7300 A, the continuum model predicts the bands given in Table I. The agreement of the observed data and the predictions of the simple theory are surprisingly good. The F_2^+ transitions for the 3.62-A separation are not in close agreement but this type of F_2^+ center is expected to show some asymmetric(19) character while the F_2^+ center for the 5.46-A separation is expected, from consideration of the lattice structure to be symmetric. The predicted infrared band at 0.41 ev occurs in the molecular absorption bands of the azide ion. Investigation showed, however, that one of the bands at 0.49 ev occurred only when there was a high density of F_2^+ centers in the crystal and further this band bleached when the F_2^+ band was thermally bleached.

The continuum model also predicts four transitions for the F_2 centers. Two of these bands are superimposed. Some, but not all, of the "hard" character of the F centers may be due to this situation. The band at 4850 A is very weak and for the present is not identified.

The interpretation of the compound optical absorption band at 6100 A as one due to a single electron trapped at a double anion vacancy is further strengthened by the ESPR data. The ESPR resonance associated with the F_2^+ centers or 6100-A band is asymmetric

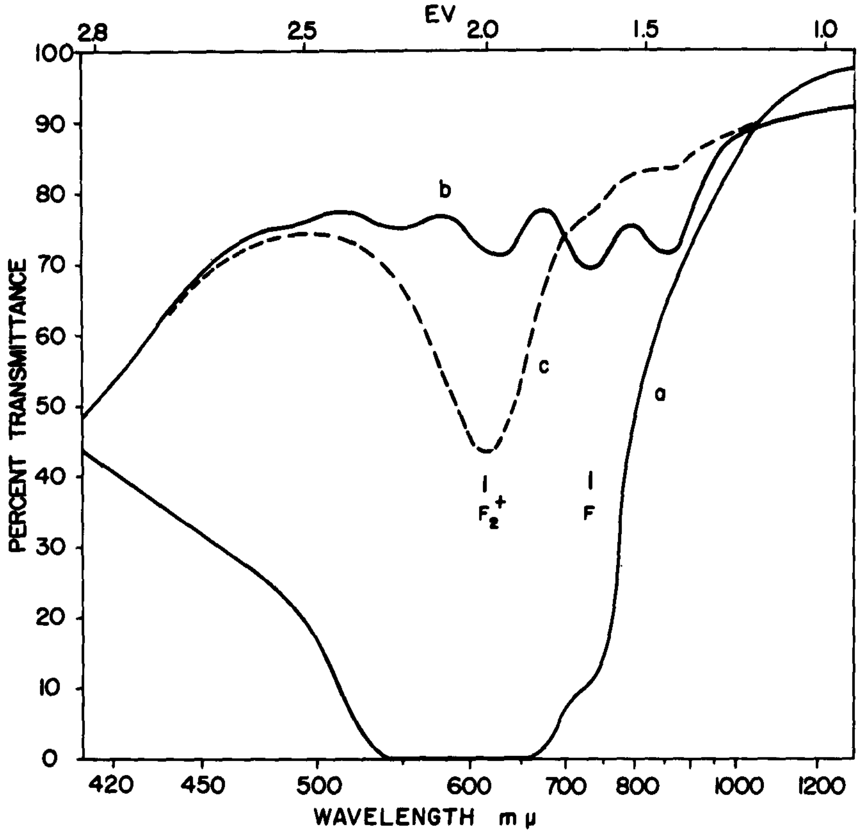

Figure 6. (a) NaN_3 exposed to Hg vapor lamp for 18 hours at 77° K. (b) Same crystal after thermal bleaching at 298° K for a few seconds. (c) Same crystal as (b) after exposure to filtered tungsten lamp. (All wavelengths greater than 420 mμ removed.) Curves measured at 77° K.

on the powdered material and has a negative g-value shift from that of a free electron. The asymmetry of the resonance is produced by the anisotropic structure of the center and the anisotropic crystalline effects in sodium azide. The negative value of the g shift is in accord with the idea that the center is a trapped electron.

Presumably the preferential formation of the F_2^+ centers instead of the F_2 centers is connected with initial conditions during formation of the double vacancy. The relaxation of the lattice to accommodate the vacancies, and conditions such as precise location of lattice ions around the vacancies are presumed to be the determining processes. Once the conditions suitable for the existence of an F_2^+ center are established, the stability against capture of a second electron may be influenced by lattice polarization effects.

TABLE I

Predicted band positions on the basis of the continuum model for color centers in NaN_3. The internuclear separation of the vacancies is given in Angstroms and the energies of the corresponding optical transitions in electron volts and in millimicrons.

R(A)	Transition	E Calculated, ev	E Observed, ev (mμ)
	F_2^+ Transitions		
3.62	$1S\sigma_g \longrightarrow 2p\pi_u$	2.46	2.27(547)
5.46	$1S\sigma_g \longrightarrow 2p\pi_u$	1.97	1.97(625)
3.62	$1S\sigma_g \longrightarrow 2p\sigma_u$	0.84	None
5.46	$1S\sigma_g \longrightarrow 2p\sigma_u$	0.41	0.49(2520)
	F_2 Transitions		
3.62	$'\Sigma_g^+ \longrightarrow {}'\Sigma_u^+$	1.45	1.45(850)
5.46	$'\Sigma_g^+ \longrightarrow {}'\Sigma_u^+$	1.33	
3.62	$'\Sigma_g^+ \longrightarrow {}'\Pi_u^+$	1.70	F band 1.70(730)
5.46	$'\Sigma_g^+ \longrightarrow {}'\Pi_u^+$	1.65	

VII. PHOTOEMISSION EXPERIMENTS IN SODIUM AZIDE

Once a sodium azide crystal has been used for F-center experiments and then allowed to warm to room temperature, it is considered to be "old" since it contains large amounts of sodium metal(3,8). This is seen as a large band centered at 3300 A due to atomic sodium. It is possible to bombard "old" sodium azide crystals with dense internal electron showers by irradiating the sample with a tungsten lamp, thus producing photoelectrons from the sodium metal. The tungsten lamp otherwise produces no vacancies in the crystal since the wavelengths are too long to be active. This property is used to investigate the stability of vacancies in sodium azide without perturbing the number of vacancies present.

The crystal discussed in the previous section and shown in Fig. 6(b) is considered to be an old crystal. During the short-time (about 1 min) bleaching at 298° K the electrons in the color centers are thermally promoted from the vacancies and the vacancies are made mobile. When the crystal is immediately recooled to 77° K, the less mobile vacancies are trapped in the lattice. The absorption bands in Fig. 6(b) are only from the "hard" remnants which have managed to retain their electrons. The vacancies which have low mobility, being still present, can now retrap an electron if there is a sufficient density of electrons available. Irradiation with a tungsten lamp supplies the electrons. The growth of the F_2^+ bands at 5470 A and 6250 A into the 6100-A composite band can be studied in detail by this method. Figure 6(c) shows the condition of the crystal originally having the optical character of Fig. 6(b) after 2 hours of irradiation at 77° K with a filtered tungsten lamp. It is apparent from the regrowth of the F_2^+ bands that many double vacancies were trapped in the lattice. The double vacancies have low mobility and high stability in comparison to the single F vacancies. The apparent simultaneous bleaching of the 7300-A and 8500-A bands indicates that a large part of the 7300-A band in this experiment may not be due to hard F centers but rather to F_2 centers. The continuum model (see Table I) predicts bands near 7300 A and 8500 A for the four transitions of the F_2 center. It is conceivable that these bands are produced by F centers which have coagulated in special sites and are found. Capture of electrons to form F' centers may be responsible for the apparent bleaching.

At the present time, experiments are being conducted which use this method to measure directly the mobilities of the vacancies in sodium azide. It has been found that if the thermal bleaching of the sample lasts 12 hours at room temperature, that no amount of tungsten lamp irradiation will cause band growth at 77° K.

The most important conclusion of the experiment represented in Fig. 6 is that the double vacancies resulting in the F_2^+ bands do not result from coagulation of single vacancies but have an independent existence. The 12-hr thermal bleaching experiment, above, indicates also that none of these double vacancies are present in the crystal previous to uv irradiation at 77° K. The experiments do not preclude the formation of double vacancies by coagulation but statistically one would expect the F band then to be much larger than the F_2^+ bands. Presumably, the small band at 8500 A in Fig. 6(b) is a coagulation band, probably an F_2 band.

VIII. ESPR EXPERIMENTS ON SODIUM AZIDE SINGLE CRYSTALS

Most of the ESPR work was done on powders to allow a large number of experiments to be performed and yet conserve a small supply of good single crystals available for use. In addition, future work comparing normal sodium azide with nitrogen-15 tagged sodium azide was intended and growth of large crystals containing this material is very costly. The information found in single crystal ESPR experiments confirms the results and interpretations of the powder experiments.

Crystals selected for ESPR experiments were required to satisfy the same criteria as those for use in optical experiments. Particular attention was given to optical clarity and absence of twinning. This latter defect and related stacking faults produce temperature dependent variations in structure which result in spurious optical bands at low temperatures.

The supply of ten excellent crystals was selected from five large batches which were grown at different times. Each batch contained a minimum of 500 large (10 X 10 X 0.1 mm) crystals of good optical clarity. All ESPR measurements performed on crystals from this select sample agreed quantitatively in results.

The uv irradiation at 77° K of the sodium azide crystals was performed in the same manner as with the microcrystalline powders. In addition, the thermal and optical bleaching experiments were redone. In every case, the conclusions reached using the powdered material were supported by the data taken on crystals.

For a single crystal oriented with the dc magnetic field in the [III] direction (Fig. 5), the ESPR signal is almost entirely attributable to the hyperfine structure of the F center (Fig. 7). The line separation is approximately 9 gauss and the peak-to-peak-on-the-derivative linewidth is approximately 5 gauss. While the envelope of the ESPR trace changes shape markedly for other orientations, a set of lines having very closely the same line separation and linewidth as the F-center resonance can easily be found, regardless of crystal orientation (see Figs. 8 and 9). The close maintenance of the line spacing and linewidth of the F-center resonance hyperfine lines (Fig. 7) in all orientations is assurance that the large distortion of the resonance envelope in some orientations is produced by at least one other independent and separate center. At the same time this situation gives evidence of the isotropy of the F center, which reflects the good isotropy of the six sodium ions which form the first shell around the anion vacancy.

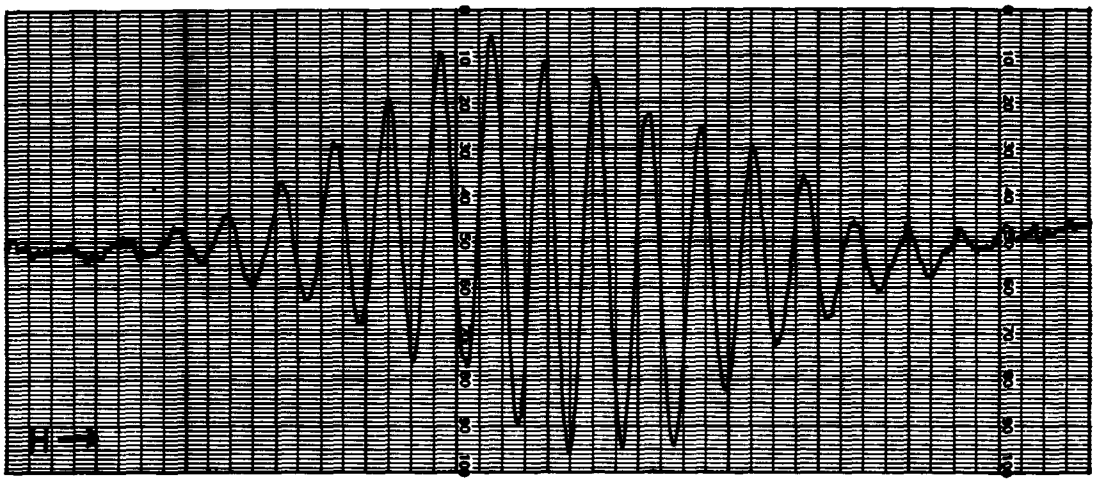

Figure 7. The slope $d\chi''/dH$ of the ESPR absorption in a sodium azide single crystal. The field of the magnet is in the [111] crystal direction. The temperature is 77° K. Spin density approximately 10^{18} per cm3.

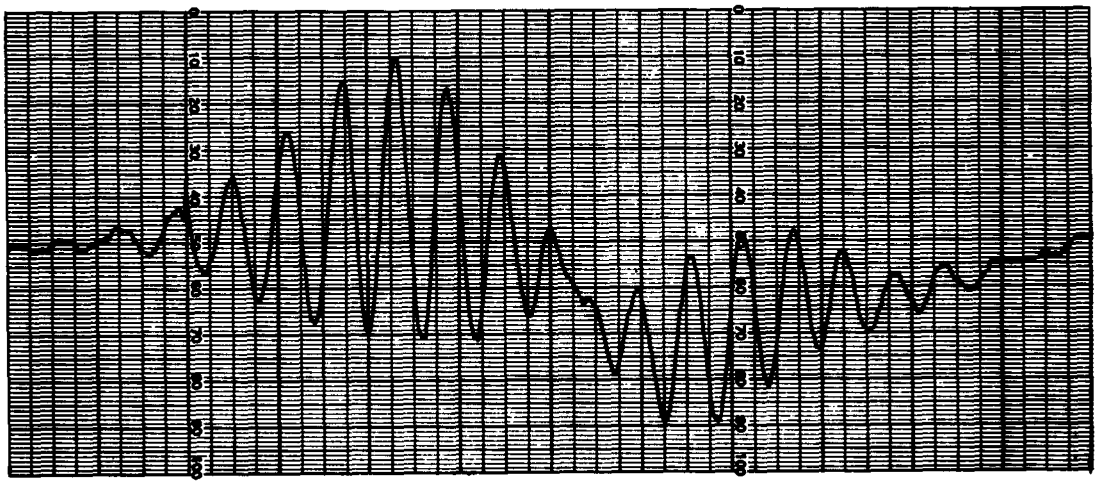

Figure 8. The slope, $d\chi''/dH$ of the ESPR absorption in sodium azide single crystal. The angle between the [111] direction and dc magnetic field is approximately 45°.

(P-A10)

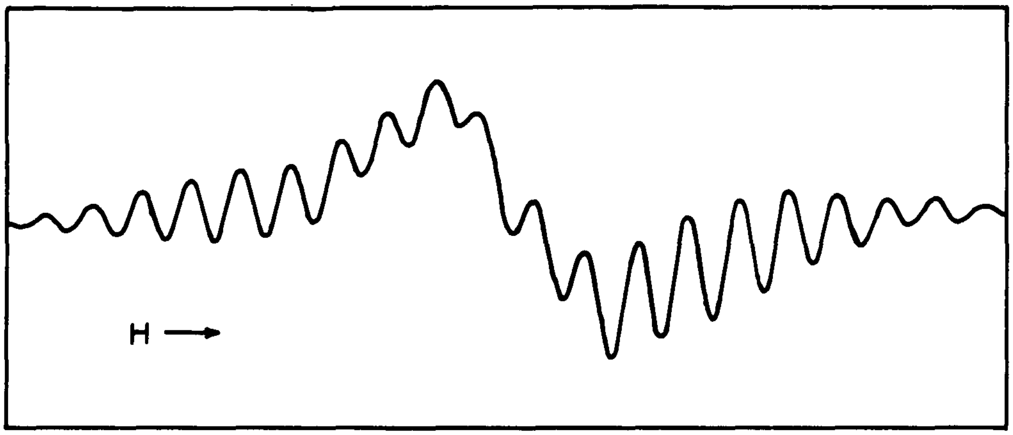

Figure 9. The slope, $d\chi''/dH$ of the ESPR absorption in sodium azide single crystal. The angle between the [111] direction and the dc magnetic field is 90°. Temperature is 77° K.

The distortion of the F-center resonance curve as shown in Figs. 8 and 9 is attributed here to the F_2^+ center. It was previously shown (Sec. III) that the 7300-A optical F band bleaches thermally at 195° K and F_2^+ centers remain. The corresponding ESPR experiment was performed to separate the F- and F_2^+-center resonances. The crystal was uv irradiated at 77° K and the ESPR curves were obtained as a function of angular orientation with respect to the dc magnetic field. The crystal was then bleached for 20 min at 195° K and orientational studies repeated under exactly the same conditions as in the previous experiment. A comparison of the ESPR traces for the same crystal and the same orientation before and after bleaching is afforded by Figs. 9 and 10. The ESPR lines having the 9-gauss separation have bleached in Fig. 10, which is in agreement with the powder data (Figs. 1 and 3). It is apparent that the largest part of the shape of the envelope of Fig. 9 is supplied by the resonance shown in Fig. 10. Comparison of the bleached and unbleached signals for other orientations shows the same general result. Where the envelope of the series of lines with the 9-gauss separation appears strongly "modulated," the signal remaining after bleaching is strong and its over-all shape is that of the apparent modulation of the unbleached signal for the particular orientation. Figure 7 represents a relatively pure F-center ESPR signal. It was found that the F_2^+ signal corresponding to the orientation of Fig. 7 was sufficiently broad to preclude its simultaneous display when the spectrometer was set to display the narrow F-center hyperfine lines.

(P-810)

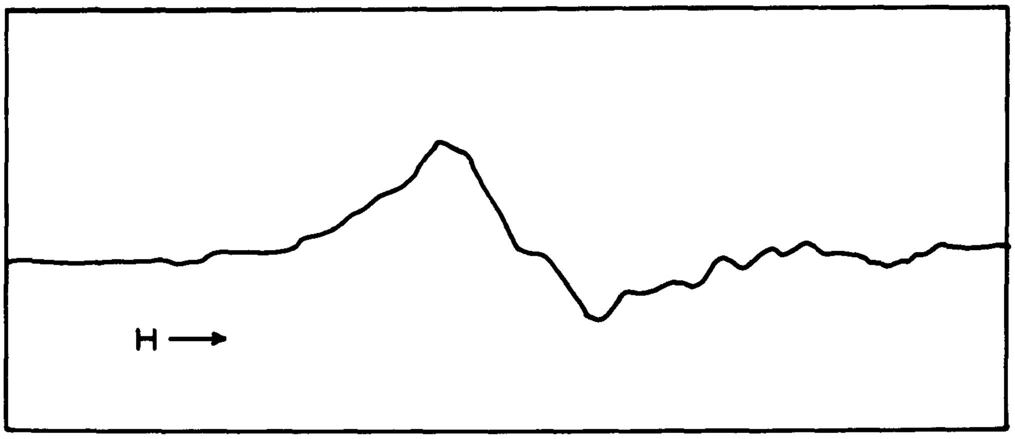

Figure 10. The slope, d_{x}''/dH, of the ESPR absorption in sodium azide single crystal after bleaching for 20 min at 195° K. The same crystal and orientation as in Fig. 9 and identical spectrometer settings. Temperature is 77° K.

The central g value of the F-center resonance appears to be constant for all orientations of the crystal. It is difficult to make statements concerning the central g value of the resonance curve of the 195° K bleached crystals. It is apparent that these curves generally consist of at least two wide line resonances of from 30 to 50 gauss peak to peak and several other partly resolved narrow lines. The rather complicated ESPR behavior of the F_2^+ center is to be expected. Because the F_2^+ center will reflect the symmetry of the crystal, the magnitude of the hyperfine interactions should be dependent on crystal orientation with respect to the dc magnetic field. Because there are two sets of F_2^+ centers and also the crystal structure is complex there will generally be many sets of nonequivalent F_2^+ centers displayed for any given crystal orientation. This situation, in addition to the broad linewidths, will tend to suppress ESPR signals from the F_2^+ center.

The orientational studies clearly show that there are at least two separate centers present one of which, the F center, has an isotropic ESPR behavior and the other, an anisotropic behavior. Further, there is a direct correlation between the existence of the 7300-A optical band and the F-center ESPR band. In addition, the 6100-A optical band has a counterpart in an ESPR band which belongs to the center having anisotropic hyperfine interactions. It has not been possible using simple techniques to analyze the orientational anisotropy effects because of their complexity.

IX. X RAY EXPERIMENTS

Besides ultraviolet light, we have also used x rays in our radiation damage studies(20). The experimental techniques were identical with those previously described, except that the portion of the sample tube to be placed in the microwave cavity was shielded from the x rays in order to avoid unwanted signals from the quartz. The NaN_3 was irradiated at 77° K with x rays from a General Electric x ray generator with a tungsten tube operating at 220 kvp and 10 ma. Upon placing the sample in the EPR spectrometer at 77° K the resonance shown in Fig. 11 was obtained. It is apparent that there is an anomalously shaped resonance in addition to the previously discussed resonances. When the microwave power in the sample cavity is reduced this anomalous resonance becomes symmetrical and well defined (Fig. 12).

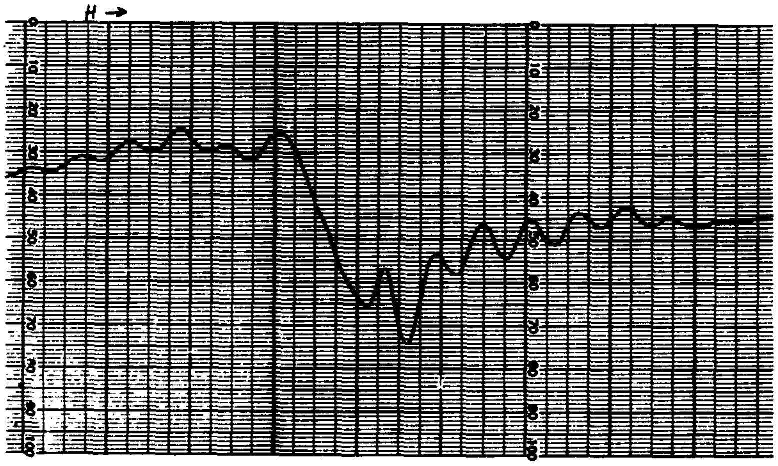

Figure 11. The slope, $\frac{dx''}{dH}$ of the electron spin resonance of x-ray irradiated NaN_3 showing the partially saturated N^{14} resonance in addition to the F center resonance.

Computer analysis of the ESPR spectrum (Fig. 12) shows that the resonance can be fitted by three equal Lorentzian lines having equal spacing about a central g value of 2.0021 ± 0.0001. The lines are separated by 6.2 oersteds. The equality of the absorption lines and the ease of resolution in the powdered sample indicates that the resonance is basically isotropic in nature. Experiments with single crystals show that the structure does not change with orientation of the crystal.

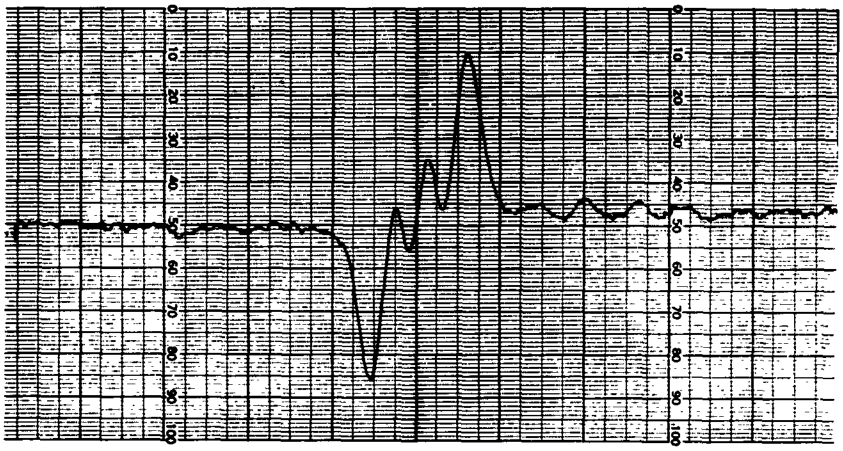

Figure 12. The derivative of the electron spin resonance absorption, $\frac{d\chi''}{dH}$, of N^{14} atoms trapped in the lattice of x ray irradiated NaN_3 at 77° K. The small peak on the right is part of the F center resonance which is still visible at low power.

This information and the negative g-value shift from the free-electron value indicate that the structure responsible for the resonance is not a V-center. Since triplet line structure is produced by the nuclear magnetic hyperfine field of the $2I + 1 = 3$ states of the N^{14} nucleus, we assume the resonance is strongly centered on a single N^{14} atom and is, in fact, the resonance of N^{14} trapped in the NaN_3 lattice.

The character of the trapped N^{14} atom in various matrices is well known(21). The three line ESPR resonance structure is ascribed to the magnetic transitions in the $^4S_{3/2}$ ground state of N^{14}. The four allowed magnetic states are split into three lines each by the nuclear hyperfine fields, but selection rules allow only nice transitions which coalesce to give three triply degenerate absorption lines.

Comparison with the available data on N trapped by various other methods strengthens the evidence for identification of this resonance with trapped N. Nitrogen trapped at very low temperatures in matrices of frozen gases always shows three main lines which are sensitive to the matrix material as far as splitting of the lines is concerned, but shows a central-line g value which is nearly unshifted. For purposes of comparison, the data from Foner, Jen, Cochran, and Bowers(22) are partially repeated in Table II. Our data show a line width slightly larger than that found in other investigations which were performed at liquid helium temperature. Since the rigid matrix here is crystalline, one expects dipolar and other forms of broadening to be stronger than for N trapped in condensed gas matrices. The deviation of A, the hyperfine coupling constant, from the free gas value is positive, which is typical of the N behavior but not for some other trapped radicals(21).

TABLE II

A comparison of the electron spin resonance properties of N trapped in different matrices[a].

MATRIX	g_J	APPROXIMATE LINE SEPARATION (OERSTEDS)
Free	2.00215(3)	--
H2	2.00202(8)	4.1
N2	2.00200(8)	4.3
CH_4	2.00203(8)	4.8
NaN_3	2.0021(1)	6.2

[a] The numbers in the parenthesis indicate experimental and/or conversion errors in the last figures of the associated values.

The deviation is sensitive to environment and is larger than that encountered in other matrices which reflects the rigidity of the matrix and the relatively high temperature.

The thermal properties of the N^{14} resonance are similar to those of the F center. Both the F-center and N^{14} atom spin resonances are fairly stable at liquid-nitrogen temperature but bleach very rapidly at dry-ice temperature. A faint blue glow from the NaN_3 is observed by eye when a sample containing F centers and trapped N is suddenly warmed from liquid nitrogen to room temperature. Whether this is associated with the N-atom recombination or the F-center decay, or both, is not known at present.

The thermal stability of N atoms in the NaN_3 lattice is at first glance, somewhat surprising. These experiments, however, are similar to the experiments of Livingston, et al., in which atomic H was stabilized in frozen acid at 77° K for several months(23).

The production of atomic N may result from the x ray photoreaction $N_3^- + h\nu \dashrightarrow N_2 + N + \epsilon$ in which the participants may be in an excited state to accommodate correlation rules. Another interaction may also occur according to the formula
$N_3^- + h\nu \dashrightarrow N_2 + N^+ + 2\epsilon$.

In this case the N^+ is ejected from the anion lattice site to an interstitial site where it captures an electron and is trapped.

ACKNOWLEDGMENTS

The work of M. D. Kemp in the difficult and hazardous preparation of the pure compound is gratefully acknowledged. The successful effort of O. F. Kezer in the production of large clear crystals has been of great value. The interest of Dr. Z. V. Harvalik, Group Director, is much appreciated.

REFERENCES

1. G. J. King (unpublished data).
2. W. E. Garner and D. J. B. Marke, J. Chem. Soc. 1936, 657.
3. J. Cunningham and F. C. Tompkins, Proc. Roy. Soc. (London) A251, 27 (1959).
4. B. L. Evans and A. D. Yoffe, Chem. Revs 59, 515 (1959).
5. H. G. Heal, Trans. Faraday Soc. 53, Part 2, 210 (1957).
6. H. Rosenwasser, R. W. Dreyfus, and P. W. Levy, J. Chem. Phys. 24, 184 (1956).
7. F. Seitz, Revs. Modern Phys. 26, 7 (1954).
8. B. S. Miller, J. Chem. Phys. 33, 889 (1960).
9. G. J. King, B. S. Miller, F. F. Carlson, and R. C. McMillan, J. Chem. Phys. 32, 940 (1960).
10. F. F. Carlson, G. J. King, and B. S. Miller, J. Chem. Phys. 33, 1266 (1960).
11. N. F. Mott and R. W. Gurney, ELECTRONIC PROCESSES IN IONIC CRYSTALS (Oxford University Press, New York, 1950), Chap. 8, p. 265.
12. M. D. Kemp, J. Chem. Educ. 37, 142 (1960).
13. O. F. Kezer (to be published).
14. J. R. Singer and S. D. Johnson, Rev. Sci. Inst. 30, 92 (1959).
15. J. A. Cape, Phys. Rev. 122, 18 (1962).

16. P. W. M. Jacobs, "1959 International Symposium on Color Centers in Alkali Halides," Oregon State College, Corvallis, Oregon (unpublished).

17. R. Herman, M. C. Wallis, and R. F. Wallis, Phys. Rev. 103, 87 (1956).

18. B. S. Gourary and F. J. Adrian, Solid State Phys. 10, 127 (1960).

19. W. Ya. Zevin, Soviet Phys. JETP 36 (9), 81 (1959).

20. G. J. King, F. F. Carlson, B. S. Miller, and R. C. McMillan, J. Chem. Phys. 34, 1499 (1961).

21. C. K. Jen in Formation and Trapping of Free Radicals, edited by Arnold M. Bass and H. P. Broida (Academic Press, Inc., New York, 1960), Chap. 7.

22. S. N. Foner, C. K. Jen, E. L. Cochran, and V. A. Bowers, J. Chem. Phys. 28, 351 (1958); Phys. Rev. 112, 1169 (1958).

23. R. Livingston, H. Zeldes, and E. H. Taylor, Phys. Rev. 94, 725 (1954).

ELECTRON SPIN RESONANCE EXPERIMENTS ON ALPHA LEAD AZIDE

by

G. J. King, R. C. McMillan,
B. S. Miller, and F. F. Carlson
Basic Research Group
U. S. Army Engineer Research and Development Laboratories
Fort Belvoir, Virginia

Our approach has been to perform electron spin resonance studies on alkali azides as preparation for the study of more complicated lead azide. This approach has been found useful since some resonances in Pb azide have similarities to those found in KN_3 and other azides.

The work is of a preliminary nature. Orthorhombic lead azide prepared by Kemp from organic solvents was x-rayed (40 kv at 40 ma) at 77° K and maintained at that temperature. Organic solvent content was checked by infrared techniques by Kemp and none was found. We find no resonances ascribable to organic materials in our work. In addition, the crystals show remarkable clarity and form stability under treatment by ultraviolet and x rays when irradiation is performed at low temperature.

Typical electron spin resonance curves for x ray irradiated lead azide crystals at 77° K are shown in the figures. The following statements are offered in explanation and discussion of the electron spin resonance results.

1. The entire experimental work was designed to keep the crystals at 77° K at all times. Irradiation at room temperature permits direct chemical decay by normal methods.

2. No electron spin resonance signals were detected in samples previous to x-irradiation.

3. All electron spin resonance signals were unstable (some even at 77° K) and vanished irreversibly when the crystals were allowed to warm to room temperature for very short periods.

4. In no case did any blue color become apparent. A slight yellowish hue did appear in the lead azide after irradiation and this color was permanent at room temperature. We find no electron spin resonance signal attributable to this color.

5. Ultraviolet light sources (in our case we have only mercury lamps) have little or no apparent effect on the crystals. Some

extremely weak signals of doubtful origin were observed after mercury lamp irradiation but these are not reproducible.

6. One crystal was given one hour of x ray treatment followed by eight hours of ultraviolet irradiation at 77° K without apparent change in optical clarity or color even when allowed to warm to room temperature.

7. This same crystal was then heated for one hour at 110° C and it darkened slightly. Heating overnight at 170° C caused the crystal to fracture severely and turn totally black.

8. Blackened lead azide gives no observable electron spin resonance signal at 77° K. This blackened sample contained large macroscopic amounts of lead metal as indicated by the low "Q" of the electron spin resonance cavity. Since the skin depth at 10 kmc is of the order of 0.6 microns, we assume the particles were larger than this.

9. The electron spin resonances in x ray irradiated alpha lead azide are sufficiently narrow that a sensitive spectrometer can use crystals of 2 or 3 mm size. In our experiments the irradiation time was one hour at 40 kv and 40 ma (tungsten target) and roughly 10^{16} unpaired spins were formed in the crystal. It is estimated that less than 10^{-4} of the beam was incident on the sample area. The x ray beam was filtered by 1 mm of quartz.

10. In PbN_6 x-rayed and maintained at 77° K, we recognize four groups of lines. These are:

a. Sharp - high power series - Shown on the high field side of the resonances in Figure A. These are also apparent in Figure D and generally at low attenuator settings (6 db) but tend to diminish when microwave power is turned down (high attenuator settings) as in Figures B and C. The spacing of the lines is approximately 15 gauss for orientations shown.

b. Symmetric Doublet - This structure is marked in Figures B and C. It occurs either at high or low power but is more apparent when power is lower. The line separation is 230 gauss as shown in Figure B. The splitting is dependent on crystal orientation. The size of the splitting in this compound indicates that it is fine structure rather than hyperfine structure. The doublet is symmetric about $g = 2$. It is possible that the "doublet" is actually three lines with a central line at $g = 2$ mixed in with the complicated line structure at the center of the spectrum.

c. Central Group - Shown in Figure B. The group of very narrow lines at the center of the spectrum around $g = 2$. The line

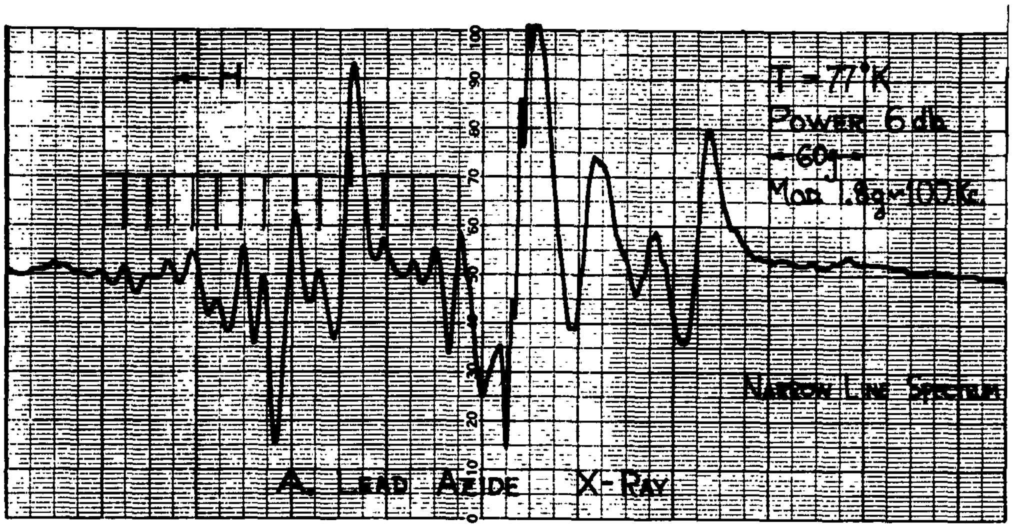

Figure A

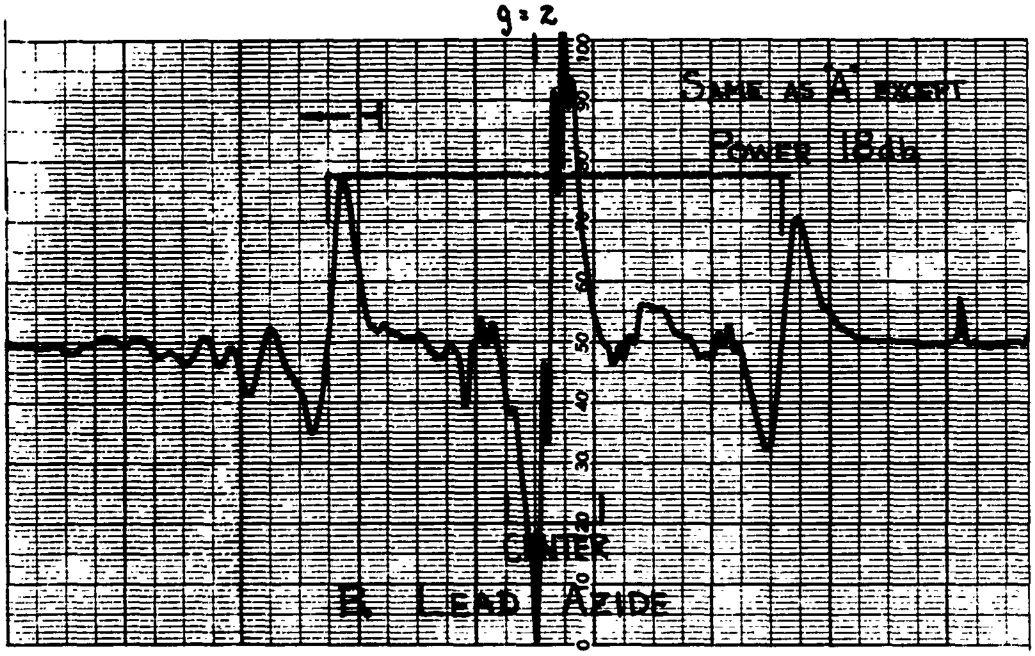

Figure B

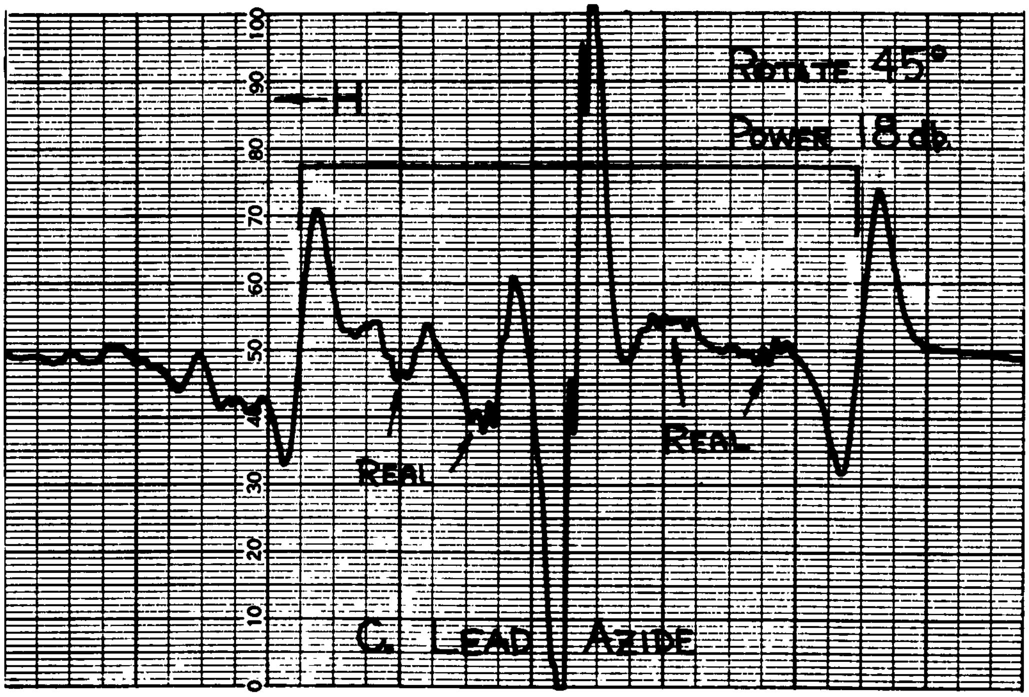

Figure C

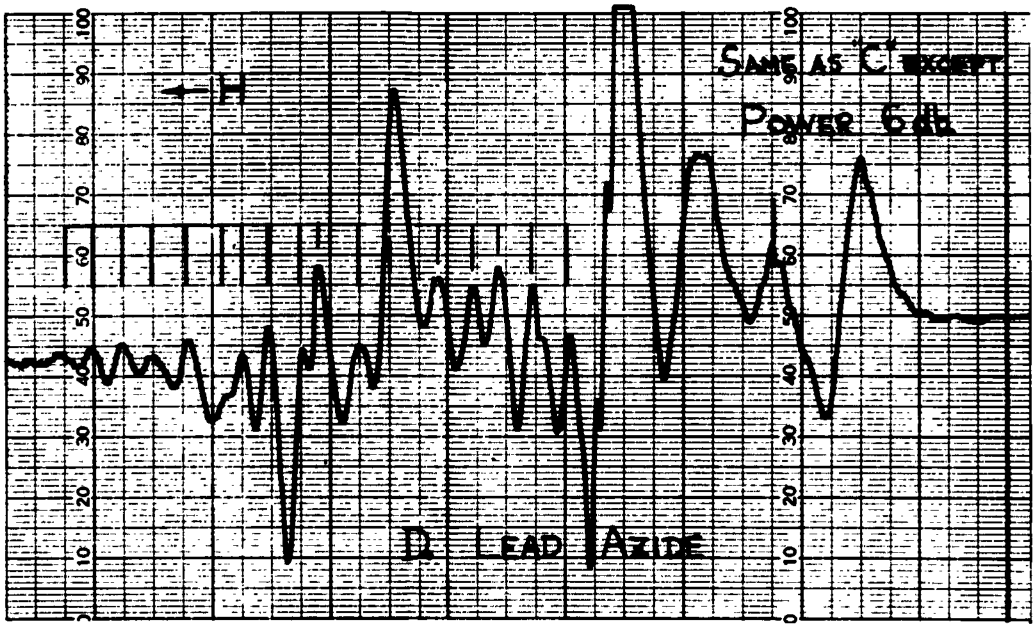

Figure D

spacing is approximately 5 gauss and the structure appears to be isotropic.

d. Other narrow line Group - These are pointed out in Figure C. These very small lines are reproducible and nearly blanket the spectrum. At high power (6 db setting) they are covered up.

The origins of the resonances are nitrogen fragments produced during the x ray bombardment. The multiple line structure is very likely produced by nitrogen-metal compounds and nitrogen chain or ring structures. The sharp high power series (a) is similar in appearance to the N_2 - N_4 resonances in irradiated KN_3. The central group (c) is very similar to the N resonance in irradiated NaN_3. The other narrow line group (d) is probably nitrogen ring structure and may simply be an inequivalent resonance pattern of groups from the sharp high power series (a). The multiple line structure of groups (a), (c), and (d) can be explained as hyperfine structure caused by electronic interaction primarily with nitrogen nuclei. The symmetric doublet (or triplet?) splitting is apparently produced by a different mechanism than the other lines. One possibility is that the two lines represent transitions in a low lying triplet electronic state. If the resonance is three lines than it most likely is a ligand field interaction of nitrogen with a damage site in the lattice. Power saturation, optical bleaching, thermal bleaching, reversible thermal effects and chemical treatment will have to be used before any definite conclusions can be reached. In addition complete crystal rotational studies in two different microwave regions will be required for precise information from electron spin resonance experiments.

In addition to the spectra shown in Figures A, B, C, and D, there are other broad line spectra underneath the narrow lines. These have been tuned out from observation by using narrow modulation. The origin of the broad spectrum is unknown.

We wish to express our thanks to Franklin E. Wawner for structural analyses of these crystals given in the monthly report of the Project 8F07-11-001-02 of October 1960. In addition we wish to thank M. D. Kemp for all phases of research and growth of these crystals.

PARAMAGNETIC RESONANCE IN POTASSIUM AZIDE IRRADIATED AT 77° K

by

R. B. Horst and J. H. Anderson*
University of Pittsburgh
Pittsburgh, Pennsylvania
and
D. E. Milligan
Mellon Institute
Pittsburgh, Pennsylvania

Abstract

Single crystals of potassium azide have been irradiated at 77° K with ultraviolet light. Two new paramagnetic centers, N_2 and A, have been found. A third center, N_4, appears to be the same as that discovered by Shuskus, Young, Gilliam, and Levy in potassium azide irradiated at room temperature. The g tensor for the N_2 center has only orthorhombic symmetry. Its principal values are $g_x = 2.0008$, $g_y = 2.0027$, $g_z = 1.9832$. The x axis is parallel to the [001] crystal axis and the y and z axes are parallel to the $[\bar{1}10]$ and [110] axes respectively. The hyperfine tensor is approximately axially symmetric with $T_x = 3.8G$, $T_y = 12G$, $T_z = 4.0G$. The models N_2^- and N_2^+ for this center are discussed. Although they explain many features of the resonance, neither model can account for the signs of the g shifts. It is concluded that the center probably consists of an unpaired spin trapped by two nitrogen atoms associated with a lattice defect. The paramagnetic center thus formed lacks a center of symmetry.

We have made electron spin resonance measurements on single crystals of potassium azide (KN_3), irradiated and maintained at 77° K. Three different paramagnetic centers were found. We have dubbed these centers N_2, N_4, and A. The N_4 center has been previously reported[1] in KN_3 irradiated at room temperature. This report is concerned primarily with the N_2 center.

As suggested by the notation, we consider this center to consist of an unpaired spin associated with a pair of nitrogen atoms. Our interpretation of the resonance spectrum provides strong evidence for this. In order to proceed to a more specific model of the center we have considered the theory of the g factor and hyperfine structure of the centers. The results have been mainly negative, since they suggest that the simple model of a diatomic N_2^+ or N_2^- ion cannot explain our data.

---

* This research was supported by the U. S. Air Force through the Air Force Office of Scientific Research of the Air Research and Development Command.

Sample preparation is treated in section 1 of this paper. Some details of the microwave technique are given in section 2. The resonance spectrum is discussed in section 3. Section 4 describes some preliminary observations on thermal stability. A brief account is given in section 5 of growth rate studies. In section 6 we discuss possible models for the N_2 center.

1. Sample Preparation and Handling

Single crystals of KN_3 were obtained by crystallization from aqueous solution. The solution was prepared by dissolving polycrystalline KN_3 in demineralized water at 35-40° C and was then filtered, covered, and allowed to cool slowly to room temperature. After six weeks, in the dark, crystals in the form of flat plates, normal to the c axis, had formed. Their size was about 1 x 6 x 6 mm. Polycrystalline KN_3 was prepared by treating Fisher reagent grade NaN_3 with Fisher reagent grade H_2SO_4 and bubbling the resulting HN_3 gas through a solution of Fisher reagent grade KOH. The material was not generally subjected to recrystallization, although one batch was. Frequently on dissolving the KN_3 in water we observed a yellow color in the solution. The virgin single crystals were tested for paramagnetism by searching for resonance at room temperature and at 77° K. No absorption lines were found.

The crystals were cut either with a sharp razor blade or a wet thread. The cleanest cuts were obtained with the wet thread. The cuts were always made parallel to a [110] axis. This axis was confirmed by x-ray analysis to be parallel to an edge of the tabular crystal. Two shapes of sample were used: a flat plate (in which case a virgin crystal could often be used) and a rough, right circular cylinder. The cylinder axis was parallel to the [110] axis of the crystal and, therefore, perpendicular to the [001] and $[1\bar{1}0]$ axes.

The flat plates were mounted in the resonant cavity of the spectrometer either on the bottom (end) of the rectangular cavity or at a point on the narrow side wall distant $\ell/4$ or $3\ell/4$ from the end of the cavity, ℓ being the length of the cavity. The side wall location has the advantage that the microwave magnetic field at the sample is always normal to the static magnetic field and thereby maximum intensity of the resonance is maintained as the cavity is rotated relative to the static magnetic field.

The cylindrical sample was cemented to a button on a bevel gear (Fig. 2) which fitted into a hole in the middle of a narrow side wall of the cavity. The gear could be rotated through 360°.

1.1 Irradiation of the sample. Irradiations were carried out in the apparatus shown in Fig. 1. The light source was a G. E. H85-C3 uv lamp with a rated output of 0.49 watt in the wavelength region from 250 to 280 mμ. We estimate about 7×10^{14} photons/cm^2 sec reached the sample. Following irradiation for the desired time, the cavity was attached to a precooled waveguide coupling section and transferred to a pyrex dewar between the poles of an electromagnet.

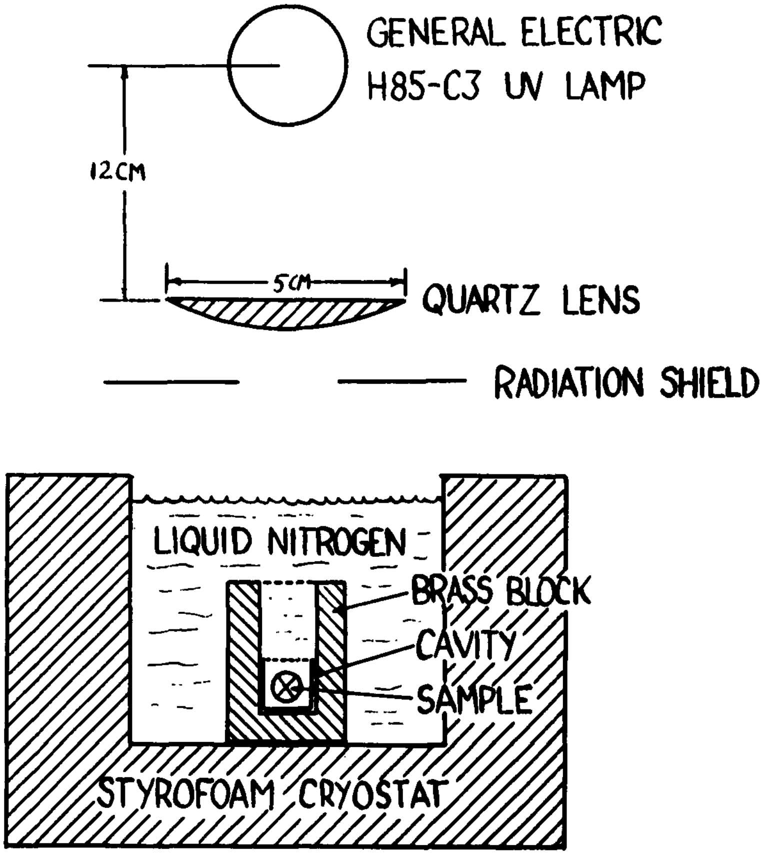
GENERAL ELECTRIC
H85-C3 UV LAMP
12CM
5CM
QUARTZ LENS
RADIATION SHIELD
LIQUID NITROGEN
BRASS BLOCK
CAVITY
SAMPLE
STYROFOAM CRYOSTAT

Figure 1. Setup for irradiating sample with uv light.

2. Microwave Measurements

All spin resonance experiments were performed at about 77° K. Frequencies of 9.33 and 23.9k Mc/sec were used. The spectrometer was a home-made instrument of the standard low frequency magnetic field modulation variety. A magic tee bridge was used. It was balanced so as to detect the absorption mode.

The sample cavity was rectangular and resonated in the TE_{012} mode. It was provided with a set of removable coupling irises so as to permit the attainment of optimum coupling to the remainder of the microwave circuit. The cavity was fitted into a brass block which could be screwed onto the waveguide coupling section. The cavity which was used with the cylindrical sample was fitted with a bevel gear, shown in Fig. 2, which could be driven by another gear mounted outside the dewar vessel. This permitted us to rotate the sample through 360° about a horizontal axis. Since the waveguide section which coupled to the cavity was connected to a waveguide joint which could be rotated through 360° about a vertical axis, any desired orientation of the static magnetic field with respect to the crystal axes could be achieved. The mechanism for sample rotation functioned quite well except that, after a number of transfers of the cooled apparatus into and out of the dewar, enough ice formed on moving parts so as to interfere with rotation.

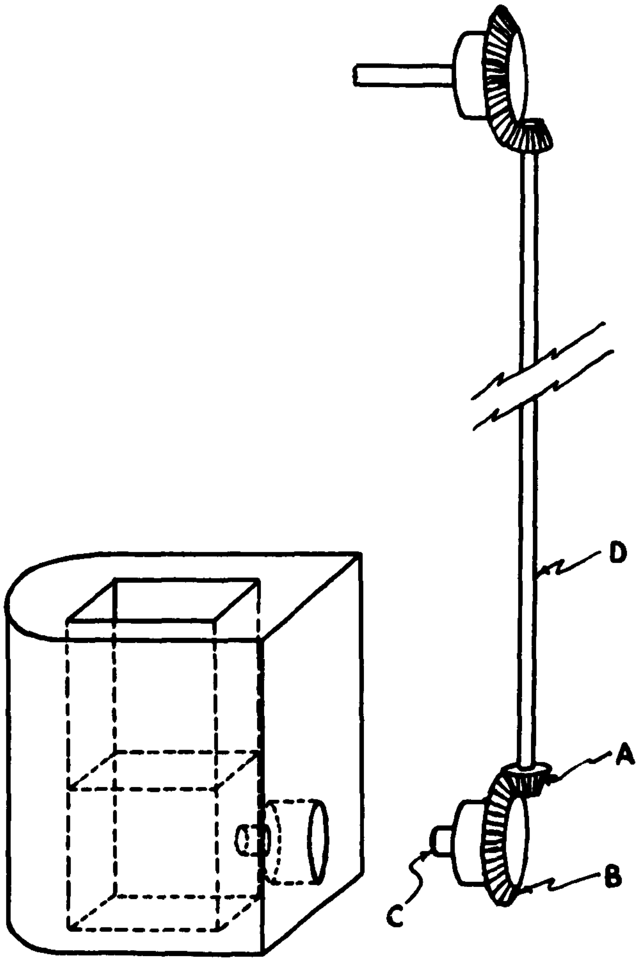

Figure 2. The sample rotator.

The g values were measured by a relative method, using diphenyl picryl hydrazyl as a reference. The recorder chart was calibrated, for this purpose, in terms of magnetic field, using the proton magnetic resonance signal. The g values were obtained by means of the expression

$$g_{line} = g_{hyd} - g \frac{\Delta H}{H_{hyd}}$$

$$= 2.0036 - \frac{2 \Delta H}{8500} ,$$

where the g factor for powdered hydrazyl is taken as 2.0036.[2]

3. The Microwave Spectra

The paramagnetic resonance data for both the N_2 and the N_4 center may be summarized by the spin hamiltonian:

$$\mathcal{H} = \beta(g_x S_x H_x + g_y S_y H_y + g_z S_z H_z) + T_x S_x I_x$$

$$+ T_y S_y I_y + T_z S_z I_z ,$$

where β is the Bohr magneton, S_i and I_i are the components of the electronic and nuclear spin angular momentum operators, respectively (measured in units of $\hbar$) and H_i is the ith component of the magnetic field. The coordinate system has its x axis parallel to the [001] crystal axis; the y and z axes are parallel to [110] and [$1\bar{1}0$] crystal axes and are crystallographically identical, of course. The values of the parameters g_i and T_i are given in Table I. The g tensors have only rhombic symmetry; the T tensors are approximately axially symmetric. As may be inferred from Table I, the resonances of the N_2 and N_4 centers overlap at many orientations of the crystal. This overlapping renders difficult the process of deducing principal values of the tensors from angular variation of the spectrum. Fortunately, a difference in thermal stability of the centers permits one to get rid of the N_2 center and thus to obtain better data for the N_4 center. We have not found a way to observe the N_2 resonance alone. For this reason, the principal values for the N_2 center are less accurately known. The center which we have called N_4 was discovered prior to our work by Shuskus, Young, Gilliam, and Levy[1] in KN_3 which had been irradiated at room temperature and cooled to 77° K in order to examine the paramagnetic resonance. Our results for the g and T tensors are substantially the same as theirs except

Table I. The Principal Values of the g and T Tensors for the N_2, N_4, and A centers

THE N_2 CENTER	Axis	Principal Values of the g Tensor	Principal Values of the T tensor
	x	2.0008 ± 0.0004	3.8 ± 0.2 gauss
	y	2.0027 ± 0.0010	12 ± 4 gauss
	z	1.9832 ± 0.0004	4.0 ± 0.2 gauss
THE N_4 CENTER	Axis	Principal Values of the g Tensor	Principal Values of the T tensor
	x	1.9876 ± 0.0004	2.8 ± 0.2 gauss
	y	2.0016 ± 0.0004	9.2 ± 0.2 gauss
	z	2.0051 ± 0.0004	2.8 ± 0.2 gauss
THE A CENTER	Axis	Principal Values of the g Tensor	Principal Values of the T tensor
	x	2.053 ± .002	19 ± 2 gauss
	y	0	
	z	0	

for our value of g_x which is about 0.5 percent lower than theirs. This is a substantial disagreement, since the significant parameter is the g shift:

$$\Delta g = g_i - g_o = g_i - 2.0023,$$

which is the difference between the principal value and the free electron value. Our g shift is almost three times the measured shift of Shuskus et. al.

3.1 The Angular Variation of the Spectrum. Since this paper has the nature of a preliminary report with some of our conclusions subject to more careful verification, we shall describe briefly the appearance of the spectrum at several orientations. This should indicate the nature of the difficulties encountered in interpreting the spectrum and enable the reader to form a better estimate of the reliability of our numbers.

3.1.1 The spectrum with H parallel to the [001] axis. Shown in Fig. 3 are the first derivative spectra of the N_2 and N_4 centers with the crystal oriented so that the static magnetic field is parallel to the [001] axis (c axis) of the crystal. The spectra were obtained at 1 cm wavelength. The two lines are separated by about 55G. The A center line appears at a field of about 200G lower than the N_2 line, so that it is off the figure to the right. The N_2 line has a partially resolved structure; a slight indication of structure appears in the N_4 line.

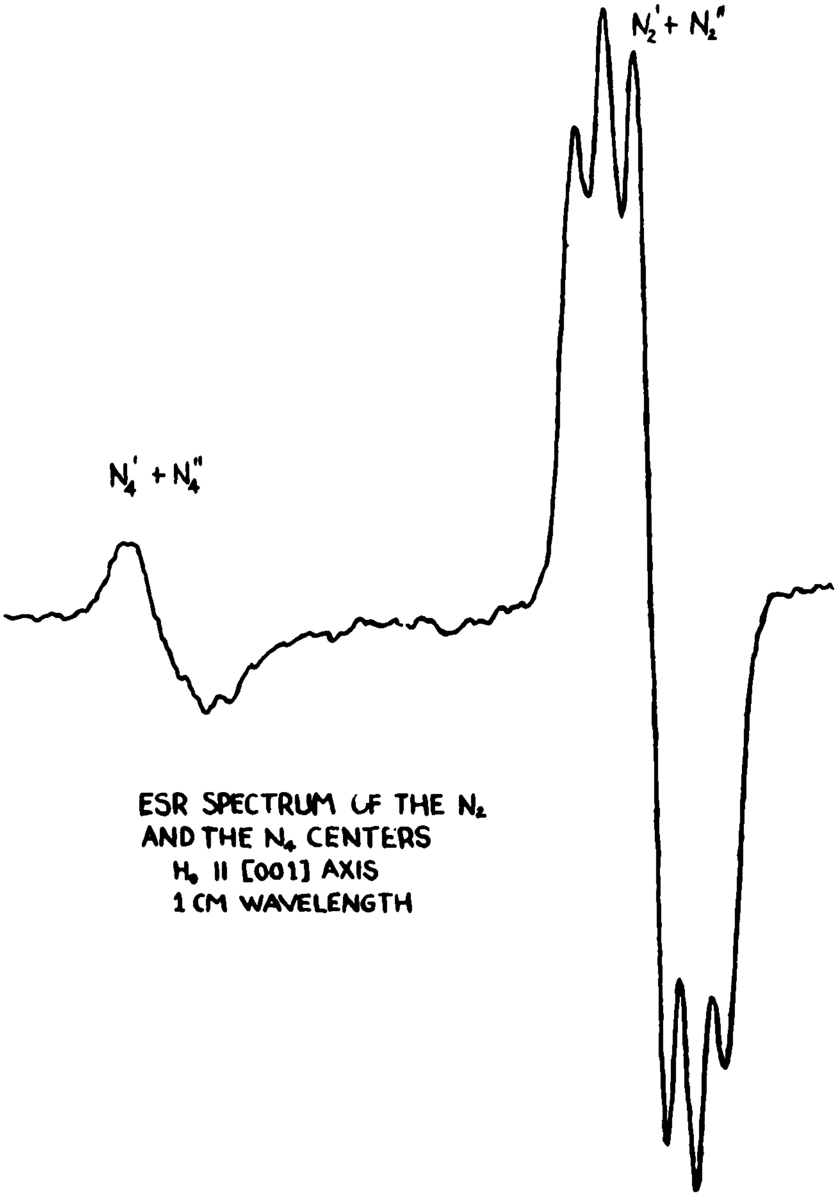

Figure 3

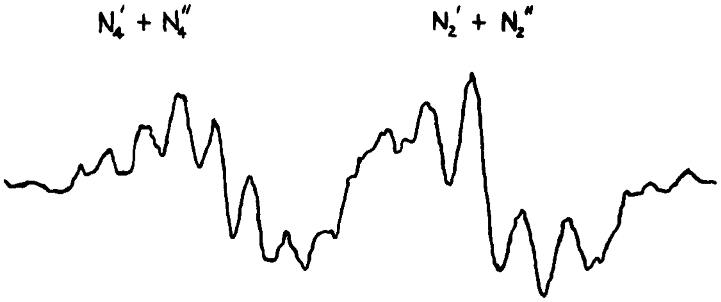

ESR SPECTRUM OF THE
N_2 AND THE N_4 CENTERS
$H_0 \parallel$ [001] AXIS
3 CM WAVELENGTH

Figure 4

Figure 4 shows the spectra of the N_2 and N_4 centers for the same orientation, but recorded at 3 cm. Both lines now show partially resolved structure. Their centers are now closer together, as expected, since the frequency is smaller than at 1 cm. The separation of the components of the lines is the same as at 1 cm, indicating that the structure is due to nuclear magnetic hyperfine interaction. The number of component hyperfine lines is 5 for N_2 and 9 for N_4. The relative intensities are: for N_2, 1:2:3:2:1; for N_4, 1:4:10:16:19:16:10:4:1.

3.1.2 The spectrum with H in the $(1\bar{1}0)$ plane. When the crystal is rotated so that the static magnetic field is no longer parallel to the [001] crystal axis, both the N_2 and the N_4 lines break up into two equivalent lines. There are never more than two equivalent lines for each center. The A line shows a partially resolved structure consisting of four lines at crystal orientation such that the magnetic field makes an angle with the [001] axis of less than five degrees. This line is so anisotropic and broadens so rapidly as the angle with the [001] axis increases that we have not yet been able to study it in detail.

A complete study of the angular dependence of the N_2 and N_4 spectra establishes unequivocally that the principal axes of the $\underline{g}$ and $\underline{T}$ tensors of these centers are along the [001] axis (four fold symmetry axis) and the [110] and $[1\bar{1}0]$ axes (two fold symmetry axes). These principal axis locations are consistent with the strictures which the crystal symmetry places on the anisotropic, second rank tensors when a maximum of only two equivalent lines for each center appears at any orientation of the crystal.

Unfortunately, on account of the relatively complex hyperfine structure of the lines, the two fold equivalence of lines, and their tendency to overlap, to follow the angular variation of the g factors is difficult. The spectrum in Fig. 5, which is a relatively simple one, will illustrate the difficulty. Only one of the four lines is resolved, the one which we have labeled N_2'. The other three lines, consisting of the other N_2 line: N_2'', and the two N_4 lines: N_4' and N_4'', overlap so that one cannot clearly identify any of them. The center of this conglomerate is about 85G distant from the center of the N_2' line.

A study of the angular dependence of the N_2' spectrum when the magnetic field H is in the plane of the [001] and [110] axes, i.e. in the (1$\bar{1}$0) plane, enabled us to show that its g factor varies according to the expression

$$g^2 = g_x^2 \cos^2 \theta + g^2_z \sin^2 \theta$$

where θ is the angle between H and the [001] axis. The N_4 lines were more difficult to study. Fortunately, we were able to obtain these lines in the absence of the N_2 lines and to study their angular variation without interference. Since we are chiefly concerned here with the N_2 center, we shall not give the details.

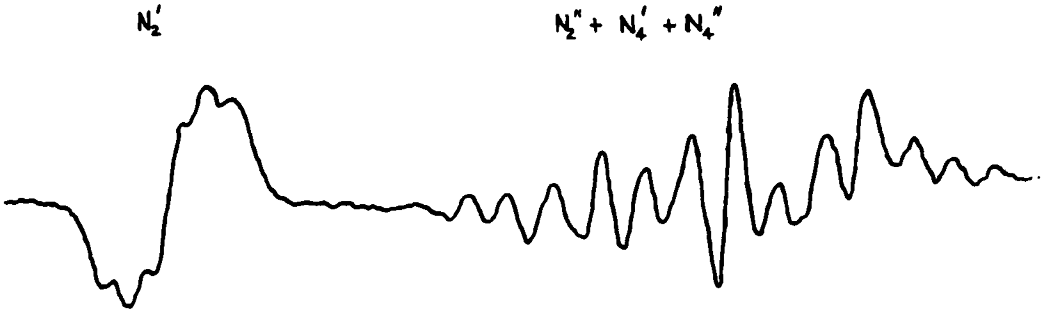

ESR SPECTRUM OF THE N_2 AND THE N_4 CENTERS
$H_0 \parallel [110]$ AXIS
1 CM WAVELENGTH
Figure 5

3.1.3 The spectrum with H parallel to the (001) plane. The spectrum obtained with H parallel to the [1$\bar{1}$0] axis is identical to that with H parallel to the [110] axis, shown in Fig. 5. This was to be expected from crystal symmetry. Only the labeling of the lines with respect to primes and double primes needs to be reversed. With H bisecting the [110] and [1$\bar{1}$0] axes the primed and double primed lines coincide, of course. At this orientation all lines overlapped badly. As a matter of fact, when the crystal was rotated so that H was in the (001) plane, it was possible to follow the N_2' and N_2'' lines as distinct entities only out to angles of ± 35° with the [110] or [110] axes. Nevertheless, we were able to plot the g value versus ϕ (ϕ is the angle H made with the [110] axis) and obtain the results shown in Fig. 6. The two sets of points shown in the graph are for $0^\circ < \phi < 45^\circ$ and $-45^\circ < \phi < 0^\circ$. They should coincide. The discrepancy shows the extent to which our inferred g values are unreliable. The value of g^2_y was obtained by extrapolating to $\phi = 90^\circ$ a straight line with slope equal to the average of the two straight lines drawn through these points. In this way the principal values of g were determined.

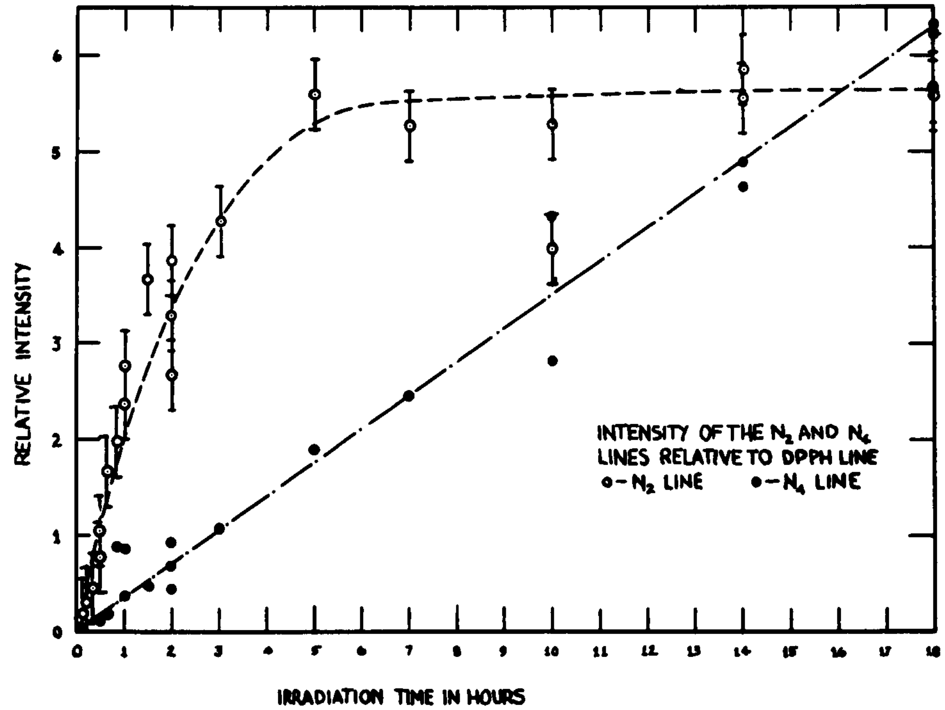

Figure 6. Growth of the N_2 and the N_4 lines.

The determination of the principal values of T for N_2 was more difficult. The data for H in the $(1\bar{1}0)$ plane, i.e. the plane of the [001] and [110] axes could be handled in a straightforward manner to give T_x and T_z since the N_2' line is resolved in this plane. The value of T_y had to be found in a manner similar to that used for g_y, except that it was necessary to estimate the hyperfine splitting from the peak-to-peak line width in those cases where hyperfine structure was not visible. For this reason, the estimated error of T_y is rather large.

3.1.4 Reconstruction of experimental spectra. The experimentally determined g and T tensors in Table I have been used to reconstruct the spectra for certain special orientations of the crystal. Computations were made on a desk computer using gaussian lines with widths of 4.0G between points of maximum slope. Relative intensities of 1:2:3:2:1 for the lines and separations of 3.8 G gave curves which matched the appearance of the experimental spectrum for N_2 with $\underline{H}$ parallel to the [001] axis very closely. The spectrum of the N_4 lines only, obtained by the method discussed in section 4 below, was reconstructed by means of an IBM 7070 computer program. We have performed the reconstruction only for $\underline{H}$ parallel to the [110] axis. The reconstructed spectrum agrees with the experimental spectra obtained in several different runs within experimental error. We are at present reconstructing the $N_4' + N_4'' + N_2$ spectrum which appears in Fig. 5.

4. Thermal Stability of the N_2 and N_4 Centers

A crystal which had been irradiated with uv light for 18 hr at 77° K and in which the N_2 and N_4 centers appeared to be stable was warmed to about 195° K. This was accomplished by removing the resonant cavity from liquid nitrogen, wrapping it in a plastic bag and immersing it in dry ice. The time required for the cavity to warm to 195° K was about 1 hr. The sample was shielded from light at all times except during the brief interval required for transfer of the cavity from liquid nitrogen to dry ice. After the sample had remained at 195° K for about 14 hr, it was returned to 77° K and the resonance spectrum was remeasured. The intensity of the N_4 resonance was found to be 70 percent of the original and that of the N_2 resonance 50 percent of the original. After this treatment, the crystal was warmed to room temperature. It was maintained at room temperature in the dark for 12 hr, then returned to 77° K. The N_2 resonance could no longer be observed. The intensity of the N_4 resonance was found to be reduced to 50 percent of the original. After the crystal was held at room temperature for an additional 30 hr the N_4 resonance also disappeared.

Sketchy as these data are, it is interesting to compare them with observations on the effect of warming on the optical absorption bands produced in uv - irradiated potassium and sodium azide.[3a,b] Tompkins and Young[3a] found that the 3600 A band is removed by warming the crystal to 195° K for 10 min. At the same time the 5500 A band is reduced by about 5 percent and a band at 7250 A is not affected at all. Since neither the N_2 nor the N_4 center is completely removed by maintaining the crystal at 195° K even for 14 hr, these centers certainly do not correspond to the 3600 A band. Since they are bleached to some extent, they probably do not correspond to the 7250 A band either. Whether either center corresponds to the 5500 A band cannot be decided from our data. The N_4 center seems, however, more likely than the N_2 center to correspond to the 5500 A band.

5. The Growth of the N_2 and N_4 Centers

The relative intensities of the N_2 and N_4 resonances were measured as a function of irradiation time at 77° K. As a precaution against changing shapes or linewidths, the intensities were obtained by a double integration of the resonance curves. In order to make sure that no build-up or decay of centers occurred in the dark, the last run of each day was repeated the following day. These two runs always agreed within experimental errors. The results are shown in Fig. 6. The concentration of N_4 centers appears to increase linearly over the entire range. This suggests that these centers are not associated with lattice defects, because, toward the end of the irradiation period, the concentration of centers is approaching a level such that the finite number of lattice defects ought to cause the coloring rate to fall off. The N_2 concentration, on the other hand, definitely approaches a saturation level, as would be expected if impurities or lattice defects present only in limited amounts are required for formation of the center.

6. The Structure of the N_2 Center

6.1 The Hyperfine Structure. The magnitude of the hyperfine splitting and the relative narrowness of the hyperfine lines suggest a model for the N_2 center in which the unpaired spin is fairly tightly bound in a complex containing two nitrogen atoms. That the spin interacts equally with the two nitrogen nuclei is shown by the number and intensity of the hyperfine lines. The magnitude of the hyperfine splitting is typical of nitrogen-containing radicals: e.g., for atomic nitrogen it is about 3.7 G[4], for nitrogen in NaN_3, it is 6.2 G[5]. If the wave function of the unpaired electron were fairly diffuse, we should expect fairly broad, unresolved lines such as the F center line in K Cl[6], or, possibly resolved lines showing much structure as in the F center in NaN_3.[7]

The hyperfine tensor may be written as the sum of two parts:

$$\underline{T} = \underline{T}^{(0)} + \underline{T}^{(2)} \quad , \tag{1}$$

where $\underline{T}^{(0)}$ is a zero rank tensor (scalar) given by

$$\underline{T}^{(0)} = \frac{8\pi}{3} g_0 \beta \gamma_I \hbar S_z^{-1} \langle \Psi_G \mid \Sigma_k \; \delta(r_k) \, s_{zk} \mid \Psi_G \rangle$$

and $\underline{T}^{(2)}$ is a traceless, second rank tensor, the components of which are given by

$$T_{ij}^{(2)} = g_0 \beta \gamma_I \hbar \langle \Psi_G \mid (3r_i r_j - r^2 \delta_{ij})/r^5 \mid \Psi_G \rangle$$

In these expressions the magnetic moment of the electron is given by $g_o\beta$, that of the nucleus by $\gamma_I\hbar$; s_{kz} is the component of the spin of electron k along the direction of the external field; S_z is the component of the total spin in the direction of the external field; $\delta(\underline{r}_k)$ is the three-dimensional Dirac delta function; $\underline{r}$ is the electron-nucleus distance; and δ_{ij} is the Kronecker delta. The averages are taken over the ground state $|\ \psi_G >$ of the radical. (It is evident that we are considering only first order terms.) The scalar interaction $\underline{T}^{(0)}$ is just the Fermi contact interaction of an electron with the nucleus which vanishes for all but s wave functions. It does not, in general, vanish for s electrons in closed shells. Therefore $\underline{T}^{(0)}$ involves a sum over all electrons. On the other hand, contributions to $T_{ij}{}^{(2)}$ are made only by unpaired electrons; s electrons do not contribute to $T_{ij}{}^{(2)}$ since they have isotropic wave functions; whereas $T^{(2)}$ is anisotropic.

If we assume that the N_2 center may be described in terms of an unpaired electron occupying a combination of s and p orbitals only:

$$|\psi_G > = a\,|\,p > + \,b\,|\,s > \tag{2}$$

we can easily show (for the principal axis system of N_2) that

$$T_y{}^{(2)} = -2T_z{}^{(2)} = -2T_x{}^{(2)} = 2\ P.$$

We can then write

$$T_x = \underline{T}^{(0)} - P,$$

$$T_y = \underline{T}^{(0)} + 2P,$$

$$T_z = \underline{T}^{(0)} - P,$$

but we must be careful to avoid the assumption that the hyperfine interaction has been divided into a part p which is the contribution of the p orbital and a part s which is the contribution of the s orbital. As a matter of fact, the nitrogen atom, which has a ground state configuration $(1s)^2\ (2s)^2\ (2p)^3\ {}^4s$, has an isotropic hyperfine constant of 3.7G, even though the unpaired electrons are p electrons. The isotropic interaction arises from polarization of the core by the p electrons.

We can attempt to decompose our observed hyperfine constants as in equation (1), but we have the difficulty that only absolute magnitudes are determined by the resonance experiments. Furthermore, we have not yet been able to determine the relative signs of the hyperfine constants. Let us assume that T_y = 12G and $T_x = T_z = \pm$ 4 G. Then we have either

$$\underline{T}^{(0)} = 6.7, \qquad P = 2.7 \qquad \text{(a)}$$

or

$$\underline{T}^{(0)} = 1.3, \qquad P = 5.3 \qquad \text{(b)}$$

If we assume that T_y = -12 G, we obtain negative values for P, which is impossible. Negative values for $\underline{T}^{(0)}$ are also obtained, which seems unlikely in view of the fact that $\underline{T}^{(0)}$ is positive for free atomic N^4 and for the nitrogens in diphenyl picryl hydrazyl.[8] Assuming, therefore, that T_y is positive, we have the problem of deciding between alternatives (a) and (b). Our inclination is to favor (a) with the larger value of $\underline{T}^{(0)}$ on the basis of the free nitrogen value and the values for N trapped in various solids quoted by King et al.[5]

Even the larger value of $\underline{T}^{(0)}$ is quite small compared with that to be expected for a 2s electron, which is about 520 G if one uses the values of $|\psi_{2s}(0)|^2$ given by Dousmanis[9] or Mizushima[10]. Using a Hartree function, Lord and Blinder[7] estimate $\underline{T}^{(0)}$ = 600 G for a nitrogen 2s electron. The value of $\underline{T}^{(0)}$ is so small, that it seems quite likely that $\underline{a}$ in (2) is equal to zero and that the isotropic hyperfine interaction is due to core polarization. A similar conclusion was reached by Lord and Blinder[8] in studying nitrogen hyperfine structure in hydrazyl and carbazyl. It appears likely, therefore, that the unpaired electron is not in a bonding orbital which is likely to have considerable s admixture, but is, rather, in a p orbital, perpendicular to a bond, i.e. a $p\pi$ orbital.

Lord and Blinder have calculated the anisotropic constant P for a nitrogen 2p electron using a Slater orbital. They obtained P = 10.2 G. If the unpaired electron in the N_2 center spends half its time on each nitrogen, this number should be reduced by 1/2. The result 5.1 G, agrees closely with alternative (b) for the P term of the N_2 hyperfine coupling but is about twice as large as the value of P in alternative (a) which we have favored. The reason for this smaller value of P might be that the electron is distributed over a larger complex than one consisting of only two N atoms.

6.2 The g tensor. We can use the measured g tensor to attempt to obtain further information about the structure of the N_2 center. The principal values of the g tensor are given according to the theory of Abragam and Pryce[11] by

$$g_i = g_o - \frac{\zeta\,|\langle\psi_G|\ \ell_i\,|\psi_E\rangle|^2}{E_E - E_G} \qquad (3)$$

where g_o is the free electron g, ζ is the spin-orbit coupling parameter, ℓ_i is the ith component of the orbital angular momentum operator, ψ_E is an excited state, and E_G and E_E are the energies of the ground and the excited states respectively. If we try as a model for the N_2 center the N_2^- or N_2^+ ion, we might assume that the order of molecular orbitals formed from 2p functions is as shown in Fig. 7, which is the order for N_2. The π levels are depicted as split by the interaction with the crystal environment. Each level is doubly degenerate so that the ground state configuration of N_2^+ would be $(\pi_{uy})^2\ (\pi_{ux})^2\ \sigma_g$ which is unacceptable, since the unpaired electron must be a π electron; that of N_2^- would be

$$\text{(I)}\quad (\pi_{uy})^2\ (\pi_{ux})^2\ (\sigma_g)^2\ \pi_{gy}$$

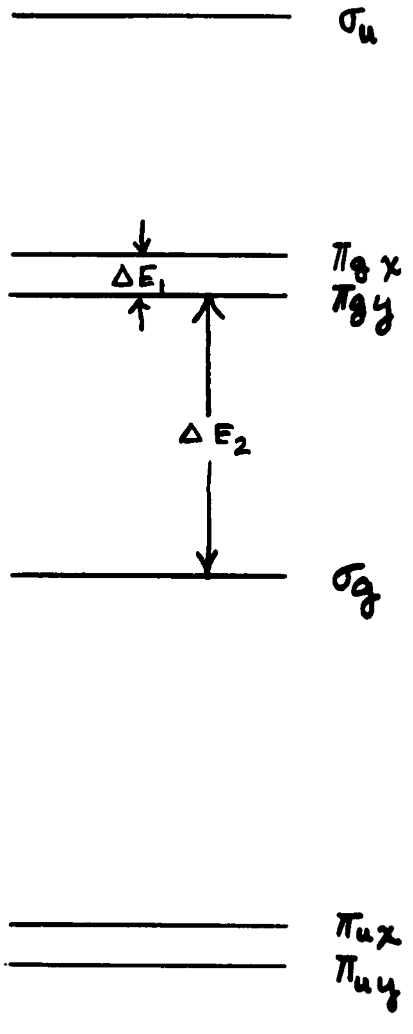

Figure 7. Schematic representation of possible energy level diagram for the N_2 center.

The only non-vanishing matrix elements in equation (3) are those between states of like parity. We assume that all orbitals except the ones we have shown are so much higher in energy that we can ignore them. The excited configurations for N_2^- are, therefore,

$$\text{(II)}\ (\pi_{uy})^2\ (\pi_{ux})^2\ (\sigma_g)^2\ \pi_{gx}$$

and

$$\text{(III)}\ (\pi_{uy})^2\ (\pi_{ux})^2\ \sigma_g\ (\pi_{gy})^2$$

It is easy to show from equation (3) that $g_y = g_o$. We therefore identify g_y with the value 2.00027, and $T_y = 12G$, which is consistent with the labels we have already used. It can be shown, moreover, that the contribution to the shift in g_z is produced by the excited state (II) and the shift in g_x is produced by excited state (III). Since equation (3) shows that the g shifts are inversely proportional to the excitation energies, we expect, on the basis of our postulated level scheme, the shift in g_z to be relatively large and the shift in g_x to be relatively small. This, too, is consistent with observations (Table I). Using Mizushima's[10] value: $\zeta = 100\ \text{cm}^{-1}$, we can use equation (3) to calculate ΔE_1. It turns out to be 1.29 eV, a not unreasonable number for a crystal field splitting. Likewise, a calculation of ΔE_2 gives 22 eV, which is large, but not outrageously so. Disaster strikes suddenly, however, when we consider the signs of the g shifts. Equation (3) predicts that g_x should be shifted above g_o, contrary to observations.

The consideration of other energy level schemes does not help us out of this difficulty. For instance, the scheme in Fig. 8 is consistent with N_2^+ or N_2^- as far as fulfilling our requirement that the unpaired electron be a p electron, but either center would have g values both above and below g, contrary to Table I. Other level schemes appear very unlikely on the basis of qualitative energy considerations.

A way out of our dilemma is to assume that the color center consists of more than just a pair of nitrogen atoms. It might, for example, consist of two nitrogen atoms combined with impurity atoms or with a vacancy. Any scheme will do which destroys the center of symmetry, for then the parity restriction breaks down. It is now easy, in a purely qualitative way, to explain the fact that both g_x and g_z are less than g_o. All one has to do is to assume that, instead of the excited configuration (III) associated with Fig. 7, one has the configuration

$$\text{(IV)}\ (\pi_{uy})^2\ (\pi_{ux})^2\ (\sigma_g)^2\ \sigma_u$$

Other considerations such as the appearance of saturation in the

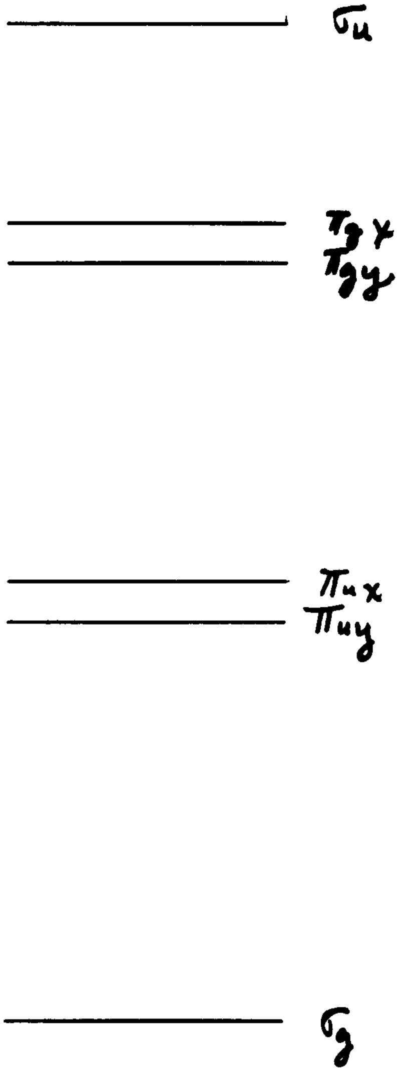

Figure 8. Alternative scheme of possible energy levels for the N_2 center.

growth curve of N_2 and the small value of P are indicative of the insufficiency of the $N_2^{\pm}$ group alone as a model for the center.

We are at present, or shall be in the near future, engaged in extending our resonance measurements to helium temperatures, improving measurements on thermal bleaching and attempting to obtain higher purity crystals. We are hopeful that these efforts will lead to a more definite model of the center.

7. Acknowledgments

The x-ray analyses on the crystals were performed by Mr. Sundaralingam of the Crystallography Laboratory at the University of Pittsburgh. We are grateful to Dr. Jeffrey of that laboratory for arranging for this work to be done. To Dr. M. H. Cohen and to Dr. J. J. Pearson we are grateful for discussions of the interpretation of the experiments. The ideas for our interpretation sprang out of conversations with Dr. Cohen, but he is not responsible for their present exposition. The reconstructions of experimental curves employing the IBM 7070 computer were performed by Mr. Leroy Colquitt.

Footnotes

1. Shuskus, Young, Gilliam, and Levy, J. Chem. Phys, 33, 622 (1960).
2. Holden, Yager, and Merritt, J. Chem. Phys. 19, 1319 (1951).
   C. H. Townes and J. Turkevitch, Phys. Rev. 77, 148 (1950).
3. a. F. C. Tompkins and D. A. Young, Proc. Roy. Soc. A236, 10 (1956).
   b. J. Cunningham and F. C. Tompkins, Proc. Roy. Soc. A251, 27 (1959).
4. Anderson, Pipkin and Band, Phys. Rev. 116, 87 (1959).
5. King, Carlson, Miller, and McMillan, J. Chem. Phys. 34, 1499 (1961).
6. C. A. Hutchison, Jr. and G. A. Noble, Phys. Rev. 87, 1125 (1952).
7. Carlson, King, and Miller, J. Chem. Phys. 33, 1266 (1960).
8. N. W. Lord and S. M. Blinder, J. Chem. Phys. 34, 1693 (1961).
9. G. C. Dousmanis, Phys. Rev. 97, 967 (1955).
10. M. Mizushima, Phys. Rev. 105, 1262 (1957).
11. A. Abragam and M. H. L. Pryce, Proc. Roy. Soc. A205, 135 (1951).

EXO-ELECTRON EMISSION AND RELATED ELECTRON-EMISSIONS FROM SOLIDS*

by

H. J. Mueller
Basic Research Group
U. S. Army Engineer Research and Development Laboratories
Fort Belvoir, Virginia

By exo-electron emission (EE), sometimes also called "Kramer-effect" or "delayed electron emission", one understands nowadays certain phenomenologically related but basically different electron emission phenomena, observable on solid surfaces. It is characteristic for this type of electron emission that it only occurs after excitation of the surface of the sample by energy interaction (for example: irradiation by light, x and gamma rays; bombardment with electrons, ions or alpha particles; mechanical treatment).

Such an excited surface does not emit electrons yet; it is only in the position for emission which has to be stimulated by an additional energy interaction (heat, light). It is typical that the emission of free electrons which is observed as the result of the stimulation, i.e., the EE, decreases with progressing time, although quality and intensity of the stimulation may remain constant.

The intensity of the emission currents is generally of the order of 10^{-18} - 10^{-15} $[A/cm^2]$. Thus, it is necessary to use counting methods instead of dc measurements for the detection of exo-electrons (E). The small kinetic energy of the emitted E necessitates the utilization of either open secondary electron multipliers or specially constructed unsealed Geiger counters in which the sample is made part of the counter wall.

To give some typical examples of an EE: (1) On warming up, many substances show an emission of electrons subsequent to uv or x-irradiation (Fig. 1). Usually the emission passes through several maxima as a function of temperature (glow curve). Sometimes even the ambient temperature provides enough stimulation for such excited samples to emit spontaneously (Fig. 2). (2) Spontaneous emission of E has been often observed subsequent to fragmentation or deformation of inorganic crystals, or (3) as a result of certain phase transitions.

---

* This paper is, in essence, a summary of USAERDL Research Report 1704-RR to be published. Literature references have been omitted in this text since the cited report also includes a complete literature survey to which the reader is referred.

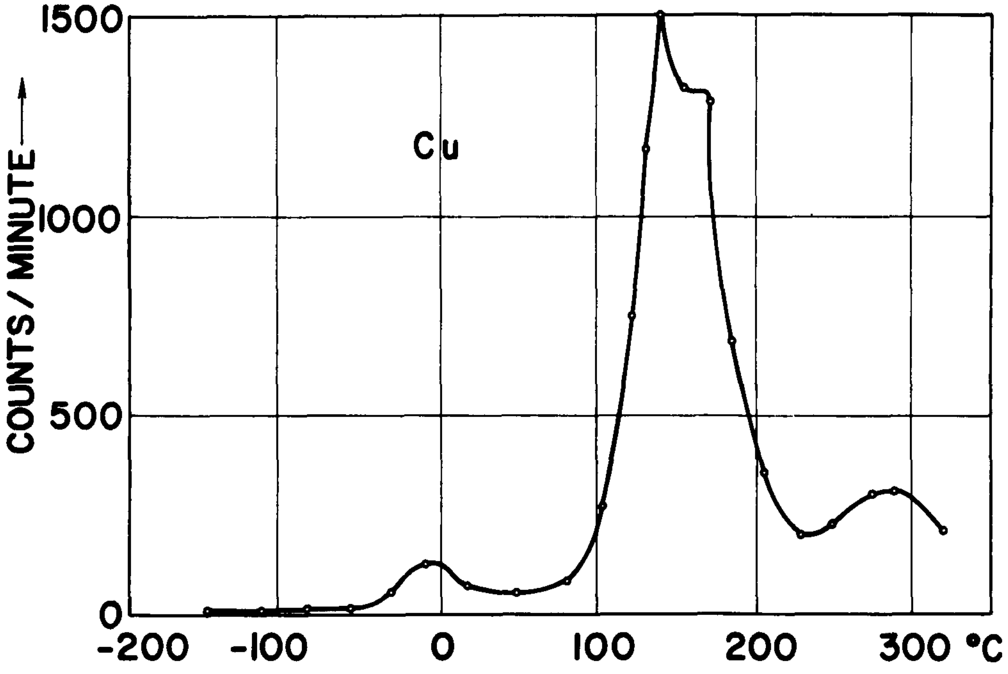

Fig. 1. Exo-electron glow curve of x irradiated Cu (after H. Mueller).

The emission of E is a very common effect and its late discovery was only due to the fact that the small emission currents escaped the attention of earlier investigators. However, a generally applicable theory of the EE does not yet exist. This, despite the fact that a considerable amount of experimental material has accumulated over the years and many attempts have been made to arrive at a satisfactory theoretical understanding.

It is the author's intention to give in the present paper a summary of the problems of EE and to indicate at the same time the potentialities in using E for the study of lattice imperfections, surface conditions and surface phenomena.*

The earliest observations of EE were made on metal samples which had been excited by mechanical treatment (polishing, abrasion, machining, etc.). At the same time it was found that during phase transitions, for instance the solidification of a metal melt, an outburst of free electrons can also be observed. This led J. Kramer, the discoverer of EE, to the conclusion that in both cases, the emission of electrons is caused by an exothermal reaction, and, therefore, the

---

* In this context we will understand by surface a region of several 100 Å thickness.

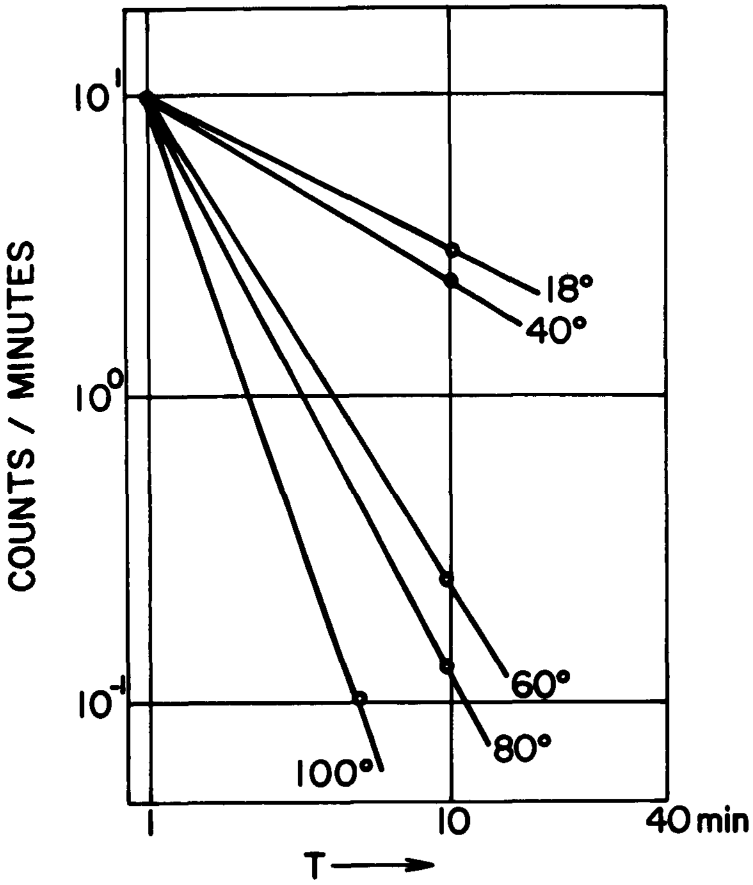

Fig. 2. Decay of the spontaneous exo-electron emission of x irradiated NaCl (after J. Kramer) at various temperatures.

name exo-electrons. In the case of mechanically excited metals, the exothermal reaction was assumed by Kramer to consist of the transition of a hypothetical non-metallic modification of the metal, unstable at ambient and elevated temperature, into the normal metallic modification. He assumed the non-metallic phase to be formed by the deformative mechanical treatment of the metal surface while in the "metallic" state.

This interpretation of the EE, however, was not applicable to the emission from radiation-excited metal samples and to the EE observed on non-metallic substances. Investigations performed on alkali halides showed that for these substances, the emission of E follows a mechanism which is practically identical with the well established trap model of recombination-luminescence (Fig. 3): lattice defects, acting as electron traps are filled by the excitation process. The stimulation process promotes in the usual manner

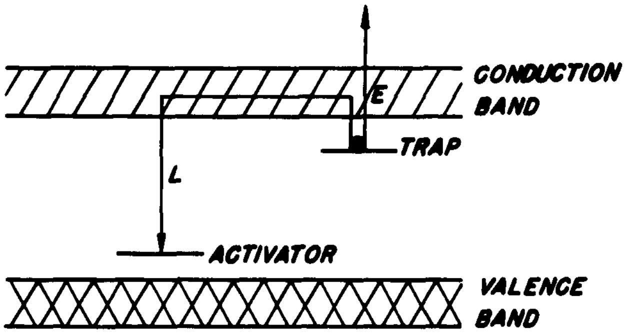

Fig. 3. Trap model of luminescence and exo-electron emission.

previously trapped electrons into the conduction band where they have the choice either (1) to recombine with activator terms, thus giving rise to luminescence, (2) to recombine non-radiantly or (3) to leave the crystal surface entirely by virtue of a mechanism not yet known, thus causing EE. For alkali halides, this model is well supported by experimental evidence, especially by the frequently observed simultaneous occurrence of luminescence (Fig. 4) and enhanced electrical conductivity as well.

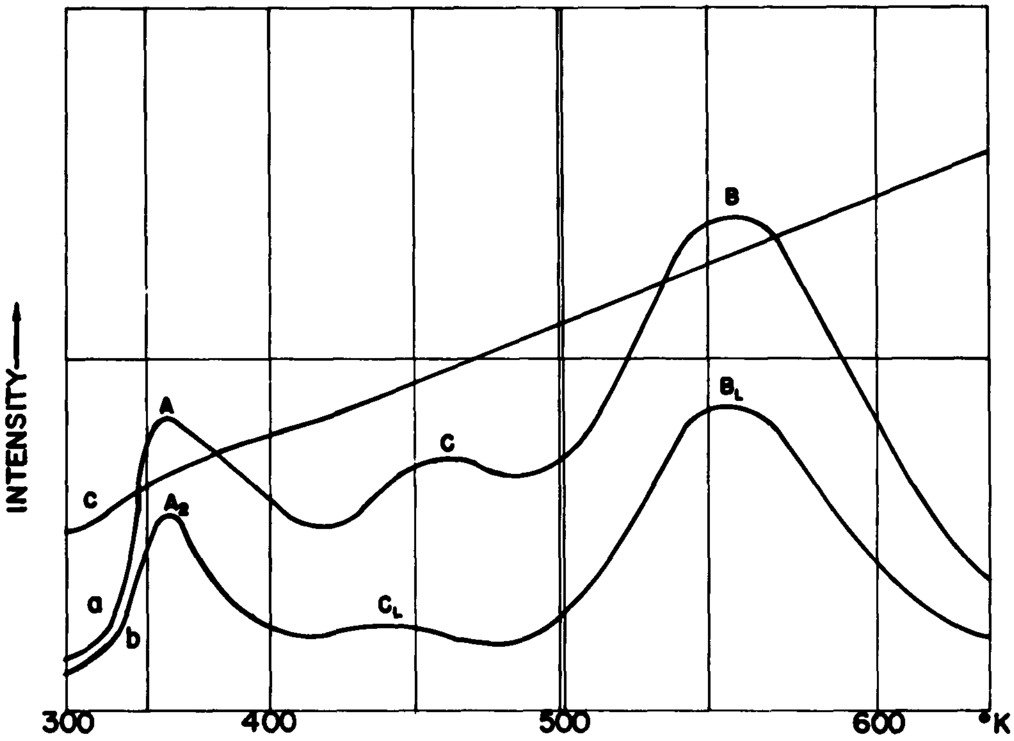

Fig. 4. Exo-electron and luminescence glow curves of CaF_2 after excitation by x rays (after A. Bohun).

Still pending though is the question how the E are finally ejected since, once in the conduction band, the experiment shows that obviously no additional energy supply from outside is necessary to achieve emission. Proposed mechanisms for this act of ejection are: (1) emission via energetically shallow surface traps; (2) emission from preferred sites on the surface which possess an extraordinarily low electron work function due to the presence of structure defects or adsorbed molecules; (3) facilitation of the electron emission by a hypothetical electric dipole layer in the surface region;* (4) emission as a consequence of the Maxwell energy distribution of the electrons in the conduction band. Those few electrons with unusually high kinetic energies should be able to leave the crystal. However, experimental results obtained so far do not yet permit a decision in favor of one of the aforementioned models.

The interpretation of the EE from metals underwent a drastic change when it became evident that the E are not emitted from the metal as such but from the crystalline, non-metallic surface layers (oxides, etc.), by which metals are always covered under normal conditions. Moreover, it was found that these surface layers had to be deformed in order to be excitable to EE. Now, the electron trap model, which successfully explained the EE from alkali halides, was also applied to the emission from metals, i.e., from oxides, sulfides, etc. However, it soon appeared that it was not possible to interpret by the simple luminescence model certain results obtained with these substances, of which many exhibit semiconductor characteristics. It was found, for example, that EE sometimes occurs without a detectable population of the conduction band by electrons. It further could be shown that in certain cases the electron traps (centers) which are responsible for luminescence and EE, respectively, were not the same.

A systematic investigation of the x ray excited EE from various metals and their respective oxides and sulfides led to amazing results: the glow curves of all studied metals were qualitatively alike, i.e., with respect to the position of the individual glow curve maxima (Fig. 5). The situation was similar in the case of metal oxides and sulfides (Fig. 6). In particular a maximum at 160° C was characteristic for oxides and oxidic surface layers, whereas a maximum at 140° C obviously is typical for sulfides. These and other facts, too, led to the present opinion that the orthodox luminescence type model of the EE cannot generally be used for non-metallic substances. Although this model certainly holds true for ionic crystals of the alkali halide type, the EE of the majority of substances seems to follow a different pattern, of which we do not yet know very much.

---

* This layer shall be formed due to different diffusivity for electric negative and positive point defects (vacancies).

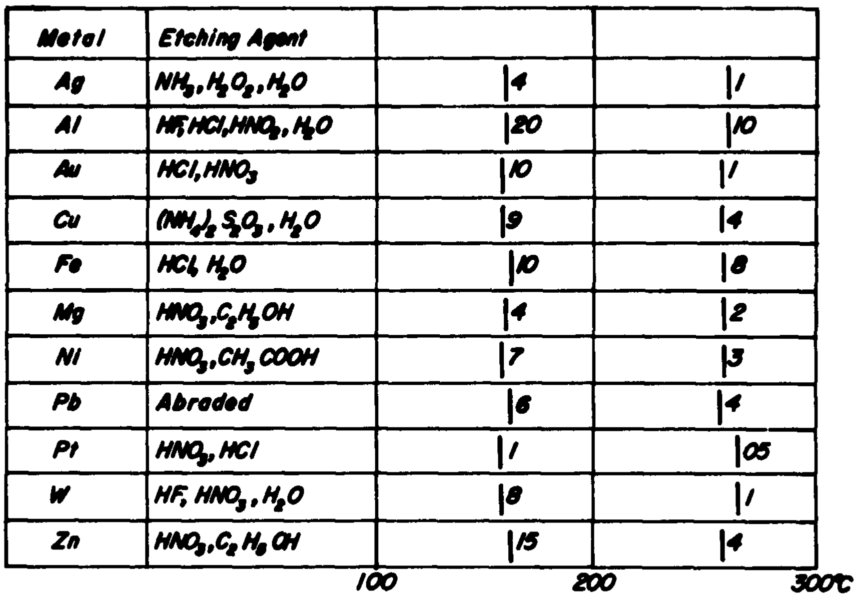

Fig. 5. Positions of the maxima in the exo-electron glow curves measured on x irradiated metals. The samples were cleaned by etching prior to the experiments (after H. Hieslmair and H. Mueller).

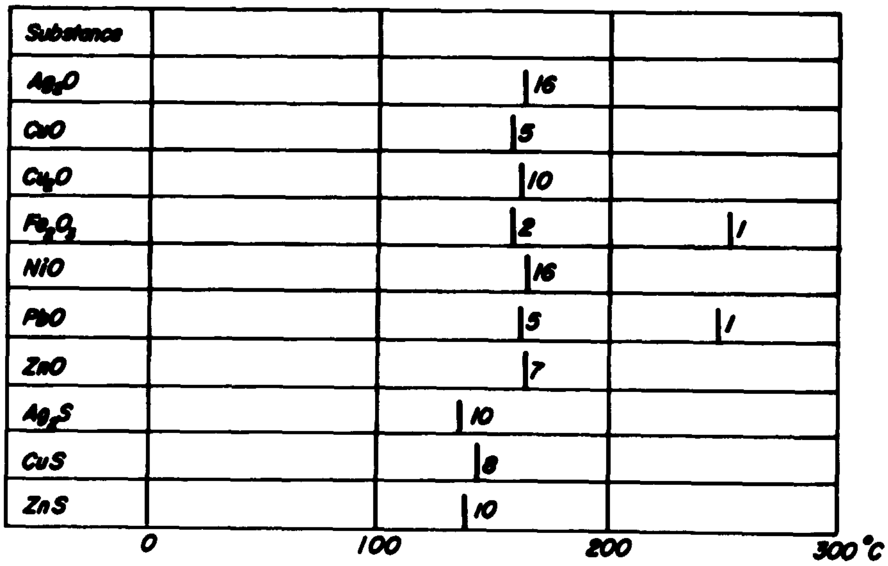

Fig. 6. Positions of the maxima in the glow curves of x irradiated oxides and sulfides (after H. Hieslmair and H. Mueller).

Apparently, the E are sometimes emitted due to a direct interaction of filled electron traps with other lattice defects without utilizing the conduction band. Emission by such a mechanism is, of course, restricted to the surface region only, which is perfectly consistent with recent experimental results. It seems, furthermore, that adsorption phenomena at the emitting surface not only influence strongly and characteristically the emission of E, but obviously are even responsible for the formation of emission centers in some cases. The aforementioned similarity of the electron glow curves of various metals, for instance, force this assumption.

The most obvious characteristic of an EE is the fact that the intensity of the emission current decreases as time progresses after termination of the excitation process: a constantly decreasing "after-current" of electrons is observable. Under certain conditions, however, electron after-currents have been detected which were not caused by a trap mechanism as discussed before, although this has been called EE too. It is advisable to distinguish correctly between these only phenomenologically similar electron emissions and the "true" EE which involves a trap mechanism, by calling them what they really are, namely, chemi-emission, enhanced photoemission, etc.

Important examples of such "pseudo" EE are (1) the electron emission observed on abraded metal surfaces or freshly evaporated metal films, (2) the electron emission observed during oxidation or reduction processes and (3) the electron emission observable upon irradiation of light on abraded or freshly evaporated metal samples.

Whereas the emissions under (1) and (2) are examples of chemi-emission, i.e., the emission of electrons associated with chemical reactions (here the oxidation of the clean metal surface or the reduction of the non-metallic surface layers), the electron emission under (3) is a photoemission caused by the sensitization of a clean metal surface by traces of oxygen. It shall be emphasized that the latter phenomenon is not a case of light-stimulated EE: the formation of an oxide film on such a clean metal surface gradually annihilates the sites of extremely low work function originally created at the surface by adsorption. This results in a decrease of the emissivity for photoelectrons as time progresses and, thus, the pattern of an after-current is obtained. In the case of chemi-emission (oxidation, reduction), the course of the reaction is simply reflected by the electron emission.

Still problematic is the interpretation of the EE observable during certain phase transitions. Figure 7 shows the electron emission peak during the solidification of molten metal. Figures 8 and 9 illustrate how E measurements can be used under certain circumstances to establish a phase diagram. The mechanism of the electron emission during phase transitions is not yet clear. In the case of

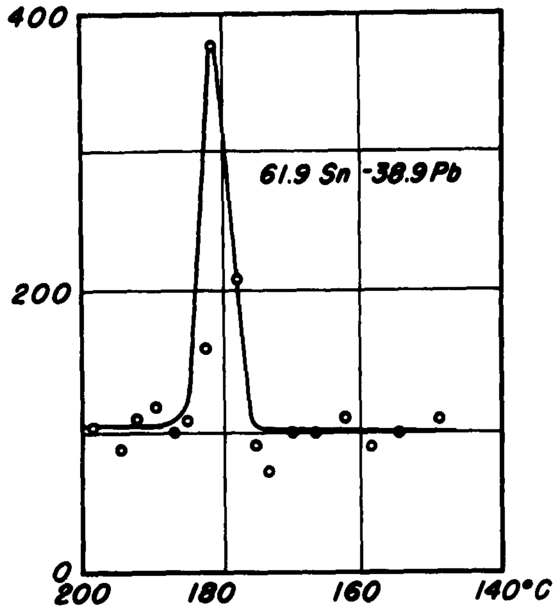

Fig. 7. Electron emission peak observed during the solidification of an eutectic Sn-Pb alloy (after F. Futschik et al).

liquid-solid transitions of metals it is probably the result of the formation and eventual deformation of thin non-metallic surface layers. Further studies will have to provide a satisfactory answer.

Summarizing, one can say that our understanding of exo-electron phenomena and similar after-current effects is gradually improving, although we are far from standing on firm theoretical ground. It becomes more and more evident that these after-currents are extremely structure dependent. They reflect sensitively the physical conditions prevailing on the emitting surface although only too often the interpretation of the emission is complicated. The information one gets stems from a surface region which is, according to the experiments, certainly not thicker than 1000 Å. More recent results indicate, however, that the emission process obviously takes place in a much thinner region or even only within the range of surface adsorption.

Besides the basic scientific interest in studying E processes, this phenomenon can be used as a tool for surface investigations. The advantage of the E method lies in the fact that the energy action with the probe is small and, hence, one may expect that the surface conditions under study are not going to be changed by the measurement itself. On the other hand, the E technique is not yet a self-supporting method of investigation. It has to be combined, for example, with measurements of luminescence, electrical conductivity, diffraction techniques, etc. But then, valuable new information can be gained despite the present lack of a full theoretical understanding of the phenomenon.

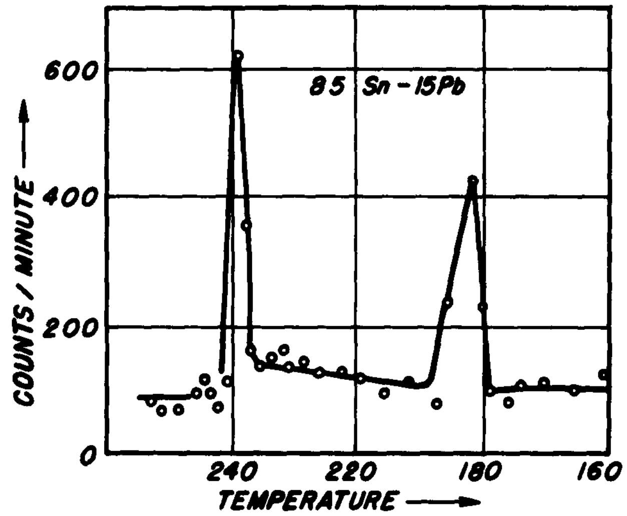

Fig. 8. Electron emission observed while passing the liquidus and eutectic temperatures of a Sn-Pb alloy (after F. Futschik et al).

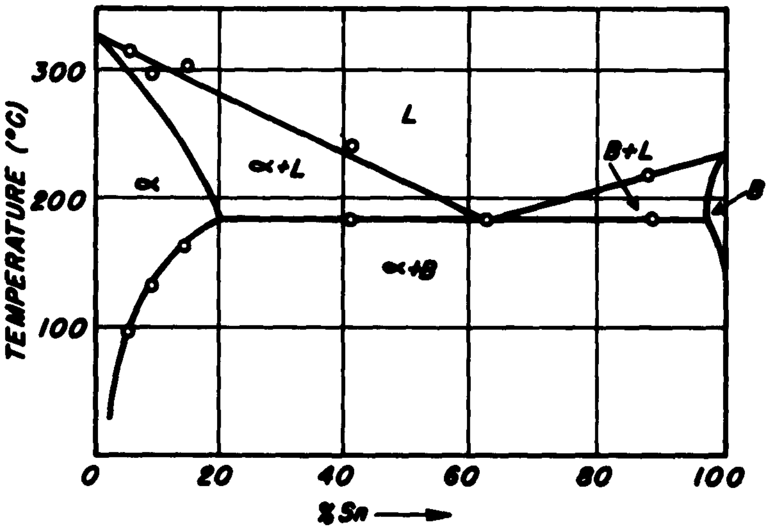

Fig. 9. Phase diagram of the binary system Sn-Pb. The dots represent the temperatures at which electron emission maxima were observed while cooling samples of this particular composition (after F. Futschik et al).

IRRADIATION PRODUCED PARAMAGNETIC DEFECT CENTERS IN SINGLE CRYSTAL POTASSIUM AZIDE

by

D. Mergerian and S. A. Marshall
Illinois Institute of Technology and Physics Division
Armour Research Foundation
Chicago, Illinois

A magnetic resonance adsorption centered about $g = 2$ and showing no evidence of fine structure is reported in x-irradiated single crystals of potassium azide. Six main absorption lines, which are clearly resolved, are studied in detail and are shown to be a composition of two distinct spectra, each consisting of three nuclear hyperfine components. One of these two sets of lines exhibits an anisotropic hyperfine splitting which varies between 38 and 3 oersteds, while the other set is likewise anisotropic and ranges between 62 oersteds and 31 oersteds. The former set of lines is attributed to NO molecules trapped at azide ion vacancies while the latter set is attributed to NO_2 molecules trapped at potassium ion vacancies. These molecular species are formed during the irradiation process from nitrate impurities contained in the lattice. The latter set of lines further exhibits a partially resolved seven line structure which is interpreted to be the result of interaction between the unpaired electron and next to nearest neighbor potassium ions. The saturation behavior of these spectra is studied and an attempt is made to explain the partially inhomogeneous saturation of the latter set of lines on the basis of a broadening mechanism based on the partially resolved seven line structure.

STUDIES OF PREPARATION AND PROPERTIES OF ALKALI AZIDES AND EFFECTS OF THIS ACTIVITY ON THERMODYNAMIC AND THERMOCHEMICAL DATA

by

K. Torkar and H. Krischner
Technische Hochschule Graz.
Graz, Austria

The studies being carried on under our contract are mainly concerned with the preparation and examination of azides, in particular of Na azide, in active form. In this case, "activity" can be defined as the state of a solid due to which it will take part in chemical reactions in a more active way than it would in its inactive state. This increased reactivity is caused by a higher energy content, which may be due to lattice disorders, enclosed impurities, or smaller size of particles. Although "active" solids play a very important part in many technological processes - just think of "fluidized bed" reactions, ceramic industry, powder metallurgy, or catalytic reactions - the theoretical aspect of activity has not been paid sufficient attention until now.

Active substances show other specific properties than inactive ones. They may, therefore, take part in reactions in an entirely different way. This also very often accounts for the insufficient correspondence between the results of experiments and those of calculations based on tabulated values. In order to be able to apply calculations to actually occurring reactions it is necessary to indicate as precisely as possible all those values in which the active substance differs from the inactive state as characterized by tabulated data. This aim can only be achieved by satisfactory explanation of the causes of "activity".

One of the reasons of the energy surplus is to be found in disorders of the lattice structure. Deviations from the ideal crystal structure may be due to lattice distortions, dislocations and vacancies. Classification of these irregularities depends on the viewpoint one is going to adopt. According to Huttig, for instance, lattice disorders can be classified as reversible or irreversible. We are using a classification enabling us to detect such deviations from the ideal crystal by means of X-ray diffraction techniques, which renders it possible to make quantitative statements.

Changes in the lattice structure can be due to internal stresses of first order. Within macroscopic ranges, the extent of lattice distortions is constant. Over a larger area, atoms have been removed from their normal position. Internal stresses of first order thus result in a displacement of diffraction patterns, but without broadening them. This displacement also causes a uniform change in the position of interferences, accompanied by deviations from the lattice constant. This type of lattice disorders may, for instance, be caused by mechanical stress.

With internal stresses of second order, lattice distortions are constant within one particle; they will, however, differ from one particle to another one. This causes a broadening of interferences which is not dependent on the angle of diffraction. Such lattice distortions have been observed, for example, where differences in concentration of solid solutions occurred.

If deviations from the ideal crystal are due to internal stresses of third order, that is due to short-range lattice disorders within the particles themselves, broadening of interferences has been proved to depend on the angle of diffraction. The broadening of reflections in such cases is proportional to the tangents of the angle of diffraction and can be given as the percentage mean change $\frac{\partial a}{a}$ of the lattice constant.

Another reason for the broadening of interferences is the small size of primary particles. Based on this assumption, it is possible to determine the average size of primary particles of crystalline substances down to approximately 20 Å. This broadening occurs proportionally to the reciprocal cosine of the angle of diffraction. Thus it can be distinguished in most cases from internal stresses of third order.

In active substances there may, however, also exist structural disorders which may condition other disturbances similar to quenched in heat vibrations. Since this results in a decreased intensity of the interferences, these structural disorders can be expressed quantitatively.

Vacancies can also be proved by diffraction methods, as they produce a scatter radiation, which can be detected by background analyses under strictly comparable recording conditions.

All these investigations are rendered difficult by the fact that lattice disorders will occur much more frequently on the surface than in the interior of a crystal. But even in this case statements concerning the extent of the zone of disorder - the "Oberflaechenraum", as we call it - can be made by determination of surface energies.

The aforementioned causes of the activity are also responsible for the different reaction behavior of active substances. From the qualitative viewpoint, based on the experience gained in industry and laboratory research, we can say that active preparations will show an earlier, quicker and more vehement reaction than inactive substances; in many cases the reaction will even take a different direction.

It is the aim of our work in this field to make quantitative predictions concerning the changing reaction behavior of active substances on account of differences of their properties. For all these questions, the energy conditions of the preparations are of paramount importance.

Due to lattice disorders, active substances have a higher content of enthalpy $(H_T^* - H_T)$. It is comparatively easy to determine this surplus of total enthalpy, for instance by determining heats of solution or by DTA measurements. For further calculations, however, this total enthalpy must be divided into free and latent energy:

$$G_T = H_T - T.S_T \qquad (1)$$

But since S_T is difficult to determine by direct methods, this equation is very often, though not quite correctly, expressed in the following way:

$$G_T = H_T - T.\int_0^T \frac{C_p}{T} .dT \qquad (2)$$

or, taking into account the differences between active and inactive states:

$$(G_T^* - G_T) = (H_T^* - H_T) - T.\int_0^T \frac{C_p^* - C_p}{T} .dT \qquad (3)$$

I am not going to discuss here in detail all these calculations, which base on well-known methods. I am rather going to concentrate on one point which, although of great importance, is normally not given sufficient consideration.

Theoretical considerations and practical measurements show that the molar heat C_p^* of the active state is greater than C_p of the inactive substance. But in most cases, the measured difference is found to be so insignificant that many authors assume the difference of total enthalpies being identical with the difference of free enthalpy:

$$(G_T^* - G_T) \sim (H_T^* - H_T) \qquad (4)$$

This assumption, however, is only permissible, if in the expression for the temperature dependency of the entropy the value S_0, that is the zero point entropy, will be equal for zero:

$$S_T = S_0 + \int_0^T \frac{C_p}{T} . dT \qquad (5)$$

Considering inactive substances, this assumption generally holds true. This is, however, not the case for an active preparation the lattice disorders of which will even subsist at 0° K. Consequently, an active substance will have a zero point entropy S_0^* different from zero, since it does not reach the ideal lattice-order at zero absolute. A clue, with respect to the possible amount of zero point entropy of active substances is obtained from the following consideration: The more lattice disorders a substance is showing and the higher its activity will be, the closer will it come to a state of general disorder. Such a state of disorder exists to a large extent in amorphous substances; it is ideally present in the amorphous state of melting. The difference between the two entropies of the solid and liquid states, the melting entropy, will therefore represent the maximum of possible disorder of a solid. The zero point entropy of active solid substances will thus be found between zero and the melting entropy; it will normally amount to a certain percentage of the melting entropy. Measurements have given values corresponding to about 30 percent of the melting entropy. If we now define activity as the difference in free enthalpy between the active and inactive states of a substance, giving it the symbol A_T^*, equation (3) should be written, more correctly, in the following form:

$$(G_T^* - G_T) = A_T^* = (H_T^* - H_T) - T.S_0^* - T.\int_0^T \frac{C_p^* - C_p}{T} . dT \qquad (6)$$

With the aid of this equation we can give a quantitative description of the reactions of solids. Since ΔG is not equal to ΔH, direct conclusions, for example from the heats of solution to the affinity of a reaction, are not possible without considering the value of S_0^*.

The difference in total enthalpy, $H_T^* - H_T$, shows how much more vehemently a reaction will take place in the case of an active substance. The difference in free enthalpy, $G_T^* - G_T$, on the other hand, indicates how much earlier a reaction will occur, because $G_T^* = -RT \ln K_p$, thus being related to the equilibrium constant.

In order to determine how much faster a reaction will take place, we can also use kinetic methods:

$$k = A \cdot e^{-\frac{\Delta G\ akt.}{RT}} \qquad (7)$$

The free reaction enthalpy of activation is closely related to activity. This enables us, therefore, to combine kinetic measurements with thermodynamic calculations.

After this short review of causes and effects of activity I should like to give you a survey of the methods we are using or intend to use in preparing and examining active sodium azides.

In order to obtain active NaN_3, we first introduced saturated solutions of this azide into other liquids in which it is insoluble or only slightly soluble. By varying the conditions of precipitation we obtained preparations of different degrees of activity. Size of the particles of these preparations was between 20 and 1 μ, depending on the conditions of precipitation. In order to obtain finer particles of higher activity, we constructed a special atomizing apparatus. In this atomizer, an alcoholic solution of Na azide is sprayed by a nozzle in a nitrogen atmosphere. The evaporation effect is further increased by low pressure in the atomizing chamber. By careful selection of the most suitable test conditions we hope to obtain preparations of high activity.

For the determination of total enthalpies, that is of H_T values, we at first used for measuring heats of solution a calorimeter with a thermopile. With the aid of this apparatus, the heat of solution of NaN_3 (a product of the Merck firm) was found to be 3.170 ± 40 calories/mol. This value is consistent with those given in the literature.

Heats of solution of the precipitated preparations were, however, mostly within the margins of error of our apparatus. We therefore built a new micro-differential calorimeter, which, though working with smaller quantities, permits more exact measurements. Temperature is measured by means of thermistors; changes in temperature are registered graphically by a compensation recorder. All values can be determined either by absolute measurements or by the differential method.

Since our DTA apparatus proved unsuitable for the examination of NaN_3, we designed a new apparatus. The new plan will consist of a DTA set working in a nitrogen atmosphere, suspended from the lever of an analytical balance. In this way thermogravimetric measurements can be carried out simultaneously with the differential thermal analysis.

As already mentioned, it is very important for the characterization of an active substance to know the difference in specific heats which permit conclusions as to its zero point entropy. We built therefore a drop calorimeter which can also be used at low temperatures. The sample to be examined is heated or cooled to the desired temperature in a Dewar vessel. For the measurement, the sample is then dropped into the metal block below. The change in temperature of the metal block is measured by comparison with an analogous metal block of constant temperature. Calibration tests carried out so far have yielded satisfactory results.

For surface measurements we have a BET apparatus at our disposal. Since this has been designed for large surfaces only, whereas in measurements of sodium azide we usually deal with small surfaces, we have also adapted the apparatus to this condition.

For investigation of kinetic processes, we set up an apparatus to decompose NaN_3 under strictly defined conditions. The reaction can be followed by reading the increase in pressure. It has been observed that azide samples of different preparation showed different patterns of pressure increase. By isothermal heating of NaN_3 (Merck) we were able to determine the energy of activation of thermal decomposition, which was found to be 34,8 kcal ± 3% per mole.

Furthermore, tests are being carried out in order to study the activity by means of the reaction of NaN_3 with hydrogen. This requires, however, a more detailed investigation of the mechanism of such reactions.

Our new X-ray apparatus enables us to make Guinier patterns with the big double chamber according to Professor Jagodzinsky. This photographic method seems especially suitable for our studies, not only on account of its high resolving power but also because of the fact that the preparation can be moved while being partially exposed to the radiation. This is a great advantage, as it prevents extensive irradiation of the sample.

In addition, we can also carry out diffraction measurements by means of a Geiger-counter tube goniometer. In order to be able to determine the width of lines without a calibration substance, we have calculated correction tables for this apparatus. Using these tables, we can easily determine the size of particles and detect lattice distortions.

In the course of our studies of sodium azide we have found that our active preparations are subject to considerable changes when exposed to atmospheric air. For example, by short friction of a preparation in air the temperature of decomposition was considerably reduced. We are therefore building a device which will permit us to handle our preparations in an inert atmosphere (nitrogen) so that they will not be exposed to atmospheric oxygen. In this way we hope to create strictly defined conditions for our experiments.

It was only half a year ago that we began our studies in the field of azides. Until now, we have been mainly concerned with perfecting our equipment. Our next task will be the preparation of Na-azide of very high purity using ion exchangers. The azides thus obtained will then be "activated" either by suitable methods of preparation or by introduction of impurity ions, so that it will be possible to study the influence of these parameters in full details.

INFRARED SPECTRA OF THE AZIDE ION IN ALKALI HALIDE LATTICES*+

by

James I. Bryant++ and George C. Turrell
Department of Chemistry, Howard University
Washington 1, D. C.

I. INTRODUCTION

If a polyatomic ion is introduced as a substitutional impurity into a crystal lattice, the vibrational frequencies of the ion are dependent upon the potential function which governs its interactions with the lattice. Thus if a satisfactory model of impurity ion-lattice interaction can be developed, a quantitative method of determining the interionic potential function is provided by measuring the vibrational frequencies of a given impurity ion as functions of the nature of the lattice and as functions of temperature. Hence the introduction of an impurity ion as a "probe" into a crystal lattice offers a powerful method of investigating interionic forces.

Small polyatomic ions have been incorporated into the lattices of some fifteen to twenty alkali halides. The alkali halides are particularly convenient matrices because of their transparency in much of the infrared region of the spectrum. In 1956 Ketelaar, Haas, and van der Elsken[1] compared the infrared absorption spectra of different bifluorides in alkali-halide disks with spectra of the corresponding Nujol emulsions. Evidence of lattice intermixing (solid solution) in the pressed disks was reported. Somewhat later van der Elsken[2] considered in some detail the roles of induction, short-range, and electrostatic forces in effecting the frequency shifts of the asymmetric stretching mode of the bifluoride ion in alkali-halide lattices. From these studies of the bifluoride ion,

---

* Based on a Dissertation submitted by James I. Bryant to the Graduate School, Howard University, in partial fulfillment of the requirements for the Ph.D. degree, June, 1961. Presented in part at the Annual Symposium on Molecular Structure and Spectroscopy, The Ohio State University, June, 1961.

+ This work received the financial support of the Basic Research Group, U. S. Army Engineer Research and Development Laboratories, Fort Belvoir, Virginia, under Contract DA-44-009-ENG-4532, Project No. 8F07-11-001-02.

++ Present address: Basic Research Group, U. S. Army Engineer Research and Development Laboratories, Fort Belvoir, Virginia.

it was concluded that the effects of matrix polarization (dipole-induced dipole forces) must be seriously considered, while the short-range repulsive forces are of little importance.[3]

In the recent work of Maki and Decius[4] the cyanate ion has been extensively studied as a substitutional impurity in KI, KBr, KCl and NaCl lattices. A detailed vibrational energy expression was deduced which included most of the anharmonicity constants for the cyanate ion. Consideration of the interionic forces suggested that, although the induction energy exerts a measurable influence on the frequencies, the repulsive (short-range) interaction is predominant.

The above studies, and others,[5-7] have prompted further consideration of spectra of impurity ions in alkali-halide matrices, especially with respect to the relative magnitudes of the various interaction forces between the substituted ion and the surrounding matrix.

In this paper a model of a linear ion substituted in a cubic host lattice is developed. An experimental test is provided for the proposed model by measuring the vibrational frequencies of the azide ion, N_3^-, in various alkali-halide lattices and over a suitable temperature range. The contributions of inductive, short-range and Coulombic forces to the potential energy expression for vibrations of this ion in KI, KBr and KCl matrices are calculated.

II. SYMMETRY CONSIDERATIONS

A. Symmetry of the Azide Ion

Several x-ray diffraction studies[8-10] have indicated that the azide ion is linear and symmetric with a N--N distance of 1.15 A. However, Bassiere[11] has suggested that the azide ion in sodium azide is asymmetric with bond lengths of 1.10 and 1.26 A. The latter conclusion is in direct conflict with the spectroscopic evidence.[12,13] In the present work the symmetric structure will be assumed to be correct.

A triatomic molecule of point group $\mathcal{D}_{\infty h}$ has three fundamental vibrational frequencies, a symmetric stretching mode ν_1 ($a_{1g} \equiv \Sigma_g^+$), a doubly degenerate bending mode ν_2 ($e_u \equiv \Pi_u$) and an asymmetric stretching mode ν_3 ($a_{2u} \equiv \Sigma_u^+$). The symmetric stretching fundamental is of course infrared inactive.

The harmonic frequencies corresponding to the two infrared-active fundamentals are given by[14]

$$4\pi^2\omega_2^2 = 6\,k_2^0/m \tag{1}$$

and

$$\pi^2\omega_3^2 = 3\ k_3^0/m \qquad (2)$$

where m is the mass of a nitrogen atom, $k_2^0 = f_{22}$ and $k_3^0 = f_{33}-f_{13}$, with the f_{ij} the elements of the potential energy matrix.

B. Symmetry of the Azide Ion in a Cubic Site

When a linear and symmetric ion is introduced as a substitutional impurity into a cubic lattice, the site symmetry ($\mathcal{O}_h$) will be reduced to an extent which is dependent on the orientation of the impurity ion within the site. Possible orientations are shown in Table I with the resulting subgroups of $\mathcal{O}_h$, the symmetry species of the normal vibrations and the infrared or Raman activity. Table I also includes the symmetry species of the nonvanishing frequencies of rotational (librational) and translational motions of the ion.

Table I. Representations of $\mathcal{D}_{\infty h}$ in $\mathcal{O}_h$

Subgroup (orientation)	$\mathcal{D}_{\infty h}$ ("free")	$\mathcal{D}_{4h}$ (on C_4)	$\mathcal{D}_{3d}$ (on C_3)	$\mathcal{D}_{2h} \equiv \mathcal{V}_h$ (on C_2)	$\mathcal{C}_i$ (on no C)	Activity
ν_1	Σ_g^+	A_{1g}	A_{1g}	A_g	A_g	Raman
ν_3	Σ_u^+	A_{2u}	A_{2u}	B_{1u}	A_u	I.R.
ν_2	Π_u	E_u	E_u	B_{2u} B_{3u}	A_u A_u	I.R.
(R_x,R_y)	Π_g	E_g	E_g	B_{2g} B_{3g}	A_g A_g	Raman
T_z	Σ_u^+	A_{2u}	A_{2u}	B_{1u}	A_u	I.R.
(T_x,T_y)	Π_u	E_u	E_u	B_{2u} B_{3u}	A_u A_u	I.R.

It can be seen from Table I that the perpendicular vibrations of the azide ion should exhibit site-splitting if the orientation is either along the twofold axis or a more general one. The apparent absence of splitting of the perpendicular vibrations of the cyanate ion, plus the observed temperature dependence of the vibrational fundamentals (increasing with decreasing temperature) strongly suggest that it is oriented along the threefold axis of the cubic cell.[4] If the same orientation can be assumed for the azide ion in an alkali-halide matrix, the resulting subgroup is $\mathcal{D}_{3d}$ and the representations are as given in Table I. A diagram of the azide ion in such a matrix is shown in Fig. 1.

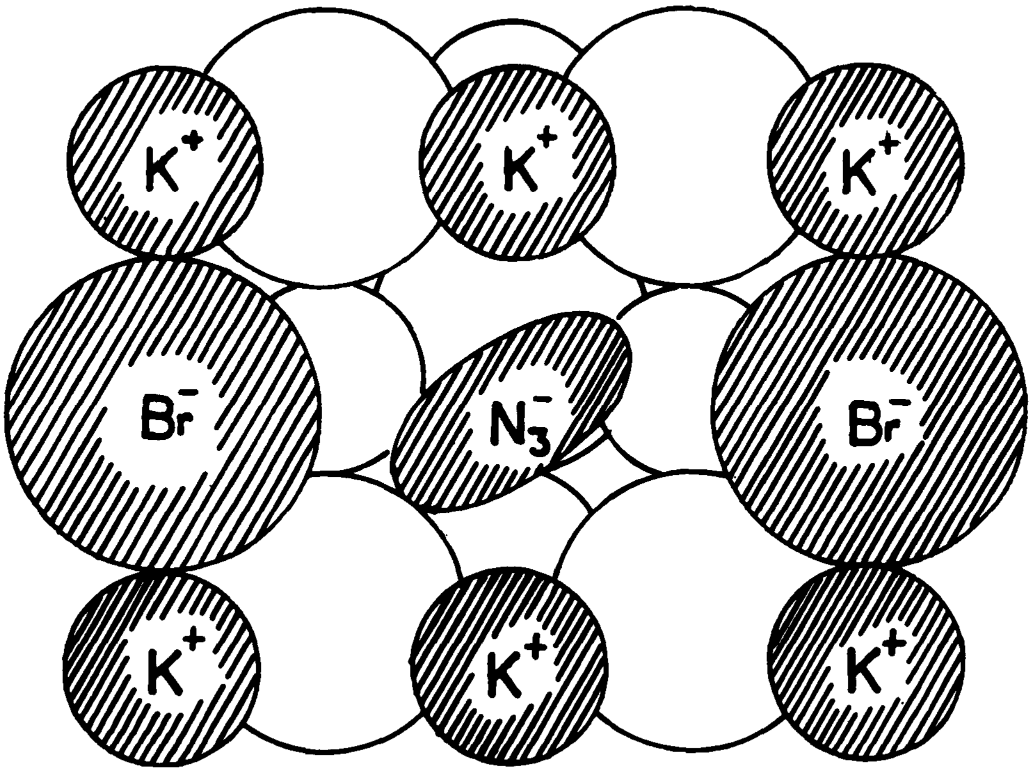

Figure 1. Azide ion in a cubic lattice (C_3 orientation).

III. EXPERIMENTAL PROCEDURE

A. Sample Preparation

The first efforts in sample preparation were directed toward growing crystals from aqueous solution. Due to the decomposition of N_3^- at temperatures far below the melting point of the alkali halides, samples could not be prepared by the more convenient method of growing crystals from the melt.

A rather detailed study was made of the effects of temperature, rate of evaporation, rate of stirring, size of the seed crystal, pH, and azide ion concentration on the size and quality of single crystals grown from saturated solutions of the various alkali halides. It was indicated at the outset, and was repeatedly confirmed in later studies, that a strong rejection of the azide ion by the alkali-halide lattice occurs. Hence the azide-to-lattice concentration ratio was invariably much smaller in the crystals than in the solution from which the crystals were grown. It was, therefore, impossible by this method to obtain samples which yielded strong spectra.

The following procedure furnished the most concentrated samples obtained by crystal growth from solution. Cleaved optical blanks of KI, KBr, KCl and NaCl approximately 20 mm X 10 mm X 2 mm were placed into saturated solutions of the respective alkali halide containing approximately 1% of the corresponding alkali azide. Upon slow evaporation growth took place on the faces of the cleaved blanks producing samples which could be conveniently handled and which were of sufficient size to intercept most of the radiation when the samples were placed in a conventional low-temperature cell.[15] By this method samples of azide-substituted KI and KBr single crystals were obtained. Samples of KCl and NaCl prepared by the same procedure yielded spectra which indicated that no substitution had taken place, i.e., the crystal growth which took place on the faces of the blanks consisted entirely of the respective alkali halide.

In view of the limitations of the samples prepared by the crystal-growth method, which yielded spectra with weak fundamentals and little or no observable fine structure, other methods for preparation of the desired solid solutions were sought. Recently several investigators[1,7,16] have reported preparation of samples in which small diatomic and triatomic anions were introduced into the lattices of alkali halides by various modifications of the pressed-disk technique. In the present work the following procedure was adopted for the preparation of pressed-disk samples.

A dilute solution containing 0.5 gram of the alkali azide and 20 grams of the corresponding alkali halide was quickly frozen with liquid nitrogen in a chamber of a freeze-drying cell. An adjacent chamber was then surrounded by a Dewar flask containing liquid nitrogen and the cell was evacuated. In about twenty-four hours the solvent sublimed into the latter chamber leaving a very finely divided and highly intermixed residue. Before pressing, the residue was heated in a vacuum oven to approximately 200° C. The disks, which were 1/2 inch in diameter, were pressed in an evacuable die by the application of approximately 12 tons for a period of 45 to 60 minutes. By this method, samples of the azide ion in KI, KBr, KCl and NaCl matrices were prepared.

The sodium and potassium azides used were technical grade salts and were purified by several recrystallizations. The alkali halides used were all analyzed reagent grade salts which received no further treatment.

B. Spectral Measurements

A Perkin-Elmer Model 21 infrared spectrometer equipped with a NaCl prism was used to obtain survey spectra of all samples over the region from 5000 cm^{-1} to 630 cm^{-1}. This instrument was also used for detailed investigations of frequency shifts of the bending fundamental with temperature and with changes of the host lattice. The region of the strong asymmetric stretching fundamental, ν_3, was investigated using a Perkin-Elmer Model 112 infrared spectrometer equipped with a lithium fluoride prism.

Samples were studied at room temperature and downward to approximately 120° K using the low-temperature cell with dry ice or liquid nitrogen as refrigerants. Temperatures of the samples were monitored by means of a chromel-alumel thermocouple attached to a supporting rocksalt window.

IV. RESULTS

The frequency dependencies of the fundamentals ν_3 and ν_2 of the azide ion on the nature of the matrix are shown in Figs. 2 and 3, respectively. Figure 4 shows the temperature dependence of ν_3 in KI, KBr, KCl and NaCl hosts, while the analogous results for the bending mode are presented in Fig. 5. Frequencies were measured with a precision approaching ± 0.1 cm^{-1} by expanding the normal abscissa of the spectrometer and measuring the midpoints of the bands using dividers and a scale. In fitting the curves more weight was given to the temperature equilibrium points (room temperature, dry ice-acetone temperature and liquid-nitrogen temperature) than to intermediate, nonstatic temperature points. Due to imperfect contact between the thermocouple and the effective absorbing region of the sample, the accuracy of the reported temperatures is estimated not to exceed ± 10° K.

It is felt that the above results, besides furnishing the desired frequency shift-temperature information, provide considerable evidence for the occurrence of lattice intermixing in pressed disks. Although the absence of splitting of the bending fundamental of the azide ion in pressed-disk samples is not proof of the occurrence of lattice intermixing, it does support such an assumption. The strongest evidence for solid solution in the pressed-disk samples is furnished by the agreement of frequencies of the strong asymmetric

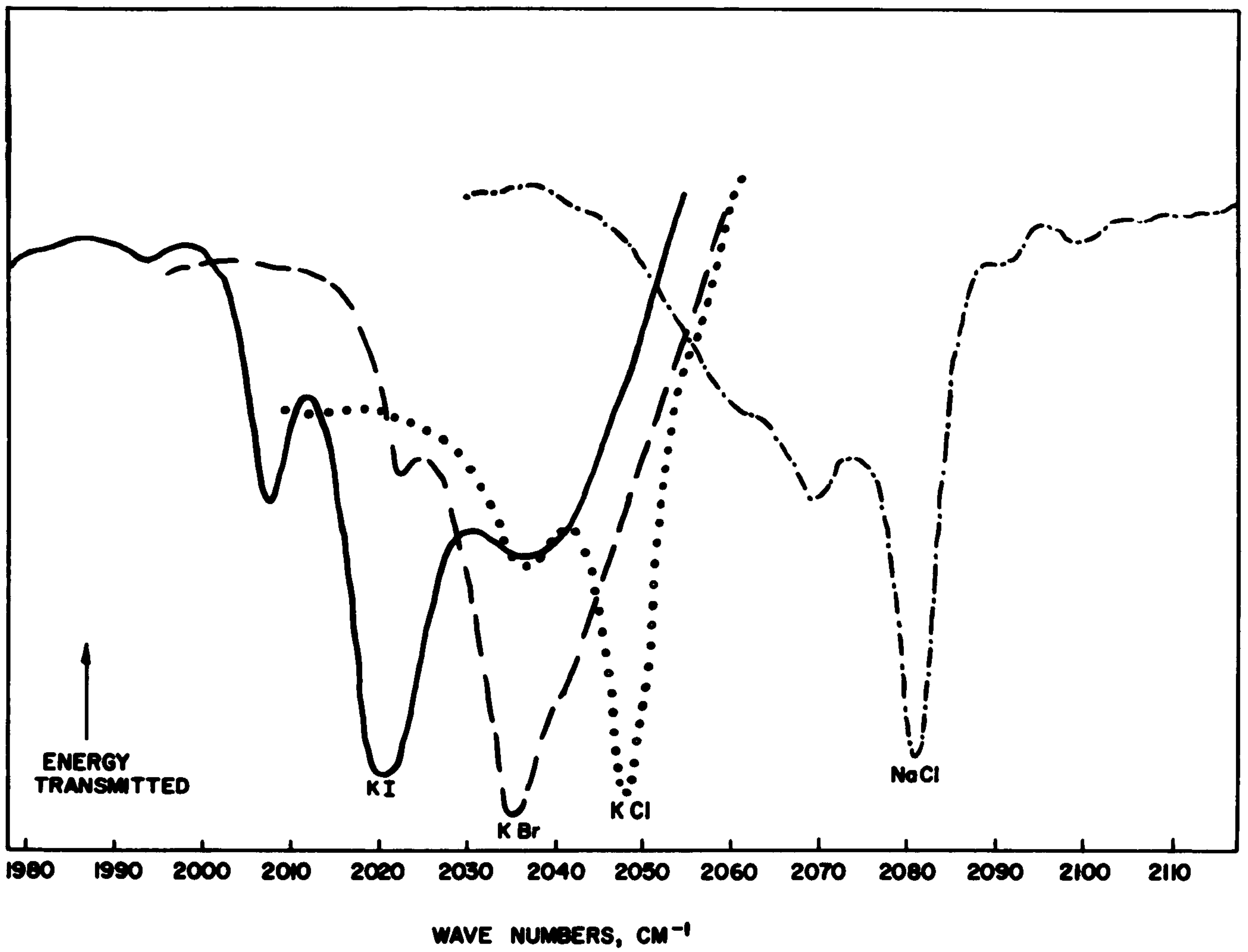

Figure 2. Asymmetric stretching fundamental, ν_3, of the azide ion in various lattices.

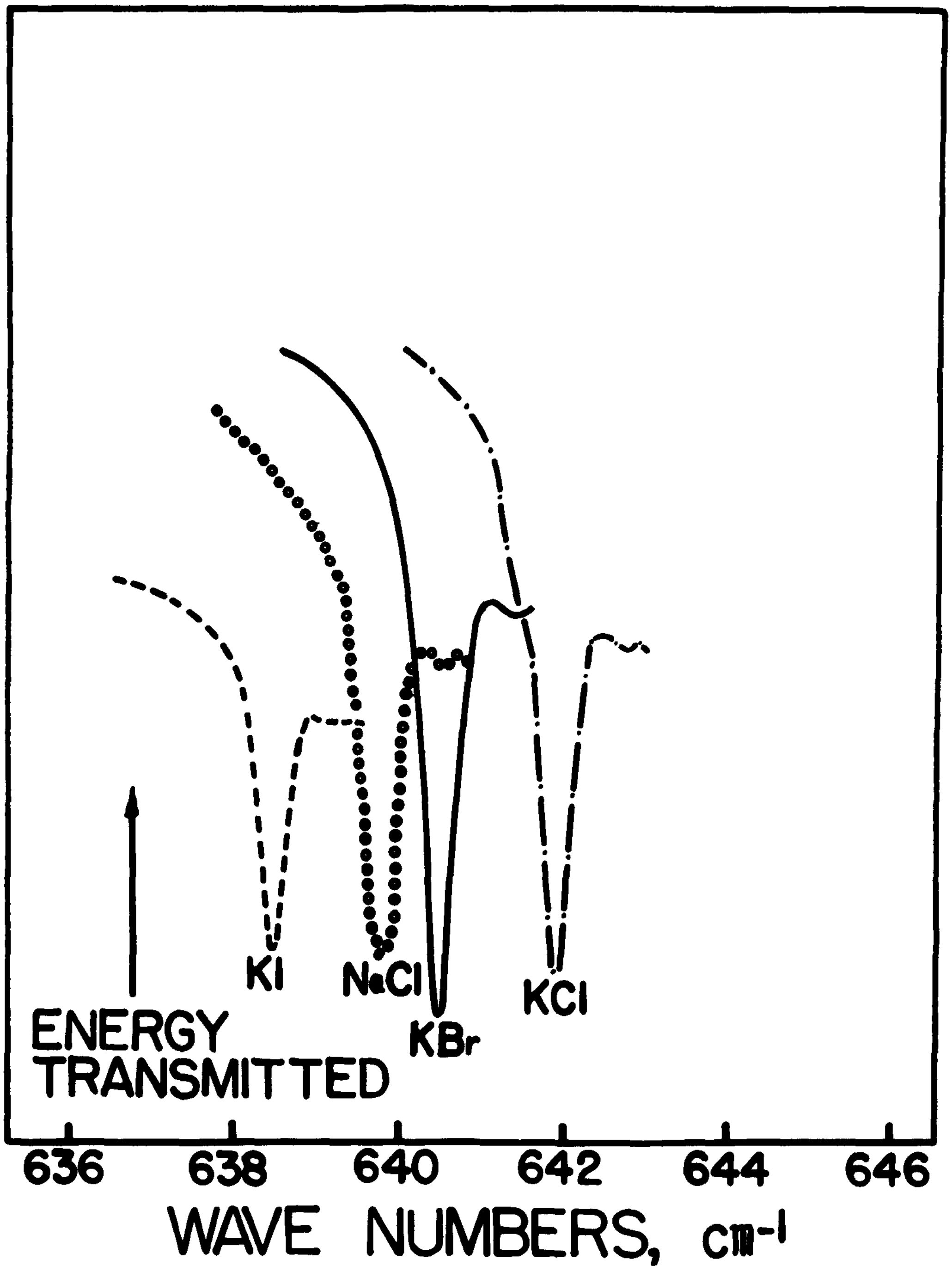

Figure 3. Bending fundamental, ν_2, of the azide ion in various lattices.

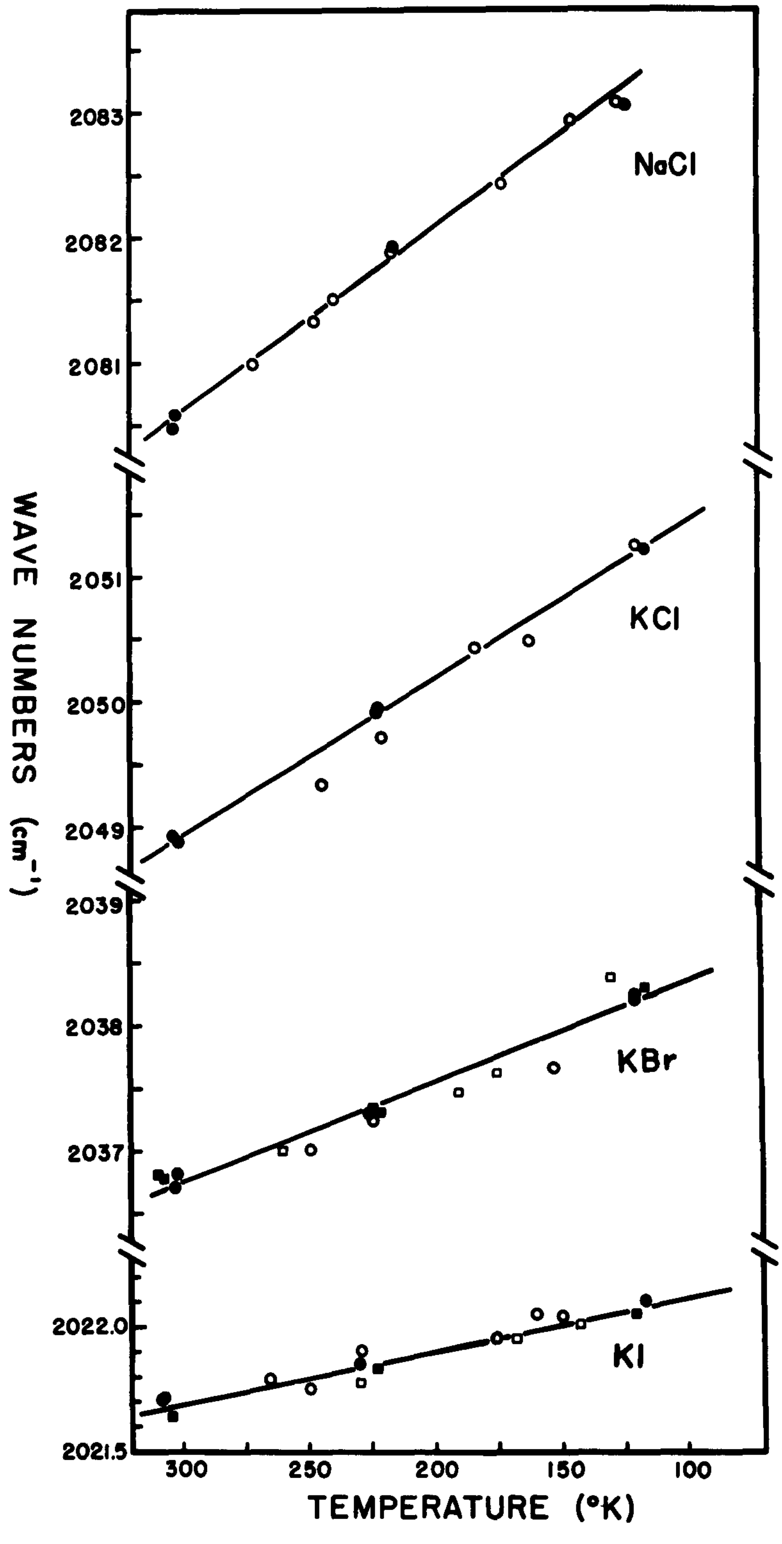

Figure 4. Temperature dependence of the asymmetric stretching frequency, ν_3, in various lattices. Note breaks in ordinate scale.

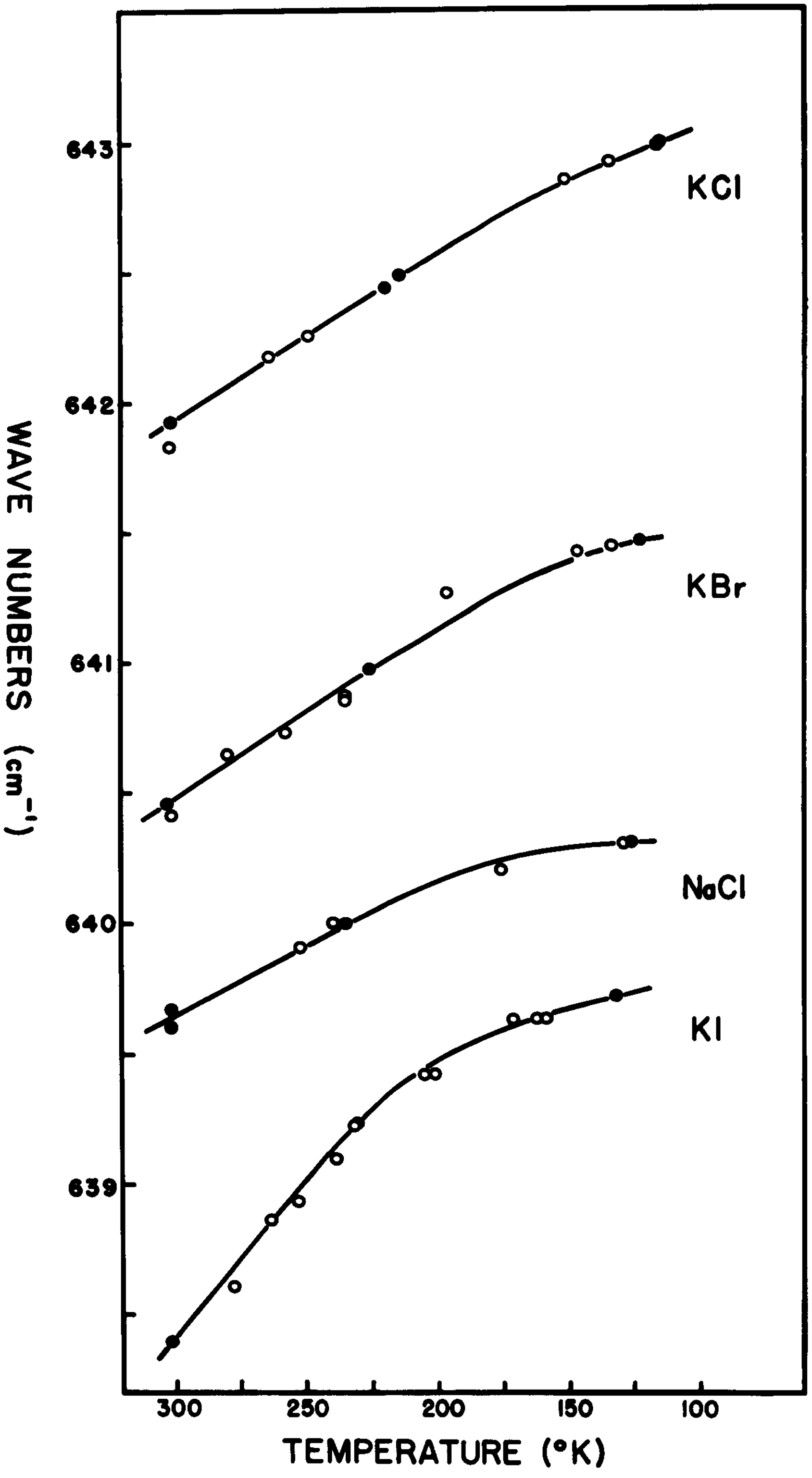

Figure 5. Temperature dependence of the bending frequency, ν_2, in various lattices.

stretching fundamental in pressed-disk samples with those observed in single crystals grown from aqueous solutions. This observation, plus the agreement of the shift of the frequency of this fundamental with temperature in samples prepared by the two methods, leads to the conclusion that virtually complete lattice intermixing can be obtained by careful application of the pressed-disk technique.

V. INTERIONIC FORCES

When the azide ion is substituted at a negative site in a NaCl-type cubic lattice, the potential function can be considered to be that of the "free" ion plus a perturbing potential function due to the surrounding cubic matrix. This perturbing potential function, V', has two distinct effects on the ion being considered, viz.,

(i) The second derivatives of the perturbing potential with respect to appropriate symmetry coordinates represent additional contributions to the effective force constants of the impurity ion.

(ii) The first derivatives of the perturbing potential represent forces which modify the equilibrium interatomic distances in the ion. Although in the harmonic approximation, the latter effect would not alter the frequencies, when cubic or higher terms are included in the intraionic potential function, the change in the interatomic distances will cause further modifications in the effective force constants for the impurity ion.

In order to carry out a quantitative evaluation of shifts in the vibrational frequencies of the ion, it is necessary to develop an explicit form for the perturbing potential V'. This is conveniently done by dividing the potential into an inductive term V_i, a Coulombic term V_c, and a short-range term V_s. The resultant, perturbing potential is then given by

$$V' = V_i + V_c + V_s.$$

A. Induction Potential

Bauer and Magat[17] have derived an expression for the shift in frequency to be expected on account of dipole-induced dipole forces between an oscillator and a polarizable solvent. Their relation was modified somewhat by Maki and Decius[4] in order to obtain an expression for the shift in the vibrational frequencies of a linear ion substituted into a NaCl-type cubic lattice. The resulting expression is

$$\Delta\nu_i/\nu_i^o = -(\partial\mu/\partial Q_i)_o^2 \left[8C_6\alpha^- + (64A_6 - 8C_6)\alpha^+\right] /\lambda_i^o a^6, \qquad (3)$$

where $\Delta\nu_i = \nu_i - \nu_i^o$ represents the frequency shift of the ith normal mode of a hypothetical "free" ion, $\lambda_i^o = 4\pi^2\nu_i^{o2}$, and $(\partial\mu/\partial Q_i)_o$ is the derivative of the dipole moment with respect to the ith normal coordinate at equilibrium. The constants $C_6 = 14.4539$ and $A_6 = 8.4019$ are the lattice sums calculated by Lennard-Jones and Ingham;[18] the unit cell dimension is represented by a, while α^+ and α^- are the polarizabilities of the cations and anions of the host, respectively. Thus it can be seen that the results depend on the quantities $(\partial\mu/\partial Q_i)_o$, which in principle can be evaluated from measurements of absolute intensities. In this approximation frequency shifts result from induction only through effect (i) above.

It should be pointed out that a more general treatment of induction forces would include the effect of quadrupole and higher moments of the azide ion. While it is customary to consider only the dipole moment in the first approximation, for ions such as azide, which have no permanent dipole moment, the molecular quadrupole may play a significant role.

B. Coulombic Potential

The electron distribution in the azide ion has been represented by Bonnemay and Daudel[19] by the superposition of a point charge and an extended quadrupole.

$$\begin{array}{ccccccccccc} N & — & N & — & N & \qquad & N & — & N & — & N \\ 0 & & -e & & 0 & \qquad & -0.83e & & 1.66e & & -0.83e \end{array}$$

If it can be assumed that for small displacements of the end atoms a constant charge $\epsilon = -0.83e$ moves with the nuclei, the Coulombic potential is given by $V_c = \epsilon\, e/R$ for the interaction of a given lattice ion of charge e with an effective charge ϵ located a distance R from the lattice ion. A lattice ion can be located by means of the usual set of indices h, k, ℓ, where the unit distance is taken to be a/2 and a is the unit cell dimension. Hence,

$$R(h,k,\ell) = a/2\Big[(h - \eta\sqrt{3}\sin\theta\cos\Phi)^2 + (k - \eta\sqrt{3}\sin\theta\sin\Phi)^2 + (\ell - \eta\sqrt{3}\cos\theta)^2\Big]^{\frac{1}{2}}, \quad (4)$$

where $\eta = 2r/a\sqrt{3}$ and r is the distance between an end atom and the center of the impurity site. The angles θ and Φ have their usual significance in spherical polar coordinates in which the z axis is taken to be collinear with a C_4 axis of the unit cell.

The total Coulombic potential acting on one end atom of the impurity is that given by

$$V_c = -\sum_{h,k,\ell}{}' \varepsilon\, e(-1)^{h-k-\ell}/R(h,k,\ell), \tag{5}$$

where $R(h,k,\ell)$ is obtained from Eq. (4) and the sign alternation has been included to account for the charges on the anions and cations of the lattice. The prime on the summation sign indicates that the term $h = k = \ell = 0$ (the impurity site) is omitted from the sum.

A completely analogous treatment is carried out for the central nitrogen atom, which is assumed to carry a constant net charge of $\delta = +0.66e$. In the case of the bending mode the central atom plays an important role. However, in the stretching mode it is sufficiently well-shielded so that its interaction with the lattice is negligible.

The Coulombic interactions considered above include only the direct effect of the electrostatic field of the host lattice on the charge distribution of the azide ion. A detailed treatment of the electrostatic interaction of the asymmetric stretching mode of a linear impurity ion with a lattice has been presented by van der Elsken,[2] who concluded that in addition to the interaction described above, one must consider lattice polarization of the end atoms of the impurity ion, which in turn interact with the effective charge on the central atom. This effect is found to result in changes in the effective force constant for ν_3 given by $(6\alpha_N \delta/\varepsilon \ell^4)\ (\partial V_c/\partial r)_o$, where the polarizability of a nitrogen atom is taken to be $\alpha_N \approx 1 \times 10^{-24}$ cm^3. For the bending mode this effect vanishes in the limit of small vibrations.

The working equations for calculating the dependence of ν_2 and ν_3 on the Coulombic potential are developed in the Appendix.

C. Short-Range Potential

The short-range repulsive forces will be represented here by an exponential function of the distance between each atom of the impurity ion and a given ion of the lattice. The potential is then of the form

$$V_s = \zeta \exp(-R/\rho). \tag{6}$$

The constants ζ and ρ are interpreted physically as a relative electronic charge density and an effective charge radius, respectively. These constants have been determined for a number of systems including rare gases[20] and pure alkali-halide crystals.[21]

Applying Eq. (6) to each ion of the lattice and summing yields the expression

$$V_s = \sum_{h,k,\ell}' \zeta^* \exp\left[-R(h,k,\ell)/\rho^*\right] , \tag{7}$$

where * = + if h + k + ℓ is odd and * = - if h + k + ℓ is even. The superscripts on ζ and ρ then indicate whether a given interaction is with a cation or an anion of the host lattice.

As before, the central atom does not contribute significantly to the potential for the stretching mode. Furthermore, since the repulsive potential falls off much more rapidly than the Coulombic potential, it is not necessary to carry its summation beyond the seven lattice ions which occupy the same octant of the unit cell as the impurity atom being considered. The equations which are presented in the Appendix permit calculation of the effect of short-range forces on the frequencies ν_2 and ν_3.

D. Frequency Shifts

With an explicit expression available for the perturbing potential, it becomes possible to evaluate the frequency shifts. In terms of the usual symmetry coordinates the total potential energy expression is given by

$$V = \tfrac{1}{2}(f_{11} + f_{13})S_1^2 + 9f_{22}(S_{2a}^2 + S_{2b}^2)/2\ell^2 + \tfrac{1}{2}(f_{33} - f_{13})S_3^2$$
$$+ \alpha S_1^3 + \beta S_1(S_{2a}^2 + S_{2b}^2) + \gamma S_1 S_3^2 + V', \tag{8}$$

where the three non-vanishing cubic intraionic potential parameters have been included in order to allow an estimate to be made of the magnitude of effect (ii) above.

The cubic potential constants α, β, and γ, which are defined in Eq. (8) in terms of symmetry coordinates, are closely related to the analogous constants a, b, and c defined by Dennison.[22] A comparison of the potential functions yields the relations

$$\alpha = 8\pi^3 a\omega_1 mc\,(\omega_1 m/h)^{\frac{1}{2}},$$
$$\beta = 12\pi^3 b\omega_2 mc\,(\omega_1 m/h)^{\frac{1}{2}}, \tag{9}$$
and
$$\gamma = (8/3)\pi^3 c\omega_3 mc\,(\omega_1 m/h)^{\frac{1}{2}}.$$

If the anharmonicities are small, the change in equilibrium position found by setting $\partial V/\partial S_1 = 0$ are given by

$$S_1^o \approx -\sqrt{2}(\partial V'/\partial r)_o\ (f_{11} + f_{13})$$

and (10)

$$S_3^o \approx 0.$$

Effective force constants for ν_1, ν_2, and ν_3 are found to be

$$k_1 = (\partial^2 V/\partial S_1^2)_o = f_{11} + f_{13} + 6\alpha S_1^o + (\partial^2 V'/\partial r^2)_o, \tag{11}$$

$$k_2 = (\partial^2 V/\partial S_2^2)_o \ell^2/9 = f_{22} + 2\ell^2\ \beta S_1^o/9 + (\partial^2 V'/\partial \theta^2)_o/18$$

$$+ (\partial^2 V'/\partial y^2)_o \ell^2/9, \tag{12}$$

and

$$k_3 = (\partial^2 V/\partial S_3^2)_o = f_{33} - f_{13} + 2\gamma S_1^o + (\partial^2 V'/\partial r^2)_o$$

$$+ (6\delta\alpha_N/\epsilon\ell^4)(\partial V_c/\partial r)_o. \tag{13}$$

Upon substituting Eq. (10) one obtains the following expressions for the changes in the effective force constants for the two infrared-active fundamentals of N_3^-.

$$\Delta k_2 = -2\sqrt{2}\ell^2\ \beta(\partial V'/\partial r)_o/9(f_{11} + f_{13}) + (\partial^2 V'/\partial \theta^2)_o/18$$

$$+ (\partial^2 V'/\partial y^2)_o \ell^2/9 \tag{14}$$

and

$$\Delta k_3 = -2\sqrt{2}\ \gamma(\partial V'/\partial r)_o/(f_{11} + f_{13}) + (\partial^2 V'/\partial r^2)_o/9$$

$$+ (6\delta\alpha_N/\epsilon\ell^4)(\partial V_c/\partial r)_o. \tag{15}$$

Finally, making use of the equation

$$\Delta k_i/2k_i^o = \Delta\omega_i/\omega_i^o \approx \Delta\nu_i/\nu_i^o \tag{16}$$

the small observed frequency shifts can be related to the various contributions to the perturbing potential. Expressions for the derivatives appearing in Eqs. (14) and (15) are given in the Appendix.

VI. CALCULATIONS AND DISCUSSION

Using the relations developed in the previous section calculations have been made of the frequencies of the two infrared-active fundamentals of the azide ion in KCl, KBr, and KI matrices. Frequencies were calculated for the above samples at temperatures of 300° K and 120° K, which represent the limits of the experimental temperature range covered.

In carrying out the frequency calculations it was found to be more convenient first to determine the frequency shifts due to dipole-induced dipole forces by means of Eq. (3). As suggested by rough relative intensity measurements carried out on similar disks containing azide and cyanate ions, the values $(\partial\mu/\partial Q_i)_0^2$ were taken to be twice the corresponding values for cyanate reported by Seshadri and Decius.[23] The resulting frequency shifts, which are listed in Table II, were then subtracted from the corresponding observed frequencies. The corrected frequencies of ν_2 and ν_3 for the azide ion in KCl and KBr lattices at room temperature were used to determine the intraionic potential parameters k_2^0, k_3^0, β, and γ by means of Eqs. (14-16). The contributions to Δk_2 and Δk_3 from each type of potential acting through effects (i) and (ii) were then computed for the three potassium halide lattices. Calculations were not made for the NaCl lattice because no intensity data were available for impurities in this lattice.

In the numerical evaluation of the short-range forces estimates of the constants ζ^+, ζ^-, ρ^+, and ρ^- were made by analogy with the short-range potential function usually employed for pure alkali halide crystals. Coulson[21] has expressed the function in the form $\xi \exp\left[-(R - d_1 - d_2)/\rho\right]$, where $\xi = 4 \times 10^{-12}$ ergs, R is the distance between neighbors in the crystal, $\rho = 0.345$ A and d_1 and d_2 are "effective ionic radii" for the two interacting species. The d_1 have values of 1.475 A, 1.600 A and 1.785 A for Cl^-, Br^-, and I^-, respectively. It has been assumed here that for an end atom in the azide ion, the effective ionic radius is approximately $1.15 \times 1/2 = 0.575$ A, where 1.15 A is the N — N bond length. The potential function given by Coulson can be reduced to the form of Eq. (6) by writing the function in the form $\xi \exp\left[(d_1 + d_2)/\rho\right] \exp(-R/\rho)$, the identifications $\rho = \rho^+ = \rho^-$, $R = R(h,k,\ell)$, and $\zeta = \xi \exp(d_1 + d_2)/\rho$ can be made. In this manner one finds, taking $d_1 = 1.185$ A for K^+, the value $\zeta^+ = \xi \exp\left[(d_1 + d_2)/\rho\right] = 5.563 \times 10^{-10}$ ergs. The values of ζ employed in the present calculations were estimated using the above scheme.

Table II. Effect of the induction forces

Lattice	$(\partial\mu/\partial Q_3)_0^2$ $(10^3$ esu/g$)^a$	$(\partial\mu/\partial Q_2)_0^2$ $(10^3$ esu/g$)^a$	Temperature (^{o}K)	$-\Delta\omega_3$ (cm^{-1})	$-\Delta\omega_2$ (cm^{-1})
KCl	30	1.9	120	5.41	1.13
			300	5.22	1.09
KBr	34	1.8	120	5.48	0.93
			300	5.27	0.89
KI	50	2.3	120	6.88	1.03
			300	6.59	0.98

^{a}Data from Reference 23.

The best fit to the observed frequency-shift data is provided by the choice of the parameters

$$f_{22} = 7.64 \text{ X } 10^{-12} \text{ dyne-cm},$$

$$f_{33} - f_{13} = 11.08 \text{ X } 10^5 \text{ dynes/cm},$$

$$B = \beta\ell^2 2\sqrt{2}/9(f_{11} + f_{13}) = 2.06 \text{ X } 10^{-9} \text{ cm},$$

and

$$C = \gamma 2\sqrt{2}/(f_{11} + f_{13}) = -3.84 \text{ X } 10^8 \text{ cm}^{-1}.$$

The constants f_{22} and $f_{33} - f_{13}$ represent the force constants for a hypothetical "free azide ion, neglecting anharmonicity corrections. Hence the resulting vibrational frequencies of the "free" azide ion are $\nu_2^o = 648.04$ cm^{-1} and $\nu_3^o = 2006.9$ cm^{-1}.

The values of B and C found above can be used to calculate the cubic potential parameters $\beta = 74.6 \text{ X } 10^{12}$ dynes/cm^2 and $\gamma = -204 \text{ X } 10^{12}$ dynes/cm^2. These values lead in turn to $b = 39.6$ cm^{-1} and $c = -156$ cm^{-1} for the azide ion, which can be compared with the analogous results $b = 71.3$ cm^{-1} and $c = -250$ cm^{-1} obtained by Dennison[22] for carbon dioxide.

An independent determination of the cubic constants for the azide ion can in principle be made from a complete anharmonicity treatment of the ion. A total of seven anharmonicity constants, plus the three harmonic frequencies, would have to be found from

Table III. Contributions to Δk_3 from various matrix forces

Host Lattice	Temp. (^{o}K)	Force (10^{-4} dynes)		Δk_3 (ii)^a (10^4 dynes/cm)	Δk_3 (i) (10^4 dynes/cm)			Δk_3 [(i)& (ii)] (10^4 dynes/cm)
		Coulombic	Short Range		Coulombic	Short Range	Charge-induced dipole	
KCl	120	0.7805	0.9960	6.8567	0.1968	0.5888	-2.1291	5.5131
	300	0.7596	0.9477	6.5525	0.1919	0.5484	-2.0720	5.2208
KBr	120	0.6271	0.7330	5.2199	0.1606	0.4993	-1.7106	4.1602
	300	0.6087	0.6789	4.9419	0.1562	0.4444	-1.6604	3.8822
KI	120	0.4557	0.4504	3.4777	0.1191	0.3411	-1.2432	2.6947
	300	0.4407	0.4179	3.2955	0.1154	0.3102	-1.2022	2.5188

[a] Taking C = 3.838×10^{8} cm^{-1}.

Table IV. Contributions to Δk_2 from various matrix forces

Host Lattice	Temp. (^{o}K)	Force (10^{-4} dynes)		Δk_2 (ii)^a (10^{-12} dyne-cm)	Δk_2 (i) (10^{-12} dyne-cm) end atom		center atom		Δk_2 [(i)&(ii)] (10^{-12} dyne-cm)
		Coulombic	Short Range		Coulombic	Short Range	Coulombic	Short Range	
KCl	120	0.7805	0.9960	-0.3677	-0.1312	0.3363	-0.1132	0.1634	-0.1124
	300	0.7596	0.9477	-0.3514	-0.1283	0.3194	-0.1112	0.1548	-0.1166
KBr	120	0.6271	0.7330	-0.2799	-0.1097	0.2222	-0.0982	0.1089	-0.1567
	300	0.6087	0.6789	-0.2650	-0.1071	0.2089	-0.0964	0.1022	-0.1574
KI	120	0.4557	0.4504	-0.1865	-0.0849	0.1179	-0.0801	0.0588	-0.1748
	300	0.4407	0.4179	-0.1767	-0.0827	0.0984	-0.0784	0.0489	-0.1844

[a] Taking B = 2.058×10^{-9} cm.

the values of observed fundamentals, combinations, and overtones. A treatment of the Fermi resonance between ν_1 and $2\nu_2$ would yield a value for b. On the other hand the constant c can be found only if the nine nonvanishing cubic and quartic potential constants can be determined. In the absence of a knowledge of rotational interactions, there is insufficient information for the complete determination of the cubic and quartic terms.

The results of the calculations of the interionic forces are summarized in Tables II - IV. Table III shows the contributions from Coulombic and short-range forces, which modify the equilibrium interatomic distances, and the resulting values of Δk_3. Table IV lists contributions to Δk_2 from effects (ii) and (i) while the observed and calculated frequencies are compared in Table V. Finally, Figs. 6 and 7 show experimental and calculated values of ν_3 and ν_2, respectively, for various matrices and as functions of temperature. For each mode only the two endpoints of the theoretical curves were calculated. In the figures the points have been connected by broken lines to suggest the slopes, although this procedure is not intended to imply linearity.

Table V. Comparison of observed and calculated frequencies

Host Lattice	Temp. (°K)	ν_3(cal.) (cm^{-1})	ν_3(obs.) (cm^{-1})	ν_3 (obs-cal)	ν_2(cal.) (cm^{-1})	ν_2(obs.) (cm^{-1})	ν_2 (obs-cal)
KCl	120	2051.39	2051.18	-0.21	642.14	642.96	1.02
	300	2048.93	2048.93	0.00[a]	641.92	641.92	0.00[b]
KBr	120	2039.15	2038.20	-0.95	640.46	461.47	1.01
	300	2036.76	2036.76	0.00[a]	640.47	640.47	0.00[b]
KI	120	2024.45	2022.07	-2.38	639.60	639.74	0.14
	300	2023.09	2021.68	-1.41	639.24	638.40	-0.84

[a] Observed frequencies used to evaluate k_3^0 and γ.

[b] Observed frequencies used to evaluate k_2^0 and β.

It can be observed in Fig. 6 that for the stretching vibration good agreement was obtained between experimental and theoretical frequencies. This agreement strongly suggests that the forces considered in the model make the predominant contribution to the interaction of the azide ion with the surrounding matrix. It should be pointed out concerning the above agreement for change of matrix, that for each fundamental two experimental frequencies were used to calculate the intraionic potential parameters, thus forcing agreement at these points.

The most unsatisfactory aspect of the theoretical results arises from the inability to explain the strong temperature dependence of ν_2. In contrast to ν_3, the bending mode shows its strongest temperature dependence in the KI-matrix sample. Since this is just the matrix which offers the largest site, it is the KI matrix which would be expected to provide the smallest perturbation. Therefore, it must be concluded that compensation for the increased site size is provided by some specific property, such as the polarizability or the short-range parameters of the iodide ion. A stronger temperature dependence can be detected in the calculated frequency shifts,

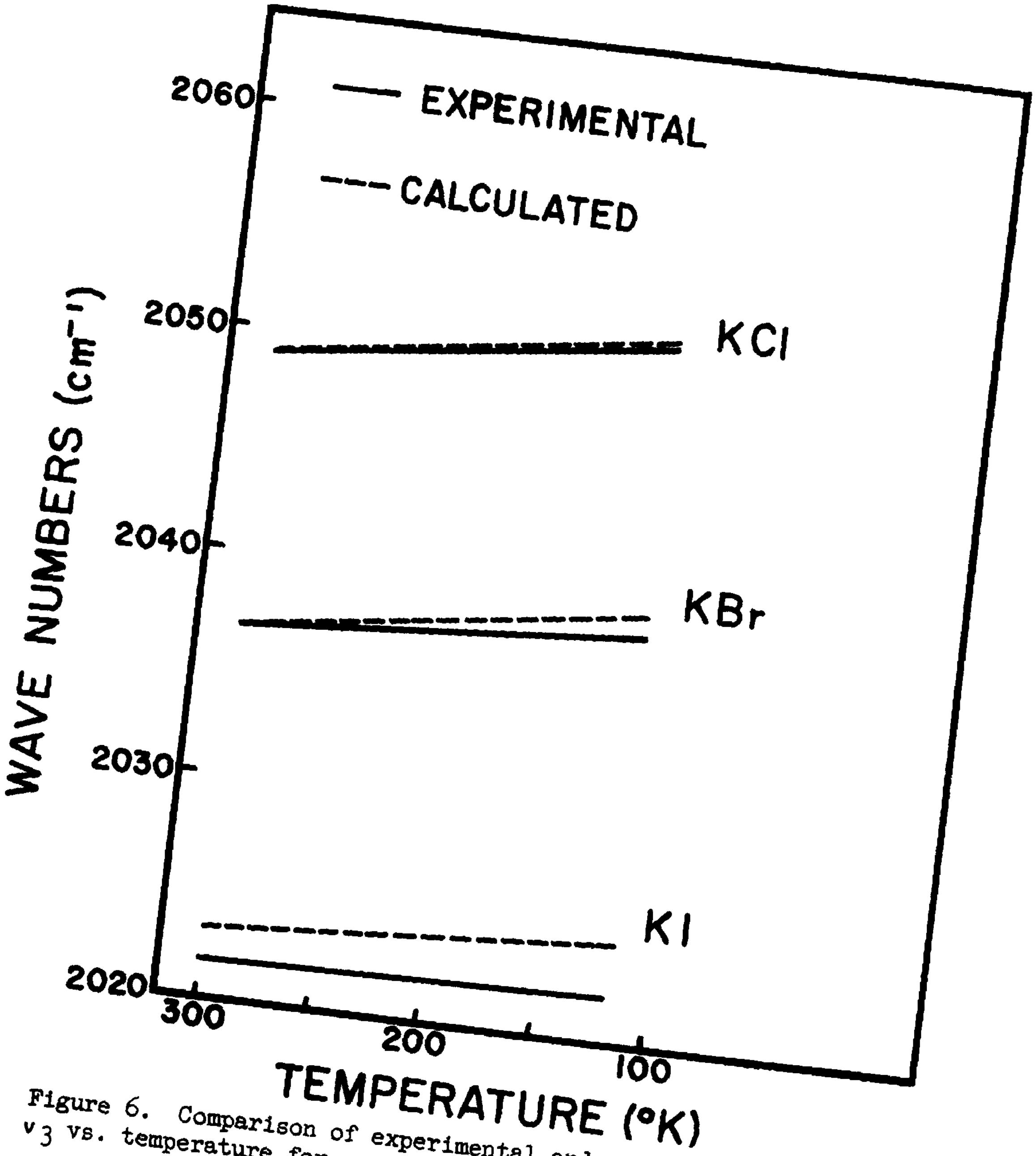

Figure 6. Comparison of experimental and calculated values of ν_3 vs. temperature for various lattices.

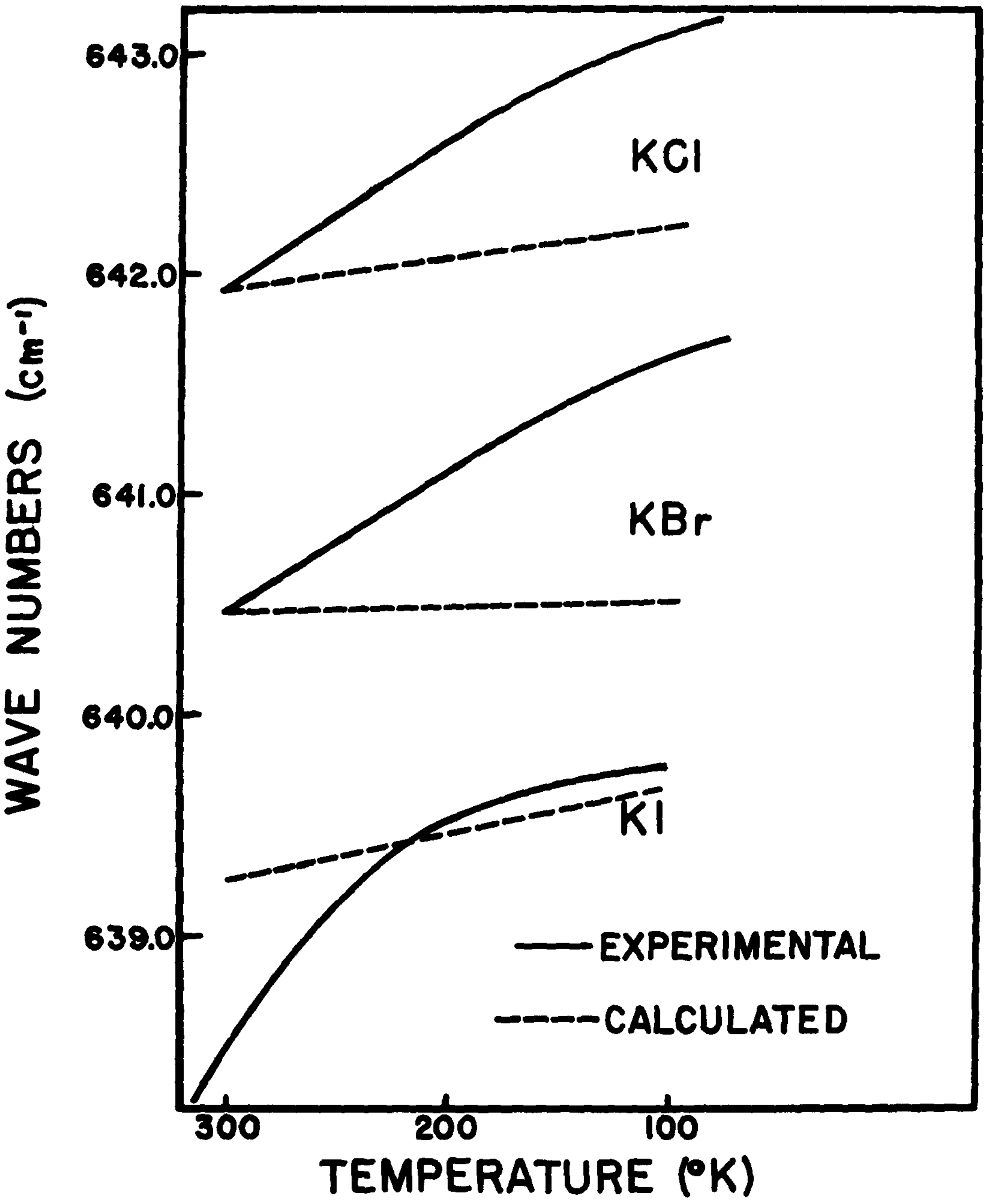

Figure 7. Comparison of experimental and calculated values of ν_2 vs. temperature for various lattices.

for the KI-matrix samples compared with those of KCl and KBr, although it is far too weak to provide agreement with experiment. It must be concluded then that further effects, probably inductive in nature, must be considered before a satisfactory treatment of the bending vibration can be made.

VII. CONCLUSIONS

The two infrared-active fundamentals of the azide ion in KI, KBr, KCl and NaCl lattices have been measured as functions of temperature and the nature of the lattice. A comparison has been made of the spectra of samples grown from aqueous solutions with those prepared by the pressed-disk technique. Strong evidence of lattice intermixing (solid solution) was provided by the spectra of the pressed-disk samples.

The observed frequency shifts are consistent with a simple electrostatic model of impurity ion-lattice interaction. It is shown that inductive, Coulombic, and short-range forces all provide significant contributions to the lattice perturbations.

A study of the overtone and combination bands of the azide ion in various lattices is being carried out in an effort to obtain the anharmonicity parameters and some of the cubic and quartic potential parameters. If values of b and c can be obtained from the anharmonicity treatment, they will provide a check on the values of these two parameters, which were estimated in the present work.

ACKNOWLEDGMENT

We should like to thank Mr. H. H. Smith of the Data Processing Center, USAERDL, Fort Belvoir, Virginia, for writing the computer programs and for evaluating the lattice sums needed in this work.

REFERENCES

1. J. A. Ketelaar, C. Haas, and J. van der Elsken, J. Chem. Phys. 24, 624 (1956).
2. J. van der Elsken, Doctoral Dissertation, University of Amsterdam, June, 1959.
3. J. A. Ketelaar and J. van der Elsken, J. Chem. Phys. 30, 336 (1959).
4. A. G. Maki and J. C. Decius, J. Chem. Phys. 31, 772 (1959).
5. J. A. Ketelaar and F. N. Hooge, paper presented at the European Molecular Spectroscopy Conference, Freiberg, 1956.
6. J. L. Mack, A. S. Toma, and G. B. Wilmot, paper presented at the Annual Symposium on Molecular Structure and Spectroscopy, The Ohio State University, June, 1960.
7. A. G. Maki, private communications.
8. S. B. Hendricks and L. Pauling, J. Am. Chem. Soc. 47, 2904 (1925).
9. L. O. Brockway and L. Pauling, Proc. Natl. Acad. Sci. U. S. 19, 860 (1933).
10. L. K. Frevel, J. Am. Chem. Soc. 58, 779 (1936).
11. M. Bassiere, Compt. rend. 208, 657 (1939); J. chim. phys. 36, 71 (1939); Mem. serv. chim. état (Paris) 30, 33 (1943).
12. J. W. Moore, Report No. 23/R/55 ERDE, Waltham Abbey, Esses, England.
13. H. A. Papazian, J. Chem. Phys. 34, 1614 (1961).
14. G. Herzberg, Molecular Spectra and Molecular Spectra II., Infrared and Raman Spectra of Polyatomic Molecules, D. Van Nostrand Company, Princeton, N. J., 1945.
15. E. L. Wagner and D. F. Hornig, J. Chem. Phys. 18, 296 (1950).
16. T. E. Slykhouse and H. G. Drickmer, J. Chem. Phys. 27, 1226 (1957).
17. E. Bauer and M. Magat, J. phys. radium 9, 319 (1938).

18. J. E. Lennard-Jones and A. E. Ingham, Proc. Roy. Soc. (London) 107A, 636 (1925).

19. A. Bonnemay and R. Daudel, Compt. rend. 230, 2300 (1950).

20. J. O. Hirschfelder, C. F. Curtiss and R. B. Bird, Molecular Theory of Gases and Liquids, John Wiley & Sons, New York, 1954.

21. C. A. Coulson, Valence, Oxford University Press, Oxford, 1960.

22. D. M. Dennison, Revs. Modern Phys. 12, 175 (1940).

23. K. S. Seshadri and J. C. Decius, paper at the Annual Symposium on Spectroscopy and Molecular Structure, The Ohio State University, June, 1960.

APPENDIX

A. Coulombic Potential

Combining Eqs (4) and (5) and defining the C_3 orientation of the impurity ion by $\cos\theta = 1/\sqrt{3}$ and $\cos\Phi = 1/\sqrt{2}$, required derivatives evaluated at equilibrium ($r = r_o$) become

$$\left.\frac{dV_c}{dr}\right|_o = -\frac{4\varepsilon e}{a^2\sqrt{3}} \sum_{h,k,\ell}{}' \frac{(h+k+\ell-3\eta_o)\,(-1)^{h+k+\ell}}{\left[(h-\eta_o)^2+(k-\eta_o)^2+(\ell-\eta_o)^2\right]^{3/2}} \qquad \text{(A-1)}$$

and

$$\left.\frac{d^2V_c}{\partial r^2}\right|_o = \frac{8\varepsilon e}{a^3} \sum_{h,k,\ell}{}' \frac{(-1)^{h+k+\ell}}{\left[(n-\eta_o)^2+(k-\eta_o)^2+(\ell-\eta_o)^2\right]^{3/2}}$$

$$\times \left\{1 - \frac{(h+k+\ell=3\eta_o)^2}{(h-\eta_o)^2+(k-\eta_o)^2+(\ell-\eta_o)^2}\right\} \qquad \text{(A-2)}$$

where $\eta_o = 2r_o/a\sqrt{3}$.

For the bending mode the required second derivative is found by making the substitutions $r = r_o$, $\sin\theta\cos\Phi = \sin\theta\sin\Phi = 1\sqrt{3} + \Delta\theta/\sqrt{6}$, and $\cos\theta = 1/\sqrt{3} - \Delta\theta\sqrt{2}/\sqrt{3}$, which are valid for infinitesimal displacements from the equilibrium position. The result is given by

$$\left.\frac{d^2V_c}{d\theta^2}\right|_o = \frac{4r_o^2\varepsilon e}{a^3} \sum_{h,k,\ell}{}' \frac{(-1)^{h+k+\ell}}{\left[(h-\eta_o)^2+(k-\eta_o)^2+(\ell-\eta_o)^2\right]^{3/2}}$$

$$\times \left\{2 - \frac{(h+k-2\ell)^2}{(h-\eta_o)^2+(R-\eta_o)^2+(\ell-\eta_o)^2}\right\}. \qquad \text{(A-3)}$$

An equivalent expression can be developed for $\left.\dfrac{d^2V_c}{d\Phi^2}\right|_o$

The center-atom interaction is found by substituting $r = y$, $\sin\theta = 1/\sqrt{3}$ and $\sin\Phi = 1/\sqrt{2}$ in Eq. (5). The second derivative with respect to y, the center-atom displacement, evaluated at equilibrium ($y = 0$) is

$$\left.\frac{d^2V_c}{dy^2}\right|_o = -\frac{4\delta e}{a^3}\sum_{h,k,\ell}\frac{(-1)^{h+k+\ell}}{(h^2+k^2+\ell^2)^{3/2}}\left[2-\frac{(h+k+2\ell)^2}{h^2+k^2+\ell^2}\right] . \qquad \text{(A-4)}$$

The above sums were evaluated using an IBM-650 computer. The indices were allowed to run from -15 to +15 to insure four-digit accuracy. However, the above equation yield sums which are correct to better than 3% if only the 26 ions of the unit cell surrounding the impurity site are included (taking h, k, ℓ from -1 to +1).

B. Short-Range Potential

The corresponding derivatives of the short-range potential are given below.

$$\left.\frac{dV_s}{dr}\right|_o = \frac{a\sqrt{3}\zeta^+\,(1-3\eta_o)\,e^{-N}}{2(\rho^+)^2N} - \frac{a\sqrt{3}\zeta^-\,(2-3\eta_o)\,e^{-M}}{2(\rho^-)^2M} + \frac{\zeta^+}{\rho^+}\,e^{-a\sqrt{3}\,(1-\eta_o)/2\rho^+}, \qquad \text{(A-5)}$$

$$\left.\frac{d^2V_s}{dr^2}\right|_o = \frac{3\zeta^+}{(\rho^+)^2N}\left[\frac{a^2(1-3\eta_o)^2\,(1+1/N)}{12\rho^2N}-1\right]e^{-N} + \frac{3\zeta^-}{(\rho^-)^2M}\left[\frac{a^2(2-3\eta_o)^2\,(1+1/M)}{12(\rho^-)^2M}-1\right]e^{-M} + \frac{\zeta^+}{(\rho^-)^2}\,e^{-a\sqrt{3}\,(1-\eta_o)/2\rho^-} \qquad \text{(A-6)}$$

$$\left.\frac{d^2V_s}{d\theta^2}\right|_o = \frac{3a^4\eta_o^2}{16}\left[\frac{\zeta^+}{N^2(\rho^+)^4} + (1 + 1/N)\ e^{-N} + \frac{\zeta^-}{M^2(\rho^-)^4}\ (1 + 1/M)\ e^{-M}\right] \tag{A-7}$$

and

$$\left.\frac{d^2V_s}{dy^2}\right|_o = \frac{2\zeta^+}{\rho^+}\left(\frac{1}{\rho^+} - \frac{4}{a}\right) e^{-a/2\rho^+} + \frac{\zeta^-}{3\rho^-}\left(\frac{11}{\rho^-} + \frac{7\sqrt{2}}{a}\right) e^{-a/\rho^-\sqrt{2}} + \frac{4\zeta^+}{9\rho^+}\left(\frac{4}{\rho^+} - \frac{1}{a\sqrt{3}}\right) e^{-a\sqrt{3}/2\rho^+}, \tag{A-8}$$

where $N = a(1 - 2\eta_o + 3\eta_o^2)^{1/2}/2\rho$

and $M = a(1 - 2\eta_o + 3\eta_o^2/2)^{1/2}/\rho\sqrt{2}$.

PHOTOCONDUCTIVITY, ELECTRON MICROGRAPHS AND THE MECHANISM OF THERMAL DECOMPOSITION OF LEAD AZIDE*

by

Melvin A. Cook, N. Lawrence Head
Robert T. Keyes and Ronald R. Rollins
Institute of Metals and Explosives Research
University of Utah
Salt Lake City, Utah

ABSTRACT

The decomposition of lead azide was studied by photoconductivity, optical and electron micrographs and by electron bombardment. In photoconductivity single crystals, pressed pellets of pure PbN_6 and pellets of colloidal and dextrinated lead azide were used. Samples "aged" (heat treated at high temperatures) for various times showed photocurrents to increase exponentially in time, owing to the degree of decomposition and lead nuclei formation as seen by correlation studies with electron micrographs. Low temperature photoconductivity of PbN_6 exhibited the saturation and space charge effects of typical semi-conductors with frozen in "holes". Crystal imperfections manifesting themselves on the surfaces of lead azide as growth steps, dislocation networks, sites for the deposition of pure lead (lead nuclei), contamination nuclei (probably nitrides) and sites for nitrogen gas evolution in thermal decomposition were revealed in sequential optical and electron micrographs. The complex patterns shown by these micrographs may be explained by a standard n-type semi-conductor model in which excitons are assumed to decompose largely on lead nuclei (that grow largely on (010) faces) to release N_2 at these sites and charge the lead nuclei negatively. The negative nuclei then attract to them Pb^{++} ions which discharge the nuclei and cause their continued growth as thermal decomposition proceeds.

PHOTOCONDUCTIVITY OF LEAD AZIDE

Lead azide is a weak photoconductor with the maximum in its spectral distribution occurring at about 365 mμ(1) and an absorption edge at 400 mμ.(2) Any absorption at frequencies below the band edge is due to residual free carriers and can be used to give an indication of the purity of the sample. The primary photoelectric current is due to the motion of photoelectrons and possibly also

---

* This investigation was supported by Sandia Corporation under Purchase Orders 15-6358-A and 13-3126.

positive holes depending on the temperature. As long as this current is flowing no electrons can enter the crystal from the cathode except to neutralize any positive holes which might be drawn there under the influence of an applied field. In some crystals the continued passage of a primary current breaks down the resistance of the crystal so that electrons are able to enter from the cathode and pass through it as in a semi-conductor; this current is termed the secondary photoelectric current. In the case of silver azide the photocurrent is proportional to the strength of the applied electric field for field strengths up to about 250 V/cm. If the field is increased above this value the resistance of the crystal begins to break down with a rise in the dark current followed immediately by an explosion of the crystal.(3) There are at least two ways in which the secondary current may arise: (1) When the crystal is illuminated from one electrode to the other the space charge near the cathode may become large enough to induce a flow of electrons from the cathode. (2) The space charge may enhance any inherent dark electronic conductivity if it exists. If the positive holes do not migrate, as in the case of lead azide and silver halides at low temperature, no electrons can enter the crystal to replace those which have been pulled away under the influence of the field. Consequently, a space charge is set up in the crystal, and if illumination is continued, the effective field drops to a small fraction of its original value with a corresponding drop in the photocurrent. The crystal may be returned to its original state by warming or illumination with intense infra-red radiation.

In the photoconductivity work on lead azide by McLaren and Rogers(3) compressed powder pellets were used because it was not possible to grow sufficiently large single crystals. Measurable photocurrents were obtained and the photoconducting characteristics were found to be similar to those in silver azide. Under illumination the photocurrent increased rapidly at first reaching a saturation value after about 30 sec. With continued illumination the photocurrent decreased in a typical exponential decay. Photoelectrons migrate toward the anode, thus producing the initial increase in the primary photocurrent, but when the centers from which these photoelectrons are released remain filled, space charge is set up in the crystal with the result that the current is reduced. This occurred in lead azide with the result that the primary current was reduced to about 1/5 of its maximum value. A linear relationship between the primary photocurrent and the electric field strength was found for lead azide which indicated that most of the photoelectrons were trapped before reaching the anode. Saturation of the photocurrent with an increase in the field strength was not possible. (Saturation would occur if all the electrons reached the anode without being trapped.) Under such circumstances no valid computation of the quantum efficiency and the mean range of photoelectrons could be made.

Evans and Yoffe(1) used a 100 watt mercury vapor lamp at 10 cm from a sample in order to detect a photocurrent in lead azide. A glass-walled water cell was placed between the mercury vapor lamp and the sample to act as a heat filter and as a short wavelength filter eliminating photoelectric emission from the silver electrodes. The measurements were made using two Kodak light filters, numbers 18A and 35. The wavelength of the spectral lines emitted by the mercury vapor lamp and the wavelength transmission of the filters were determined using a Hilger quartz prism spectrograph. It was found that the filters transmitted, with rapidly decreasing intensity, the following mercury vapor lines,

$$\text{Filter 35}\ \begin{cases} 435.8\ \text{m}\mu \\ 404.6\ \text{m}\mu \\ 365\ \ \text{m}\mu \end{cases} \qquad \text{Filter 18A}\ \begin{cases} 365\ \ \text{m}\mu \\ 334.1\ \text{m}\mu \\ 313\ \ \text{m}\mu \end{cases}$$

the desired wavelength of 365 mμ being common to both. The photocurrents observed for these filters were as follows:

Filter	Photocurrent
Glass water cell	$2.3\cdot10^{-12}$ amps
+ 18A	0.72 "
+ 35	0.8 "
+ 35 + 18A	0.52 "

Taking the transmission characteristics of the filters into account it was found that 75% of the observed photocurrent was due to the 365 mμ line. The ohmic resistance of the lead azide at room temperature was found to be $1.5\cdot10^{13}$ ohms/cm^3.

As lead azide was irradiated at the proper wavelength decomposition proceeded with the formation of metallic lead nuclei and the escape of nitrogen gas. The presence of these lead nuclei apparently catalyze the reaction. The nitrogen gas is evolved at the surface of the crystal or at internal flaws or crystal imperfections. Dumas(4) determined the rate of photolysis (and the magnitude of the photoelectric current) in amorphous lead azide samples as a function of the spectral quality of the incident light, and found it to be proportional to the intensity of illumination with the peaks occurring at 280 mμ and 240 mμ. Photoelectric currents were obtained for partially decomposed samples, no photocurrents being detected in freshly prepared samples.

Lead azide was found to darken when exposed to ultra-violet light. Upon heating this darkening disappeared, a result which would not be expected if the darkening were due to the formation of nuclei, since they would increase in number and/or grow bigger as decomposition proceeds. Peaks at 280 mμ and 240 mμ were ascribed to two exciton bands. An F-center was assumed to be formed from the excitons by the trapping of an electron at an anion vacancy. The holes from the dissociation of the exciton then supposedly diffused to the surface and combined to produce nitrogen gas. Dumas found that at photon energies lower than required to produce photolysis no photoelectrons were observed in freshly prepared samples, and that after some exposure in the ultraviolet photocurrents were observed. Subsequent photocurrents were observed at lower photon energies, presumably due to ionization of F-centers. He also found that upon ultraviolet irradiation the sample turned a yellowish brown color and slowly darkened with continued exposure. This coloration bleached, but the nuclei did not disappear.

Upon the basis of these observations the following mechanism was proposed by Dumas, for the photolysis of lead azide: (1) Absorbed photons produce excitons. (2) Excitons diffuse through the crystal lattice i.e., electrons and holes migrate until they encounter an anion vacancy and form an F-center. (3) The hole (an azide or N_3 radical) diffuses to the surface to release nitrogen when it combines with another hole (which may be trapped at the surface).

Dodd et al reported rate-time and rate-intensity curves for sodium, mercurous, and lead azides.(5) The sample, mounted in vacuo upon a thermocouple sample holder, was illuminated through a water filter by a low-pressure mercury arc. The resulting absorbed energy caused deflection of a sensitive galvanometer connected to the thermocouple, and the nitrogen evolved by the decomposition was measured by an increase of pressure in the system as detected by an ion gauge. Dodd et. al., observed an initial rapid rise in the rate of nitrogen evolution, finally (nearly) leveling off at $6.5 \cdot 10^{12}$ N_2 molecules/sec for an intensity of $8.22 \cdot 10^{13}$ photons/sec after about 10 minutes of illumination. Their experimental quantum yield was 0.056, the maximum value being chosen as that of the initial excitation process, a value considered by them to be low because sample decomposition became appreciable after only a few minutes of exposure. Using this value for the quantum yield the optical absorption constant was calculated to be $2 \cdot 10^7$. Since the method of obtaining the quantum yield depended upon a linearity of the rate-intensity plot, which was only a fair approximation for lead azide, this constant was regarded as approximate only.

The proposed model of Dodd et al, for photolysis of azides may be summarized as follows: (1) Each absorbed quantum has a probability P of forming an active center of some sort. (2) These active centers may diffuse away from the point of formation with a diffusion constant D. (3) The active centers experience a first-order homogeneous termination process which does not yield nitrogen. (4) The active centers upon reaching a surface of the sample undergo a first-order termination to form nitrogen gas, which escapes and is the only observable reaction product. (5) The incident radiation was assumed to be absorbed according to the usual law $I = I_o e^{-kx}$, where k is the absorption constant of the azide for the wavelength employed.

From a plot of decomposition rate vs $t^{1/2}$ the diffusion constant D was calculated to be $2 \cdot 10^{-17}$ cm^2/sec. Since this value is quite small it cannot apply to hole or ionic, much less exciton, diffusion. The rate controlling step in photolysis might, however, be diffusion of some good-sized entity, e.g., a radical. Dodd et. al., considered it conceivable that the diffusion entity was molecular nitrogen, formed along grain boundaries, and that the observed diffusion rate measured the migration of these molecules to the surface, rather than through the lattice.

Experimental

One of the major problems in lead azide studies is the difficulty of obtaining sufficiently large, pure, single crystals. For this reason compressed pellets made (a) from small crystals of lead azide grown in this laboratory and (b) commercially prepared colloidal lead azide were used in the majority of the photoconductivity experiments. Single crystals were prepared by the diffusion method which utilizes the reactions of hydrazoic acid vapor on a lead nitrate solution containing a non-ionic surface active agent(6,7). In this procedure 5 ml of 10% lead nitrate solution containing 0.1% "Tween 20" were exposed to the vapor from 5 ml of 4% Hydrazoic acid solution in a closed container (one liter) for 24 hours. The solutions were contained in small open crucibles or capsules. The acid vapor may be generated by the addition of sulfuric acid to a sodium azide solution. The crystals were grown in the dark, removed from the solution, filtered, washed with distilled water, rinsed with acetone, and dried. Well-formed crystals approximately 5 mm long and 1 mm in diameter grown in this manner, were pressed into pellets using a 1/4 inch diameter die.

Since pressed pellets were used to conduct the experiments, a sample holder which could be used to hold the pellets during illumination had to be built. It was constructed of copper and mounted in pyrex dewar flasks to facilitate either cooling or warming the sample as well as evacuating the sample to prevent oxidation of its surface. The pellet was mounted between two spring-loaded silver electrodes electrically insulated from the copper block. Electrical connections were made through tungsten leads sealed through the pyrex dewar section. Quartz windows were utilized to permit maximum transmission of light in the ultra-violet region, the windows being placed on both sides of the assembly to facilitate absorption measurements. The sample holder was mounted in a plastic block and placed in a Beckmann DK-2 Spectrophotometer which was used to provide the source of monochromatic radiation. The sample was mounted in series with a battery or variable D.C. supply and a Keithley Electrometer with a decade shunt which in combinations with the Electrometer formed a very sensitive micro-microammeter. The sample was illuminated, using an Osram HBO-200 high pressure mercury lamp, Model 520-Q, supplied by the American Optical Company. Under the influence of the potential field a small dark current was observed. The photocurrent was taken as the increase in current obtained when the sample was illuminated.

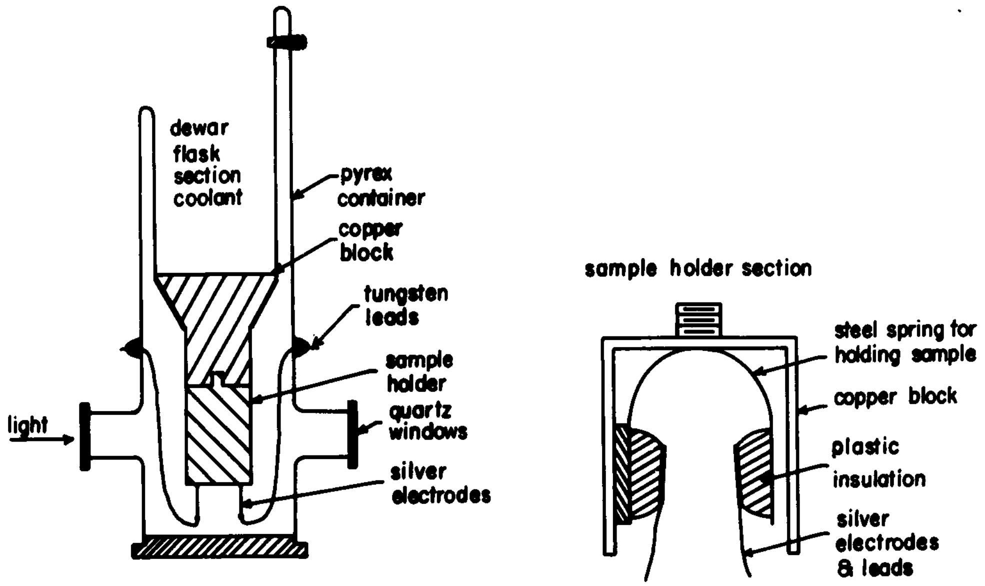
dewar flask section coolant
pyrex container
copper block
tungsten leads
sample holder
quartz windows
silver electrodes
light
sample holder section
steel spring for holding sample
copper block
plastic insulation
silver electrodes & leads

Figure 1. Sample holder used in the photoconductivity experiments.

Results

Initial experiments were conducted utilizing the full output of the 200 watt merc-arc lamp on a 0.25" diameter pellet made from single crystals grown in this laboratory. These preliminary tests were made at 32° C and 650 mm Hg pressure, the photocurrent being measured as a function of time. By varying the distance between the lens and the arc, thereby changing the intensity of the light striking the sample, the photocurrent could be increased or decreased, and in this manner the optimum adjustment of the lamp was determined. The distance from the quartz lens of the light source to the sample was 15 cm. The only filter used was a glass plate which served both as a heat filter and short wave-length filter to prevent photoelectric emission from the electrodes. The results are shown in Fig. 2. A silver azide sample was also mounted in the

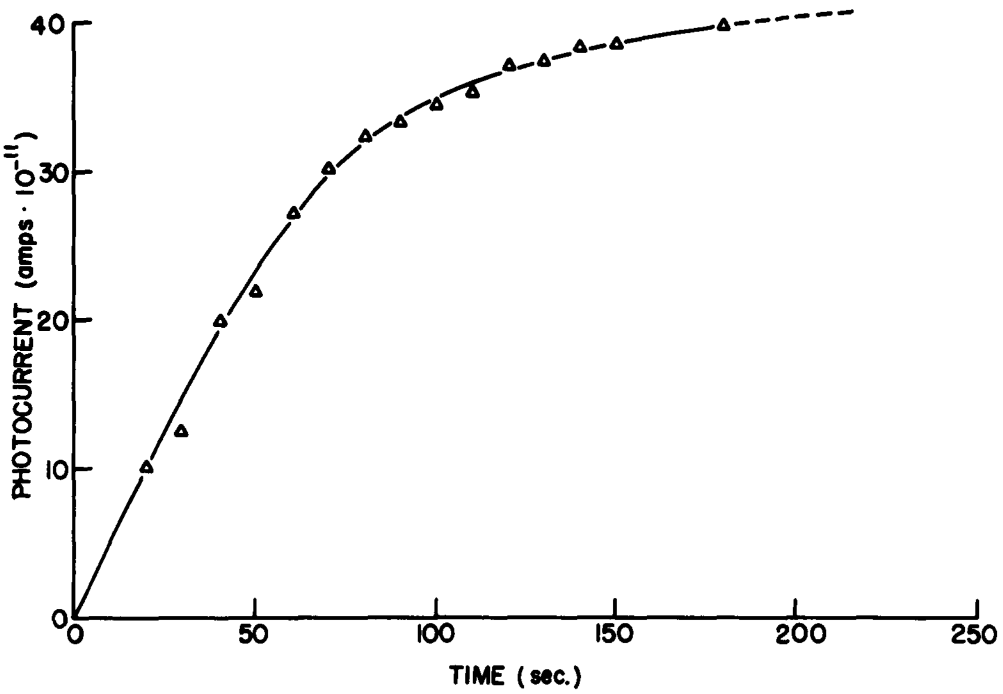

Figure 2. Photocurrent vs time for lead azide.

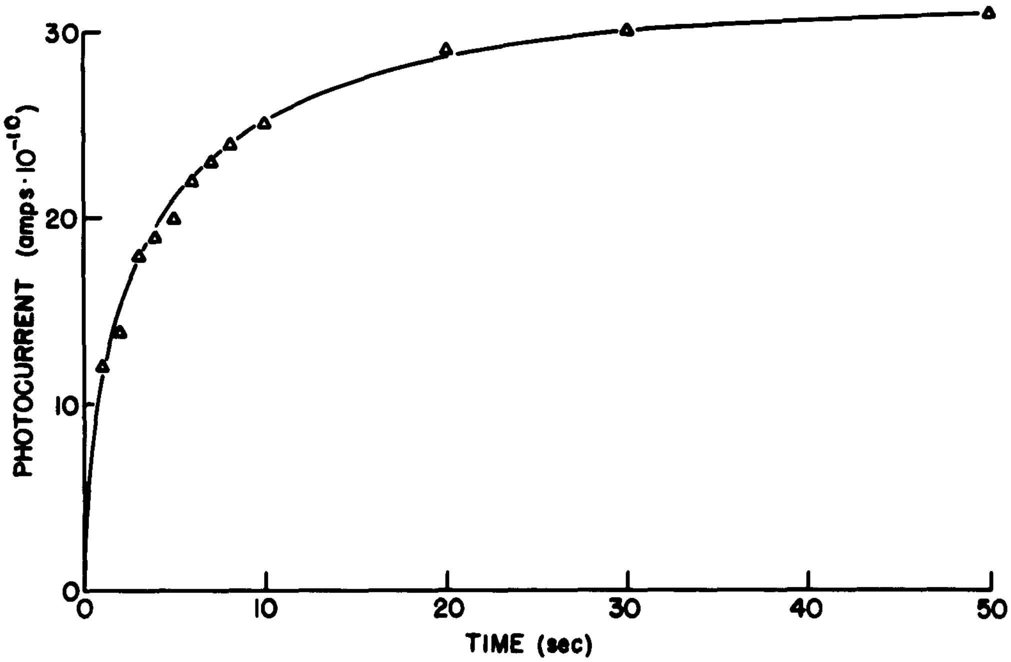

Figure 3. Photocurrent vs time for silver azide.

holder and run for comparison in the same manner (Fig. 3), the only difference being the distance from the lens to the sample which in this case was 25 cm. For lead azide the current after 180 seconds was $4 \cdot 10^{-10}$ amps while for silver azide it reached $3 \cdot 10^{-9}$ amps after only 30 seconds. Thus, the rise time for lead azide was much longer than for the silver azide; lead azide is, of course, also a much weaker photoconductor.

Monochromatic light was then used to illuminate similar samples. Kodak Wratten Filters #18A and #35 were used to isolate the 365 mμ mercury line which corresponds to the peak of the strongest absorption band of lead azide. In this case a heat filter comprised of a glass-walled water chamber was also used being placed next to the lens of the light source. Owing to this reduction in intensity of the incident light the photocurrent from silver azide was reduced to 10^{-11} amps, while that from the lead azide was reduced to 2 to $3 \cdot 10^{-13}$ amps. The latter current corresponds practically to the threshold of detection.

Runs were then made in a vacuum at -80° C using dry ice and acetone in the dewar flask section of the cell and then at -195° C using liquid nitrogen. The full output of the lamp was needed to obtain detectable readings. Upon illumination of the sample the current was observed to increase to a maximum value and then to decrease upon continued illumination to a small fraction of the maximum value. The drop in the photocurrent was attributed to buildup of space charge in the sample due to the comparatively slow migration at low temperatures of positive holes created when electrons were raised to the conduction band. This space charge could be removed by permitting the sample to warm up to room temperature and remain overnight with no applied field. At elevated temperatures the space charge disappeared more rapidly. The photocurrents at reduced temperature were considerably lower than at room temperature. This was attributed to absorption of a quantum of radiation to move the electron into an excited state in the potential hole around the vacant lattice point rather than to eject it into the conduction band. The electron then could make a contribution to the current only by thermal excitation of sufficient magnitude to eject it into the conduction band before it had a chance to drop back into its normal state. It will be noticed that there are some peculiar flat sections on the curves of Fig. 4, which show the photocurrents as a function of temperature. These have been rechecked several times and found to be real. In runs (b) and (c), which were essentially the same, it will be noticed that the maximum was only about half that in the first run indicating that the space charge was still present to limit the current. Tests using the full output of the lamp were run at 30° C using besides a control sample (#1) pressed pellets made from four different samples of lead azide of somewhat different sensitivity obtained from Aerojet General Corporation

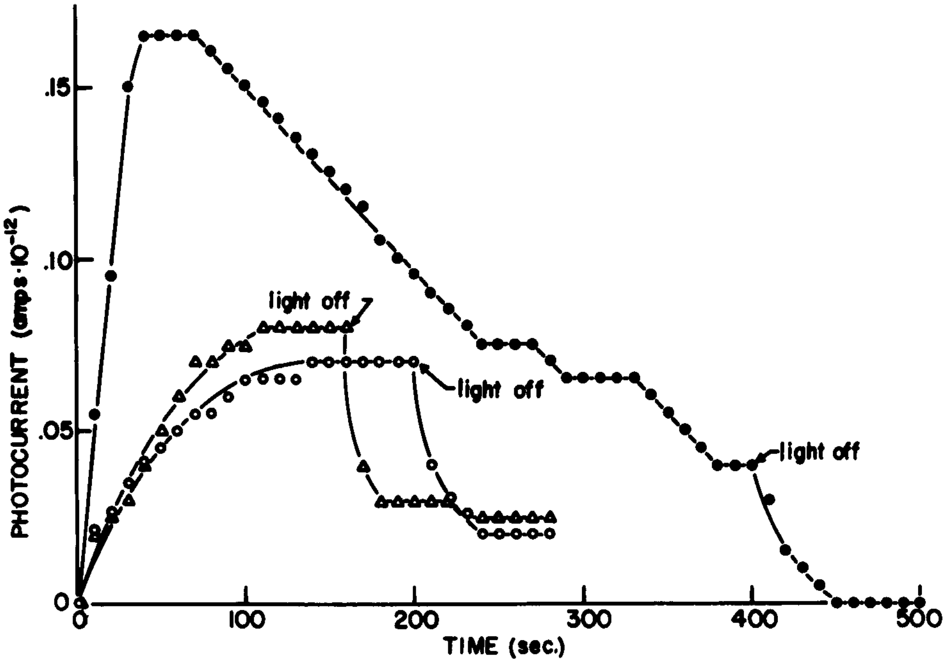

Figure 4. Photocurrent vs time for lead azide at -80° C.

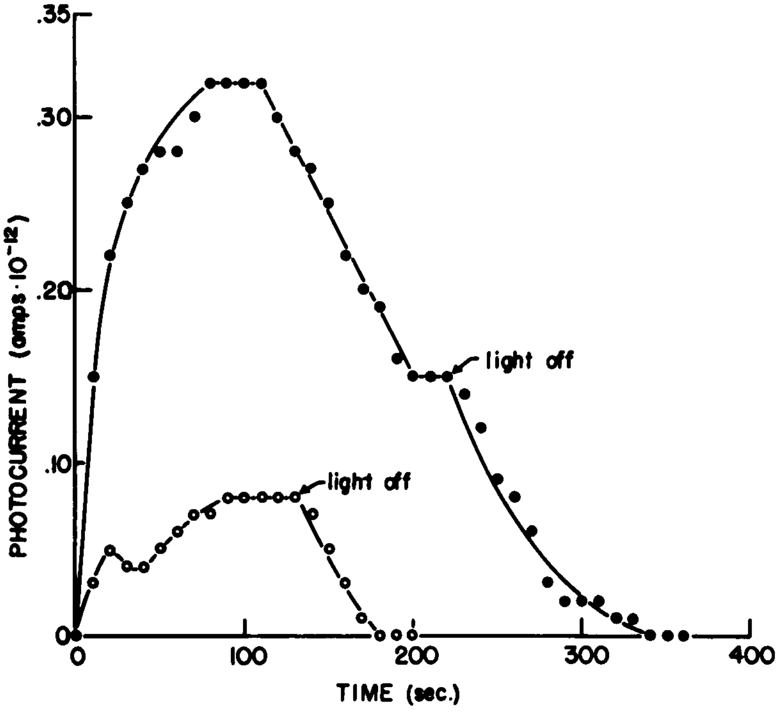

Figure 5. Photocurrent vs time for lead azide at -195° C.

(designated samples #2, #3, #4, and #5). The results are shown in Fig. 6. These measurements were made with the sample placed 15 cm from the lens using the unfiltered output of the lamp, except for the glass walled water chamber which served primarily as a heat filter. When the light was turned on, photocurrent began to flow, rising until a steady value was reached after several minutes. When the light was turned off the photocurrent decayed to zero, the

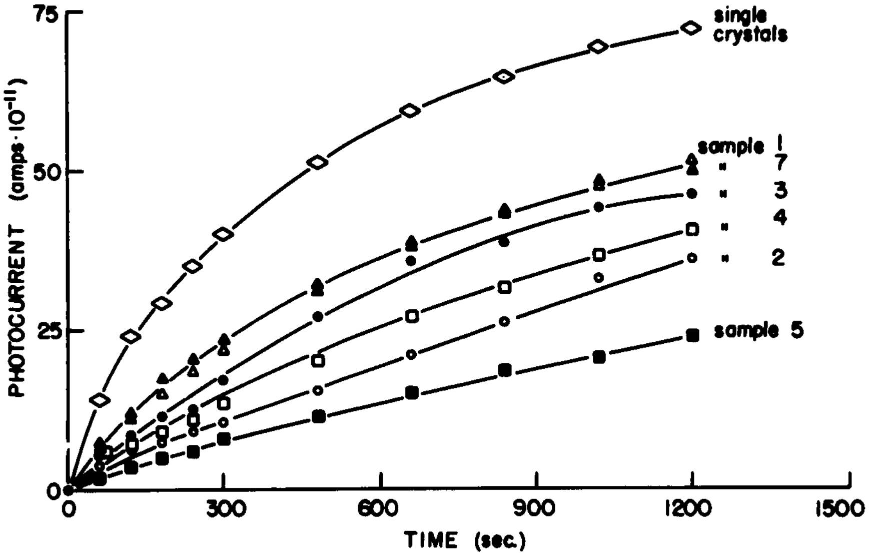

Figure 6a. Photocurrent vs illumination time for various lead azide samples.

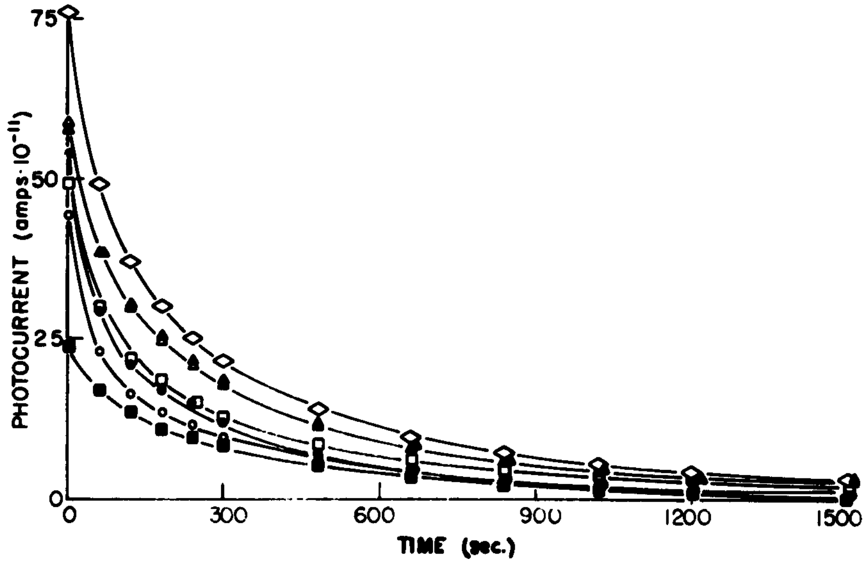

Figure 6b. Photocurrent vs time after illumination was terminated.

decay time being generally less than the rise time. Significant and reproducible differences in the rise times, maximum currents, and decay times were noted in the samples. Different pellets of these same samples were then studied in a vacuum at 30° C as shown in Fig. 7. The most striking observation was the reversal of the order, except for sample number 4. The photocurrents of the different samples after 600 seconds of illumination are compared in

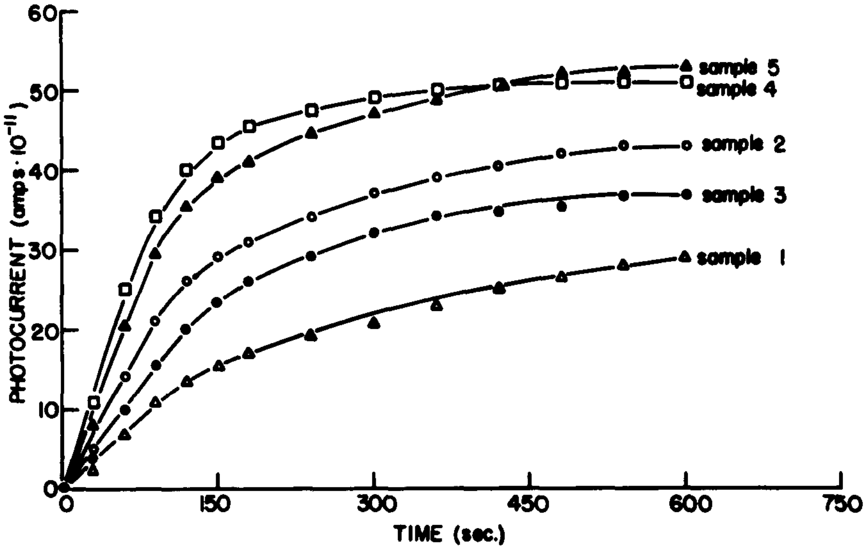

Figure 7a. Photocurrent vs illumination time for various lead azide samples.

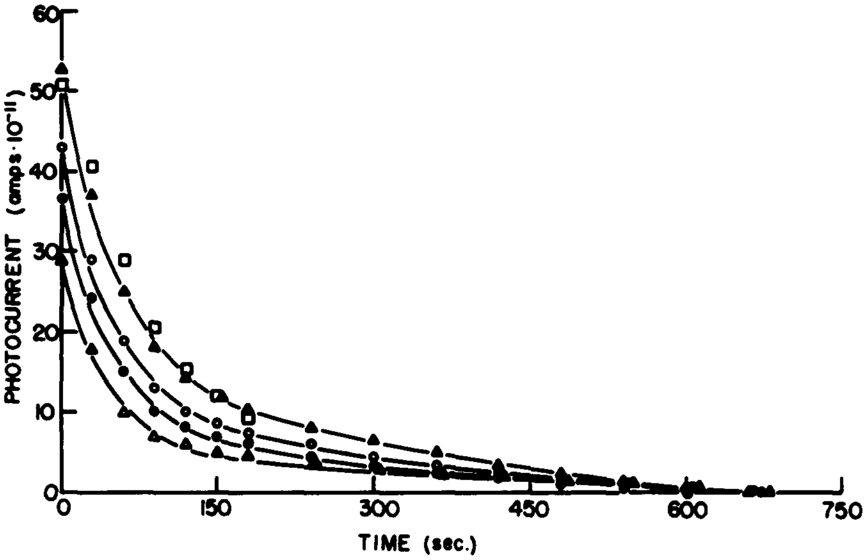

Figure 7b. Photocurrent vs time after illumination was terminated.

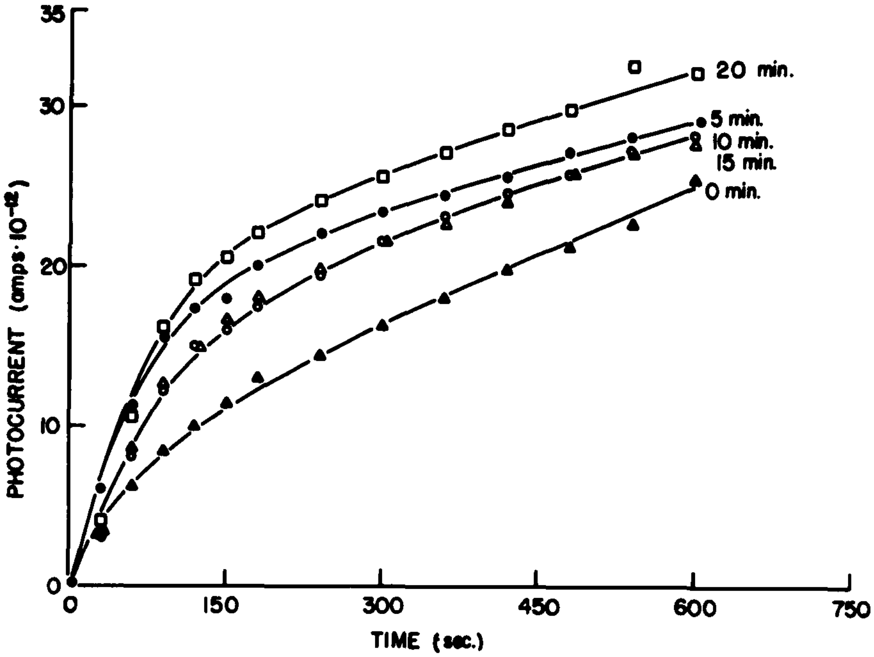

Figure 8a. Photocurrent vs illumination time for aged colloidal lead azide samples.

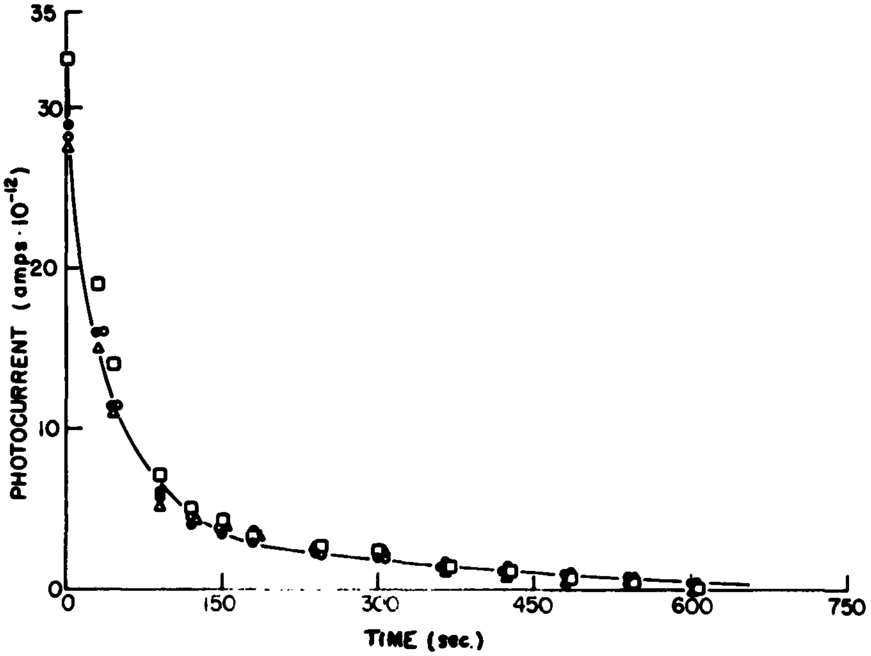

Figure 8b. Photocurrent vs time after illumination was terminated.

Table I. Runs were also made on colloidal lead azide samples heated to 250° C and maintained at this temperature for periods ranging from 5 minutes to 20 minutes. Differences in photocurrent were noted after such treatments, the currents being higher than in non-treated samples (Fig. 8). Interesting changes of sensitivity as determined in a miniature "card-gap" test and "light ignition" tests have been noted after such treatment(8).

Table I - Photocurrent after 600 seconds

Lead Azide*	Photocurrents (Amps x 10^{-10}) at 65 cm Hg	in vacuum
#1	3.7	2.9
#3	3.3	3.6
#4	2.5	5.1
#2	2.0	4.3
#5	1.4	5.3

* all dextrinated

Photocurrents in colloidal lead azide samples were measured using monochromatic radiation obtained by passing the beam of the Merc-Arc lamp through the quartz prism Monochromator section of the Beckmann DK-2 Spectrophotometer. One of the sample cells was modified to hold 1/8" diameter samples, the electrode spacing also being reduced to 1/8". This also made possible increasing the width of the insulation between the electrodes and the copper case. A D.C. power supply was used so that the electric field in the sample could be varied from 0 to 1600 volts/cm. One run was made on fresh colloidal lead azide (sample #1) with an applied voltage of 175 volts (550 volts/cm). Another run was made using another fresh sample of colloidal lead azide with the same potential. The results are designated in Fig. 9. All readings were taken over 10 sec duration. The desired wavelength was set on the monochromator, the sample being shielded from the light, then illuminated for 10 sec which was long enough for the current to reach its maximum value. The light was then cut off and the electrometer allowed to return to zero before the next reading was taken at a new wavelength.

In order to determine the influence of the electric field strength on the photocurrent applied voltage vs observed photocurrent data were obtained (Fig. 10) at 250° C, 650 mm Hg, and at a constant wavelength of 406 mμ. Note that the photocurrent varied nearly linearly with applied voltage. This linear relationship between the primary photocurrent and the electric field strength

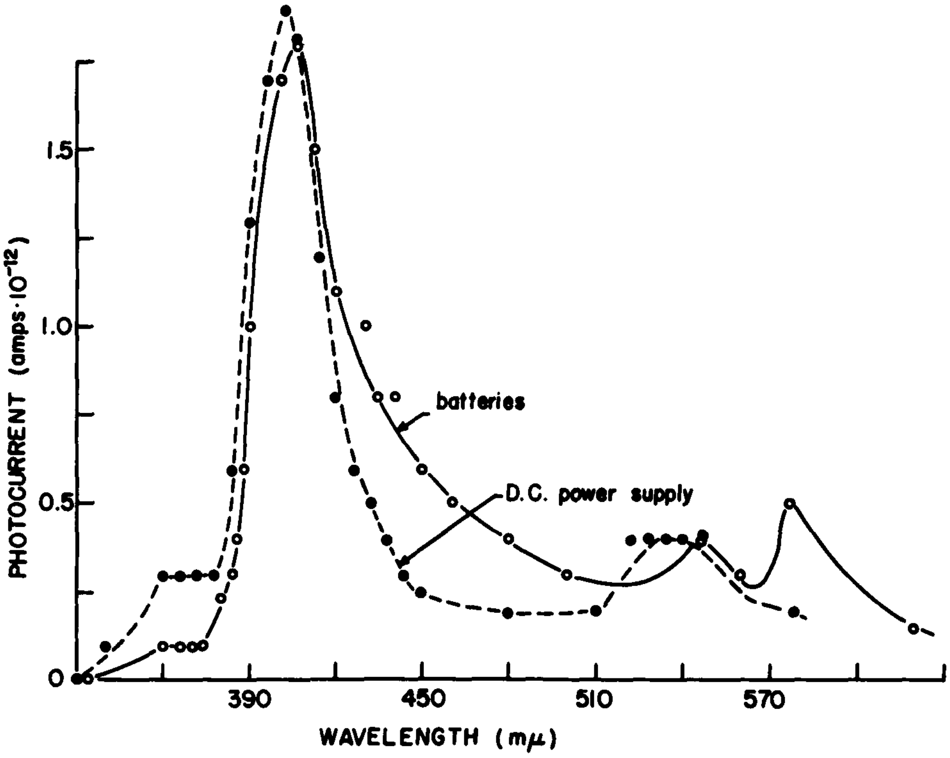

Figure 9. Photocurrent vs wavelength for colloidal lead azide.

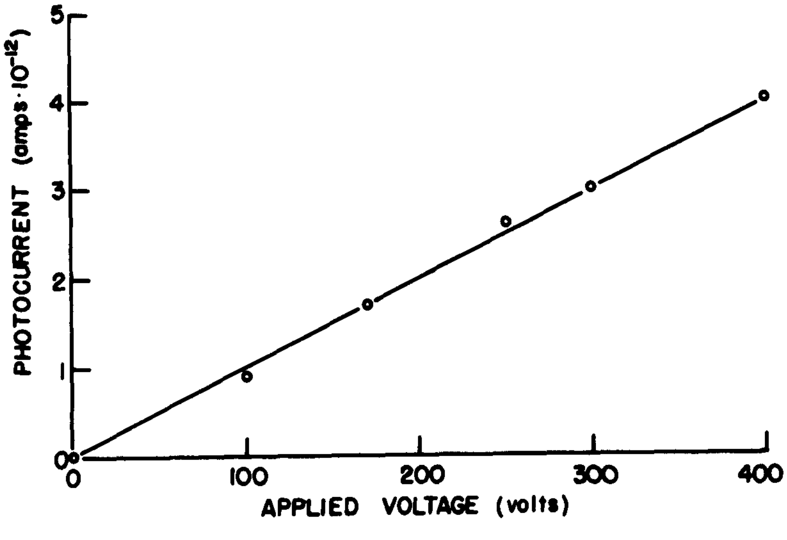

Figure 10. Photocurrent vs applied voltage for colloidal lead azide (sample #7).

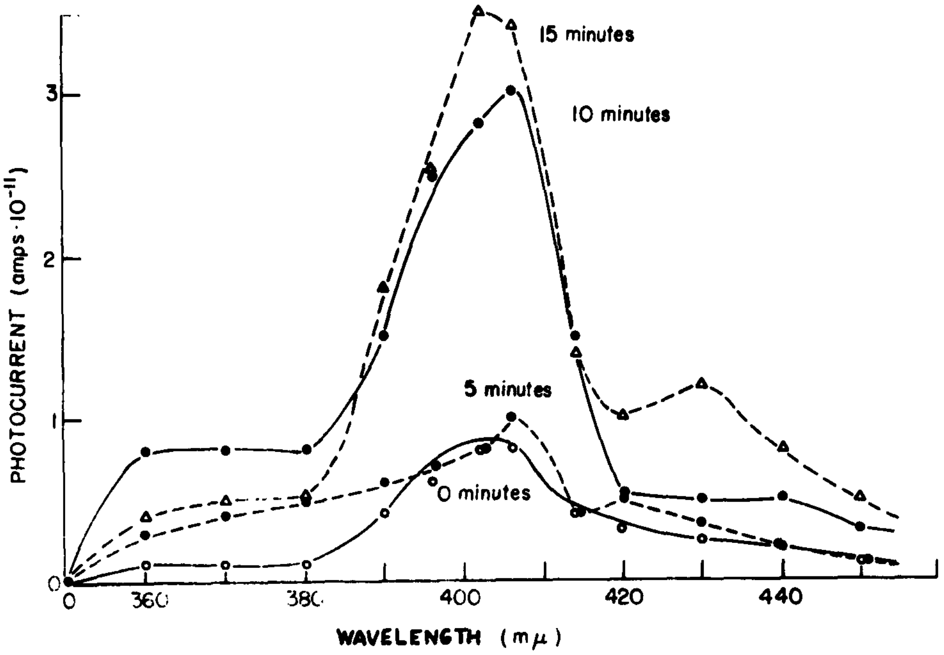

Figure 11a. Photocurrent vs wavelength for aged colloidal lead azide (sample #7).

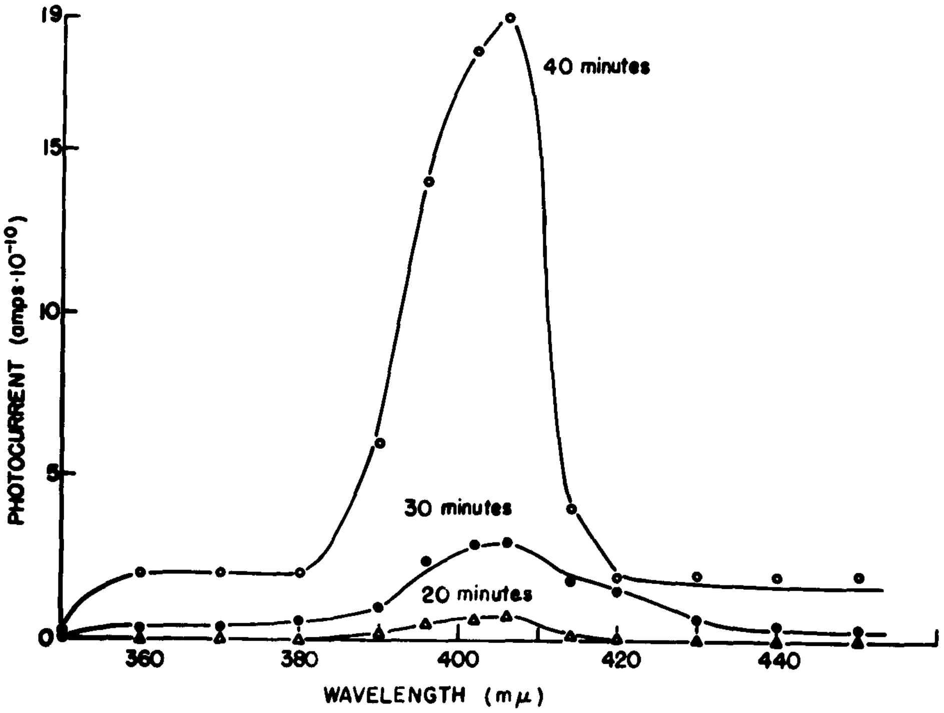

Figure 11b. Same as Figure 11a but with longer aging times.

indicated that most of the photoelectrons were trapped before reaching the anode. Applying Ohm's law a resistivity of about $1.5 \cdot 10^{13}$ ohms/cm^3 was obtained in agreement with the value given by Evans and Yoffe(1).

Similar tests were made on "aged" (heat treated) samples of colloidal lead azide (sample #7). Batches of the material were aged for 0, 5, 10, 15, 20, 30, and 40 minutes at 250° C. The samples were all run under the same conditions, i.e., 25° C, 650 mm Hg, 500 volts potential (1575 volts/cm), and mounted in the sample cell with the 1/8" electrode spacing. The photocurrent vs wavelength data are shown in Fig. 11. The maximum photocurrent in all cases occurred at 406 mμ. This maximum plotted against the aging time in minutes gave the results depicted in Fig. 12. In the range from 0 to about 20 minutes aging the photocurrent was small, but between 20 and 40 minutes aging it increased very rapidly. This suggested that the photocurrent is related to the number and size of the lead nuclei

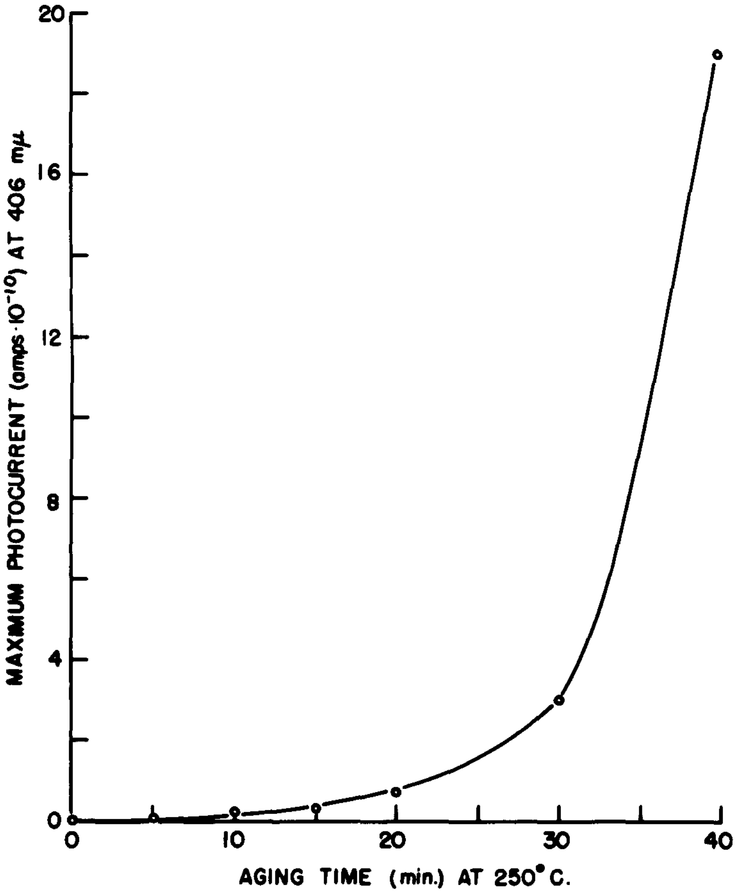

Figure 12. Maximum photocurrent vs aging time for colloidal lead azide. (Maxima were taken from Figures 11a and 11b.)

formed during decomposition, which was confirmed by electron microscopic studies presented in part II.

A summary of the different tests carried out on the various aged or heat treated and non-aged lead azide samples is presented in Tables II and III.

Table II: Results of different tests on Lead Azide

Measurement	Sample #1*	Sample #2*	Sample #3*	Sample #4*	Sample #5*	Sample #7**
Lead Azide Value (%)	91.29	91.94	90.80	90.63	92.11	95.95
50/50 point card gap test (cm)	3.17	3.13	3.17	3.43	2.93	3.36
50/50 explosion point (volts)-spark test	2934	3046	2830	2858	1902	2714
Time to explosion at 300° C (sec)	7.6	5.6	6.2	5.8		
Critical explosion temperature in a molten metal bath (°C)	285	276	262	266	260	348
Activation energy E (kcal/mole) (from metal bath test)		13.0	15.8	12.1	13.4	
Crystallite size (Å)		530	92	440	530	
Maximum photocurrent at 406 mμ (amps 10^{-12}) 1/8" cell, 550 v/cm)	1.0	1.0	5.0	1.0	<0.5	1.8
Maximum photocurrent, full output of lamp after 20 min. 1/4" cell 160 v/cm (10^{-11} amps)	51.5	36.0	46.0	40.5	22.5	50.0

* dextrinated
** colloidal

Table III: Results for "Aged" (heat treated at 250° C) Colloidal Lead Azide Samples

Aging time	Maximum photocurrent at 406 mμ, 1/8" cell, 1570 v/cm
0 (min)	$8 \cdot 10^{-12}$ amps
5	10
10	30
15	34
20	70
30	300
40	1900

ELECTRON MICROGRAPHIC ANALYSIS OF LEAD AZIDE

Bowden(9) studied silver azide with a reflection electron microscope in which he continuously scanned crystals to observe the physical changes taking place during decomposition. His observations showed that the azide crystals break up into small blocklets which may be a fraction of a micron in size. The conclusion reached was that reaction occurs not only on the surface of crystals but also at defects within the crystal. Silver nuclei were seen to form on the crystal surface. Bowden also has shown(10) that silver nuclei grow two-dimensionally at first, then at early stages of decomposition the two-dimensional growth becomes three-dimensional, with a redistribution of silver within or between nuclei so that the total area of the nuclei falls, and the partial ordering of the silver in the nuclei is lost.

In connection with the ordering of surface nuclei of silver in AgN_3, Camp(11) demonstrated the effect of a high intensity electron beam, showing that electrons decompose the AgN_3 not thermally, but by bombardment. When AgN_3 was decomposed by bombardment "ordered" silver nuclei formed as a background network on the surface of the crystals amongst which were larger nuclei 1000- to 2000 Å in size. The large nuclei were unordered and it was supposed that they were associated with some surface crystal imperfection, e.g., the point of emergence of a dislocation. The fact that ordered silver nuclei were produced as a result of bombardment by electrons is a matter of interest since it provides an insight into the nature of decomposition e.g., it indicates the formation of a pseudo-lattice in which the azide is driven to the surface leaving silver atoms or ions in the azide lattice positions. Additional silver atoms add to this new pseudo-lattice which eventually becomes unstable and changes to the normal silver lattice structure.

Apparently very little electron microscopy has been done with lead azide. This study utilized methods for producing shadowed carbon replicas of reliable quality so that one may be assured that what has been observed is indeed a true replica of the surface of the lead azide crystals. Furthermore a method is described that permits an examination of a single crystal through its stages of decomposition. Utilizing reliable replicating techniques "pure" crystals of PbN_6 were examined and compared with those obtained after thermal decomposition and electron bombardment. Thermal decomposition is relatively slow compared to the decomposition caused by high intensity bombardment. Crack formation can be followed visually during electron bombardment; a great number of microcracks form and then lead nuclei soon begin to appear, at first in small pits on the surface or possibly edge dislocations, then as a cover over the entire surface. The nuclei are observed to follow "preferred" directions inferring a dislocation model in nucleation on the surfaces.

Apparatus and Experimental Methods

Philips electron microscopes EM-75-B and EM-100 were employed in this study. The EM-75-B offers a choice of (direct) magnification of 1200 to 12,000 diameters. This may be increased approximately ten fold without excessive loss of detail by enlargement. The resolving power is better than 35 Å. The EM-100 offers a choice of (direct) magnification up to approximately 100,000 diameters, again with a multiplication of ten in the enlargement of the negative. Obviously sample preparation must be properly done to achieve such magnification. The resolution of the EM-100 is 15 to 25 Å and using the anode assembly of the Ladd Research Laboratories this resolution can be improved to 10 Å. Sample replication and metal shadowing were accomplished using a Kinney SC-3 High vacuum evaporator capable of attaining pressures down to 2×10^{-5} mm Hg.

The electron microscope used as a source of high energy electrons for decomposing the crystals of lead azide enabled direct observation of the crystal during decomposition, by use of special specimen carriers made by Philips. The method was to glue the crystal on this specimen carrier in such a way that the incident beam of electrons coming through the aperture of the specimen carrier was incident on a selected face of the crystal. Special conducting glue, Eccobond 56c and 60L cement of Emerson & Cumings, Inc. were found satisfactory for this purpose. All decomposition was done in the EM 75. "Positive" and "negative" replication methods were used in preparing the samples for observation. A complete description of results is given in a contract report. The method most commonly used was a "negative" replica technique specially adapted to PbN_6.

The method consists of first shadowing the crystal with germanium or another suitable metal and then replicating with carbon in the usual manner. After this step, each crystal was handled individually. The crystal was placed under a microscope in ceric ammonium nitrate replica side up and observed while the crystal was dissolving. After dissolution the carbon replica was left floating on the top of the solvent. With careful manipulation the carbon replica could be removed to a distilled water bath and rinsed free of solvent, then by approaching the replica from the underside it could be recaptured on a #200 mesh grid for examination in the electron microscope.

Furnaces of two different types were used in the decomposition, or high temperature "aging" of lead azide. One furnace was constructed in such a manner that the rate of nitrogen evolution from aging lead azide could be monitored by closing of the unit from the vacuum system and measuring the pressure increase in time. The sample was introduced into the furnace in a platinum bucket after the temperature and pressure were stabilized. The second was constructed of steel and designed so that the crystals could be observed during the entire aging cycle. This furnace permitted explosion of the sample and therefore the determination of the critical temperature of each separate sample.

Microscopic Examination of Pure PbN_6 Crystals

In general, except as otherwise mentioned only normal, undecomposed, "good" crystals were used. A crystal was considered "good" if it had uniform faces with no visible irregularities, was of sufficient size (1-6 mm long), a regular PbN_6 crystal morphology, was optically colorless and transparent, and had no internal defects as detected with a binocular microscope. Figure 13 is typical of the type of crystals found in the optical micrographs of such "pure" PbN_6. These crystals were actually better than they appeared in the micrograph because much of what was seen of the crystals was a reflection of the incident light off its faces. Note the two crystals to the extreme left of the picture were oriented in such a way as to eliminate this reflection, as a result of which they have almost disappeared. Still the crystals were not entirely perfect by the above standards.

The electron micrograph in Fig. 14 is of the (110) face of the center crystal. The appearance is one of a very smooth surface. This type of surface is characteristic of crystals that are well formed and optically clear. The black specks on the crystal face are contamination that has been extracted by the carbon replica. While Fig. 14 is typical of many faces on optically clear lead azide crystals, the micrograph of Fig. 15, which shows a different face of the same crystal, is also typical. Different surface effects may be noticed on various faces of the crystal, both in crystal growth and crystal decomposition. In this case the relative difference is not pronounced but it becomes more apparent as imperfections become more numerous. The diagonal line running through the micrograph of Fig. 15 is an uncommon occurrence in PbN_6. Note that there is interaction at its upper end with other lines of the same nature. Figure 16 is an enlargement of this surface structure showing, in addition to the structure of the line, the rugged make-up of the surface.

The crystal habit of α lead azide varies considerably but according to Miles(12) the most general habit is prismatic, with elongation being along the [100] axis and (001) plane. Elongation along the c-axis has also been described(13) the general cleavage plane is in the [100] direction, accomplished by applying the cleaving blade against the crystal along the b-direction. This convention is used here. However, in many articles the axes are interchanged. All crystals of α lead azide apparently contain faults and imperfections. The outer crystal of Fig. 13 was used to obtain the micrographs shown in Figs. 17 - 19, showing growing faces of the crystal forming along the [001] direction, the direction along which most of the growth occurs. Fig. 17 illustrates a portion of this surface with some of the accompanying crystal faults and imperfections. The apparent "preferred" direction of the surface structure of these faults usually follows along the lengthwise direction. Particularly interesting also is the fact that the small "lobes" on the surface preferentially form at surface active sites or "hot spots" located on the bases of the striated crystal faults. Additionally, the transition from a "lobe" to a small crystallite on the mother crystal face is noteworthy. Fig. 17 at 1,900 diameters illustrates the relationship between the lobes and the faults. Notice that the lobes on the more prominent fault at the left side of the micrograph show a tendency to form along the side of the fault where the energy is greatest. Fig. 18 and the enlargement in Fig. 19 show another example of this connection between lobes and faults, and the nature of "hot spot" adsorption. Note the appearance of strain at the bases of the lobes. A schematic diagram of the "hot spots" is illustrated in Fig. 20. Lobes occurring at other active sites are presumed to be due to imperfections on the surface such as emergence of dislocations(11) or an accumulation of vacancies. The possibility of such vacancy migration is discussed by Basset(14) in connection with sodium chloride crystals. It is assumed in this model, that emergent dislocations and accumulation of vacancies act to produce hot spots for added adsorption, and result in areas of accelerated growth. It should be understood that all growth processes do not show these lobes. Figures 21 to 24 illustrate other surface features common to the growing faces of lead azide crystals. Lobes are also interesting because transition from an indefinite lobe to a well defined crystallite may be observed when the crystals have very sharp, well formed and definite edges. Figures 25 and 26 show crystallites of this type growing on faces in the [001]

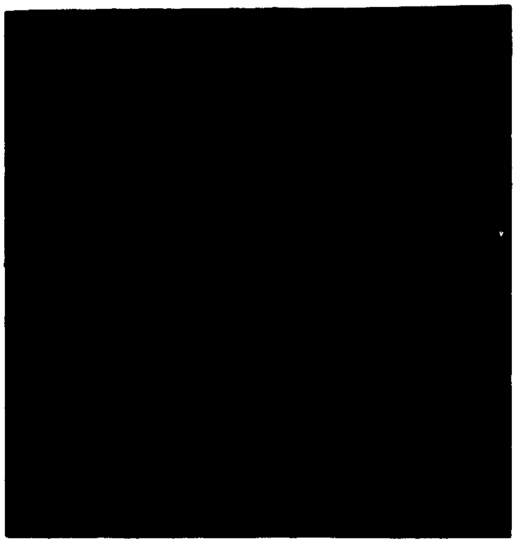

Figure 13. Optical micrograph of "good" lead azide (LA) crystals.

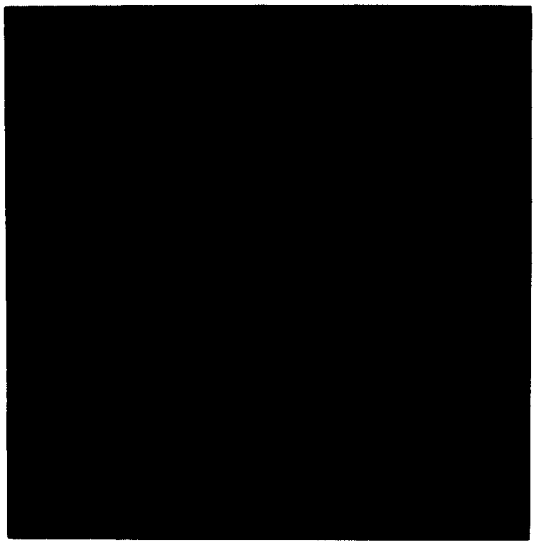

Figure 14. Electron micrograph (E.M.) of crystal. Carbon replica, 7000 X

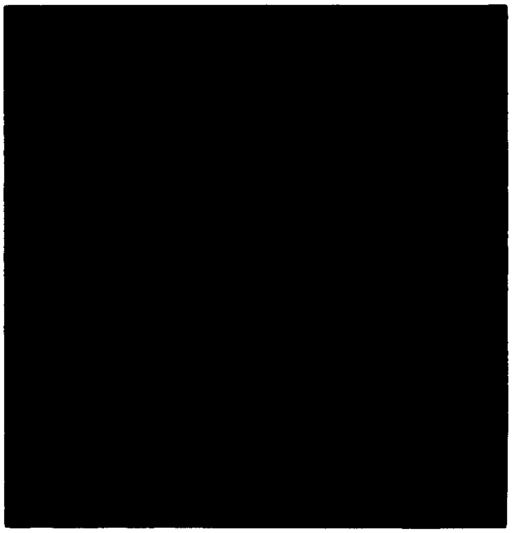

Figure 15. E.M. of LA. Carbon replica, 2500 X

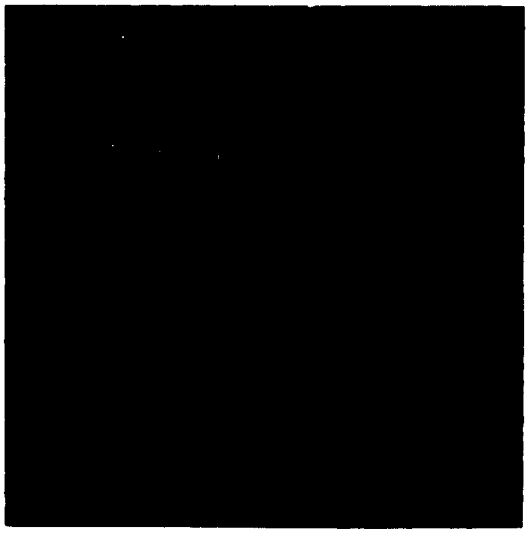

Figure 16. Enlargement of Fig. 15 12,000 X

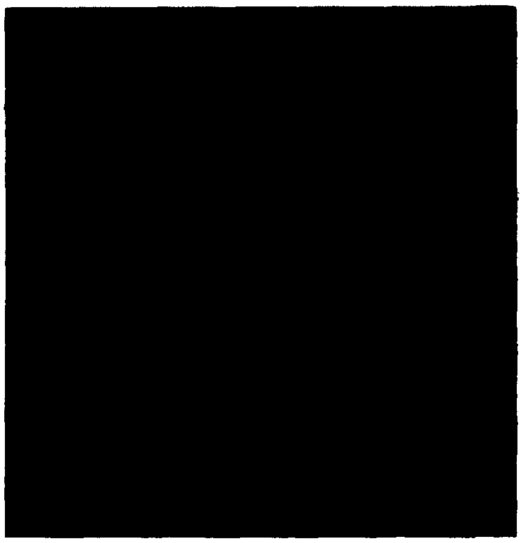

Figure 17. E.M. of growing LA. Carbon replica, 12,000 X

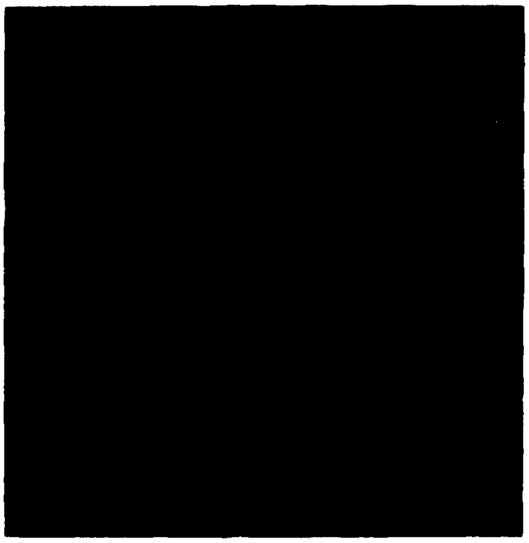

Figure 18. E.M. of growing LA Surface "hot-spot". Carbon film, 4,500 X

Figure 19. Enlargement of Fig. 18. 11,500 X

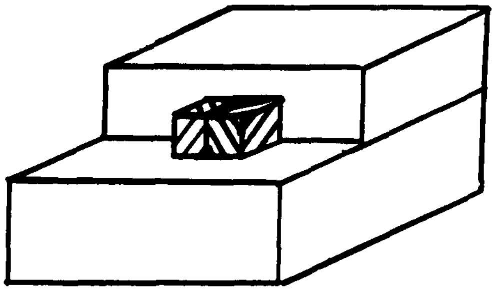

Figure 20. Schematic diagram of the "hot spot" formation.

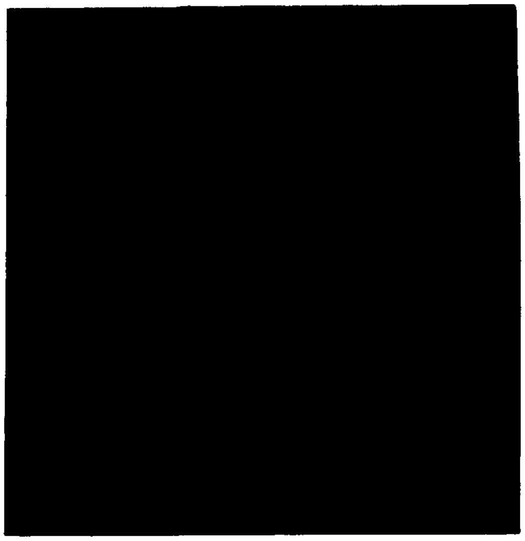

Figure 21. E.M. showing growth steps on a crystal face. Carbon replica, germanium shadowed, 5,000 X

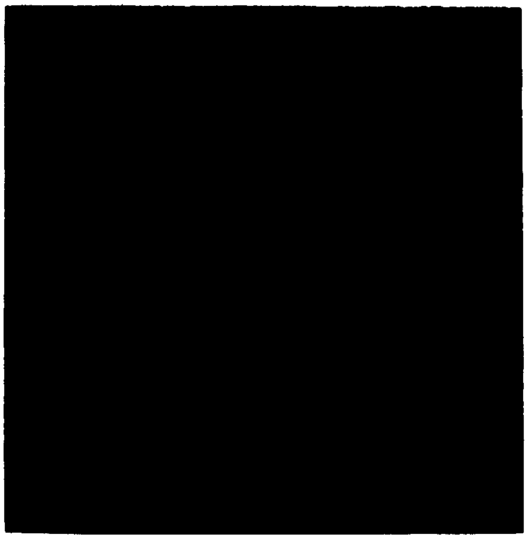

Figure 22. E.M. of LA. Carbon replica germanium shadowed, 7,000 X

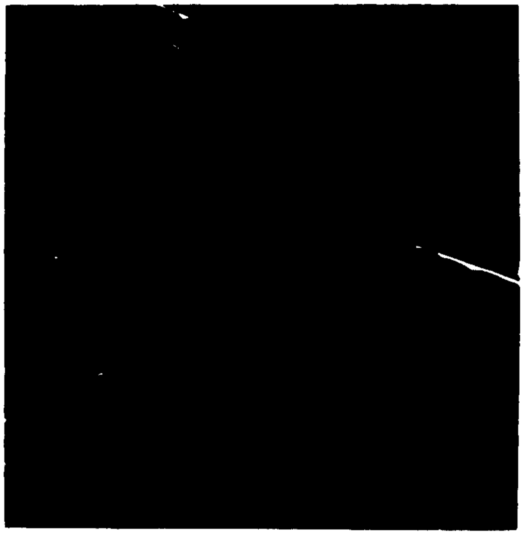

Figure 23. E.M. of LA, typical surface structure. Carbon replica, germanium shadowed. 12,000 X

Figure 24. E.M. of LA showing additional surface structure. Carbon replica, germanium shadowed, 5,000 X

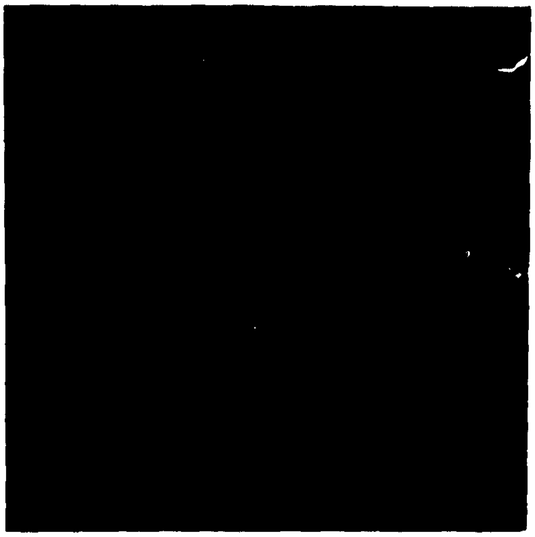

Figure 25. E.M. of pure LA, showing the transition from indefinite lobes to small crystallites. Carbon replica, germanium shadowed, 12,000 X

Figure 26. E.M. of pure LA showing unaligned crystallite structure. Carbon replica, germanium shadowed, 12,000 X

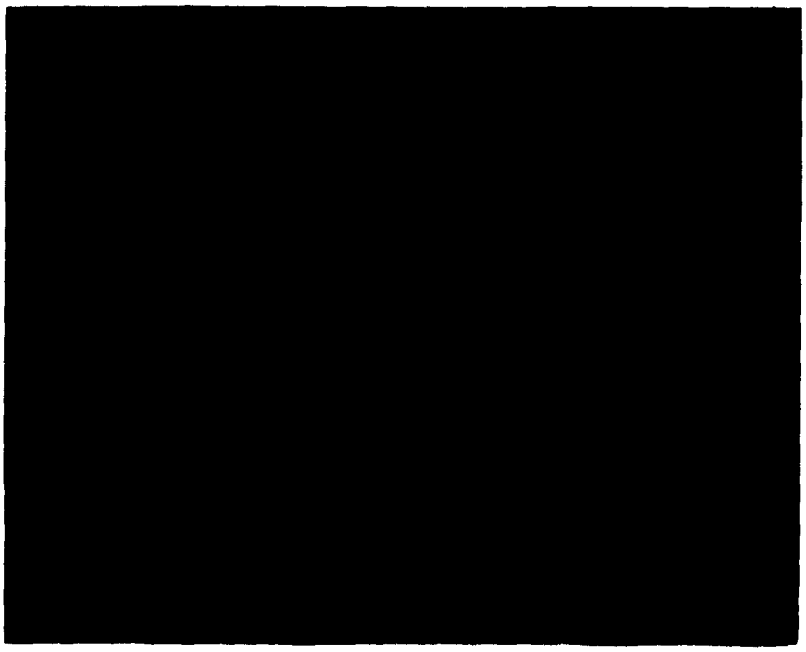

Figure 27. E.M. of pure LA showing crystallites of different orientation growing together in the later stages of their growth. Carbon replica, germanium shadowed, 12,000 X increased one half.

direction of two well formed crystals. Observe among the crystallites, lobes that have not yet transformed. The mechanism of crystallite formation on the growing faces of lead azide is not known but their presence emphasize that crystals of this type may be made up of many internal grains. Polycrystalline material can be identified by noting that there is no single orientation of the crystallites, either with respect to themselves or the mother crystal. As a consequence, the crystallites grow together as illustrated in Fig. 27. Some of the characteristics of the carbon replicas can be seen in these micrographs. The "self-shadowing" of the carbon film is evident in the deep darkening of the crystallite edges where the scattering of electrons is greatest. The "artificial" shadowing of the germanium metal evaporated onto the surface is evident from the lighter shadows cast by the crystallites. The faces of the crystallites toward the shadowing source are darkest where more germanium has deposited during the shadowing. This reversal of light and dark affects the shadows of the micrographs owing to the mode of operation of the transmission electron microscope similar, for example, to a petrographic or biological microscope in which light is removed by absorption of a portion of incident light. On the other hand, electrons are removed from the incident beam by scattering.(15) It is this fact that sometimes makes the interpretation of electron micrographs from a replica quite difficult.

The foregoing partially describes what can be seen on the surface of pure, average and good azide crystals. But since PbN_6 crystals contain numerous faults and imperfections one would expect certain surface structures to be common to them and such is indeed the case. Poor quality was more common in larger crystals, consequently the use of larger crystals required sacrifice of quality for size. The most common visible defects are cloudiness and striations. Typical striations are shown in Fig. 28. In Fig. 29 it is shown that striations are present on one crystal face (010), but in another crystallographic direction (110) there are no surface striations showing that they prefer particular directions. It is shown below that lead azide decomposes at different rates along different crystallographic directions.

By changing the conditions under which α lead azide was grown,(16) crystals were produced that were long, wide, relatively thin and contained numerous faults and crystal imperfections. The procedure was used hoping to create surface stresses that could be followed with an electron microscope. Figure 30 illustrates highly strained unusual crystals differing considerably from "conventional" α lead azide crystal. An enlargement of a single crystal is presented in Fig. 31 showing the faults and imperfections visible on the surfaces of the crystals. Figures 32 and 33 are electron micrographs of the crystal surfaces. The crystals were etched in a lead nitrate solution containing HNO_3 producing surface effects similar in some respects to

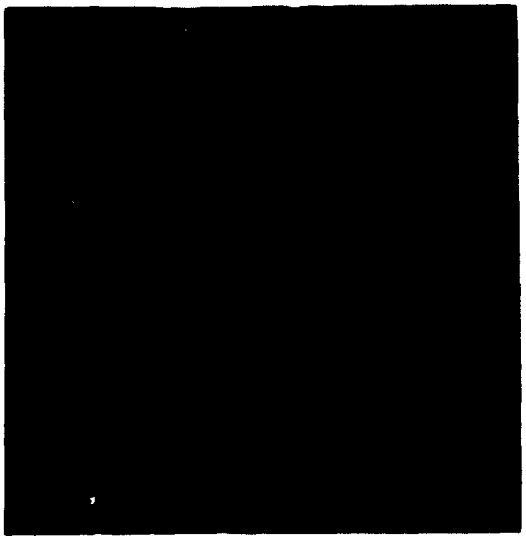

Figure 28. Optical micrograph of striated LA crystals. ca. 36 X

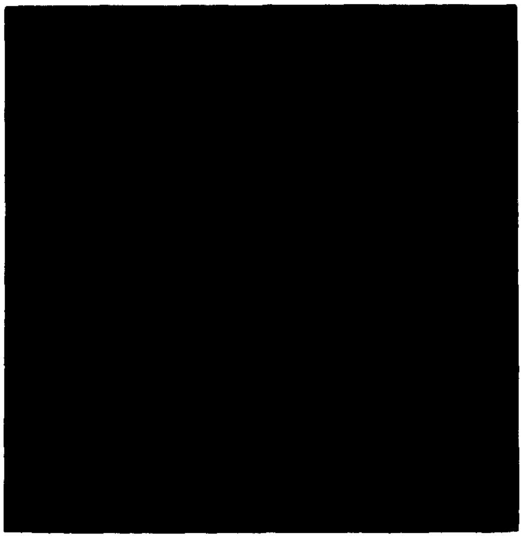

Figure 29. E.M. of LA illustrating typical striation along the [010] direction. Carbon replica, germanium shadowed, 2,500 X

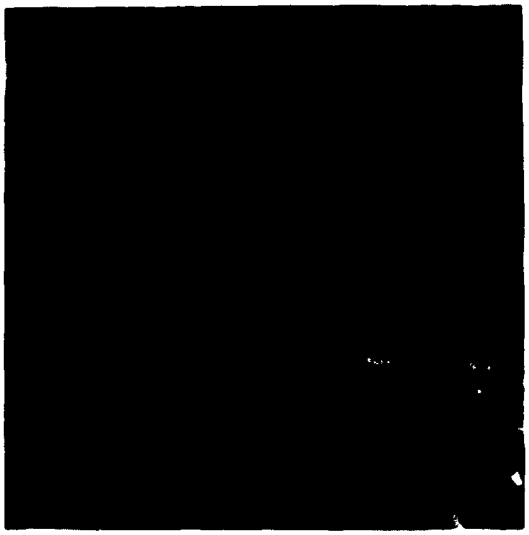

Figure 30. Optical micrograph of highly strained α lead azide, ca. 36 X

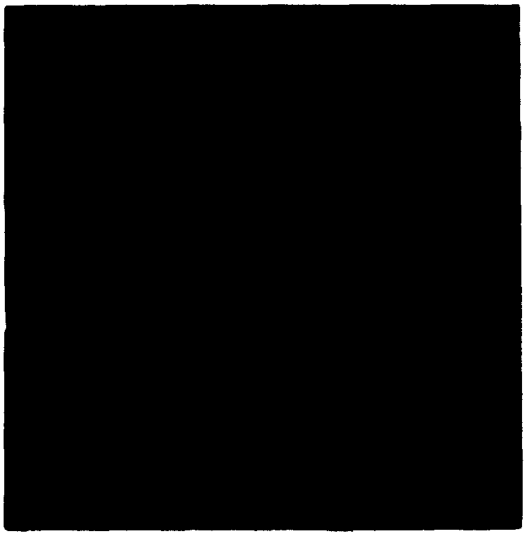

Figure 31. Enlargement of Fig. 30.

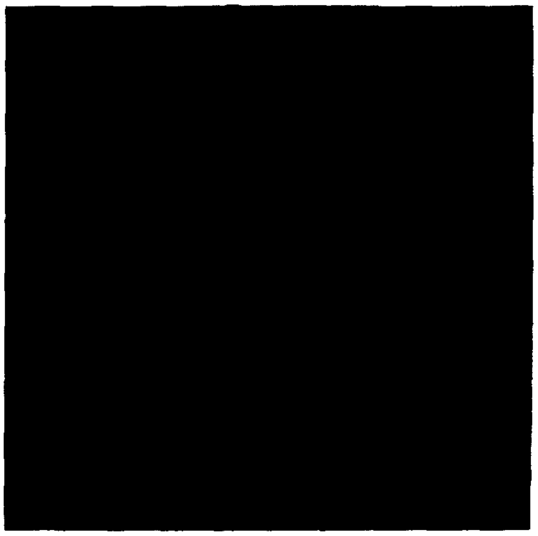

Figure 32. E.M. of α LA crystals shown in Figs. 30 and 31. Carbon replica, germanium shadowed, 2,500 X

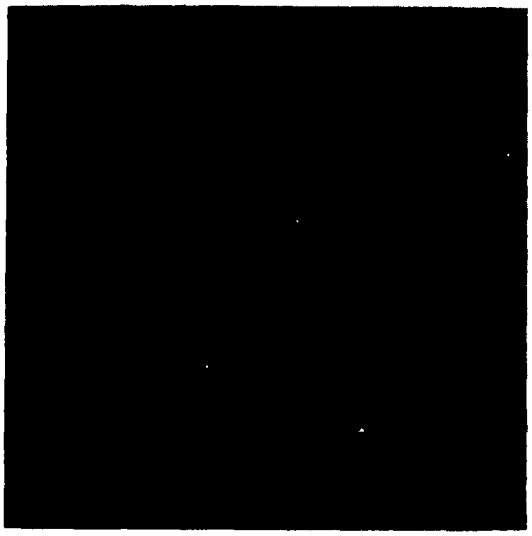

Figure 33. Enlargement of Fig. 32. Carbon replica, germanium shadowed. 12,000 X

Figure 34. Optical micrograph of LA crystals before "aging". 36 A

Figure 35. Optical micrograph of crystals aged 5 min. at 265° C. 36 X

etch pits. The object was to produce crystals in which the density of dislocations could be determined in order to study the relationship of dislocation density to decomposition rate. It is known, for example, that precipitating reactions can be initiated in silver and alkali halides along dislocations thereby "decorating" them with the alkali metal(17). No unique method has been found to precipitate the lead at dislocations, but it was hoped that these crystals would be strained enough to make some affects more apparent. This represents an initial effort in this direction. Note also, the particular arrangement of the pits in a pattern suggesting a possibility of grain boundaries. This type of surface structure, though not uniform over the face, is found in many parts of the surfaces. This evidence plus the apparent crystallite arrangement disclosed by the micrographs of Figs. 25 and 26 indicate a possibility of polycrystallinity in PbN_6. This is supported by X-ray analyses of the crystal structure of lead azide. A direct measurement of the crystallites from Fig. 27 indicated a size of 3000 Å and greater which is in the blind spot of the X-ray analysis method (10^{-3} to 10^{-5} cm), but in other cases X-ray methods indicated a range of grain sizes from 500 Å to over 1000 Å. In one instance, where a sample of ball-milled lead azide was analyzed, the grain size was approximately 95 Å.

The fact that some crystals appear polycrystalline and others show internal striation need not be disturbing. The striations could be "bundles" of sub-boundary regions of the polycrystalline grains or a series of lengthwise dislocations. In either case it appears that there is no specific relationship between the two effects; indeed there are both types of crystals present in usual methods of growing crystals, e.g. by the hydrazoic acid diffusion method.

Electron Micrographs of Lead Azide in Various Stages of Thermal Decomposition

Lead azide crystals show drastic surface changes in thermal decomposition. Severe stress and strain always accompany decomposition and are manifest by convolution and cracking of the surface. During the surface activity lead nuclei form, extremely small at first but finally in a complete shell or layer over the crystal faces. Lead nuclei form preferentially on certain of the crystal faces. In many cases lead nuclei seem to form first, and are larger, on faces of the crystal that are striated, although this may be merely coincidental. Unfortunately, it has been impossible to remove the final blackened layer from one face in order to measure its thickness relative to another. Nevertheless, cross-sectional cleavage has been attempted in conjunction with the electron microscope. While attempts along this line have not been completely satisfactory owing to the very small cross-sectional area of a crystal and the necessity of doing all such sample preparation under an optical microscope, some success has been achieved by selectively placing the carbon replica on a grid and aligning the carbon film in such a way that the replica is situated over an open area of a square grid about 73 μ wide. By this means it was observed that there is a tendency of certain faces to build up different depths of lead during decomposition emphasizing that more decomposition has taken place along certain preferred directions.

Most observers agree that lead nuclei strongly catalyse further decomposition. In fact silver nuclei on the surface of lead azide also catalyse the decomposition of lead azide even in the absence of lead nuclei(17). Since surface contamination may also be important, it became essential to know as much as possible about the detailed structure of the surface. Atoms are more easily removed, for example, from step edges, kink sites, or corners than from a site within a close-packed face. Theoretically nitrogen gas is formed in PbN_6 by the reaction $2N_3^0 \rightarrow 3N_2$ at the surfaces (and internal flaws) of the crystals. The removal of N_2 from the surfaces of a crystal would then be dependent upon the above physical conditions, since energy differences may be expected to lead to a difference in the tendency for nitrogen to escape from different parts of the surfaces. Slight changes of sensitivity possibly arise from severe strain near the core of a dislocation emergent upon a surface. It is this added strain energy of the monoclinic β lead azide that has been considered responsible for the transformation of β lead azide to α lead azide.

A typical trace of the rate of nitrogen gas evolution for PbN_6 is given below (see also Hill[19], Love[20], Reitzner[18]). It has been

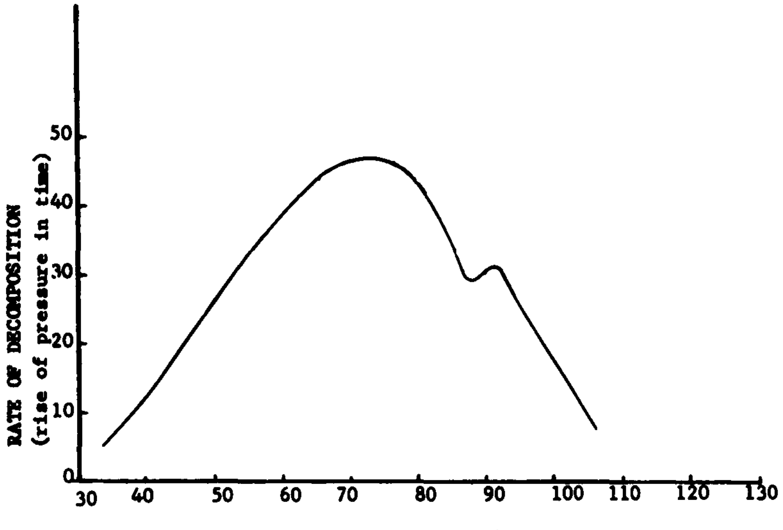

Rate of decomposition as a function of time at 255°C proposed by various investigators(19) that decomposition proceeds most rapidly at the point when the lead nuclei form a continuous layer on the surface of the azide. In studying this effect freshly grown crystals were used similar to the type pictured in the optical micrograph of Fig. 13. Henkin and McGill(21) reported the explosion temperature of lead azide as 315° C and Bartlett, Tompkins and Young(22) reported that it explodes in a vacuum at 290° C, but explosion temperatures as low as 245° C have been reported also for lead azide.(23)

Figures 34 to 41 show a sequence of optical micrographs of lead azide crystals aged (heat treated for various times at 265° C plus about a ten minute heating period to 265° C in each case). Figure 34 shows a micrograph of undecomposed crystals. The crystals before decomposition were generally clear with no trace of coloration except for the localized striations and internal faults described above. Figure 35 shows a micrograph of crystals aged 5 minutes. No external change was visible, but internally there occurred a color change from clear crystalline to a light yellow, opaque appearance. Figure 36 shows a micrograph of crystals aged under the same conditions 15 minutes. The only additional change was deepening of the yellow coloration of the crystal. Figure 37 shows a micrograph of crystals aged 30 minutes at 265° C. An external change has taken place in this case as evidenced by the beginning of a darkened layer of lead on some of the crystal faces. It should be noted that the lead is forming preferentially on the (010) faces of the crystal. Figure 38 shows a few of these crystals extracted from the rest of the group to show this effect. The crystal to the far left was cleaved in the (001) direction and rotated to expose the (110) face to show that no lead nuclei had formed except on the (010) face. With continued aging at 265° C (45 minutes) the changes taking place were more noticeable as shown in Fig. 39. The significant changes at 45 minutes were that the (010) planes were even darker and the yellow opaque coloration had begun to change to a milky white. When the aging time was extended to 75 minutes at 265° C, the black layer on the (010) became heavy and other faces became quite dark as shown in Fig. 40. A number of crystals had a heavy black deposit on the (010) with other faces now graying perceptibly. At 90 minutes aging at 265° C crystals became uniformly darkened (Fig. 41). Removal of the outer scale or cleavage of the crystals revealed a totally milk-white crystal in the interior. The color transition occurring during decomposition was therefore from a clear transparent crystalline material for the undecomposed crystal to a light yellow opaque one, gradually darkening to deeper yellow until lead nuclei became visible to the eye, after which the color in the interior of the crystals began a change from a milky yellow to a milky white, remaining this color under the lead film until completely decomposed. Figure 42 shows a crystal completely covered with lead; it is of considerable interest in revealing many of the characteristics of decomposition.

Figure 36. Optical micrograph of LA aged for 15 min. at 265° C. 36 X

Figure 37. Optical micrograph of LA aged for 30 minutes at 265° C. 36 X

Figure 38. Optical micrograph of selected LA crystals from those shown in Fig. 37 showing decomposition along the (010) plane. 36 X

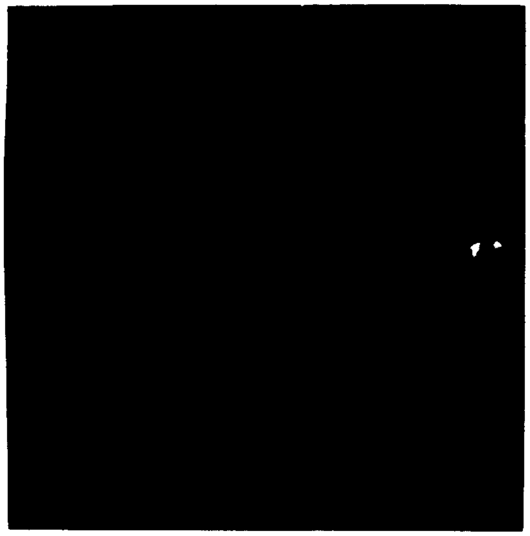

Figure 39. Optical micrograph of LA crystals aged 45 minutes 265° C. 36 X

Figure 40. Optical micrograph of LA crystals aged 75 minutes at 265° C. 36 X

Figure 41. Optical micrograph of LA crystals aged 90 minutes at 265° C. 36 X

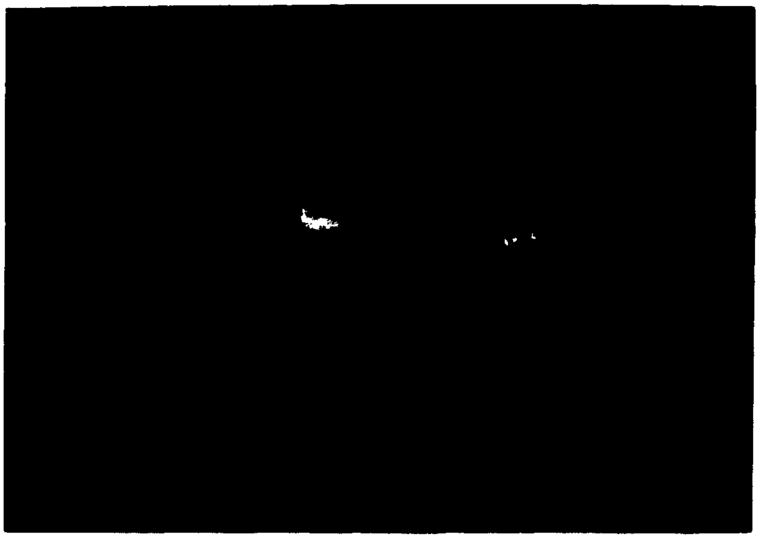

Figure 42. Optical micrograph of LA crystals aged 90 minutes at 265° C, showing self-made film and lead scale formation. 36 X

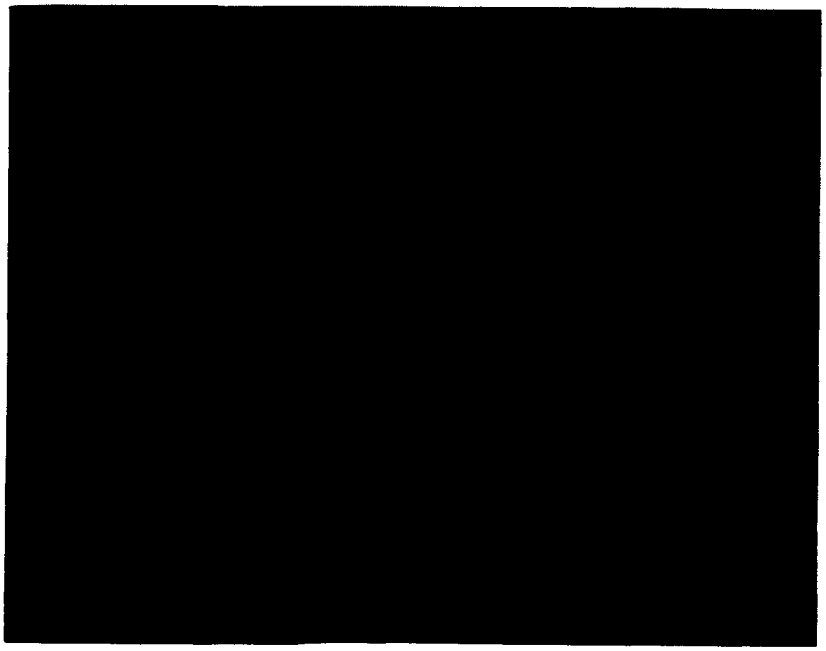

Figure 43. "Self-made" film on partially decomposed α LA aged 90 minutes at 265° C.

At the upper edge of the crystal to the right is a portion of the outer shell that was chipped off showing the white interior of the crystal. The whitened area on the upper left portion of the crystal proved to be a light colored "chip" of PbN_6 on the surface of the crystal, upon which no lead nuclei had formed. Next note the bubble formation on the surface of the crystal. This bubble structure occurred in a "self-made" film on top of the scale of lead. An electron micrograph of it is shown in Fig. 43 from which it was determined to be only about 100 to 200 Å thick. This film was discovered accidently when an unreplicated crystal happened to fall into a dilute solution of ceric ammonium nitrate while under observation with a stereomicroscope. Following the normal bubbling due to nitrogen release during dissolution, a very thin, slightly yellow film was observed floating on the surface of the solution. It was transferred to a #200 mesh grid, washed in distilled water and after drying examined in the electron microscope. A film of considerable interest was observed; it contained many "bubbles" dispersed over its surface. The bubble sizes varied extremely from greater than 73 μ to smaller than 1000 Å. It was found to be a reaction product working from the outside in, while the black layer of lead was a reaction product of an inward reaction working outward. It is not known why the bubbles do not form over all the area at one time, and are completely absent at other times, but they are regularly formed as crystals are decomposed.

When crystals are decomposed for longer times or at higher temperatures a distinctive "shell" begins to form. The surfaces of the crystal begin cracking and "peeling" to reveal inner portions which are still milky white in color. This shell can be completely removed from the crystal as illustrated in Fig. 44. The inner portions of the crystal soon begin to darken eventually to reform the shell. On the surface of this shell is a very shiny film. This "self-made" film which may be captured does not show bubble formation either in the electron microscope or the optical microscope. Apparently once the shell has formed bubble formation is quenched and the film becomes that shown in Fig. 45. The differences between the crystals shown in Figs. 42 and 44 are unknown because both types of crystals were present following decomposition. The difference may be due to a temperature differential in the sample. The electron micrographs of Fig. 45 show the actual films taken off the surface of a "shell" similar to the pieces shown in Fig. 44. The films were separated from the shells by solution in ceric ammonium nitrate. These results show (1) that a film exists on the surface of the shell and (2) that the shell is still some form of lead azide since it decomposes in ceric ammonium nitrate with the liberation of N_2 gas. However, the rate of reaction is slower for the shell than for unreacted PbN_6. The shell is perhaps a defect structure of lead and PbN_6 with a large stoichiometric excess of Pb; it is dark grey in color and brittle. The "shell" of the right crystal in Fig. 44 was 12 μ thick on the (110) faces but 18 μ on the (010) face. The relative dimensions were the same in the left crystal, illustrating a greater rate

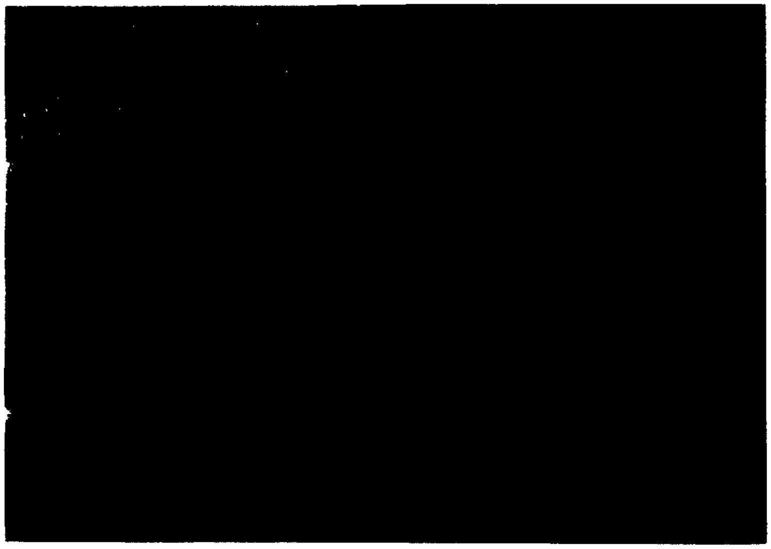

Figure 44. Optical micrograph of two decomposed α LA crystals that have formed shells which have been removed to reveal the crystal beneath. 36 X

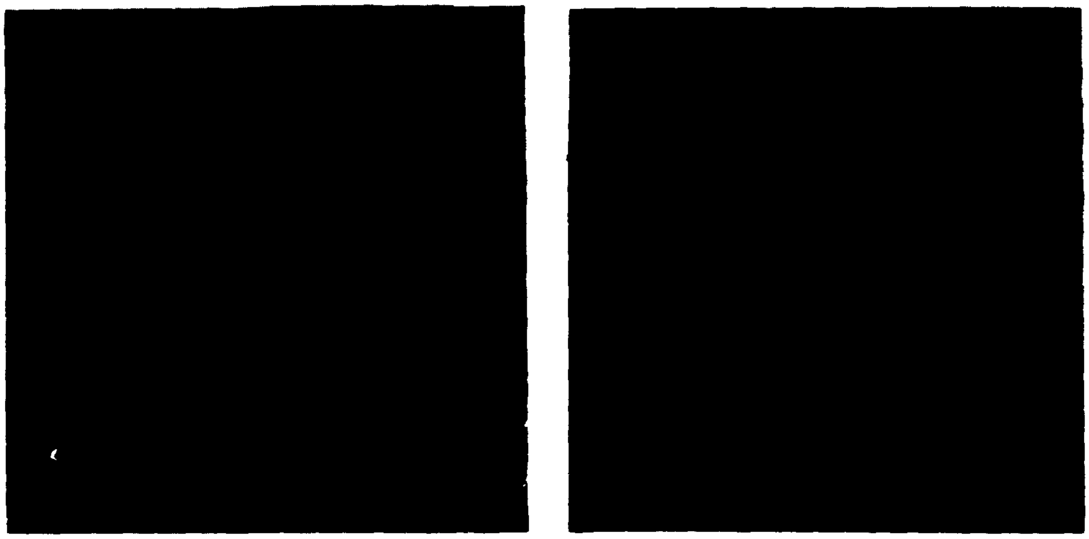

Figure 45. Two E.M. of a self-made film taken from the surface of a shell formed on the shell structure of Fig. 44. 4,600 X

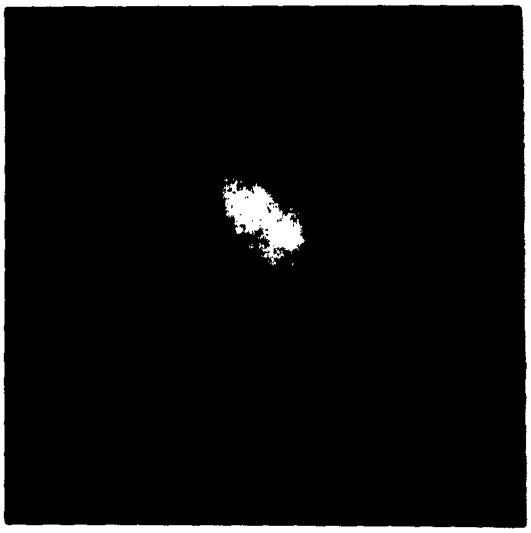

Figure 46. Optical micrograph of a cross-section along the [001] direction of α LA decomposed in air at atmospheric pressure. 36 X

of decomposition on the [010] face of the crystal. The same results were obtained in decomposition in air, nitrogen and vacuum.

A much different effect is observed where lead azide crystals are decomposed in air at atmospheric pressure. The crystal turns a pale yellow with complete opacity as it does in a nitrogen atmosphere or vacuum, gradually becoming darker in time. The transition is from the outside in. This part of the crystal is now more crystalline indicating recrystallization. As the first yellowing began a cross-section of the crystal cleaved along the (001) direction revealed that the inside of the crystal was milky white, with a granular yellow exterior. Figure 46 shows a cross-section of a typical crystal decomposed in this fashion. The outer granular (yellow) layer can be seen on the left side of the crystal. With continued heating this yellowing proceeds through the crystal. Again the milky whiteness of the crystal at the early stages of decomposition indicates lead condensing out in the interior of the crystal at dislocations and internal crystal defects. The yellow exterior layer is thought to be PbO.

Study of partially decomposed PbN_6 in the electron microscope shows interesting changes on the surface during decomposition indicating the importance of surface and lattice singularities. To eliminate as many unknowns as possible in the interpretation of electron micrographs, preliminary studies were made with artificially prepared surfaces using carbon films as the replicating medium. The purpose of this was to establish the reliability of the replica technique. In addition, lead was evaporated on the surface of pure undecomposed lead azide crystals by vacuum techniques to study its characteristics, for example, to determine possible surface mobility, or to see if lead goes preferentially to certain surface sites, or distributes itself uniformly over the surface clustering into nuclei. Figures 47 and 48 show micrographs of a specially made, featureless carbon film onto which lead was artificially deposited. It has been reported(24) that Tl (melting point of 302° C) will melt and "evaporate" in a beam of electrons. Lead however (melting point 327.43) is very stable; the electrons seem to have no influence at all on the lead deposited on a carbon film. This information greatly facilitated the interpretation of electron micrographs since a carbon film may or may not extract lead nuclei from the surface. Figures 47 and 48 show the habit of lead on an inert surface such as a carbon film. Note that the lead formed "islands" on the surface of the film. The size of these islands was about 0.5 μ. In the "shadow" of the main particle can be seen lead nuclei that range in size from 30 to 300 Å. This also indicates some mobility of the lead atoms as they contact the surface; apparently that can move about 300 Å along the surface in clustering. One might thus expect a similar migration of lead on an azide surface. In order to check this suggestion as well as to observe the habit of lead on an azide crystal face, nuclei were artificially deposited on the surface of lead azide by vacuum evaporation until the exposed faces of the crystal had a visible, continuous layer on them. These faces were then replicated with a carbon film and examined in a microscope with the results shown in Figs. 49 and 50. The lead nuclei formed in high concentrations over

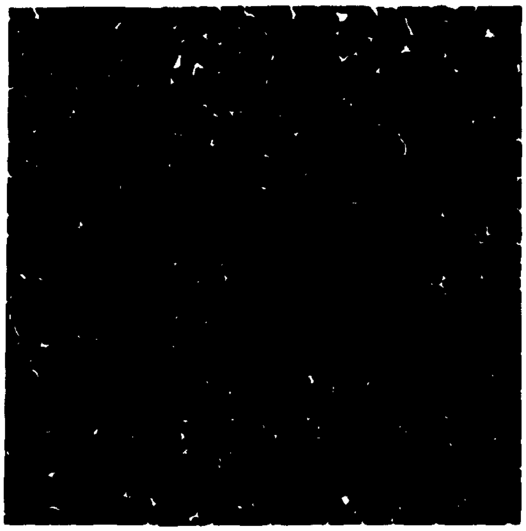

Figure 47. 12,000 X
Figure 48. 10,000 X
E.M. of pure lead evaporated on an "inert" carbon film illustrating the nature of lead on the surface.

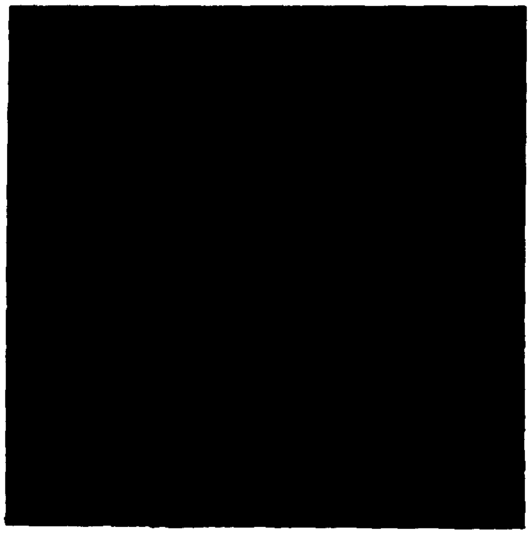

Figure 49. E.M. of artificial lead nuclei on the surface of freshly grown LA. Carbon replica, no shadowing, 10,000 X.

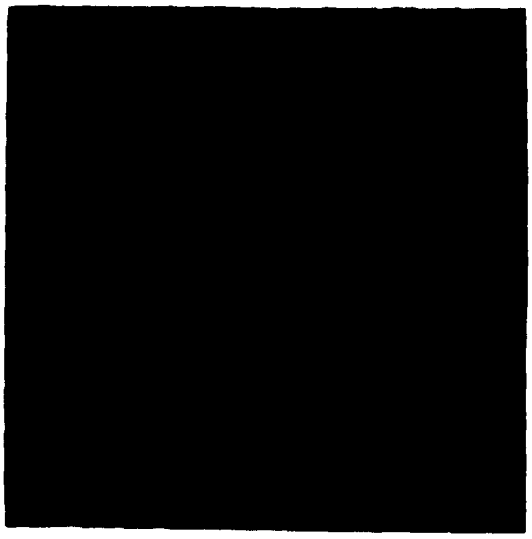

Figure 50. E.M. of artificial lead nuclei on the surface of freshly grown LA. Carbon replica, no shadowing, 12,000 X.

the surface similar to the striations on the carbon film. In these electron micrographs, the carbon formed a replica of the nuclei of nodular shape. Figure 51 shows a cross section and underside view of the surface shown in Fig. 50 giving evidence of the shape and configuration of nodules. Observe that in some cases a small portion of the lead remained in the upper portion of the carbon envelope while in other cases all lead "washed" away during dissolution of the original crystal. Therefore, if the lead nuclei become too large the carbon film will no longer "extract" them from the surface. This condition was described by Klein and Matejic in their studies of the formation and growth of silver nuclei on the surface of small microcrystals of silver halide.(25) To establish a definite and positive pattern of lead evaporated onto the surface of freshly grown crystals, numerous replicas were made, always with the same result except for fluctuations in the size of the nuclei. The heaviness of lead deposit determined the resulting size of the nuclei. The approximate average size of nuclei in Fig. 50 is 0.5 μ while that in Fig. 49 is only 0.1 μ. In the former the face of the crystal was more closely oriented to the source than in the latter with the result that more lead fell on the face.

Decomposition of lead azide takes place in stages, certain of which are difficult to observe, but others are very easily detected. In each stage there are unmistakable "repeats". Figure 52 shows an electron micrograph of an azide crystal aged for 5 minutes at 265° C. This micrograph shows a background of what is probably lead nuclei extracted by the carbon replica in the earliest stages of formation. Note also that nucleation of the lead on surface or lattice singularities has occurred about at the atomic level. This background may be shown in much greater detail by enlargement (Fig. 53). Close observation of this micrograph also reveals stages of nuclear development in which nuclei formation is more definite. Indeed, the lead specks can be traced from this early stage to positive identification as "pure" lead nuclei, that is, it can be shown that the nuclei are strictly lead and no other intermediate compound. This does not, however, rule out the possibility of various contamination compounds forming elsewhere on the surface. Figures 54 to 59 show electron micrographs of crystals aged 15 minutes at 265° C. At this stage no darkening of the surfaces has occurred, but the crystals have colored. It has been mentioned that the general coloration change in initial thermal decomposition is to a light yellow opaque tint, but in this case, the crystal changed instead of a light yellow to a light pink, indicating that color centers are being formed. This internal coloration does not occur when the crystals are decomposed by bombardment with electrons or radiation in the ultra-violet region. The surfaces of these crystals show a most interesting affect, namely the development of "pits" around the nuclei (Fig. 54). By tracing the small specks through continuous growth stages one observes that they transform ultimately into lead nuclei (Fig. 55). There are in Fig. 55

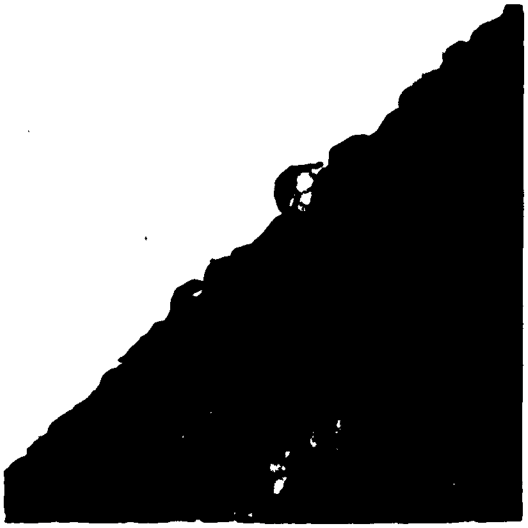

Figure 51. E.M. cross-section of Fig. 50. Carbon replica, 12,000 X.

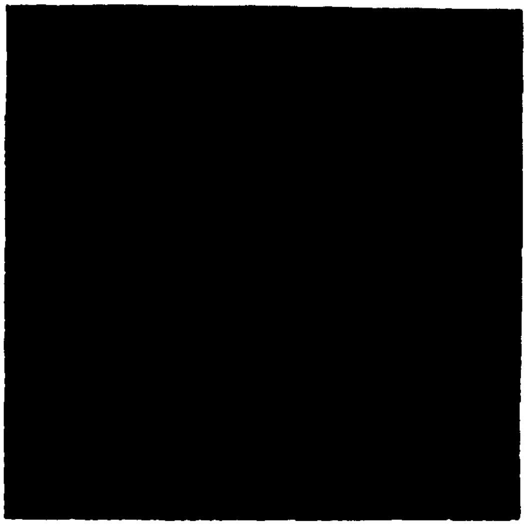

Figure 52. E.M. of LA aged 5 minutes at 265° C. Carbon replica, 4000 X.

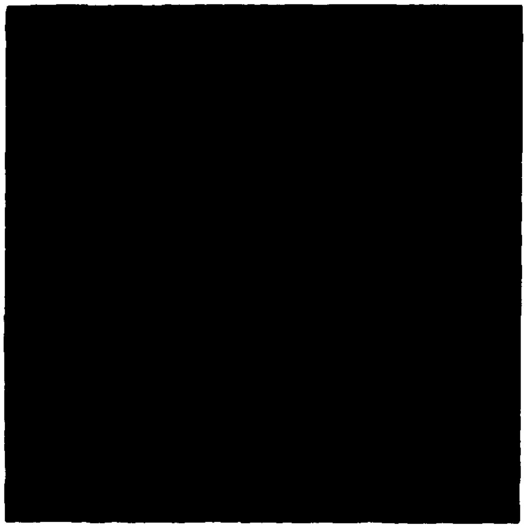

Figure 53. E.M. of LA aged for 5 minutes at 265° C, showing a fine background of lead beginning to form. Carbon replica, 10,000 X

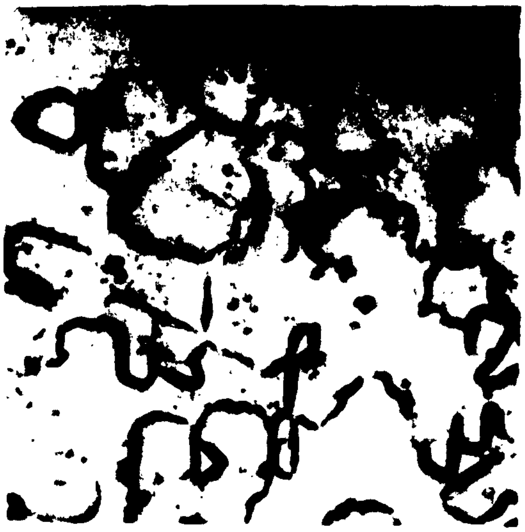

Figure 54. E.M. of partially decomposed LA showing definite lead nuclei formation in pits. Carbon replica, no shadowing, 12,000 X

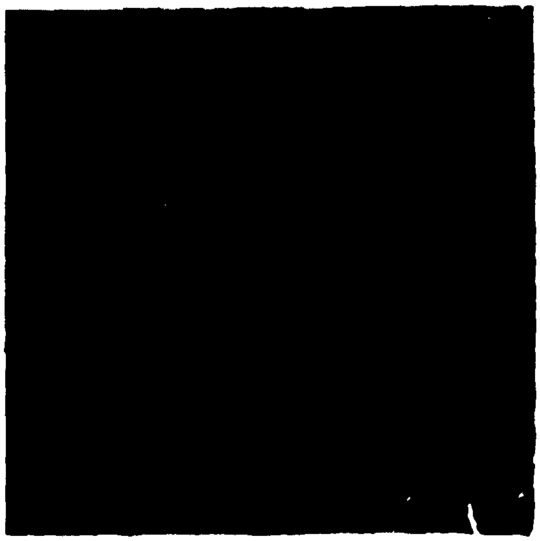

Figure 55. E.M. of aged LA showing transformation of specks to real lead nuclei. Carbon replica, no shadowing, 27,000 X

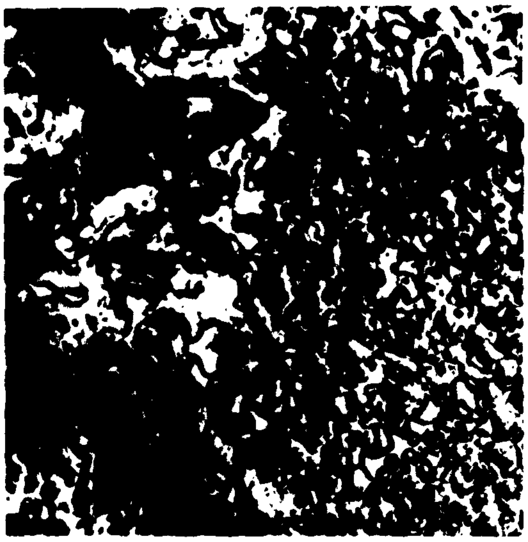

Figure 56. E.M. of partially decomposed LA showing large and small nuclei on a single crystal face. Carbon replica, 27,000 X

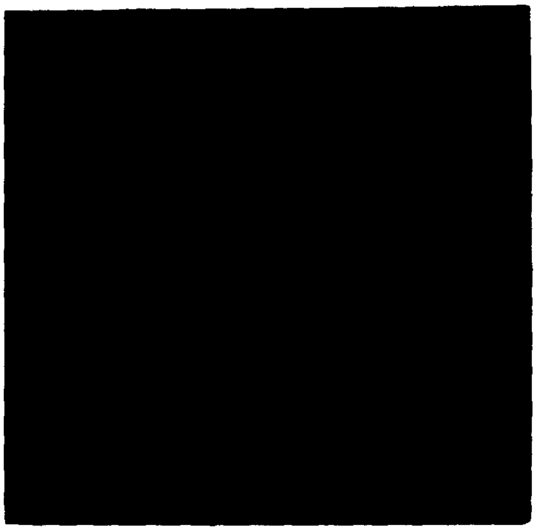

Figure 57. E.M. of LA aged 15 minutes at 265° C showing contaminant. Carbon replica 6,000 X

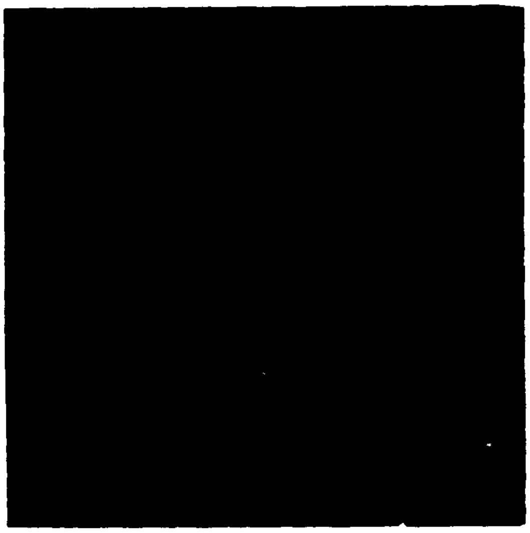

Figure 58. E.M. of LA aged 15 minutes. Nuclei along a series of emergent dislocation lines. Carbon replica, 4,000 X

nuclei ranging in diameter from 50 Å to as large as 1000 Å. An unusual effect seen in Fig. 56 is nuclei of 2000 Å and those of about half this diameter appearing immediately to the side. The most probable reason for this is the preference for lead to form on certain faces with the likelihood that the interface between the two areas is a grain boundary. The grain in the left portion is more favorably oriented for the diffusion of the lead ions.

Figure 57 shows a contamination commonly present on crystal surfaces through all stages of heat treatment. Some have suggested that this contamination may be lead carbonate or nitrides forming as intermediate products of decomposition. Since the crystals shown in Fig. 57 were decomposed under a vacuum below 0.1 μ pressure, it is more likely that the contaminants are nitrides. The growth of the contaminant structure is independent of the growth of the nuclei; both appear on the surface either together over the same area or appear separated. A common nuclear growth more prevalent than the extracted nuclei shown in Fig. 55 is the replicated surface structure shown in Fig. 58. These nuclei are larger than those shown in Fig. 55 (ca. 0.5μ) and probably account for the lead being lost during dissolution of the sample from the carbon replica. The arrangement of nuclei along certain directions is noteworthy; it is along the emergent dislocations described above. Figure 59 illustrates an early stage of a type of structure that becomes prominent with continued decomposition, namely an extremely fine background of lead nuclei beginning in a pattern like the spokes of a wheel.

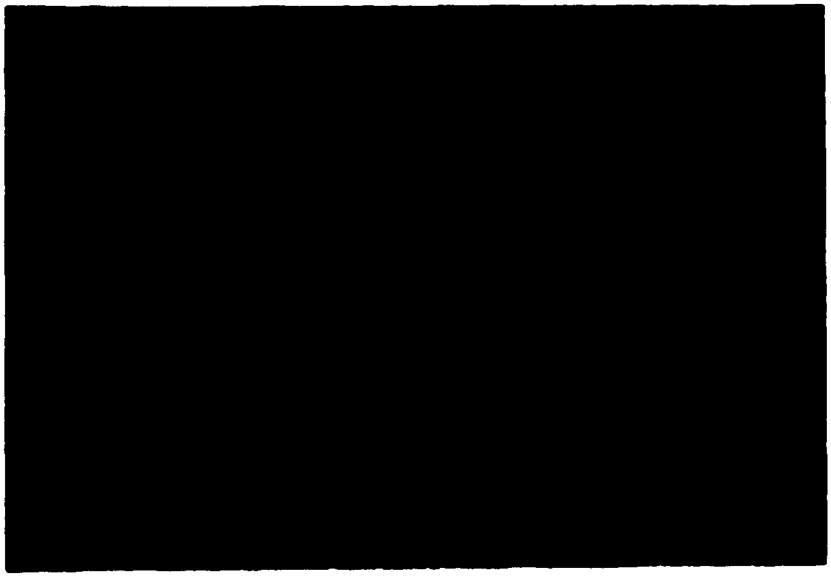

Figure 59. E.M. of LA aged 15 minutes at 265° C showing spoke-like orientation. Carbon replica, 4,000 X

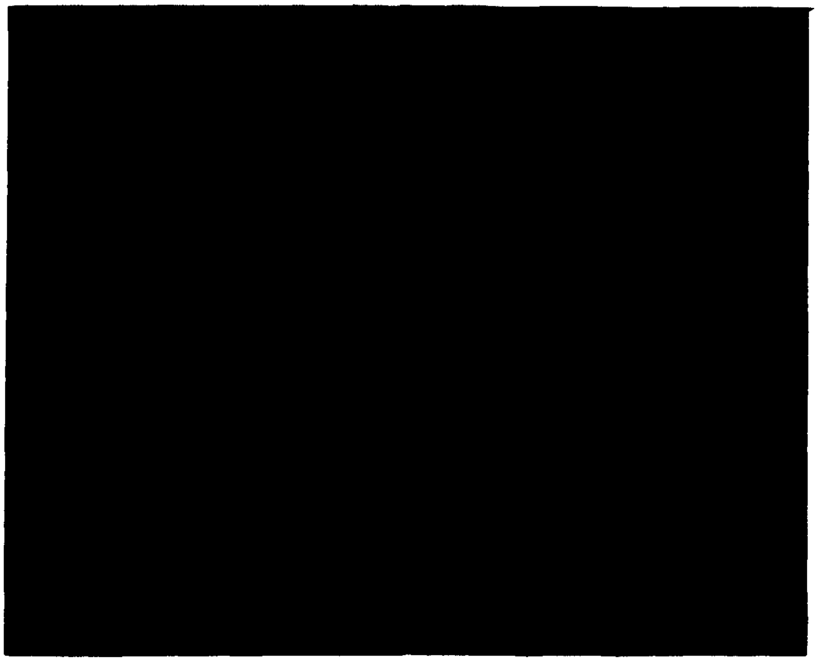

Figure 60. E.M. of LA aged 30 minutes at 265° C showing lead nuclei growth around a surface imperfection. Carbon replica, 3,000 X

Figure 61. E.M. of aged LA showing typical non-reactive face of crystal. Carbon replica, 12,000 X.

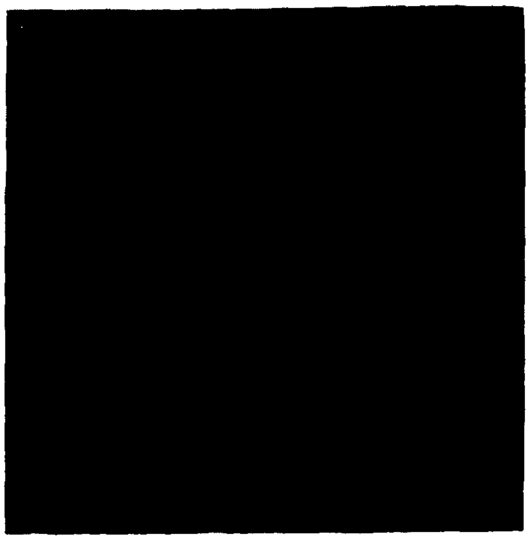

Figure 62. E.M. of LA aged for 45 minutes at 265° C showing lead nuclei on the (010) crystal faces. Carbon replica, 3,000 X

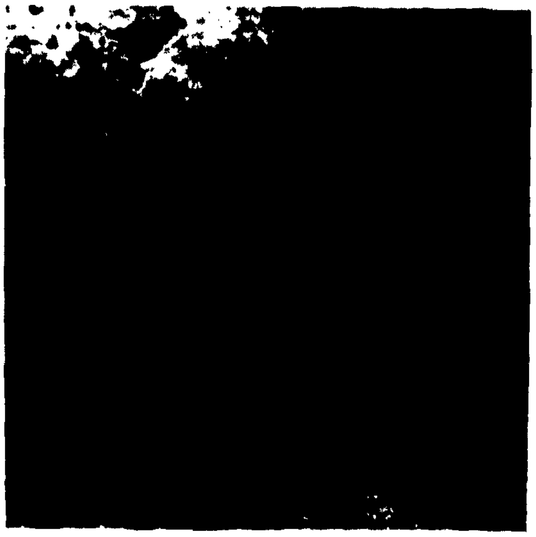

Figure 63. Enlargement of Fig. 63. Carbon replica, 12,000 X

Electron micrographs of crystals aged 30 minutes at 265° C shown previously in an optical micrograph are shown in Figs. 60 and 61. It is interesting to note in Fig. 60 that certain surface conditions catalyse the formation of lead nuclei. Such nuclei also seem to occur prominently on the (010) face. Since lead nuclei evidently catalyse the decomposition, such cancerous growths of nuclei might tend to sensitize lead azide, conversely, pure lead azide free of such growths should be less sensitive. Crystals aged for 45 minutes at 265° C show the (010) face to be much darker and these growths to be much more pronounced. Other faces remain relatively unaffected except for gradual, uniform darkening. For example, Fig. 62 shows an electron micrograph of large lead nuclei (approximately 4.3 μ in size) on the (010) face, also easily seen with an optical microscope. The lead azide crystal may be seen to shrink away from the Pb nuclei owing to the catalytic decomposition of the crystal at these sites. The result is the evolution of N_2 at the interface with a consequent production of anion vacancies. An enlarged micrograph of these nuclei (Fig. 63) show a pronounced nodular structure indicative of the mechanism of formation of the nuclei. On the other hand the micrograph taken of the adjoining face (Fig. 64) showed that no nuclei of this size and nature grew anywhere but on the (010) face, where they grew very extensively.

Another recurrent condition shown in Fig. 65 is also characteristic of decomposition of lead azide; it is evidently similar to the condition illustrated in Fig. 57.

Figure 64. E.M. of LA aged for 45 minutes at 265° C showing a portion of (010) face (lower portion of micrograph) next to the adjoining face. Carbon replica, 1,500X

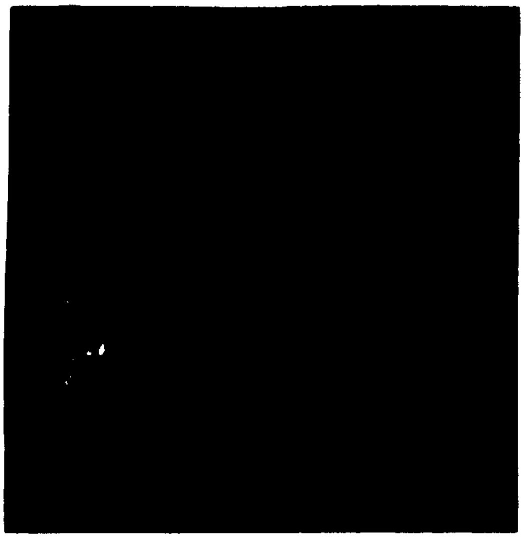

Figure 65. E.M. of LA aged 45 minutes at 265° C illustrates a recurring structure. Carbon replica, 10,000 X.

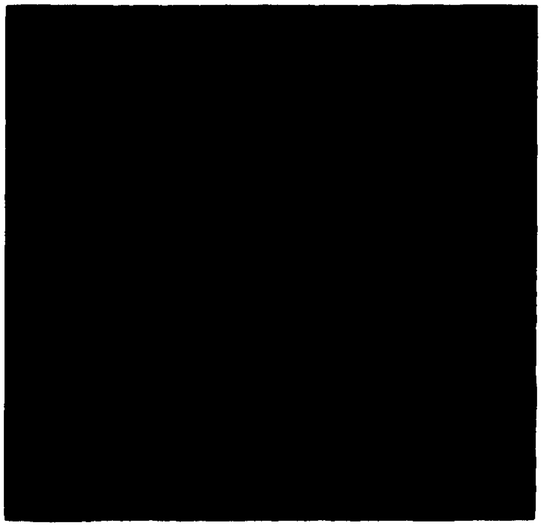

Figure 66. E.M. of LA aged for 75 minutes at 265° C showing a self-made film. Carbon replica, 2,000 X

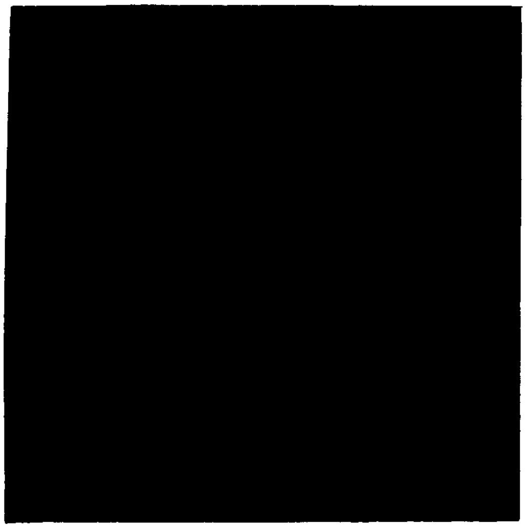

Figure 67. E.M. of LA aged 75 minutes at 265° C showing part of crystal "drying up". Carbon replica, germanium shadowed, 6,000 X

Samples aged 75 minutes at 265° C developed several new phenomena noteworthy among which is the "self-made" film described above. Figure 66 shows pieces of this film sticking to the carbon replica. It is very susceptible to damage by electrons or handling. Indeed the micrograph shows patches of cracked and broken film. It forms on the outer portion of the crystal exterior to the layer of lead scale and the "shell" formed during decomposition. It is during this stage that severe surface convolution and strain begin to develop. Where the crystal was previously relatively smooth, after aging 75 minutes at 265° C many parts of the surface took on the characteristics depicted in Figs. 67 and 68 and the even more general character shown in Fig. 69. The decomposition of the crystal followed along preferred directions. The cracking was due to the expulsion of nitrogen from the surface at its greatest rate in these directions because of the rapid lead nuclei growth in preferred directions, e.g., along edge dislocations. Additional surfaces created by this cracking process, contribute to the release of nitrogen so that large cracks become larger and deeper providing additional area for lead nuclei formation and nitrogen evolution. Over the area covered by Fig. 68, very small Pb specks (100 Å and less) have nucleated instead of the larger nuclei that form under other crystal conditions. These nuclei are located on the surfaces of small "islands" in all possible positions afforded them by the extended surfaces. The probable reason for the numerous but very

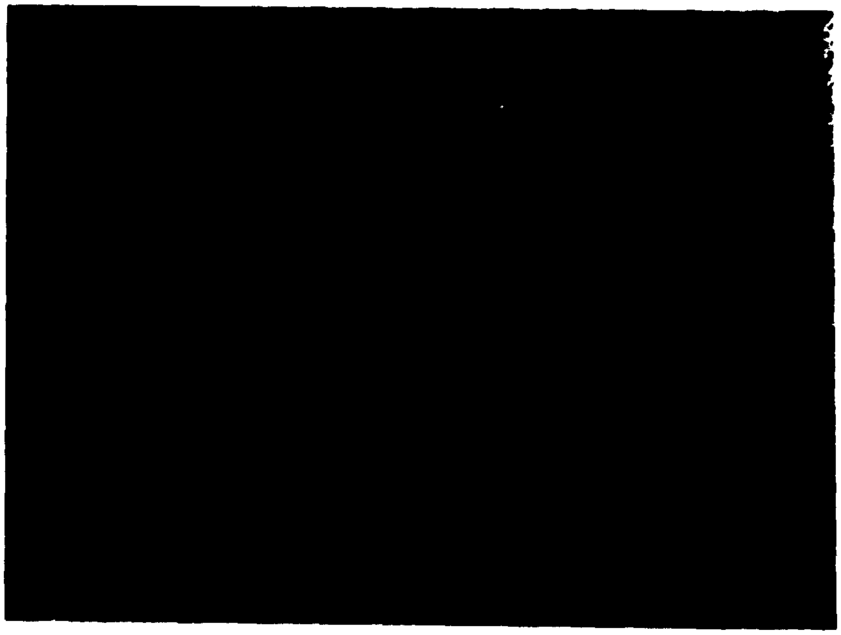

Figure 68. Enlarged E.M. of Fig. 67. Note lead nuclei formation. Carbon replica, germanium shadowed. 26,000 X.

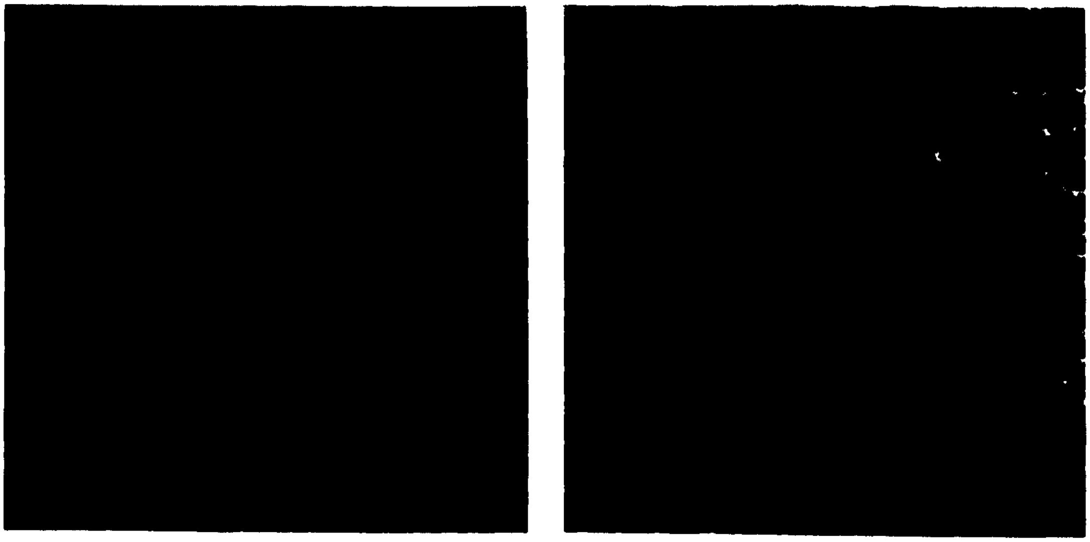

Figure 69. Two E.M. aged 75 minutes at 265° C showing surface undergoing convolution. Carbon replica, germanium shadowed. 12,000 X

small nuclei is that a great many more lead specks have nucleated on internal and external surfaces due to cracking. When the separate lead nuclei get large enough to touch, their surface tension makes them run together into a single particle like droplets of mercury, and as in artificial evaporation of lead onto the surface of freshly grown PbN_6. At this stage the growth of the lead nuclei is rapid, as illustrated in Fig. 70, a condition commonly encountered in decomposition. The carbon has "replicated" the surface so what is generally seen in the micrograph is a very high concentration of replicated nuclei. Note however that the upper portions of the envelopes still carry small quantities of lead. The high concentration is to be expected because in this stage the nuclei from the small, finely scattered original state have begun to coalesce. The space between nuclei (about 300 Å) is evidently dependent on the surface mobility of the lead as described above. These nuclei are approximately 8000 Å in diameter but they ultimately grow as large as 0.5 μ in diameter. Figure 71 shows a cross-section of these nuclei illustrating their shape and size. It is interesting to compare the similarity between the lead nuclei artificially applied to the surfaces of PbN_6 with those generated by decomposition (compare Figs. 49 and 70).

Crystals examined after 90 minutes at 265° C show no new behavior but all nuclei have increased in size (Fig. 72). In some cases where the number of nuclei per unit area was small the nuclei grew very large and upon coalescence developed rope-like instead of spherical shapes. Longer "ropes" may be seen in places where several additional large nuclei properly aligned joined onto the

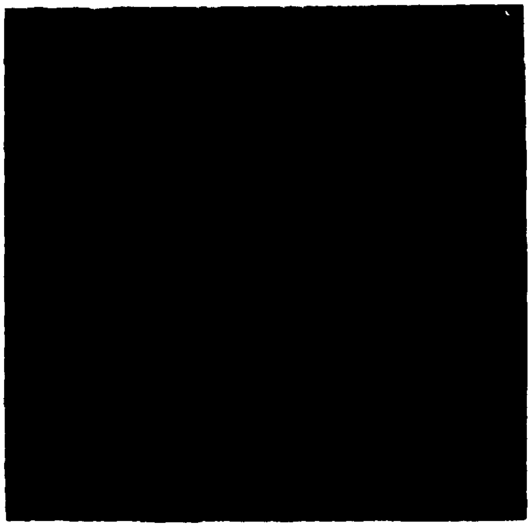

Figure 70. E.M. of LA aged 75 minutes at 265° C showing coalescence of lead nuclei. Carbon replica, 12,000 X

Figure 71. Cross-section of Fig. 70. Carbon replica, 12,000 X

Figure 72. E.M. of LA aged 90 minutes at 265° C. Carbon replica, 12,000 X

Figure 73. Cross-section of Fig. 72. Carbon replica, 12,000 X

original nucleus (e.g. by a favorable crystal defect). In random coalescence approximately spherical nuclei develop (see Fig. 70). Figure 73 is a cross-section through such nuclei. Figure 74 shows an interesting micrograph of a boundary on each side of which nuclei of differing sizes occur. On the lower half of the micrograph coalescent nuclei may be seen while in the upper portion isolated, large nuclei have developed. The rope-like structure may also be seen in this micrograph. When the decomposition reached the point where a heavy black layer had developed on the surface (but prior to the formation of the "shell") the very peculiar structure shown in Figs. 75 to 78 became prominent; the beginning of this structure may be seen in Fig. 59. While this may at first have seemed non-characteristic, it is really characteristic of advanced growth. Note the ridges, grooves and troughs characteristic of the surface depicted in the enlargements, the depth being well pictured in the cross-sectional micrograph. The central hole in Fig. 78 may be effectively a nitrogen "geyser." Note the recurring structure shown in Fig. 79 described above as a nitride. Whether or not it is such a contaminant, this structure forms concurrently with lead nuclei (see Fig. 80). This contaminant structure is extracted from the surface in the replica whereas the lead nuclei are not extracted at least at this stage.

Decomposition of PbN_6 in Electron Bombardment

Sawkill(26) and Camp(11) reported that large flakes of silver azide did not disappear even after an hour's exposure to high intensity electrons, but that ordered silver with respect to the azide was produced directly as a result. This was confirmed by decomposition using a cooling stage maintaining the sample at 0° C. The explanation of this effect is simply that the direct interaction of the electrons with the azide released nitrogen leaving behind silver ions in their lattice positions. While electron diffraction patterns taken at this stage showed the silver to be "ordered", this pseudo-lattice soon collapsed to normal metallic silver.

Thin plates are more difficult to obtain with lead azide making studies of this sort more difficult. Therefore in this study good quality, small crystals instead of plates were used. These crystals were first mounted, laying a crystal between #200 mesh grids. The electrons passing through the openings of the grids struck the crystal intermittently only on those faces that crossed over these openings. Figure 81 shows two crystals after bombardment on the grids. The areas of both crystals exposed to the electrons turned brown in color but remained transparent. The decomposition was entirely different than was observed in thermal decomposition; thermal decomposition turned the crystal opaque and light yellow.

Figure 74. E.M. of LA aged 90 minutes at 265° C showing differences across a boundary. Carbon replica, 12,000 X

Figure 75. E.M. of LA aged 90 minutes at 265° C. Carbon replica, 4,000 X

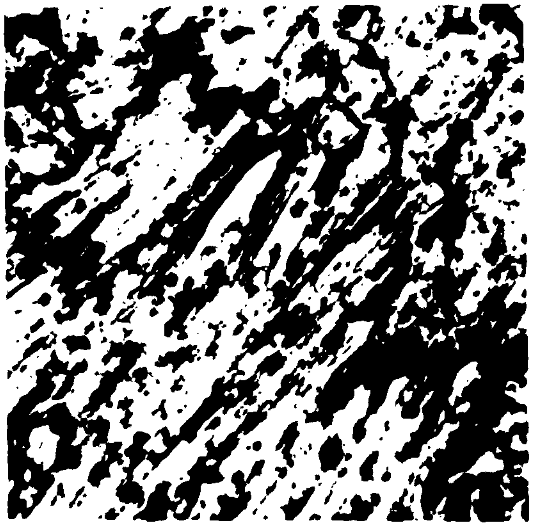

Figure 76. Enlargement of Fig. 75 showing detail of the structure. Carbon replica, self-shadowed, 12,000 X

Figure 77. Cross-section of surface shown in Fig. 76. Carbon replica. 12,000 X

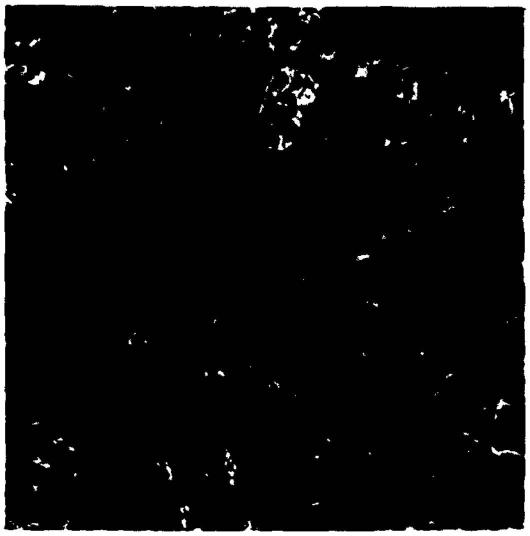

Figure 78. E.M. of LA aged 90 minutes at 265° C illustrating N_2 "geyser". Carbon replica, 12,000 X

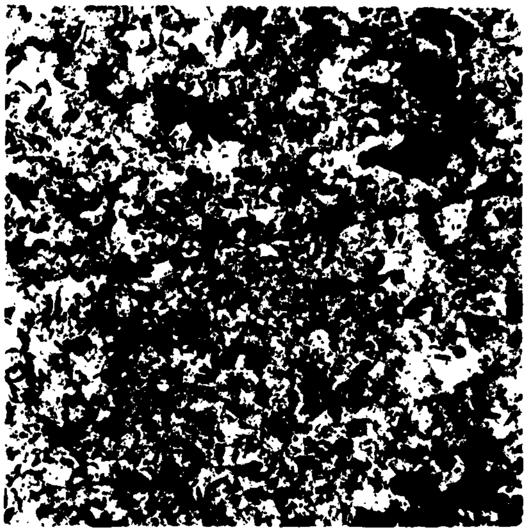

Figure 79. E.M. of LA aged 90 minutes showing recurring contaminant. Carbon replica, 2,000 X

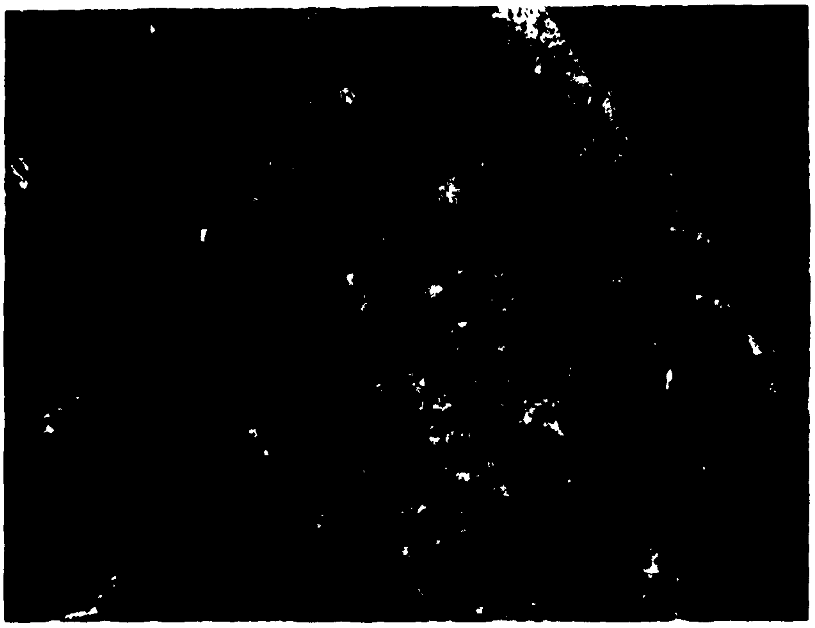

Figure 80. E.M. of LA aged 90 minutes at 265° C showing surface contaminant concurrent with lead nuclei. Carbon replica, 2,000 X increased one half.

Figure 81. Optical micrograph of LA decomposed by electron bombardment. Dark areas represent bombarded portions of crystal. ca36 X

Figure 82. Optical micrograph of LA decomposed by electrons. With electron impingement the crystal cracked and withered up, bending in a complete 90° arc toward the electron source. 36X increased two times.

Great care must be exercised in electron bombardment to avoid explosion. A unique feature of decomposition by electron bombardment is that decomposition may be controlled by voltage control and focus so that one may watch the crystal decompose directly in the microscope itself. It was observed that in electron bombardment cracks rapidly formed splitting the crystal lengthwise, following which many additional cracks developed producing rapidly progressively smaller pieces in the disintegration of the crystal. The final result was a withering and straining of the crystal until it bent in a 90° arc from the original position (Fig. 82). The bend was toward the electron source substantiating the fact that high energy electrons drive off nitrogen directly from the side of the crystal that is bombarded, collapsing the crystal structure from this side with the consequent bending in the direction toward the electron source. It was impossible to obtain a sequence of the process owing to its rapidity. That decomposition was not thermal was shown not only by the fact that the color and opacity were different, but also from the fact that the interface between the decomposed and undecomposed portions of this crystal was very sharp.

MECHANISM OF LEAD AZIDE DECOMPOSITION

Lead azide is essentially ionic with a strong interaction between the highly polarizable Pb^{++} ions and N_3^- ions. The latter are mainly operative, in this connection, through electron pairs in highly directional s,p hybrid orbitals of the terminal nitrogen atoms. Most crystalline lead salts are essentially ionic. Lead azide crystallizes in the six coordination layer structure. Lead can enter into covalent bonding in two ways: (1) through its p_x and p_y electrons giving a divalent lead atom with an angle between the bonds of approximately 90° and (2) by promoting an s electron to a p orbital forming $s\ p^3$ bonds with promotion to $6x\ 6p^2\ 6d$ thereby allowing for four tetragonal $s\ p^2d$ bonds and making $Pb(N_3)_4$ possible.

A proposed mechanism of lead azide decomposition is based on a lead nuclei mechanism with the nuclei being present on the surfaces, predominantly the (010) face, of the lead azide as a decomposition product or impurity and lead azide as an n-type impurity semi-conductor. The lead nuclei are obtained from: (1) thermal or photolytic decomposition of the lead azide by the model outlined below, and (2) as stoichiometric excess free lead found in all "pure" lead azide samples. Electrons and/or excitons find their way to one of these lead nuclei, which acts as an electron trap, charging the nucleus negatively, and in the case of excitons releasing N_2 whereupon the lead nuclei may then attract lead ions to cause the continual growth of the nuclei during decomposition. The 406 μ peak seen in photoconductivity studies is due to the ionization of lead nuclei. The ions which should migrate by the Mott and Gurney mechanism for metal speck growth are the Pb^{++} ions.(13,28) Many ionic, or partly ionic crystals are good insulators when stoichiometrically perfect, but they become electronic semi-conductors by a stoichiometric excess of one constituent, for example pure TiO_2 has a resistivity of about 10^{-10} ohm cm, but on reduction to $TiO_{1.75}$ the resistivity becomes only about 10^{-2} ohm cm. Oxides which lose oxygen when heated in a vacuum thereby gain a donor and become n-type semi-conductors. The conductivity is strongly dependent upon the amount of impurity and on temperature. The situation is similar for lead azide as shown by the results of this study. As nitrogen is lost providing more donors the conductivity increases; it also increases with temperature as in all semi-conductors.

The lead specks present on the surface of lead azide catalyse the decomposition reaction and accelerate the rate of decomposition. Since lead is a product of decomposition this corresponds to autocatalysis. The following mechanism explains the photoconductivity and the autocatalysis observed in thermal decomposition, the electron and optical micrographs of thermal decomposition and electron bombardment results described in this article:

(1) The azide radical (hole) formed from decomposition of N_3^- according to the reaction

$$N_3^- \rightarrow N_3 + \epsilon^-$$

migrates through the lattice largely as an exciton, but it could also migrate as a free electron and free hole.

(2) Two of these excitons may react as a free electron and a hole forming nitrogen gas (and two electrons). The N_2 is evidently liberated primarily on the lead nucleus only. Decomposition of the exciton can take place in the absence of other modes of excitation besides thermal only at lead nuclei which can act as electron acceptors. This is demonstrated by pits (resulting from the accumulation of vacancies) observed around small lead nuclei by electron micrographs. Thus

$$Pb_n + 2\left[N_3 + \epsilon^-\right] \rightarrow 3N_2 + Pb_n^{-2}$$

(3) Upon capture of the electrons by the lead nuclei the latter became negatively charged. More than one, in fact sometimes many, electrons may be captured by a single nucleus before it has a chance to be neutralized by Pb^{++} ions, depending on the mobility of Pb^{++} which is strongly temperature-dependent especially at low temperature.

(4) Lead ions are then attracted to the lead nuclei, and in this manner the nuclei may grow by reactions of the type:

$$Pb_n^{-a} + Pb^{++} \rightarrow Pb_{n+1}^{-a+2}$$

There is apparently a preferred diffusion of the Pb^{++} to the (010) face, a preferred nucleation on this face, or both.

(5) Small lead nuclei may be photoionized releasing electrons into the free band to produce the photocurrent. Thermal energy as well as light energy is required for this excitation, evidently via the reactions

$$Pb_n \xrightarrow{h\nu} Pb^* \xrightarrow{heat} Pb_n^+ + \varepsilon$$

The strong dependence of photocurrent on heat treatment or aging, and the correspondence of the photoconducting band with that of metallic lead provide the evidence that ionization of the lead nuclei is the primary process in the photoconductivity of lead azide.

(6) Electron and optical micrographs show that the (010) face develops lead deposits while other faces such as (100) do not even though these other faces may terminate across the preferred [010] direction of diffusion. A probable explanation is compatibility of lead atoms in metallic lead with the lattice parameter of lead azide. If this is true there should be no "ordered" lead formation prior to a general covering of all faces with a fine network of lead. This is in accordance with results that indicate the relative stability of αPbN_6 in the b-direction.

Continued investigation of lead azide by electron microscopic methods is expected to provide more information of the population of dislocations when better methods are developed to make the dislocations "visible" to the microscope. This field of study remains largely unexplored. Detailed knowledge of surface changes occurring during decomposition, and surface defects on, or near a molecular scale prior to decomposition are vitally needed for a more complete understanding of the total process. A large field of investigation remains in the development of thin films where the decomposition of lead azide can be observed directly at all stages. This would be of a great advantage over the replica technique where a different crystal must be used to observe each stage of decomposition.

BIBLIOGRAPHY

1. Evans, B. L. and Yoffe, A. D., Proc. Roy. Soc., (London) A250, 346 (1959).
2. McLaren, A. C., PhD Thesis, Cambridge University (1957).
3. McLaren, A. C. and Rogers, G. T., Proc. Roy. Soc., (London) A240, 484 (1957).
4. Dumas, H. M., Jr., A Technical Report, University of Arkansas, Aug. 31 (1956).
5. Dodd, J. G., "Studies of the Decomposition Kinetics of Lead Azide," Proceedings of the Ninth Annual Basic Research Contractors Conference and Symposium, Fort Belvoir, Virginia, P. 59, Oct. 4-7 (1960).
6. Whitbread, E. G., Waltham Abbey, Essex, England, Mar. (1960)-private communication.
7. Head, N. L., "Growing of α Lead Azide Crystals," Technical Report No. 3, Institute of Metals and Explosives Research, University of Utah, Sandia Purchase Order No. 15-6358-A, Dec. 30 (1960).
8. Cook, M. A., Flanders, H. E., Keyes, R. T., and Shetty, M. N., "Modified Card-Gap Test for the Shock Sensitiveness of Primary Explosives," Technical Report No. 1, Institute of Metals and Explosives Research, University of Utah, Sandia Purchase Order No. 15-6358-A, Sept. 1 (1960).
9. Bowden, F. P., Proc. Roy. Soc. (London) No. 1245, 29 July 1958.
10. Bowden, F. P., "The Thermal Decomposition of Explosive Crystals: A Study of Electron Microscope and Diffraction". Eighth International Symposium on Combustion, Sept. 1958, Berkeley, Calif.
11. Camp, M., "The Decomposition of Silver Azide by Electrons" Fourth International Conference on Electron Microscopy, Berlin, 1958, pp 134-138.
12. Miles, F. D., Proc. Roy. Soc. (London) A235, 125 (1935).
13. Krause, B. H. and Wawner, F. E., "Decomposition of Selected Azides Under the Influence of X-Rays". Proc. Ninth Annual Basic Research Contractors Conf., Oct. 1960, Fort Belvoir, Va.
14. Bassett, G. A., "Electron Optical Studies of Imperfect Crystals and Their Surfaces", Disc. Faraday Soc. No. 28, 11 (1959).

15. Calbeck, C. J., "Inorganic Replication: Interpretation of Electron Micrographs", Symposium on Techniques of Electron Metallography: ASTM Special Tech. Pub. #155, June 30, 1953.

16. Head, N. L. "Growing of α-Lead Azide Crystals", Tech. Report No. 3, Institute of Metals and Explosive Research, U of U. Sandia P.O. 15-6358-A Dec. 30, (1960).

17. Mitchell, T. W., "Precipitation Reactions in Crystals of Silver and Alkali Halides" Disc. Faraday Soc. No. 28, 242 (1949).

18. Reitzner, B., "Studies of the Thermal Decomposition of PbN_6", Proc. Ninth Ann. Basic Research Contractors Conference and Sym. Oct. 4-7, 1960, Fort Belvoir, Va.

19. Hill, O. H. "The Thermal Decomposition of Lead Azide", Final Rpt. on Contract DA-44-009 Eng.2566- Appendix B, 31 July 1957.

20. Love, W. F., "Thermal and Photolytic Decomposition in the Metallic Azides", Proc. of BRG Sym. and Contractor's Conf. P. 247, Aug. 1959.

21. Dodd, J. G., "Decomposition of Azides", Proc. Ninth Ann. Basic Research Contractors Conf. and Sym., Oct. 1960, Fort Belvoir, Va.

22. Bartlett, B. E., Tompkins, F. C., and Young, D. A., Proc. Roy. Soc. (London) A264, 206 (1958).

23. Thomas, J. G. N., and Tompkins, F. C., Proc. Roy. Soc. (London) A 209, 550 (1951).

24. Joebstl, J. A., "The Prep. of Thin Films of Selected Inorganic Azides and Their Decomp.", Proc. Ninth Ann. Basic Research Contractors Conf. and Sym., Oct. 1960, Fort Belvoir, Va.

25. Von Klein, E., and Matejec, R., Bildung and Wachstrum von Silbukeimen und Halogensilbermikrokristallen. Zeit. F. Electrochemie. 63, 883 (1959).

26. Sawkill, J., Proc. Roy. Soc. (London) A229, 135 (1955).

27. Love, W. G., "Thermal and Photolytic Decomposition in the Metallic Azides," Proc. BRG Sym. and Contractor's Conf. P. 254, Aug. 11-14 (1959), Fort Belvoir, Va.

28. Mott, N. F. and Gurney, R. W., "Electronic Processes in Ionic Crystals", Oxford Univ. Press, (1946).

STUDIES ON THE THERMAL DECOMPOSITION OF MOLTEN KN_3 IN THE PRESENCE OF METALS AND METAL OXIDES

by

Heinrich Egghart
Basic Research Group
U. S. Army Engineer Research and Development Laboratories
Fort Belvoir, Virginia

INTRODUCTION

At last year's contractors conference it was reported that certain metal and metal-oxides have a strong catalytic influence on the thermal decomposition of KN_3 and accelerate this reaction many hundred or thousand fold. At that time the study dealt principally with iron and iron oxides as catalysts. The oxides displayed a higher catalytic activity than the metal, but it was suggested that the oxides themselves might not be the actual catalysts. In the following months this speculation has been found to be correct, and this will be the subject of the first part of this paper. Subsequent to this, a report will follow on the behavior of some other metals as catalysts for the decomposition of KN_3.

Before entering into the body of this report, a brief description will be given of the experimental procedure.

EXPERIMENTAL

The samples were prepared by mixing the KN_3 and the additives in an agate mortar and were outgassed in the decomposition apparatus before an experiment was started. Figure 1 shows a schematic representation of the apparatus which was used. After the outgassing of the sample the valve is closed and the sample dropped into the reaction tube which is surrounded by a heated brass block. The temperature of the brass block is held constant electronically. The rising nitrogen pressure is followed by an ionization gauge, or by an Alphatron gauge, and is recorded automatically. In the work reported here, the Alphatron gauge was used and the samples were chosen so as not to exceed a nitrogen pressure of 100 microns. All experiments were carried out above the melting point of KN_3.

RESULTS

Decomposition experiments with pure KN_3 yielded the well known sigmoid-shaped decomposition curve, indicating an autocatalytic

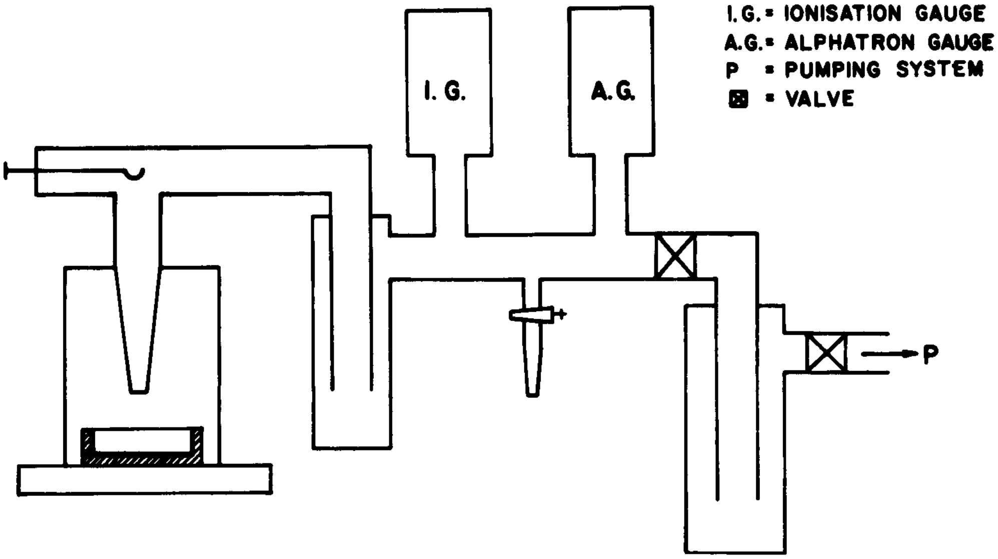

Figure 1

process. At the melting point the decomposition of KN_3 was very slow, and even above 400° C hours were required for the decomposition. It was observed that the length of the induction period, as well as the decomposition velocity, is dependent on the outgassing time of the sample. This is probably due to the consumption of metallic potassium by traces of water. When catalysts were present, however, no influence of the outgassing time on the decomposition could be observed, since the catalyst itself was the prevailing factor.

The gaseous products of the decomposition of pure KN_3, of KN_3-metal, and KN_3-metal oxide mixtures were identical and consisted almost exclusively of nitrogen. In decompositions with catalysts, the evolved nitrogen volume could be related to the decomposed KN_3 sample according to the equation $2KN_3 \longrightarrow 2K + 3N_2$ within the experimental accuracy.

Decompositions with Fe_3O_4 as an additive:

Figure 2 illustrates the decomposition curves for KN_3 with different amounts of Fe_3O_4 as an additive (decomposition at 360° C). Although the decomposition is accelerated by the presence of the Fe_3O_4 by two or three orders of magnitude, it can be concluded from Fig. 2 that Fe_3O_4 itself is not acting as a catalyst for the KN_3 decomposition. The following four points emphasize this:

1. It is known from similar experiments that the warming-up time of the samples, after dropping them into the reaction tube, is less than one second. With Fe_3O_4 as a catalyst, however, there is not much of a reaction in the first ten seconds, and the reaction velocity increases in the form of an acceleration period.

2. The length of the acceleration period is proportional to the Fe_3O_4 concentration, provided this concentration is not excessively high as in the case of curve 4.

3. The decomposition velocity does not increase linearly with the amount of Fe_3O_4 present.

4. Experiments which have not been included in Fig. 2 show that the decomposition velocity is almost independent of the specific surface of the added Fe_3O_4 powder.

All of these observations indicate that Fe_3O_4 is not the catalyzing agent, but is involved in a reaction which produces the catalyst. The energy of activation was obtained from the linear parts of the curves 1 and 4, and was found to be 32 Kcal/mol. This is considerably less than the activation energy necessary for the decomposition of KN_3 without a catalyst, which is reported to be 49 Kcal/mol.

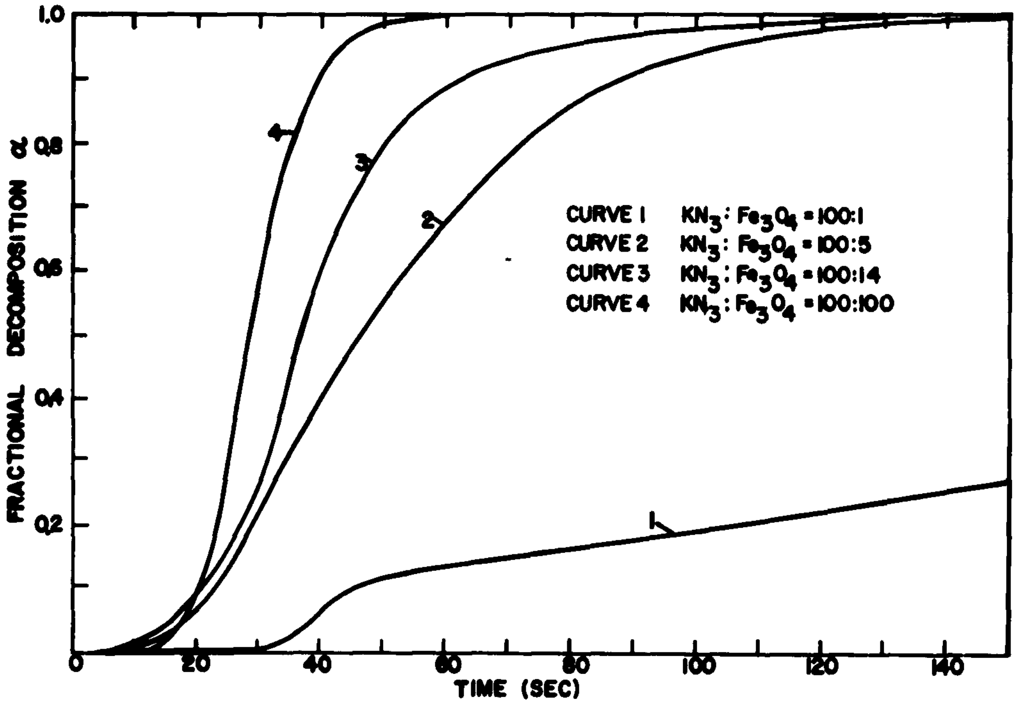

Figure 2

Decomposition with iron metal as an additive:

Figure 3 shows the decomposition curves for KN_3 with iron metal powder as a catalyst (decompositions at 360° C). The reaction starts within 1.5 seconds after the sample drop, and there is no observed acceleration period with the exception of the case when large quantities of iron metal are present. The very small acceleration period (below $\alpha = 0.01$), which is observed in the latter case, is due to the oxide layers which cover the metal surface. This will be seen later.

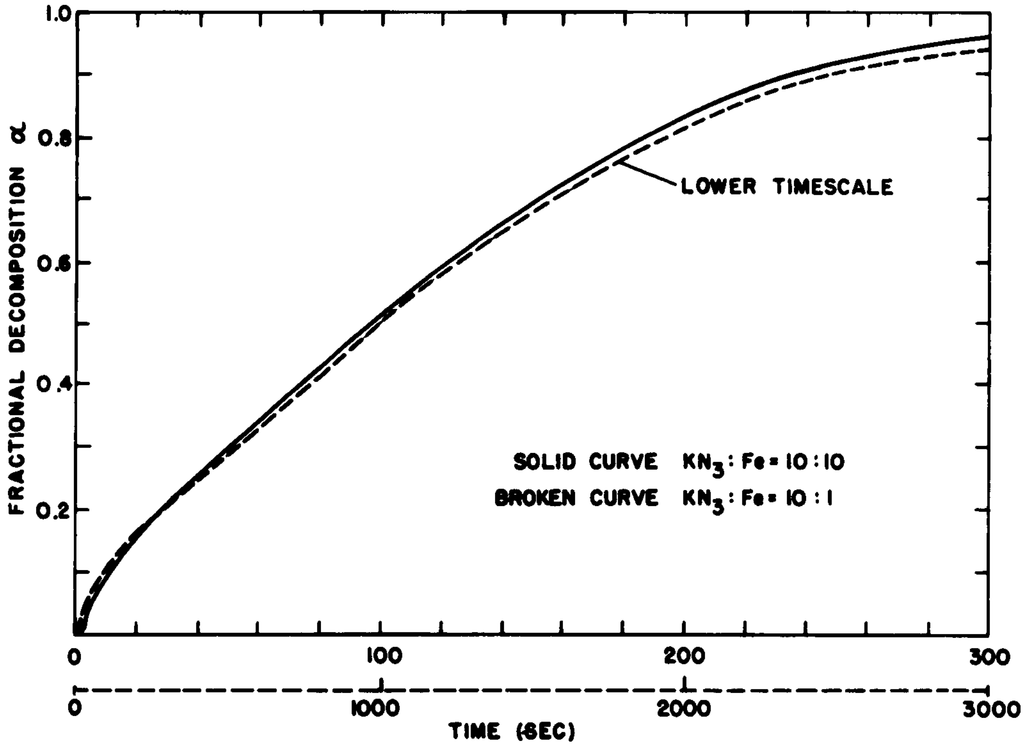

Figure 3

Up to approximately $\alpha = 0.04$, there is a rapid linear decomposition. In the interval $\alpha = 0.04$ to approximately $\alpha = 0.15$ a retrogression of the reaction velocity occurs, which terminates in the linear main part of the decomposition. (The first steep linear portion of the curve ($\alpha = 0.01 - 0.04$) could not be clearly illustrated in Fig. 3, but was observed with accuracy on the recordogram.)

In Fig. 3 the broken curve is related to a catalyst concentration which is smaller by an order of magnitude, and is, therefore, plotted on a time scale which is ten times larger. In order to keep Fig. 3 clear only two KN_3-iron ratios have been plotted. The fact that both curves in Fig. 3 fall close together, demonstrates that the characteristic of the decomposition is the same for different KN_3-iron metal ratios, and that the decomposition velocity is proportional to the amount of iron present. With this it seems evident that the iron metal itself acts as a catalyst.

The experiments with Fe_3O_4 and with iron metal as catalysts, lead to the conclusion that iron oxides of all forms are completely reduced to iron metal during the acceleration periods. This has been confirmed by x-ray analysis of the residues of KN_3 decompositions with Fe_3O_4. The observed iron powder pattern was seen to be broad and diffuse indicating a very small particle size for the freshly formed iron. This enables one to understand why high decomposition velocities are obtained when metal oxides are added to the KN_3.

In view of this, the iron oxide curves may now be interpreted in the following way: The beginning of the decomposition is very slow since no iron is present. The very slight decomposition of KN_3 which occurs without metallic iron yields some potassium metal which then reduces some iron oxide to iron. These iron specks are the sites of primary KN_3 decomposition. With this, the iron nuclei grow and the KN_3 decomposition velocity increases until all of the oxide is reduced at the end of the acceleration period, and the highest decomposition rate is obtained.

The decomposition of KN_3 with one part Fe_3O_4 in a hundred parts KN_3 (represented by Curve 1 in Fig. 2) is slow enough to show the retrogression of the decomposition velocity as it was observed with iron metal as an additive.

The energy of activation for the decomposition of KN_3 with iron metal was found, as expected, to be 32 Kcal/mol. This value was obtained both from the temperature coefficient of the decomposition rate at the linear main portion of the reaction between $\alpha = 0.15$ and $\alpha = 0.5$, and at the first steep part between $\alpha = 0.01$ and $\alpha = 0.04$. This shows that the retrogression of the decomposition velocity (between $\alpha = 0.04$ and $\alpha = 0.15$) is due to a change in the pre-exponential factor of the Arrhenius equation. The reason is possibly that the fresh iron surface, which has been produced in the initial stages of the decomposition reaction, has a larger catalytically active surface area, which becomes smaller with aging and poisoning by reaction products.

Decomposition with FeS and with Fe_2O_3 as an additive:

Figure 4 shows decomposition curves with Fe_3O_4, Fe_2O_3, and FeS as catalysts (decomposition at 360° C). In the case of FeS there is a considerable induction period which ends abruptly. The activation-energy was found to be 32 Kcal/mol for the decomposition at the first steep part of the curve (α = 0.06 - 0.14) as well as the linear main portion (α = 0.3 - α = 0.55). It seems that the induction period is caused by a delay in the reduction of FeS to iron.

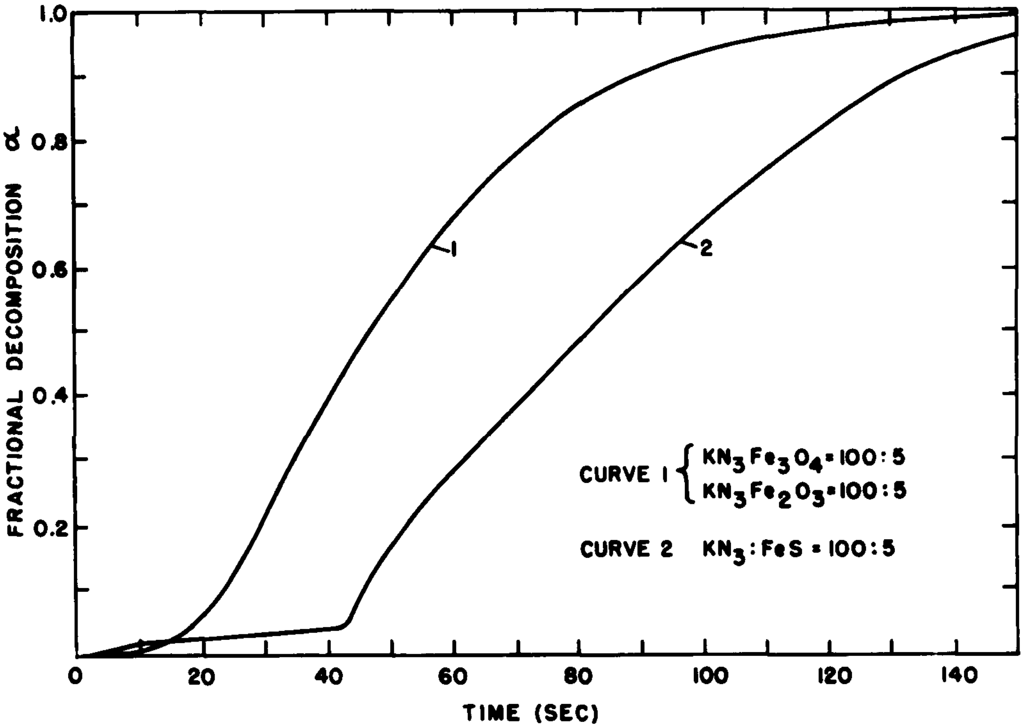

Figure 4

Fe_2O_3 added in small proportions to KN_3 behaves like Fe_3O_4 as a catalyst. Larger quantities of Fe_2O_3, however, cause discontinuous decomposition curves. Figure 5 is an example of this. This strange behavior perhaps can be understood if one considers the thermodynamics of a system containing Fe, Fe_3O_4, and Fe_2O_3. A step in the curve of Fig. 5 should appear after some iron has been formed. The resulting decomposition and related nitrogen evolution tends to mix the iron particles with Fe_2O_3 and they become oxidized to Fe_3O_4 since iron metal is unstable in the presence of Fe_2O_3. In this manner the iron which is formed is lost as a catalyst for a certain length of time.

Decompositions with repeatedly used iron catalysts:

The experiments with iron metal and also the decompositions with one part Fe_3O_4 per 100 parts KN_3 indicate that after the

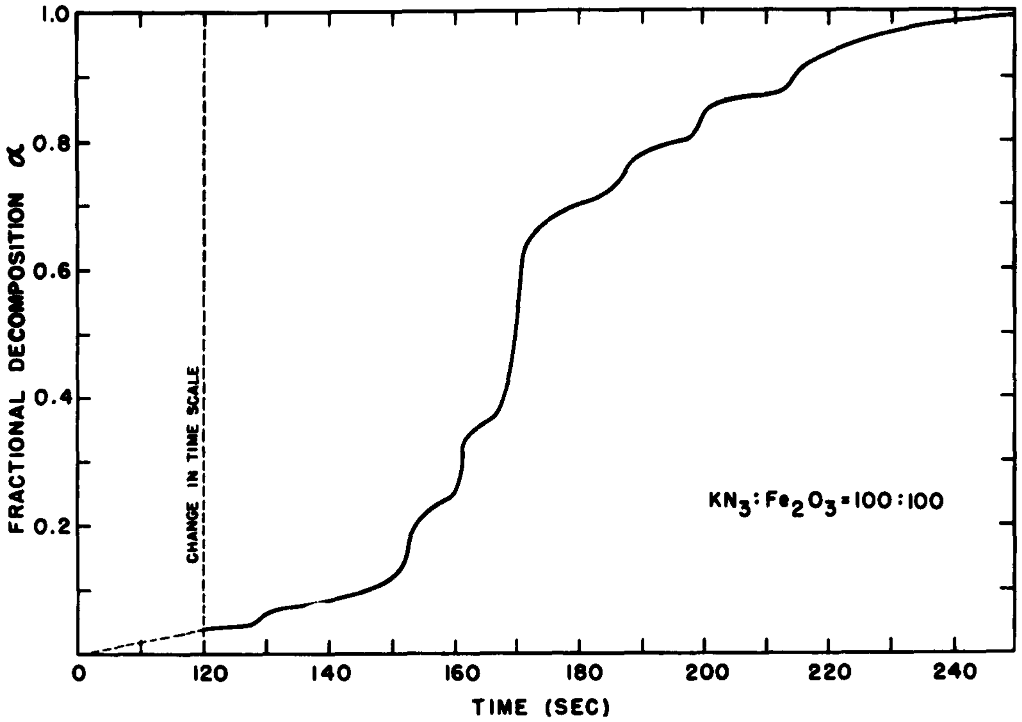

Figure 5

catalyst surface has settled down to a relatively permanent status, the decomposition of the KN_3 proceeds on the iron surface in the form of a zero order reaction. To establish this, experiments were carried out using the same catalyst two or three times. This was done in the following manner: After one decomposition experiment was carried through, the evolved nitrogen was pumped out and after closing the valve a sample of pure KN_3 was dropped, by means of a second spoon, on the catalyst which remained from the previous run. This procedure could again be repeated by using a third spoon. In this way, three experiments were carried out without breaking the vacuum in the apparatus. The results of these experiments are indicated in Fig. 6. The broken curves in this figure represent the decompositions on once- or twice-used catalysts and demonstrate that the decomposition rates are constant from the beginning of the reaction to $\alpha = 0.5$ or more. For experimental reasons it cannot be expected to obtain a constant rate until $\alpha = 1.0$.

It also seemed desirable to investigate iron metal surfaces which have been freed from the oxide layers by hydrogen treatment. For this purpose a very small sample of iron powder was placed in the reaction tube, and the apparatus multiply flushed with hydrogen. After filling the apparatus with one atmosphere of hydrogen, a heat

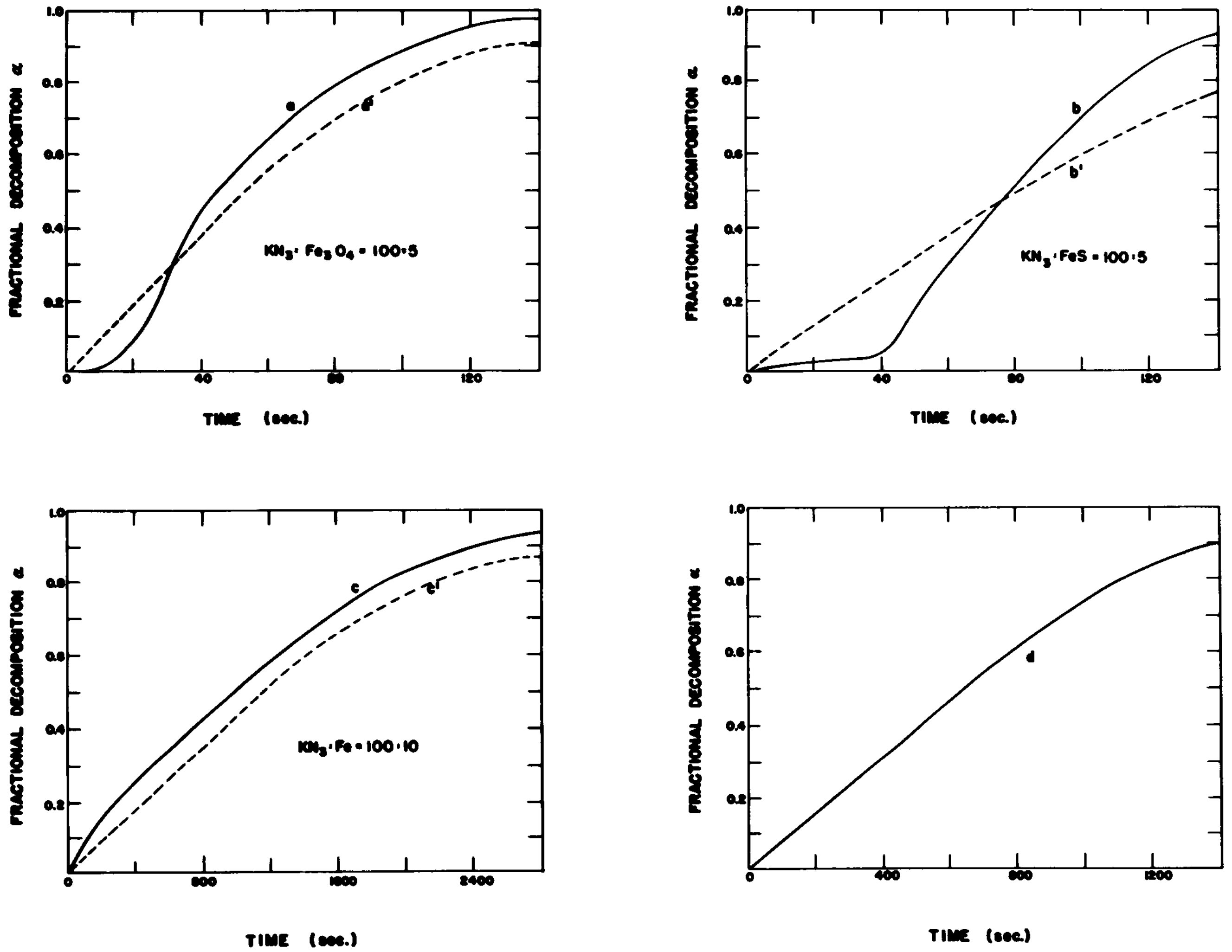
FRACTIONAL DECOMPOSITION α
1.0
0.8
0.6
0.4
0.2
0
40
80
120
TIME (sec.)
a
a'
$KN_3 : Fe_3O_4 = 100 : 5$
b
b'
$KN_3 : FeS = 100 : 5$
c
c'
$KN_3 : Fe = 100 : 10$
800
1600
2400
d
400
800
1200

Figure 6

treatment was carried out. With the re-establishment of the high vacuum, a sample of pure KN_3 was dropped on the hydrogen-treated iron. Curve (d) of Fig. 6 represents the results of these experiments which indicate that the decomposition of KN_3 on hydrogen treated oxide-free metal surfaces follows the zero order law (as well as on repeatedly used catalysts). This is advantageous since it is only in zero order reactions that the true activation-energy can be obtained.

Decomposition with selected metals as catalysts:

All of the experiments which have been described above for KN_3 decompositions in the presence of iron and iron-oxides, have been carried out with nickel and cobalt and their oxides. The decomposition characteristics with these oxides as additives are similar to those of the iron-oxides and are governed by the same rules. X-ray analysis of the residues of decompositions with NiO and Co_2O_3 as additives indicated again that the oxides are being reduced to the metal in the course of the KN_3 decomposition.

The curves with nickel and cobalt metal as a catalyst are principally the same as those with iron metal. The shape of the curves is again independent of the metal - KN_3 ratio and the decomposition velocities are directly proportional to the amount of metal present. Nickel or cobalt which has been hydrogen treated results in a constant decomposition rate of the KN_3, as was seen for iron in Fig. 6.

Manganese metal has also a very strong catalytic influence on the decomposition of KN_3, but the decomposition characteristic is different from those with iron, nickel, and cobalt as catalysts. The catalytic action is delayed and an induction period results (see the solid curve in Fig. 7). The broken curve in Fig. 7 represents the second run with the same catalyst. It is evident from these curves that manganese differs from iron, nickel and cobalt only when it is used as a catalyst for the first time.

The reason for the induction period with manganese as a catalyst might possibly be that the thermodynamic situation for the reduction of the manganese oxide layers is not too favorable. If the manganese oxide were not in a thermodynamically undefined surface state on the manganese metal, the potassium would not be able to reduce it.

A most interesting fact is that iron, nickel, cobalt, and manganese lower the activation energy for the KN_3 decomposition to the same value of 32 Kcal/mol. In view of this and considerations based on current theories related to the catalytic action of transition metals, one is led to the expectation that all transition metals with partially filled d-bands act as catalysts. This thought

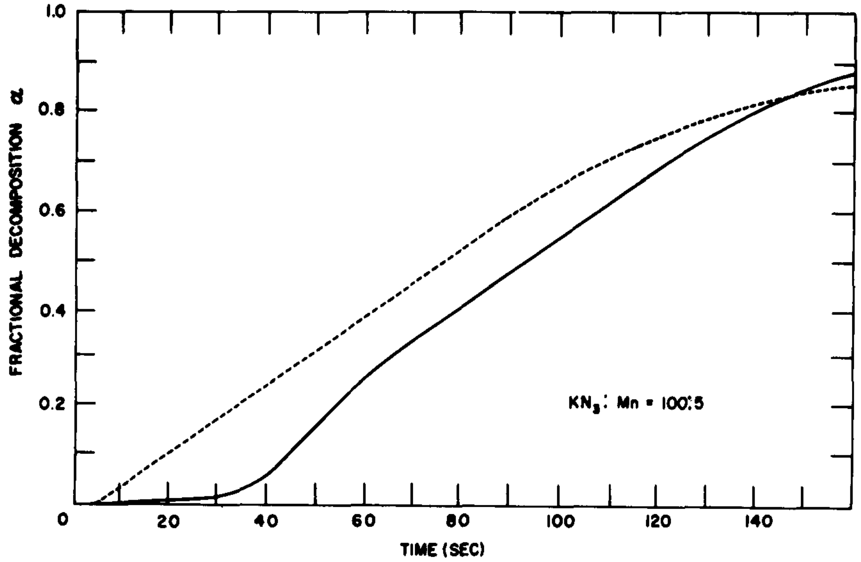

Figure 7

could not be conclusively established, however, since the oxides associated with chromium, vanadium, and titanium metal are irreducible by potassium, and the real metal surface is, therefore, not available for catalysis. This can be deduced from arguments based on chemical potentials and can be observed experimentally.

During these studies it was found that vanadium pentoxide behaves differently with regard to other oxides which have been used. It reacts vigorously with KN_3; however, the decomposition ceases with the depletion of the vanadium pentoxide since the product of this reaction does not catalyze. No vanadium metal is formed in the reaction between KN_3 and V_2O_5.

It was interesting to note that the transition metals, iron, nickel, cobalt, and manganese permit a decomposition of KN_3 at 360° C within seconds, while with copper, silver, and gold, considerable time is required at even 460° C.

Copper was investigated quantitatively and was found to accelerate the decomposition somewhat. The energy of activation with copper as a catalyst was observed to be in the neighborhood of 45 Kcal/mol. This is relatively close to the energy of activation which is required without a catalyst and explains the poor performance of copper as a catalyst.

SUMMARY

The strong acceleration of the decomposition of KN_3 which can be observed with several transition metal oxides as additives is not due to the oxide, but to the catalytic action of the metals which are formed from the oxides in the initial stages of the decomposition reaction.

The activation energy for the KN_3 decomposition with iron, nickel, cobalt, and manganese as catalysts is only 32 Kcal/mol while with copper approximately 45 Kcal/mol.

It can be shown that the KN_3 decomposition on these metal surfaces is a zero order reaction.

The data contained in this report seems to indicate that partially vacant *d*-bands are essential for catalytic action in the decomposition of KN_3. Therefore, one might propose the following mechanism. The azide ions which have sufficient excitation energy form a partly covalent bond with the unoccupied *d*-orbitals of the metal catalyst. The potassium ions are attracted to the catalytic surface and are discharged when the chemisorbed N_3's decompose to nitrogen, probably by means of a bimolecular reaction. By this reaction path an excitation energy of only 32 Kcal/mol is required.

It is hoped that further evidence in support of this mechanism will be forthcoming in the near future.

THEORETICAL STUDIES ON THE THERMAL DECOMPOSITION OF LEAD AZIDE

by

Jack G. Dodd
Roosevelt University
Chicago, Illinois

Abstract

Two mathematical models for the thermal decomposition of lead azide are presented, one involving heat generation by a surface reaction only, and the other involving homogeneous heat generation. These two models are examined for perturbations about the point of self-sustaining decomposition, and conditions are derived which define the stability of these perturbations. It is demonstrated that, for lead azide, the heterogeneous (surface) model is probably stable for upward perturbations and the homogeneous model is certainly unstable. It is further shown that the exact nature of the exothermic reaction does not effect the stability criterion in the homogeneous case. A simple calculation for the homogeneous case is shown to yield an explosive temperature in good agreement with experiment. The great importance of carefully planned thermal decomposition studies is emphasized as a tool in deciding among decomposition mechanisms. Shortcomings of past experimental work are discussed, and experimental procedures for testing of theoretical models are described.

I. HETEROGENEOUS CASE

In the final report on Contract ENG-4194, a model for the thermal decomposition of lead azide was prepared in which decomposition fragments, called "active centers," were assumed to diffuse to the sample surface where, and where only, they reacted bimolecularly to produce the heat which made the reaction self-sustaining(1). This model was described by a pair of equations:

$$(1) \qquad \frac{\partial n}{\partial t} = D \frac{\partial^2 n}{\partial x^2} - nR + \theta_o e^{-E/KT}$$

$$(2) \qquad C\rho \frac{\partial T}{\partial t} = \lambda \frac{\partial^2 T}{\partial x^2} - A \theta_o e^{-E/KT} + ARn$$

Under the boundary conditions:

(1a) $$\frac{\partial n}{\partial x}\Big|_{x=0} = 0$$

(1b) $$-D\,\frac{\partial n}{\partial x}\Big|_{x=\ell} = d\left[\theta_0\, e^{-E/KT} - (\alpha + R)\, n - rn^2\right]_{x=\ell}$$

(1c) $$n_{t=0} = n_0\,(x)$$

(2a) $$\frac{\partial T}{\partial x}\Big|_{x=0} = 0$$

(2b) $$-\lambda\,\frac{\partial T}{\partial x}\Big|_{x=\ell} = d\left[Brn^2 + RAn - A\theta_0\, e^{-E/KT}\right]_{x=\ell}$$

(2c) $$T_{t=0} = T_0\,(x)$$

The assumed sample geometry was a plane slab of thickness 2ℓ, with the X origin at the median plane.

We found a solution for the surface temperature of the sample under conditions of constant self-sustaining thermal decomposition, i.e. for $\frac{\partial n}{\partial t} = \frac{\partial T}{\partial t} = 0$, and for lead azide found this temperature to be in good agreement with Henkin and McGills explosion temperature of 315° C(2). As a matter of fact, the agreement was embarrassingly good in view of the numerous approximations made.

Now the temperature calculated from the above model may or may not be an "explosion temperature." It can be termed such only if the solution is unstable toward upward perturbations. We discuss here those conditions which must be placed on the kinetic parameters of the explosive in order for self-heating to drive the system regeneratively to explosion from the equilibrium temperature. To do this, it serves us well to transform the preceding equations into dimensionless variables.

We identify the original variables as follows:

n = activated center density, in no./cm^3.

R = linear homogeneous termination rate of the N.

θ_0 = decomposition frequency (of normal molecules into activated centers) at infinite temperature.

D = diffusion constant for activated centers.

E = activation energy for formation of active centers.

C = specific heat capacity.

λ = thermal conductivity.

ρ = density.

A = heat of formation of an activated center.

B = heat of reaction of activated centers upon formation of nitrogen at the surface (by bimolecular reaction).

r = rate constant for the above bimolecular reaction.

α = rate constant for the unimolecular surface decay of activated centers.

d = surface zone thickness.

2ℓ = sample thickness.

We now introduce the following changes of variables:

$$\phi = \frac{nD}{\theta_o \ell^2} \qquad \sigma = \frac{CPD}{\lambda}$$

$$\tau = \frac{Dt}{\ell^2} \qquad \eta = \frac{AK\ell^2\theta_o}{E\lambda} \qquad \delta = \ell/d$$

$$\gamma = R\,\frac{\ell^2}{D} \qquad m = \frac{\alpha\ell^2}{D} \qquad h = B/A$$

$$\xi = \frac{x}{\ell} \qquad \rho = \frac{\theta_o \ell^4}{D^2}\,r$$

$$W = \frac{KT}{E}$$

Many of these relations are redundant; fewer dimensionless constants could have been used. However, for algebraic calculation, which is the purpose here, simplicity is of more importance than economy, and the new constants were chosen with this in mind.

Substituting, we obtain the new dimensionless equations:

$$(3) \qquad \frac{\partial \phi}{\partial T} = \frac{\partial^2 \phi}{\partial \xi^2} - \alpha \, \phi + e^{-1/W}$$

$$(3a) \qquad \left. \frac{\partial \phi}{\partial \xi} \right|_{\xi=0} = 0$$

$$(3b) \qquad - \delta \left. \frac{\partial \phi}{\partial \xi} \right|_{\xi=1} = \left. \left(e^{-1/W} - m \, \phi - \alpha \, \phi - \rho \, \phi^2 \right) \right|_{\xi=1}$$

$$(3c) \qquad \phi_{T=0} = \phi_0 \, (\xi)$$

$$(4) \qquad \sigma \, \frac{\partial W}{\partial T} = \frac{\partial^2 W}{\partial \xi^2} + \eta \, r \, \phi - \eta \, e^{-1/W}$$

$$(4a) \qquad \left. \frac{\partial W}{\partial \xi} \right|_{\xi=0} = 0$$

$$(4b) \qquad \frac{-\delta}{\eta} \left. \frac{\partial W}{\partial \xi} \right|_{\xi=1} = \left(\rho h \, \phi^2 + r \, \phi - e^{-1/W} \right)_{\xi=1}$$

$$(4c) \qquad W_{r=0} = W_0 \, (\xi)$$

It is to the solution of this system that we now address ourselves. We shall assume, in what follows, that regular and well-behaved solutions exist; no theoretical proofs will be attempted. Further, since all physical evidence suggest $R = 0$, we shall at the outset set $r = 0$. (See reference 1)

Perturbation of the Equilibrium State

Consider

(1) $$\sigma \frac{\partial W}{\partial t} = \frac{\partial^2 W}{\partial \xi^2} - \eta \ e^{-1/W}$$

At equilibrium,

(2) $$\frac{\partial^2 W}{\partial \xi^2} - \eta \ e^{-1/W} = 0$$

Suppose we have a solution $W = Wo\ (\xi)$ for (2).

Let us attempt a perturbation solution, by adding to W_o a quantity ΔW, an infinitesimal perturbation. We have immediately:

(1') $$\sigma \frac{\partial}{\partial T} (W_o(\xi)+\Delta W(\xi,T)) - \frac{\partial^2}{\partial \xi^2} (W_o+\Delta W)-a-b(W_o+\Delta W)-c(W_o+\Delta W)^2$$

Let us drop the quadratic term. Now since $Wo\ (\xi)$ satisfies (2), (1') reduces to

(8) $$\sigma \frac{\partial \Delta W}{\partial T} = \frac{\partial^2 \Delta W}{\partial \xi^2} - b \ \Delta W$$

Let us try for a solution for ΔW of the form:

(9) $\Delta W = \Sigma\, a_n\ (\xi)\ T^n$. For this we write:

(10) $$\sigma\ \Sigma\ n\ a_n\ (\xi)\ T^{n-1} = \Sigma \frac{d^2 a_n}{d\,\xi^2}\ T^n - b\ \Sigma\ a_n\ T^n$$

(10') $$\sigma\ \Sigma\ (n+1)\ a_{n+1}\ T^n = \Sigma \frac{d^2 a_n}{d\,\xi^2}\ T^n - b\ \Sigma\ a_n\ T^n$$

Thus:

(11) $$\sigma\ a_1 = \frac{d^2 a_o}{d\,\xi^2} - b\ a_o$$

Where, from (9), $a_o = \Delta W/T{=}0 \neq 0$

Now the recursion formula develops without incident:

$$(12) \qquad n \,\sigma\, a_n = \frac{d^2 a_{n-1}}{d\,\xi^2} - b\, a_{n-1}$$

The convergence of (9) clearly depends upon the shape of the perburbation at T=0; that is, the form of $a_o(\xi)$ determines the nature of the equilibrium state.

To explain more fully, suppose first of all that a solution of the form (9) exists for some choice of a_o. Then we have found a time-dependent solution for (1) of the form $W = W_o + \Delta W$, where ΔW satisfies (8). Since Wo is an equilibrium solution (of (2)), and since ΔW is a perturbation of that solution, if

$$(13) \qquad \lim_{T \to \infty} \Delta W = Q$$

is computed, then for $Q = 0$, Wo is stable, for $Q = \pm\infty$, Wo is unstable, and for $Q = \text{constant} \neq 0$, Wo is neutral.

To begin with, let us assume that ΔW satisfies the symmetry condition $\frac{\partial \Delta W}{\partial \xi} = 0$ at $\xi = 0$. Then:

$$(14) \qquad \left.\frac{\partial \Delta W}{\partial \xi}\right|_{\xi=0} = \Sigma \left.\frac{da_n}{d\xi}\right|_{\xi=0} T^n = 0$$

Now if we set $T = 0$, then we have $a_{1/o} = 0$ from (14). Also, if Δw is symmetrical, only even values of n can be non-zero in the series development of the $a_n(\xi)$.

To get some idea of the behavior implied by these considerations, let us assume a very simple form for ΔW and compute the resulting coefficients from (11).

Suppose $a_o = \text{Cons}$. Then:

$$(15) \qquad n\,\sigma\, a_n = -b\, a_{(n-1)}$$

$$a_n = \frac{b a_{n-1}}{n\,\sigma} = \frac{b^n a_o}{n!\,\sigma^n}(-1)^n$$

and

(16) $$\Delta W = a_o \sum_0^{\infty} (-1)^n \left(\frac{b\tau}{\sigma}\right)^n / n! = a_o e^{-b\tau/\sigma}$$

(17) $$\frac{d\Delta W}{d\xi} = 0, \therefore \left.\frac{dW}{d\xi}\right|_{\xi=0} = \left.\frac{dW_o}{d\xi}\right|_{\xi=0}$$

Hence if Wo will satisfy the symmetry condition, then Wo + a_o will also. Now consider the condition considered in (13). Since from (16) ΔW is an exponential series in time, evidently

(18) $$\lim_{\tau \to \infty} \Delta W = 0$$

and ΔW will go to zero in time. Thus, for the perturbation in W simply a constant added change in W, independent of ξ, the equilibrium state is stable.

Consider now a more general type of perturbation - say, one developable in even powers of ξ (to satisfy symmetry). Such a perturbation will take the form $a_o = c_o \, (e^{K\xi} + e^{-K\xi})$, which leads to

(19) $$\begin{cases} \sigma \, a_1 = c_o \dfrac{d^2}{d\xi^2} (e^{K\xi} + e^{-K\xi}) - b \, c_o \, (e^{K\xi} + e^{-K\xi}) \\ n \, \sigma \, a_n = \dfrac{d^2}{d\xi^2} (a_n - n) - b \, a_{n-1} \end{cases}$$

(20) $$\begin{cases} a_n = \dfrac{(K^2-b)^n}{\sigma_n \, n} \, a_o; \quad \Delta W = \Sigma \, a_n \, T^n \\ \Delta W = c_o \, e \, \dfrac{(K^2-b)}{\sigma} \, \tau \, (e^{K\xi} + e^{-K\xi}) \end{cases}$$

Here, we can distinguish two cases: $K^2-b > 0$ and $K^2-b < 0$. In the former case, the result is a "run-away" distribution, but in the latter, Lim ΔW = 0 indicating stable equilibrium. The significance of this possibility of a "run-away" solution is not at once obvious. A glance at equation (1) shows that there is no net heat source. Hence, how can the perturbation lead to an indefinite increase in temperature? Yet this is the implication of the ΔW in equation (20) for $K^2 - b > 0$. The answer is that the ΔW calculated from (20) assumes the existence of an equilibrium solution Wo. However, such a solution is a function of the boundary conditions and exists only for *suitable* boundary conditions. Thus, heat sources *do exist* at the surfaces of the sample--for these are the boundary conditions which make equilibrium possible--and the significance of (20) is that for $K^2 - b > 0$, a perturbation of the sample temperature of the form given will lead to thermal "run-away." As will be seen, the choice of this perturbation was not random.

It is now necessary to examine (1) in terms of realistic boundary conditions. To do this, let us study solutions now which satisfy

$$(24) \qquad -\frac{\delta}{\eta} \left.\frac{\partial W}{\partial \xi}\right|_{\xi=1} = (\rho\ h\ \phi_1^{\ 2} - e^{-1/W_1})\ \xi = 1$$

where ϕ is a solution of

$$(25a) \qquad \frac{\partial \phi}{\partial T} = \frac{\partial^2 \phi}{\partial\ \xi^2} + e^{-1/W}$$

Satisfying the boundary condition:

$$(25b) \qquad -\delta \left.\frac{\partial \phi}{\partial \xi}\right|_{\xi=1} = \left[e^{-1/W} - m\ \phi - \rho\ \phi^2\right]\ \xi = 1$$

Clearly, appropriate solutions of (25a) must be the result of substituting an appropriate solution of the equation for W into (25a). Let us consider first solutions of the equilibrium class:

$$(26) \qquad \frac{\partial \phi}{\partial T} = 0 = \frac{\partial^2 \phi_0}{\partial\ \xi^2} + e^{-1/W}$$

It is obvious that the equilibrium solution W = Wo (ξ) is the appropriate function to be used in (26). Since by hypothesis:

$$(27) \qquad \eta\ e^{-1/W_0}\ (\xi) = \frac{\partial^2 W_0(\xi)}{\partial\ \xi^2}$$

we see at once that:

$$(28) \qquad \frac{\partial^2 \phi_o}{\partial \xi^2} + \frac{\partial^2 W_o}{\partial \xi^2} \quad \frac{1}{\eta} = 0$$

The general solution of (28) is then

$$(29) \qquad \eta\ (\phi_o - \phi_{o1}) + (W_o - W_{o1}) = 0$$

where the symmetry conditions $\left.\frac{\partial \phi_o}{\partial \xi}\right|_{\xi=0} = \left.\frac{\partial W_o}{\partial \xi}\right|_{\xi=0} = 0$ have been applied.

The first integral of (28) is:

$$(30) \qquad \eta \frac{\partial \phi_o}{\partial \xi} + \frac{\partial W_o}{\partial \xi} = 0$$

which implies from (24) and (25b):

$$(31) \qquad e^{-1/W_1} - m\ \phi_1 - \rho\ \phi_1^{\ 2} + h\ \rho\ \phi_1^{\ 2} - e^{-1/W_1} = 0$$

$$\phi_1 = \frac{m}{(h-1)}\ \rho$$

The last equation in (31) is the same as that obtained in the final report, ENG-4194, except couched in dimensionless variables. We now inquire, however, into the behavior of the equilibrium state toward perturbations.

To begin with, let us write the perturbed boundary condition for the temperature:

$$(32) \qquad -\frac{\delta}{\eta} \left[\frac{\partial W_o}{\partial \xi} + \frac{\partial \Delta W}{\partial \xi}\right]_{\xi=1} = \rho\ h\ (\phi_o^{\ 2} + \alpha\ \ \phi_o\ \Delta\ \phi + \Delta\ \phi^2)_{\xi=1}$$

$$-\frac{a}{\eta} - \frac{b}{\eta}\ (W_o + \Delta W)$$

We write here the linear approximation for the Arrhenius term. The function e^{-1/W_o} can be expanded about Wo in a Taylor's series:

$$e^{-1/W} \approx u(W) = u(W_o) + u^1(W_o)(W-W_o) + \frac{u''(W_o)(W-W_o)^2}{\alpha\,!} \ldots\ldots +$$

The series converges very slowly for Wo < 1. However, for our purposes here we may take W - Wo very small, since we are studying the solutions only in the neighborhood of Wo. Since, Wo satisfies (24) by hypothesis, (32) reduces to:

$$(33) \qquad -\frac{\delta}{\eta}\ \frac{\partial \Delta W}{\partial \xi}\bigg|_{\xi=1} = \left[\alpha\, h\, \rho\, \phi_o \Delta\, \phi - \frac{b}{\eta}\ \Delta\ W\right]_{\xi = 1}$$

where second order terms in $\Delta\,\phi$ have been discarded.

Similarly for ϕ:

$$(34) \qquad -\,\delta\,\frac{\partial \Delta\phi}{\partial \xi}\bigg|_{\xi=1} = \left[\frac{b}{\eta}\ \Delta W - (m + \alpha\,\phi\ \ \rho)\ \Delta\ \phi\right]_{\xi = 1}$$

Also, we may write:

$$(35) \qquad \frac{\partial \Delta\phi}{\partial T} = \frac{\partial^2 \Delta\phi}{\partial \xi^2} + \frac{b}{\eta}\ \Delta W$$

analogously to (8); and (35) may be solved in the same manner as (8) except that ΔW is now prescribed by (9). Thus:

$$(36) \qquad \Delta\,\phi\ =\ \Sigma\ g_n\ (\xi)\ \ \tau^n \text{ substituting;}$$

$$(37) \qquad (n+1)\ g_{(n+1)}\ \tau^n = \frac{\partial^2(g_n \tau^n)}{\partial\,\xi^2} + \frac{b}{\eta}\ \ a_n\ \tau^n$$

which yields:

$$(38a) \qquad g_1 = \frac{\partial^2 g_o}{\partial\,\xi^2} + \frac{b}{\eta}\ \ a_o$$

where:

(39) $$g_0 = \Delta\phi \Big|_{\tau=0}$$

and in general:

(40) $$ng_n = \frac{\partial^2 g_{n-1}}{\partial\ \xi^2} + \frac{b}{\eta}\ a_{n-1}$$

If $g_0 = 0$ (no initial perturbation of ϕ), we obtain:

(41) $$g_0 = 0$$

$$g_1 = b\ a_0/\eta$$

$$2g = \frac{1}{\eta}\ \frac{\partial^2 (b\ a_0)}{\partial\ \xi^2} + \frac{b}{\eta}\ a_1$$

and so forth. In other words, a perturbation in W will generate a perturbation in ϕ.

Consider now the state of affairs at $\tau = 0$. There exists some perturbation ΔW, which at $\tau = 0$ may be represented by some $a_0\ (\xi)$ (the first term in expansion (9)). Because of this perturbation, there may exist a $\Delta\phi$ in the future; but for now, ($\tau = 0$), $\Delta\phi = g_0 = 0$ (see 41).

Then from (33) and (34) we may establish boundary conditions at $\tau = 0$ and $\xi = 1$:

(42a) $$-\frac{\delta}{\eta}\ \frac{\partial\Delta W}{\partial\xi}\Big|_{\xi=1} = \left[\frac{b}{\eta}\ \Delta W\right]_{\xi=1}$$

(42b) $$-\delta\ \frac{\partial\Delta\phi}{\partial\xi}\Big|_{\varsigma=1} = \left[\frac{b}{\eta}\ \Delta W\right]_{\xi=1}$$

Since, from (9)

(43) $$\Delta W = \Sigma\ a_n\ \tau^n$$

$$\left.\begin{aligned} &(44a) \quad -\delta \frac{\partial \Delta W}{\partial \xi}\bigg|_{\xi=1} = -\delta \Sigma a_n^{1} \tau^n \bigg|_{\xi=1} = \Big[-b \Sigma a_n \tau^n\Big]_{\xi=1} \\ &(44b) \quad -\delta \frac{\partial \Delta \phi}{\partial \xi}\bigg|_{\xi=1} = \delta \Sigma g^1{}_n \tau^n \bigg|_{\xi=1} = \Big[\frac{b}{\eta} \Sigma a_n \tau^n\Big]_{\xi=1} \end{aligned}\right\} \begin{array}{c}\text{Eval-}\\ \text{uated}\\ \text{at}\\ \tau=0\end{array}$$

From these relations we find that:

$$(45a) \qquad -\delta \frac{da_o}{d\xi}\bigg|_{\xi=1} = b\, a_o\bigg|_{\xi=1}$$

$$(45b) \qquad \delta \frac{dg^n}{d\xi}\bigg|_{\xi=1} = -\frac{b}{\eta} a_o\bigg|_{\xi=1}$$

Now if the series for ΔW is given (all a_n are known) then from (41) the series for $\Delta\phi$ may be constructed.

Thus we need chiefly to see which functions ΔW are suitable perturbation conditions. The conditions are these:

a) ΔW must be symmetrical about $\xi = 0$

b) The a_n must satisfy (12)

c) a_n must satisfy (45a)

Now evidently the a_n are not uniquely determined, even so, for from (c) it is possible to specify a_o at $\tau = 0$. But once this is done, the slope is specified at the surface.

It is not clear, however, that this requirement exactly determines the a_n. That the conditions are compatible with a solution of some sort is made evident by assuming (45a) to hold not only at the boundary, but everywhere.

This leads to the value:

$$(46) \qquad a_o = A(e^{b/\delta\eta\xi} + e^{-b/\delta\eta\xi})$$

It is easy to show that, using the a_o obtained from (46), the rest of the terms may be computed without incident from (12), and all will satisfy conditions a, b and c above.

Eq. (46) is recognized as the particular perturbation function described in (19), with $K = b/\delta\eta$. Thus we may immediately write down

(47) $$\Delta W = A\, e^{[(b^2/\delta^2\eta^2)-b]\ \tau/\sigma}\left(e^{b/\delta\eta\,\xi} + e^{-b/\delta\eta\,\xi}\right)$$

as the perturbation solution of the complete equation. The final perturbed solution:

(48) $$W = W_o + \Delta W$$

is seen to relax to W_o if $\frac{b^2}{\eta^2\delta^2} < b$, to go to explosion if $\frac{b^2}{\eta^2\delta^2} > b$ and to be a neutral perturbation if $\frac{b^2}{\eta^2\delta^2} = b$.

We may also write down the general term for the g_n in (41).

(49) $$g_n = \left[\frac{b}{\eta} \sum_{i=0}^{n-1} \frac{\left(\frac{b^2}{\eta^2\delta^2} - b\right)}{i\,\sigma\, i} \left(\frac{b^2}{\eta^2\delta^2}\right)^{n-1-i} \right] \frac{A(e^{\frac{b}{\delta\eta}\xi} + e^{-\frac{b}{\delta\eta}\xi}}{n\,!}$$

and from these g_n, $\Delta\phi$ may be constructed:

(50) $$\Delta\phi = \sum_{n=o}^{\infty} g_n\, \tau^n \qquad g_o = 0$$

It is at once clear that the sign of the g_n depends upon $\frac{b^2}{\eta^2\delta^2} - b$. If $\frac{b^2}{\delta^2\eta^2} < b$, $\Delta\phi < 0$ for $A > 0$. This corresponds to the case described previously for the relaxation of the thermal perturbation, and hence verifies the condition for the return to equilibrium. Physically, the above is a statement that if $\frac{b^2}{\delta^2\eta^2} - b < 0$, an increase in surface temperature results in a decrease in active center concentration, and hence a return to equilibrium. Conversely, if $\frac{b^2}{\delta^2\eta^2} - b > 0$, then an increase in W of course increases ϕ, which leads to explosion.

We would have a complete solution had we Wo, the equilibrium distribution of temperature, and ϕ, the equilibrium distribution of centers. This would involve the solution of (2) and (26). Neither permits of solution in a closed form, and even series solutions become almost impossibly complex after the third or fourth term. Happily, the stability conclusions reached here do not depend upon the forms of these solutions, and so it is not necessary to have them for this purpose. Also, since a solution at the surface for both ϕ_o and Wo was developed in the Final Report (ENG-4194), it is possible to evaluate explosion temperatures and the like without proceeding further than we have.

However, it must be pointed out that the perturbation solutions obtained here are valid only in the neighborhood of equilibrium; i.e., for both A (see (46)) and τ small. Solutions valid over a considerable range of these parameters seem possible only numerically.

We can take up the evaluation of (47) at the sample surface, however, since we can find an asymptotic solution of equation (2) at the surface under equilibrium conditions. We have

$$\frac{\partial^2 W}{\partial \xi} - \eta e^{-1/W} = 0 \tag{51}$$

We assume that a solution exists which, when evaluated at the surface ($\xi = 1$) yields some temperature Wo (the notation has been changed, Wo now refers to the equilibrium boundary temperature). Then near the surface, we must have

$$e^{-1/W} = e^{-1/W} + \frac{1}{W_o^2} e^{-1/W_o} (W - W_o) + \text{higher terms} \tag{52}$$

Substituting (52) in (51a), making the change of variables

$$y = W - W_o \tag{53a}$$

we find

$$\frac{\partial^2 y}{\partial \xi^2} - \frac{\eta e^{-1/W_o}}{W_o^2} y = \eta e^{-1/W_o} \tag{53b}$$

Boundary conditions transform similarly from (4b)

(54) $$-\frac{\delta}{\eta}\left.\frac{\partial W}{\partial \xi}\right|_{\xi=1} =$$

$$\left(\rho\, h\, \phi^2 + \gamma\, \phi - e^{-1/W_o} - \frac{1}{W_o^2}\, e^{-1/W}\, y\right)_{\xi = 1}$$

$$= \left.\left(\rho\, h\, \phi^2 + \gamma\, \phi - e^{-1/W_o}\right)\right|_{\xi=1}$$

and the definition of y,

(55) $$\left. y\right|_{\xi=1} = 0$$

Now equation (53b) has the complete solution:

(56) $$y = W_o^2 + A\, e^{-\sqrt{a}\ \xi} + B\, e^{\sqrt{a}\ \xi}$$

where we have let "a" stand for the coefficient of y in equation (53b). Applying now the boundary condition (55):

(57) $$0 = W_o^2 + A\, e^{-\sqrt{a}} + B\, e^{\sqrt{a}}$$

and remembering that from symmetry

$$\left.\frac{\partial y}{\partial \xi}\right|_{\xi=0} = 0$$

(58a) $$\frac{\partial y}{\partial \xi} = -\sqrt{a}\ A\, e^{-\sqrt{a}\ \xi} + B\sqrt{a}\ e^{\sqrt{a}\ \xi}$$

(58b) $$0 = -A + B$$

hence A = B = P and

$$y = W_o^2 + P\left(e^{\sqrt{a}\,\xi} + e^{-\sqrt{a}\,\xi}\right) \tag{59}$$

but (57) has now become

$$W_o^2 = P\left(e^{-\sqrt{a}} + e^{\sqrt{a}}\right) \tag{60}$$

and eliminating P:

$$y = W_o^2\left[1 - \frac{e^{\sqrt{a}\,\xi} + e^{-\sqrt{a}\,\xi}}{e^{-\sqrt{a}} + e^{\sqrt{a}}}\right] \tag{61a}$$

now from (58a), we readily find:

$$\frac{\partial y}{\partial \xi} = W^2 \sqrt{a}\left(\frac{e^{\sqrt{a}\,\xi} - e^{-\sqrt{a}\,\xi}}{e^{\sqrt{a}} + e^{-\sqrt{a}}}\right) \tag{61b}$$

To complete the solution, we evaluate (61b) at $\xi = 1$ and apply equation (54) to obtain:

$$-\frac{\delta}{\eta} W_o^2 \sqrt{a}\,\tanh\sqrt{a} = \rho\, h\, \phi_o^2 + \alpha\, \phi_o - e^{1/W_o} \tag{62}$$

substituting from the definition of "a", we have

$$-\frac{\delta W_o}{\eta}\sqrt{\eta e^{-1/W_o}}\ \tan h\ \frac{\sqrt{\eta e^{-1/W_o}}}{W_o^2} = \tag{63a}$$

$$\rho\, h\, \phi_o^2 + \alpha\, \phi - e^{-1/W_o}$$

and finally, substituting from ϕ from (31):

$$-\delta\, W_o \frac{\sqrt{e^{-1/W_o}}}{\eta}\ \tan h\ \left(\frac{\eta e^{-1/W_o}}{W_o^2}\right) \tag{63b}$$

$$= \frac{\rho h m^2}{(h-1)^2} + \frac{\alpha\, m}{h-1} - e^{-1/W_o}$$

Solution of (63b) for Wo yields the surface temperature for the equilibrium distribution. If we now set $\xi = 1$ in (47), we find the surface temperature perturbation:

$$(64) \qquad \Delta W_o = A_o \, e \left(\frac{b^2}{\delta^2 \eta^2} - b \right) \frac{\tau}{\sigma} \left(e^{b/\delta\eta} + e^{-b/\delta\eta} \right)$$

Recalling that b was defined through a Taylor's expansion of $\eta e^{-1/W}$ in (41), we may write:

$$(65a) \qquad \eta e^{-1/W} = a + bW + \ldots\ldots\ldots$$

$$= \eta \, e^{-1/W_o} + \frac{\eta}{W_o^2} e^{-1/W_o} (W - W_o)$$

$$(65b) \qquad b = \frac{\eta}{W_o^2} e^{-1/W_o}$$

hence

$$(66) \qquad \log \Delta W_o = \log A_o \cosh b/\delta\eta + b \left(\frac{b}{\delta^2} - 1 \right) \frac{\tau}{\sigma}$$

$$= \log A_o \cosh \frac{b}{\delta} + \frac{\eta}{W_o^2} e^{-1/W_o} \left(\frac{\eta}{W_o^2 \delta^2} e^{-1/W_o} - 1 \right) \frac{\tau}{\sigma}$$

and going back to the original variables we find:

$$(67) \qquad \log \frac{K}{E} \Delta T_o = \log A_o \operatorname{Cosh} \frac{AE\theta_o d\ell}{K \lambda T_o^2} e^{-E/KT_o}$$

$$+ \frac{AE\theta_o}{C\rho K T_o^2} e^{-E/KT_o} \left(\frac{A\theta_o E d^2 e^{-E/KT_o} - 1}{\lambda T_o^2 K} \right) t$$

In this form, (67) reveals the possibility of testing the theory. If a sample were heated semi-adiabatically (for example, by radiation from the walls of a heated evacuated enclosure) and the surface temperature of the sample were plotted as a function of time, then as the temperature exceeded the equilibrium temperature T_o, it should suddenly and spontaneously rise exponentially. If

$$\log \frac{K}{E} \quad \Delta T_o$$

were then plotted against t, a straight line should result above T_o with a slope given by the coefficient of t. This assumes that the coefficient of $t > 0$. Whether or not this is so will depend upon the first term in the parenthesis, which must be greater than unity. For lead (II) azide, these constants are fairly well known, and if T_o is taken as the explosion temperature, we may evaluate:

$$\text{(68a)} \qquad \frac{A\phi_o E d^2}{\lambda T_o{}^2 K}\, e^{-E/KT_o} \cong 2 \times 10^{-3}$$

where the explosion temperature is that of Henkin and McGill(2), and the other parameters have been previously discussed.

The calculation shows that, for the assumed parameters, *explosion should not take place*! However, the margin is small. For example, were the reaction zone taken to be 10^{-5} cm instead of 10^{-7} cm (68a) would yield ~ 20, and explosion would be predicted. A choice of d to be 10^{-5} cm could well have been taken; but this is not a good argument.

The problem at this point seems to be whether there exists any reasonable unambiguous way to test the theory developed here. It is almost too adjustable to be satisfactory. However, two very serious objections to the general form of the theory can be raised, quite apart from the fact that it is too easy to get a desired result out of it.

(Objection 1): It is assumed that a temperature T_o can be assigned to a region, and reaction rates predicted by an Arrhenius-type law containing this temperature T_o. In view of the fact that statistical fluctuations in temperature are always present, and that local reaction rates are very strong functions of local temperature, it would seem that explosions ought to be governed by the frequency of local temperature excursions above the critical temperature, which might mean that a temperature much lower than T_o might cause an explosion in a reasonable length of time. This idea has been attacked by Ling(3) and appears promising.

(Objection 2): The theory developed here was developed on the assumption of a single, homogeneous slab of explosive material, with well-defined surfaces. This is pure fiction as applied to lead (II) azide, a material normally available only in polycrystalline powder. Such a powder is mostly surface; if the theory developed here is valid then it is strange that the behavior of lead (II) azide is not governed more strongly than it is by physical form.

II. HOMOGENEOUS CASE

The two objections cited above naturally raise the question of the behavior of a more realistic model. We have assumed in the heterogeneous case that two surface reactions were involved, one carrying away the bond-breaking energy, and thus cooling the sample, and the other--the bimolecular reaction $2\ N_3 \longrightarrow 3\ N_2$--generating the heat that keeps the reaction alive. It is difficult to see how, in the more realistic context of a polycrystalline sample where the surface of reaction must surely be internal to the free surface, the first heat loss reaction can occur appreciably. The problem in fact can be re-phrased in the following manner: Why do not all sufficiently large explosive samples explode spontaneously? Where does the heat-generated by random decomposition--escape to?

We consider here an extremely simple, almost primitive model for thermal decomposition of an azide in which the only heat loss is through homogeneous heat radiation from the sample, and the only heat source is that due to homogeneous bimolecular reactions between azide radicals. The equations defining this case are the following:

$$(69) \qquad \frac{\partial n}{\partial t} = -\,R\,n^2 + \theta\,e^{-E/KT}$$

$$(70) \qquad \rho\,C\,\frac{\partial T}{\partial t} = AR\,n^2 - B\,\theta\,e^{-E/KT} - P\,\sigma\,E\,T^4$$

In (69) and (70), A is the heat of reaction of $2\ N_3 \longrightarrow 3\ N_2 + \Delta$, and B is the energy given up by the breaking of the metal-azide bond. P is a factor which is evaluated in the following manner: We assume each lattice plane, presumably at some temperature T, to radiate heat according to the fourth power law, and to have a characteristic emissivity ε. Since the radiation constant σ is in terms of unit area, we must multiply it by the number of unit area lattice planes in a unit volume. That number is designated as P.

Now let us consider (69) and (70), which are assumed to hold per unit volume of the sample, at an equilibrium decomposition rate defined by $\frac{\partial T}{\partial t} = \frac{\partial n}{\partial t} = 0$. We then have:

(71) $$R\, n_o^2 = \theta\, e^{-E/KT_o}$$

(72) $$AR\, n_o^2 = B\ \theta\, e^{-E/KT_o} + P\, \sigma\, \epsilon\, T_o^4$$

Whence eliminating n_o^2 we obtain:

(73) $$(A - B)\ \theta\, e^{-E/KT_o} = P\ \sigma\ \epsilon\, T_o^4$$

A transcendental equation in T_o which, however, is readily solved by interaction.

We will assume $\epsilon = 1$ (black body) which is admittedly pure hypothesis. Then, substituting the constants for lead azide:

$A = 210$ k cal/mol

$B = 40$ k cal/mol

$P = 2.15 \times 10^7$ lattice planes/cm

$\sigma = 1.37 \times 10^{-15}$ K cal/cm^2/°K^4

We find

(74) $$T_o = 640^\circ\ K = 367^\circ\ C$$

Again, a remarkably close result from a remarkably crude calculation. But is this equilibrium temperature also an explosion temperature? Again, this depends upon the sample behavior toward perturbation. It is a simple matter to test this behavior. Consider the very general homogeneous model:

(75) $$\frac{\partial n}{\partial t} = \theta\ e^{-E/KT} - g(n)$$

(76) $$\frac{\partial T}{\partial t} = A\ g(n) - B\ \theta\ e^{-E/KT} - h\ (T)$$

Which are natural generalizations of (69) and (70). Denoting:

(77) $$n - n_0 = P$$

(78) $$T - T_0 = q$$

and substituting $n = P + n_0$ and $T = q + T_0$ into (75) and (76), we obtain at once:

(79) $$\frac{\partial P}{\partial t} = \theta\, e^{-E/KT_0} \left(1 + \frac{PE}{KT_0{}^2}\right) - g - \frac{\partial g}{\partial n}\Big|_0 q$$

$$= \frac{PE}{KT_0{}^2}\, e^{-E/KT_0} - \frac{\partial g}{\partial n}\Big|_0 q$$

(80) $$\frac{\partial q}{\partial t} = A \left(g + \frac{\partial g}{\partial n}\Big|_0 q\right) - B\, \theta\, e^{-E/KT_0} \left(1 + \frac{EP}{KT_0{}^2}\right)$$

$$- h\,(T_0) - \frac{\partial h}{\partial T}\Big|_0 P$$

$$= A\,\frac{\partial g}{\partial n}\Big|_0 q - P\,\frac{B\,\theta E}{KT_0{}^2}\, e^{-E/KT_0} - \frac{\partial h}{\partial T}\Big|_0 P$$

taking account of the fact that T_0 and n_0 satisfy (71) and (72).

Now P and q are assumed to be upward perturbations in the active center concentration and the temperature respectively. Clearly the weakest condition which would define the lower limit of unstable equilibrium would be if both (79) and (80) were just greater than zero for P and q greater than zero; or, in the limit,

(81) $$\frac{\partial P}{\partial t}\Big|_0 = \frac{\partial q}{\partial t}\Big|_0 = 0$$

Applying this condition to (79) and (80):

(82) $$\frac{PE}{KT_0{}^2}\, e^{-E/KT_0} - \frac{\partial g}{\partial n}\Big|_0 q = 0$$

$$(83) \qquad P\left[\frac{\partial h}{\partial T}\Big|_o + \frac{B\theta E e^{-E/KT_o}}{KT_o^2}\right] - A\frac{\partial g}{\partial n}\Big|_o \; q = 0$$

Eliminating the last terms from (82) and (83), and assuming $P \neq 0$, we obtain:

$$(84) \qquad \frac{\partial h}{\partial T}\Big|_o \leqq \frac{(A-B)\theta_o E}{KT_o^2} e^{-E/KT_o}$$

as the condition for explosivity. Assuming now that $h = P \sigma \epsilon T^4$, and employing (73), we finally find:

$$(85) \qquad \frac{E}{K} - 4 T_o \geqq 0$$

as the condition for explosivity. This condition is well met for lead azide:

$$(86) \qquad 20{,}000^\circ \text{ K} - 1468^\circ \text{ K} >> 0.$$

There are several significant conclusions to be drawn from the above.

First, (85) does not depend upon $g(n)$. That is, the stability condition is not dependent upon the manner of heat release in the explosive, not even of the molecularity of the reaction.

This could be an important result, since it is well known that the explosion temperatures of azides depends remarkably little upon their physical states. It is clear from (85) that the parameters which determine stability, E and T_o, are characteristic of the material rather than the decomposition mode. (Observe in (73) that the determining equation for T_o contains neither R nor n_o; i.e., T_o is independent of $g(n)$).

Second, this model is by no means incompatible with a realistic heterogeneous model. Suppose for example we imagine a polycrystalline mass, each crystallite of which obeys the surface-sensitive heterogeneous system discussed in detail in part I, except that the first-order active center escape term is absent from eq. (1b) because most of the "surface" is internal to the sample as a whole.

To the microscopic observer, then, the 2 $N_3 \longrightarrow 3 N_2$ reactions which occur appear homogeneously distributed throughout the sample as a whole, and can be represented by a homogeneous term g (n), as in (75) and (76), leading to (74) and (85) quite independently of whether the reaction is "really" homogeneous.

Finally, we would expect measured explosion temperatures always to be somewhat lower than those given by (73), because heat losses in any real experiment will always include conduction terms as well as radiation terms.

It remains to consider the validity of homogeneous heat loss within the sample. This assumption is tantamount to assuming that the sample is transparent to its own thermal radiation. For sufficiently thick samples this will obviously be incorrect, and because of additional heat trapping due to self-absorption we would expect such thick samples to have appreciably lower explosion temperatures. A famous example of this behavior is the explosion of the ship containing ammonium nitrate off the Gulf of Mexico a few years ago. Ammonium nitrate is not even classed as an explosive in samples of the usual size. It would be interesting, if a bit risky, to determine the explosion temperature of a few tons of lead azide. If it were substantially lower than that for microcrystalline samples of small size it might provide some quantitative clue to the self-absorption of heat radiation in this substance.

III. RECOMMENDATIONS

Adequate experimental studies designed to make possible tests of realistic models are clearly indicated.

Such tests would involve the recording of decomposition rates vs. time for adiabatically isolated samples of proper geometry. Of particular importance would be the variation of these parameters, and also of the system time constant to thermal perturbations, as the thickness of the sample was varied. Without such studies it seems almost hopeless to attempt to bring theory and data any closer together than we have here.

IV. REFERENCES

(1) Final Report, Contract DA-44-009 ENG-4194, Drury College (1960).

(2) Henkin and McGill, Ind. Eng. Chem., 44, 1391 (1952).

(3) Ling, Quarterly Report, Contract DA-44-009-ENG (6 May - 4 August 1960).

NOTE ADDED

The equilibrium temperature reported in Part II of this paper (Homogeneous Case) is in error. It should be 10^{10} °K. Thus there is no reasonable equilibrium temperature for lead azide.

A complete and correct discussion of these equations will appear shortly in a Technical Report issued under ENG-4798.

OPTICAL AND ELECTRICAL PROPERTIES OF ALKALI METAL AZIDES[1]

by

S. K. Deb*
Radio and Electrical Engineering Division
National Research Council
Ottawa, Canada

The physical and chemical properties of inorganic solids can be most conveniently discussed in terms of the electron energy levels in solids. In order to estimate the electron energy levels in a solid it is necessary to have information on the optical and electrical properties of the compound. Next to alkali halides, the monovalent inorganic azides are perhaps the simplest compounds to study experimentally, since the decomposition products are simple and not complicated to any extent by secondary reaction. In many respects the alkali metal azides show close resemblance to alkali halides, yet very little is known about the optical and electrical properties of alkali azides.

The role of excitons in the decomposition of monovalent ionic azides has been emphasized by Yoffe and his co-workers(2,3). Direct experimental evidence on the exciton spectra exists only for thallous azide and silver azide(3,4). Cunningham and Tompkins(5) first measured the absorption spectra of sodium and potassium azide and they obtained a fairly sharp absorption edge around 2500 A that exhibited no structure. Nevertheless, they assumed that the exciton transitions occur near the absorption edge. The present work was undertaken to investigate the absorption spectra and the associated photoconductivity in alkali azides with the object of gaining information on their energy band structure.

EXPERIMENTAL AND RESULTS

Apparatus

(i) Apparatus for measuring absorption spectra

The apparatus used for measurements below 2000 A was a Jarrel Ash half meter vacuum monochromator. This instrument has a Seya-Namioka type mounted grating having a dispersion of 17 A/mm. The light source is a hydrogen discharge lamp fitted with a LiF window. The cryostat which held the refrigerated sample was provided with a rotating vacuum seal by which it is possible to pass the monochromatic light through a reference path, sample and a glass filter.

---

* National Research Council Postdoctorate Fellow.

The detecting system consists of an E.M.I. 6256 B photomultiplier tube. The transmitted radiation was monitored by a sodium salicylate transmission phosphor sprayed on the LiF window fitted close to the photomultiplier tube. For measurements above 2000 A a Perkin-Elmer Model 4000 recording spectrophotometer was used.

(ii) Apparatus for measuring photoconductivity

The photoconductivity was measured with an Applied Physics Corporation Model 31 vibrating reed electrometer. This instrument is capable of detecting a current as small as 10^{-17} amps originating in a high impedance source. By taking adequate care in shielding the measuring circuit, it was possible to detect current as small as 10^{-15} amps without great difficulty. The crystal of NaN_3 was held between two electrodes made of gold plated copper. One of the electrodes has a hole of 6 mm in diameter through which the crystal can be illuminated. The other electrode is connected to the input terminal of the electrometer. Both the crystal and the electrode assembly were insulated from the metal cryostat by means of fused quartz discs. DC electric field of about 1000 volts/cm was supplied from a highly shielded battery voltage supply. The crystal could be cooled down to about -150° C and the temperature was measured by a copper constantan thermocouple. The cryostat was mounted on the exit end of the vacuum monochromator. The photocurrent was recorded by a Varian recorder connected to the output of the electrometer.

Absorption spectra of thin films of azides

Since the absorption coefficient of most of the insulators in the fundamental absorption region is very light, of the order of 10^5 - 10^6 cm^{-1}, the measurement of absorption spectra has to be made on very thin films in order to resolve any structure in absorption. The normal method of film deposition by vacuum evaporation technique cannot be applied in azides because they decompose on heating. However, the alkali azides are sparingly soluble in absolute alcohol and this makes it possible to prepare thin films by careful evaporation from solution. The substrates used were plates of Harshaw single-crystal LiF which had negligible absorption in the spectral range investigated. The result obtained on the absorption spectra of thinner films (0.1 to 0.2) of NaN_3, KN_3, RbN_3 and CsN_3 at room temperature, liquid nitrogen and liquid helium temperature is shown in Fig. 1.

Absorption spectra of thicker films and thin single crystal

For measurement in the tail of the fundamental absorption edge, thicker specimens were used because the absorption coefficient was small. The results obtained with the thin single crystal of NaN_3 (55μ thick) and the thicker films (25μ to 50μ thick) of KN_3, RbN_3 and CsN_3 are shown in Fig. 2. A band having a maximum around 2225 A

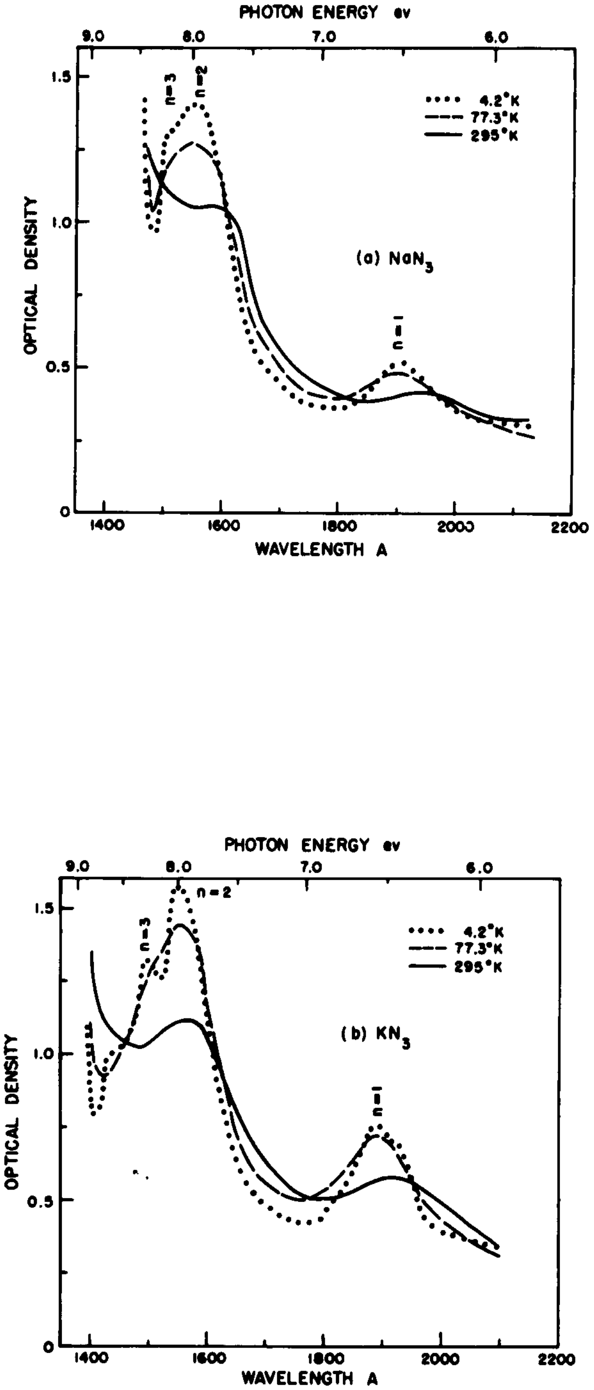

Figure 1. Absorption spectra of thin films of the alkali metal azides deposited on LiF substrate. (a) NaN_3; (b) KN_3; (c) RbN_3; (d) CsN_3.

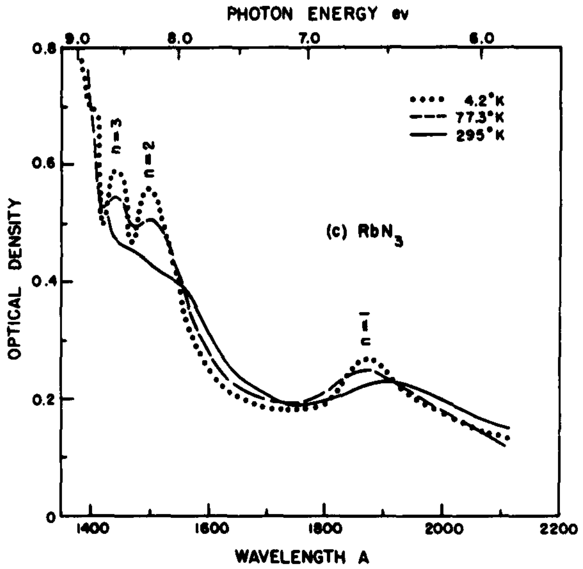

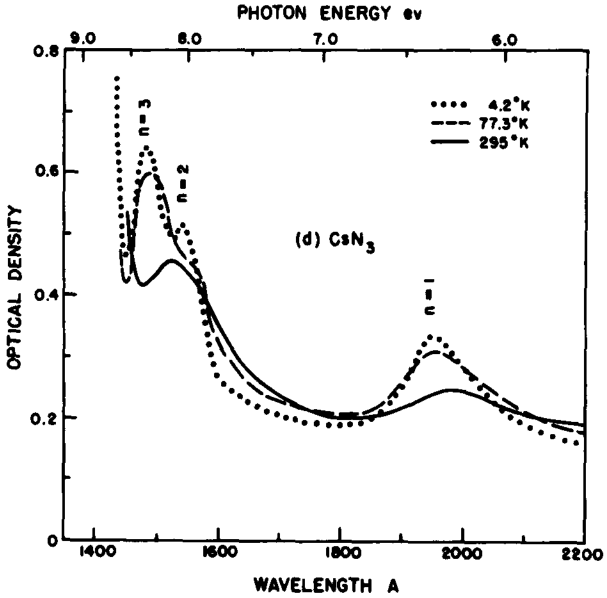

Figure 1 (cont'd)

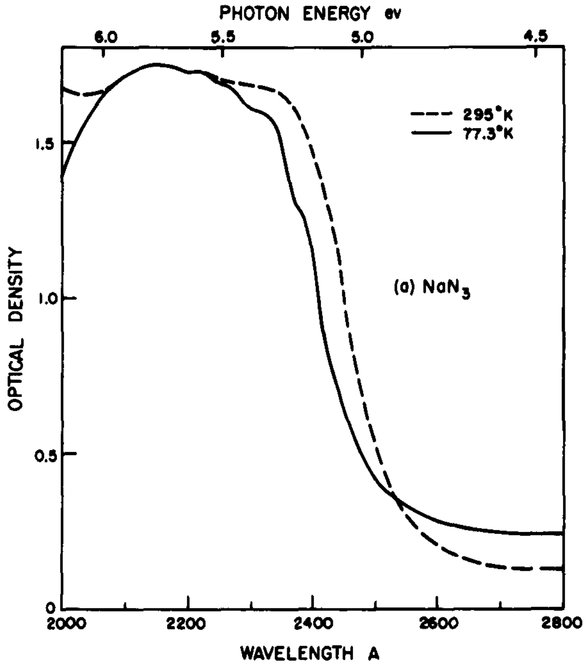

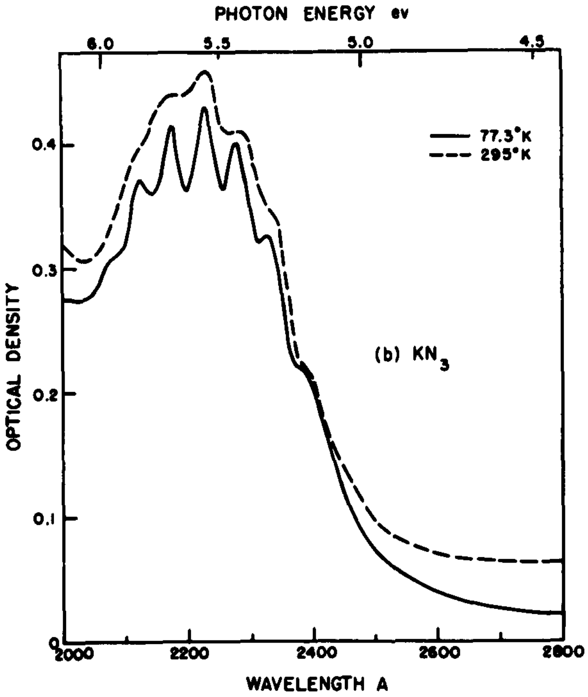

Figure 2. Absorption spectra of thin single crystal and thick films of alkali metal azides deposited on LiF. (a) Single crystal of NaN$_3$ 55 μ thick; (b) KN$_3$ film 10 μ thick; (c) RbN$_3$ film 47 μ thick; (d) CsN$_3$ film 23 μ thick.

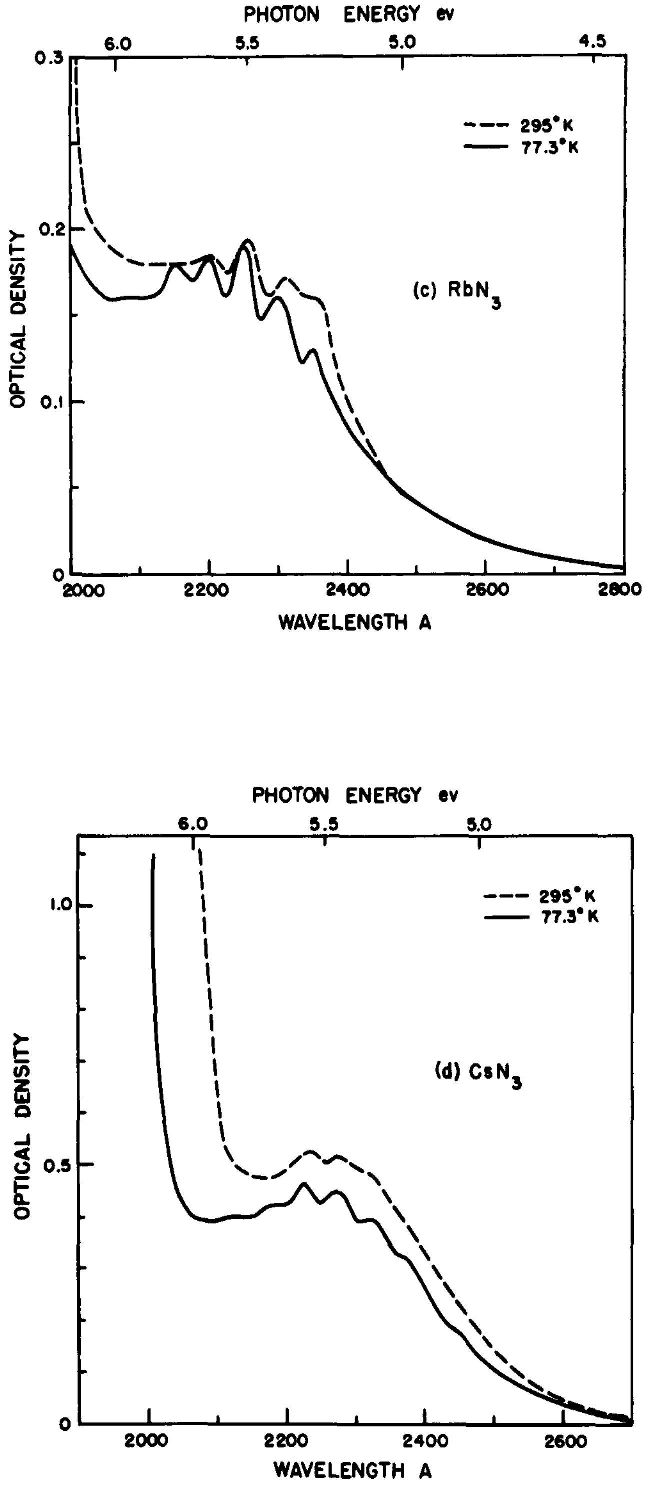

Figure 2 (cont'd)

and a multiple structure consisting of about seven bands is observed in all cases. The absorption coefficient at band maximum for NaN_3, KN_3, RbN_3 and CsN_3 are 70 cm^{-1}, 900 cm^{-1}, 90 cm^{-1} and 450 cm^{-1} respectively.

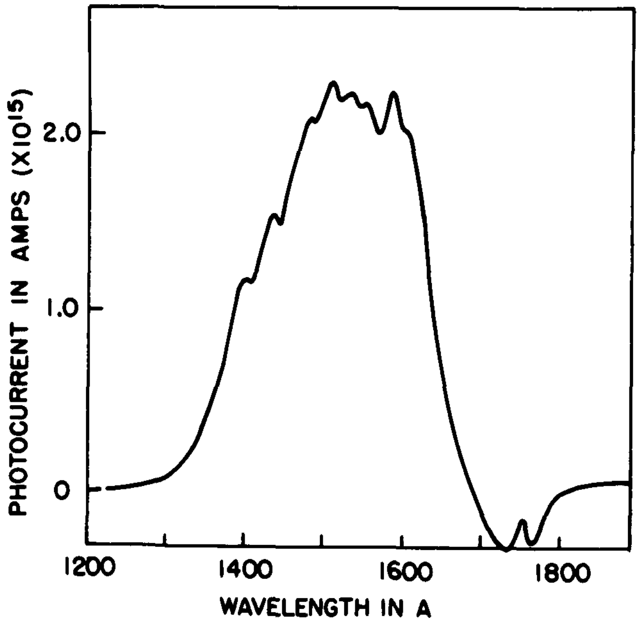

SPECTRAL DISTRIBUTION
OF PHOTOCURRENT IN SODIUM AZIDE

Figure 3. The spectral distribution of photocurrent in sodium azide crystal.

Photocurrent in sodium azide

The experiments on photocurrent measurements were done on single crystals of NaN_3 about 0.5 mm thick, obtained from the ERDL. Only some preliminary results have been obtained. The photocurrent could not be measured as a function of different parameters. However, the result obtained on the spectral distribution of photocurrent at room temperature is shown in Fig. 3. No corrections were applied for the variation in the light intensity with wavelength. The variation of photocurrent as a function of time for light of wavelength 1490 A is shown in Fig. 4. The variation of photocurrent with temperature for the full output of the hydrogen lamp has been measured over the range from -150° C to 23° C. The result obtained is shown in Fig. 5, where ln (photocurrent) is plotted against the reciprocal of the absolute temperature. The slope of the straight line gives the activation energy of about 0.01 eV.

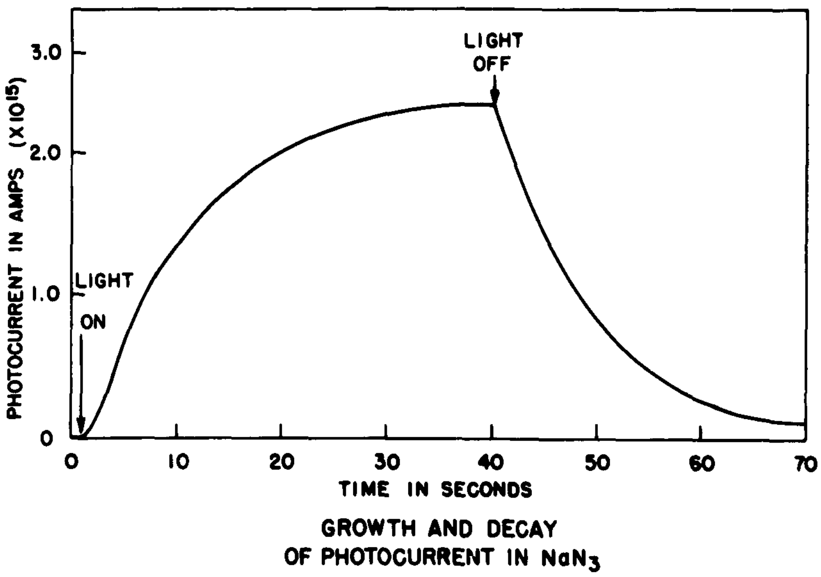

Figure 4. Photocurrent in sodium azide as a function of time for light of wavelength 1490 A.

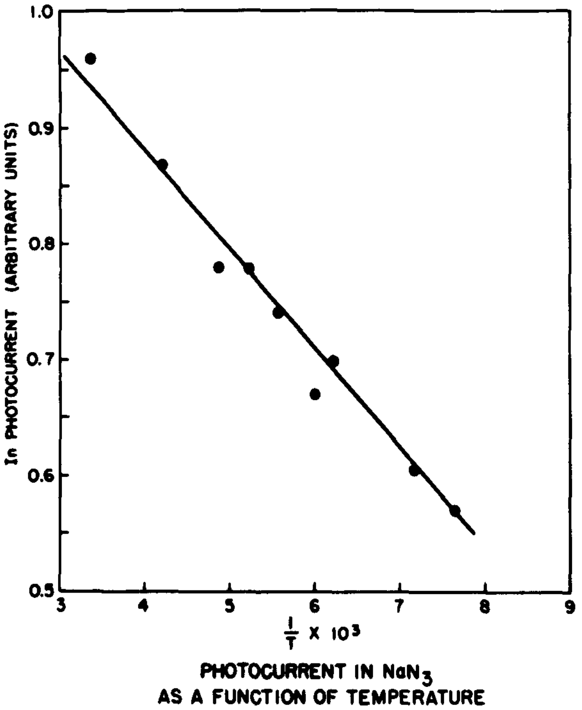

Figure 5. Photocurrent in sodium azide as a function of temperature for the full output of hydrogen lamp.

Fluorescence in azides

On irradiating a crystal of NaN_3 with monochromatic light at 2400 A a very weak blue fluorescence is observed. The fluorescence is structure sensitive and is not detectable in every crystal. In fact the crystal obtained from ERDL did not show any detectable fluorescence. The fluorescence spectrum observed in one batch of crystals of NaN_3 prepared in N.R.C. is shown in Fig. 6.

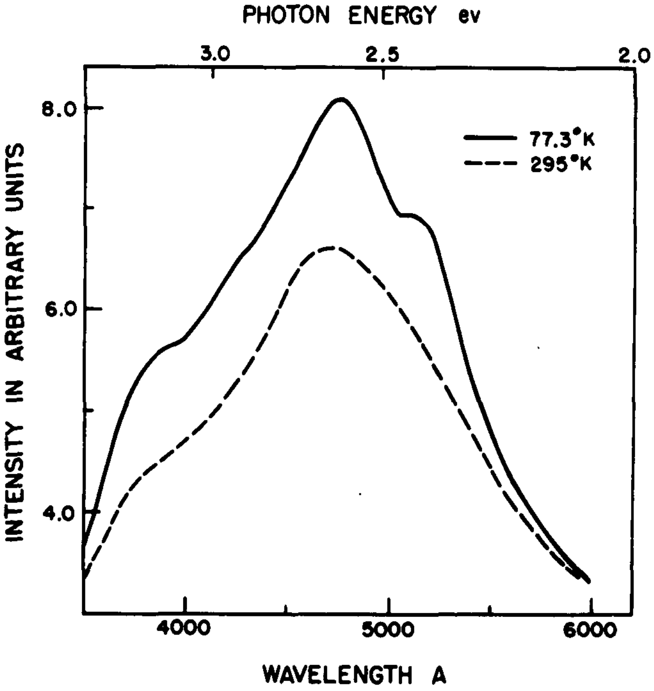

Figure 6. Fluorescence spectra of a thin single crystal (60 μ thick) of NaN_3.

X-ray irradiation of NaN_3

A single crystal of NaN_3 was irradiated at room temperature with x-rays (50 kv, 48 ma) from a Machlett tube with tungsten target and beryllium window, and the absorption spectra was measured at liquid nitrogen temperature. The result is shown in Fig. 7. It is clear that the effect of x-ray irradiation does not alter the fine structure of the band at 2225 A.

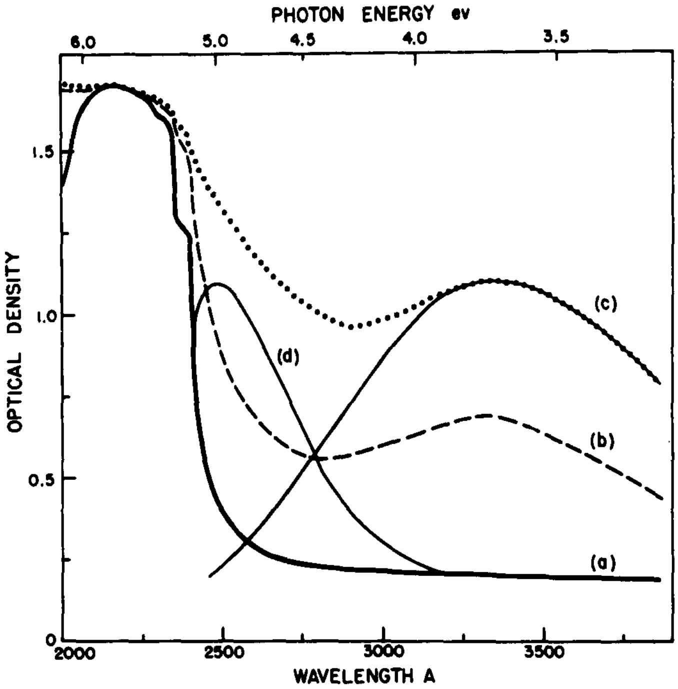

Figure 7. Absorption spectrum of NaN_3 after x-ray irradiation, measured at 77.3° K. (a) untreated crystal; (b) pure crystal after irradiation for 15 minutes at 295° K; (c) same crystal after irradiation for an additional 15 minutes at 295° K; (d) curve (c) minus curve (a).

DISCUSSION

Absorption spectra

The absorption coefficient in the neighbourhood of first absorption peak is of the order of 10^5 cm^{-1}. This indicates an allowed optical transition probably to an exciton level. Assuming the exciton spectrum follows a hydrogen-like series, it should be possible to represent the spectrum by the equation:

$$\nu_n = \nu_\infty - R\mu/K_o^2 m\ n^2 \qquad \ldots 1$$

when ν_∞ is the series limit, n is the quantum number, R is the Rydberg's constant, μ is the reduced effective mass of the electron-hole system, K_o is the high frequency dielectric constant and m is the free electron mass. And indeed the observed absorption peaks of NaN_3, KN_3, RbN_3 and CsN_3 do fit into an expression of this form. The last term in equation (1) gives the optical energy required to dissociate the excitons and it turns out that the exciton dissociation energies for quantum number n = 1 are 1.97 eV, 2.03 eV, 2.21 eV and 2.26 eV, for NaN_3, KN_3, RbN_3 and CsN_3, respectively. It is then possible to calculate the reduced effective mass 'μ' of the exciton from the equation:

$$\mu = E_1 K_o^2 m/R \qquad \ldots 2$$

The reduced effective mass of the exciton was found to be approximately 0.7 m for NaN_3 and 0.76 m for KN_3. These values are quite reasonable for ionic compounds.

The magnitude of the absorption coefficient (10^2 to 10^3 cm^{-1}) of the band with multiple structure having a maximum around 2225 A is relatively small for an allowed optical transition due to excitons. On the other hand, it is difficult to attribute it to an impurity which could give rise to such a strong band without being detected by infrared spectra. Moreover, it is unlikely that the same impurity would consistently appear in all the azides obtained from different sources. It seems more likely to be a transition of low probability to a low-lying excited state of the azide ion. The fact that the band structure is temperature dependent and the average splitting between the bands is 1044 cm^{-1}, suggests that it may be due to the vibrational frequencies being superimposed on the electronic transition of the azide ion. Such frequencies would be characteristic of the well-known vibration frequencies of the azide ion in the ground state.

The result obtained on the fluorescent spectrum is not sufficient to make a vibrational analysis of the structure. It is interesting, however, that a similar fluorescence has been observed by Sidman(6), but in the case of azide a rather high Stoke's shift is observed.

Photocurrent in azides

Until all the photocurrent is measured as a function of all different parameters, it is difficult to make any satisfactory analysis. It appears, however, that the observed photocurrent is a result of both internal and the external photoelectric effect. It is significant, however, that the positions of the observed photocurrent peaks are in good agreement with the absorption measurements. The growth and decay of photocurrent is typical of photoconductive behaviour. The activation energy is lower than what one would have expected. In the ideal case, of course, one should measure the activation energy at different photocurrent peaks. The work on the measurement of both internal and external photoelectric effect is in progress and it is hoped that we shall have a more satisfactory picture when the measurement is completed.

CONCLUSION

From the above results it is apparent that the optical energy necessary to excite an electron from the full band to the conduction band is quite high, about 8.5 eV. The thermal energy necessary to dissociate the optically formed exciton, which is given by the relation

$$E_t = E_o \frac{K_o}{K_s} \qquad \ldots 3$$

is about 0.7 eV for n = 1. This would possibly account for the relatively high stability of alkali metal azides as compared to the other monovalent azides such as TlN_3, AgN_3 and CuN_3. The probability of decomposition through exciton formation is also quite small because of the rather high energy involved in its formation and its dissociation.

ACKNOWLEDGMENT

I am very grateful to Dr. J. H. Simpson for his encouragement, advice and comments. I am also grateful to Dr. A. D. Yoffe of Cavendish Laboratory, Cambridge, for providing the sample and valuable suggestions. I would also like to thank Mr. O. F. Kezer of ERDL for supplying the sodium azide crystals. My thanks are due to Mr. E. Bolton for his skilled technical assistance.

REFERENCES

1. Part of this work is now in press for publication in the Journal of Chemical Physics.
2. B. L. Evans and A. D. Yoffe, Proc. Roy. Soc. (London) A250, 346 (1959).
3. S. K. Deb and A. D. Yoffe, Proc. Roy. Soc. (London) A256, 514 (1960).
4. A. C. McLaren and G. T. Rogers, Proc. Roy. Soc. (London) A240, 484 (1957).
5. J. Cunningham and F. C. Tompkins, Proc. Roy. Soc. (London) A251, 27 (1959).
6. J. W. Sidman, J. Am. Chem. Soc. 79, 2669 (1957).

A STATISTICAL THEORY OF INITIATION

by

Daniel S. Ling, Jr.
PEC Corporation
Boulder, Colorado

I. General Discussion

At this same conference last year I presented a statistical model of the initiation process which I termed the 'single-point' model. Since that time considerable progress has been made in the numerical treatment of this model and these results will be presented today. First, however, I feel it will be appropriate to briefly review the theory of the 'single-point' model.

Chemical reactions proceed at a speed governed by a reaction rate expression which is commonly taken to be of the familiar Arrhenius form, namely $NAe^{-E/RT}$. This expression gives the number of reactions occurring per unit time in a sample of N molecules at an absolute temperature of T degrees. E is the activation energy and A is the frequency factor. When the number of molecules, N, in the sample is very large, it is quite proper to interpret the Arrhenius expression as a reaction rate; that is, it does indeed give the number of reactions occurring per unit time. However, if N is small (say of the order of 10 or 100 molecules) then it is essential to remember that we are describing what is fundamentally a quantum mechanical process. In this case the Arrhenius expression must be interpreted as giving the reaction probability per unit time. That is, it gives the probability per unit time that a reaction takes place.

Now, presumably, the initiation process takes place in a region containing relatively few molecules. It would therefore seem important to investigate the consequences of shift of emphasis from the reaction rate to the reaction probability point of view. In particular I would like to investigate the possibility that initiation originates with a single molecular reaction. This is an idea which was proposed many years ago by Garner and others. However, this proposal has received little support because of the following type of argument. If the energy released by a single reaction is divided among nearest neighbors, the amount of energy supplied each neighboring molecule is somewhat less than the activation energy. Thus the process does not continue. If several contiguous molecules are assumed to react simultaneously, one can then supply neighboring molecules with an energy greater than the activation energy.

However, the probability that two neighboring molecules undergo a reaction simultaneously is exceedingly small.

It is my feeling that the previous argument does not adequately consider the statistical nature of the problem. If we supply neighboring molecules with an energy less than the activation energy, there is still a probability that one of these neighbors will undergo a reaction. This probability may be quite small but it is non-zero. If there are many such initial reactions occurring per unit time in a sample, it is only necessary for one of them to set off the neighboring molecules in order that the process lead to explosion.

The statistical nature of the problem may be emphasized in a slightly different manner. Consider an ensemble consisting of a large number of identical samples of an explosive. Now even at room temperature (or at somewhat higher temperatures if the samples are heated) there will be random reactions occurring in the samples due to the Arrhenius expression. I will refer to such occurrences as 'initiation sites'. In the neighborhood of these 'initiation sites' the temperature will be temporarily increased. Because of the increased temperature some of the 'sites' may induce reactions in their neighbors. This in turn will raise the temperature still more. Thus in the vicinity of each 'site' a whole spectrum of temperatures is possible. Since the sites are randomly located in both space and time every point in the samples has a spectrum of possible temperatures. Thus we cannot really refer to the value of the temperature at some particular point in a sample. Rather, we should associate a probability function, $P(T, x, y, z, t)$, with our ensemble of samples, such that $P(T)dT$ gives the probability of a temperature between T and $T + dT$ at the time "t" and at the point "x, y, z" in the sample.

Now to treat the problem from the point of view of the function described above is a rather formidable undertaking. For this reason, I have considered a much simplified model of the above problem. I have dubbed this the 'single-point model' and believe that it retains enough reality to make it well worth study. The nature of the single point model is described in the next paragraph.

Let us consider a small region about an initiation site. The region might contain perhaps ten, perhaps a hundred molecules. We will assume the region to be sufficiently small, that any energy released in subsequent reactions may be considered to be distributed immediately and uniformly over the region. This has the advantage of establishing a uniform temperature over the region, thereby eliminating the spatial dependence of the problem and hence the name, 'single-point model'. Now this region will lose heat to surroundings which are assumed to be at a constant ambient temperature T_o.

The rate of heat loss is taken as $K(T - T_0)$. Each reaction which occurs raises the temperature of the region by an amount Q. $P(T, t)dT$ will denote the probability that the temperature of the region lies between T and T + dT. Note especially that, because of the simplifying assumptions of the model, P is not a function of spatial variables. As reactions occur in the region, the number of available molecules to undergo reactions is decreased. The 'single-point model' neglects this loss of available molecules.

The derivation of the equation satisfied by P has been discussed in detail in earlier reports. The result is

$$(1) \qquad \frac{\partial P}{\partial t} = KP + K(T - T_0)\frac{\partial P}{\partial T} - p(T)P(T) + p(T - Q)P(T - Q)$$

where $p(T) = NAe^{-E/RT}$. P satisfies an initial condition $P(T, 0) = \delta(T - T_0 - Q)$ where δ is the Dirac δ function. This follows because by assumption we are studying an 'initiation site' where a first reaction has already occurred and has raised the temperature from T_0 to $T_0 + Q$. It is convenient to measure RT in units of the activation energy E and to choose a time unit such that K = 1. With these choices the equation becomes

$$(1a) \qquad \frac{\partial P}{\partial t} = P + (T - T_0)\frac{\partial P}{\partial T} - p(T)P(T) + p(T - Q)P(T - Q)$$

where $p(T) = Ue^{-1/T} \qquad U = NA$

Thus the theory involves three parameters, U, Q and T_0.

It is possible to solve this equation by assuming a solution of the form

$$(2) \qquad P(T, t) = A(t)Y(t) + \sum_{n=1}^{\infty} A_n(t)U_n(T, t)$$

The U_n's are assumed to be different from zero only in the neighborhood of $T = \theta_n(t)$ and the θ_n's are such that $\theta_{n+1}(t) \approx \theta_n(t) + Q$. Each U_n is normalized so that $\int_{T_0}^{\infty} U_n(T, t)dT = 1$. $A_n(t)$ measures the amount of probability located in the U_n bump. Preliminary calculations have indicated that the U_n's are narrow enough so that to good approximation they may be taken to be δ functions located at θ_n; thus $U_n(T, t) \approx \delta(T - \theta_n(t))$.

$Y(t)$ describes the fall in temperature of the initial δ function, $\delta(T - T_o - Q)$, and $A(t)$ describes its loss of probability. Clearly $A(0) = 1$, $A_n(0) = 0$.

It can then be shown that the A's and Θ's satisfy the following system of equations:

$$\begin{aligned}
&\frac{dA}{dt} = -Ue^{-1/Y} A \\
&\frac{dY}{dt} = -(Y - T_o) \\
&\frac{dA_1}{dt} = Ue^{-1/Y} A - Ue^{-1/\Theta_1} A_1 \\
(3)\qquad &\frac{d\Theta_1}{dt} = -(\Theta_1 - T_o) + \frac{Ue^{-1/Y} A}{A_1} (Y + Q - \Theta_1) \\
&\frac{dA_2}{dt} = Ue^{-1/\Theta_1} A_1 - Ue^{-1/\Theta_2} A_2 \\
&\frac{d\Theta_2}{dt} = - (\Theta_2 - T_o) + \frac{Ue^{-1/\Theta_1} A_1}{A_2} (\Theta_1 + Q - \Theta_2) \\
&\text{etc.}
\end{aligned}$$

As functions of time, the A's characteristically increase to a maximum value and then decrease to constant value at large time. Any probability left in a bump as $t \longrightarrow \infty$ describes a situation in which the sample failed to go to explosion. Remembering that $A + \sum_{n=1}^{\infty} A_n = 1$ for all t, the question arises; 'How do we find the probability that an explosion occurs'? The answer lies in the following observation: Define $F_m = \lim_{t\to\infty} (A + \sum_{n=1}^{m} A_n)$. Now consider the limit of F_m as $m \longrightarrow \infty$. This may very well approach a number less than one. We denote this limit by F, i.e., $F = \lim_{m\to\infty} F_m$. It is easy to see that $1 - F$ measures the amount of probability that escapes to arbitrarily high numbered bumps and therefore gives the probability of explosion.

This system of equations has been programmed for an IBM 650 computer and the results of these calculations are presented in section III.

II. Statistical Versus Non-statistical Theory

In this section I emphasize the need for a statistical approach to the problem of explosive initiation.

In the 'single-point' model the mean temperature is given by

$$\bar{\Theta} = \sum_n A_n\Theta_n = AY + A_1\Theta_1 + A_2\Theta_2 + \ldots . \tag{4}$$

The time derivative of $\bar{\Theta}$ is given by

$$\frac{d\bar{\Theta}}{dt} = \sum_n \left(\Theta_n \frac{dA_n}{dt} + A_n \frac{d\Theta_n}{dt}\right) \tag{5}$$

The time derivatives on the right-hand side of Equation (5) may be eliminated by using the Equations (3) of Section I. The result of this elimination is

$$\frac{d\bar{\Theta}}{dt} = -\,(\bar{\Theta} - T_o) + QU \sum_n A_n e^{-1/\Theta_n} \tag{6}$$

On the other hand, we could treat the single-point model in the more usual non-statistical method which ignores the possibility of a temperature distribution. In this case we would deal with a single-point whose mean temperature we will call $\bar{T}$. The 'point' loses heat by conduction at a rate given by $-(\bar{T} - T_o)$. Heat is supplied by reactions at a rate given by $QUe^{-1/\bar{T}}$, since the number of reactions per unit time is given by $Ue^{-1/\bar{T}}$ and the heat supplied per reaction is Q. In this case the change in $\bar{T}$ with time is governed by the equation,

$$\frac{d\bar{T}}{dt} = -\,(\bar{T} - T_o) + QUe^{-1/\bar{T}} \tag{7}$$

A comparison of Equations (6) and (7) exhibits very clearly the difference between a statistical and a non-statistical theory. The difference lies in the nature of the self-heating term, $QU \sum_n A_n e^{-1/\Theta_n}$ in the one case and $QUe^{-1/\bar{T}}$ in the other. It is clear that even very small probabilities A_n, for the higher temperature bumps, will be very important because of the very rapid increase of e^{-1/Θ_n} with increasing Θ_n.

Equation (7) predicts an explosion when $\overline{T}$ increases with time. If $\overline{T}$ decreases with time, then there will be no explosion.

In order to compare numerically the significance of the statistical versus the non-statistical theory, we have computed Equation (7) for the same set of parameters for which the equations of Section I were computed. The results of these computations are presented in Section III.

III. Numerical Calculations

Equation (7) for $\overline{T}$ was computed for $U = 10^6$, $Q = 0.04$ and T_0 given by:

1. $T_0 = .02$
2. $T_0 = .03$
3. $T_0 = .032$
4. $T_0 = .033$
5. $T_0 = .035$
6. $T_0 = .04$

The results of these calculations are presented in Figure 1. We see that for an ambient temperature somewhere between 0.032 and 0.033, we pass from the case of no explosion to an explosion.

We also have computed the equations of Section I for $U = 10^6$, $Q = 0.04$ and T_0 given by:

1. $T_0 = .0075$
2. $T_0 = .008$
3. $T_0 = .02$
4. $T_0 = .022$

The results of these calculations are presented in Figure 2 for the case $T_0 = .022$.

The A_n approach constant values for sufficiently large time and these final values are presented in Table I. We have previously pointed out that in the theory of the single-point model, the probability of explosion is given by 1 - F. Table I also lists the explosion probability 1 - F.

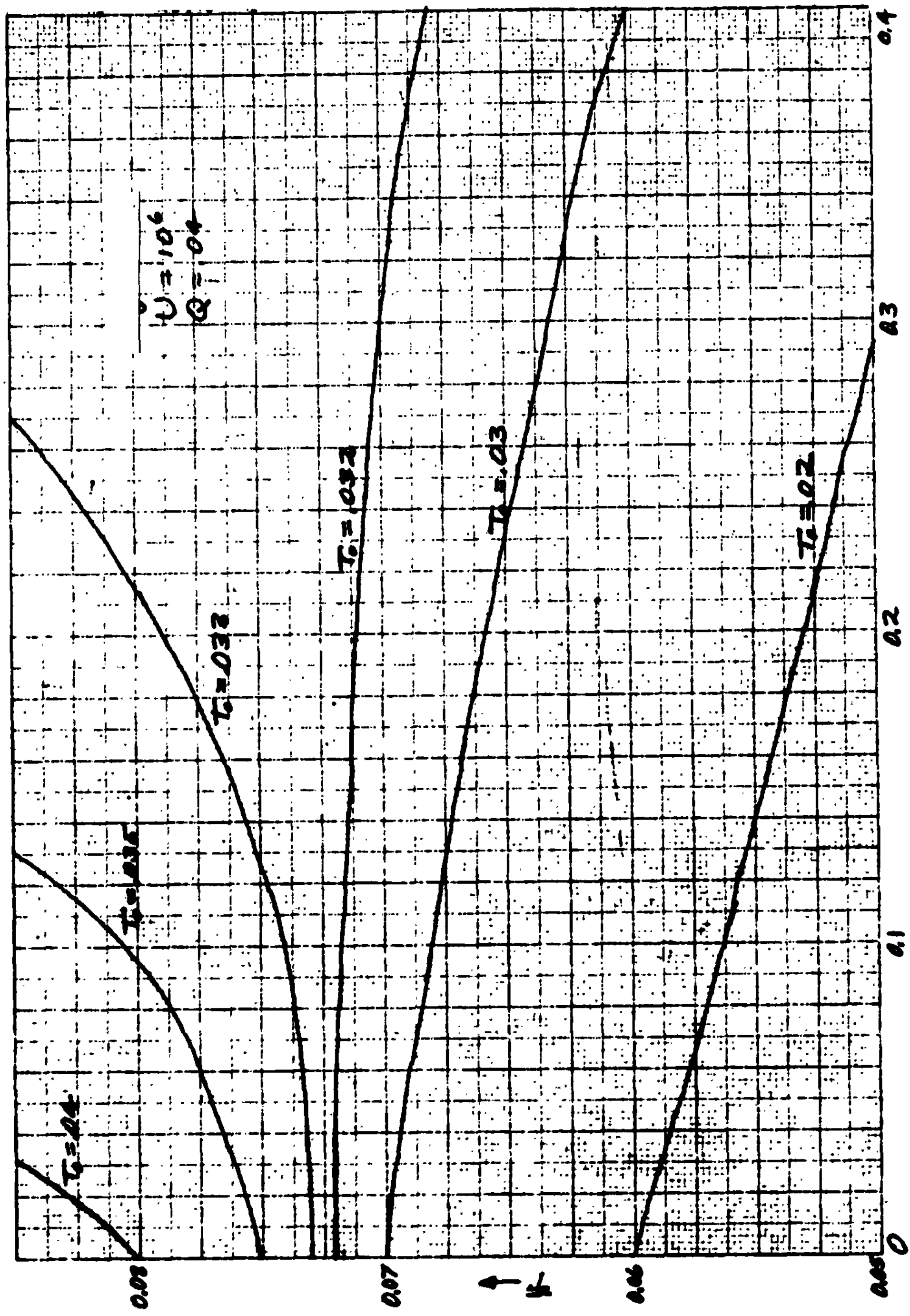
U = 10⁶
Q = .04
T₀=.04
T₀=.035
T₀=.033
T₀=.032
T₀=.03
T₀=.02
0
0.1
0.2
0.3
0.4
t →
0.05
0.06
0.07
0.08
T ←

Figure 1

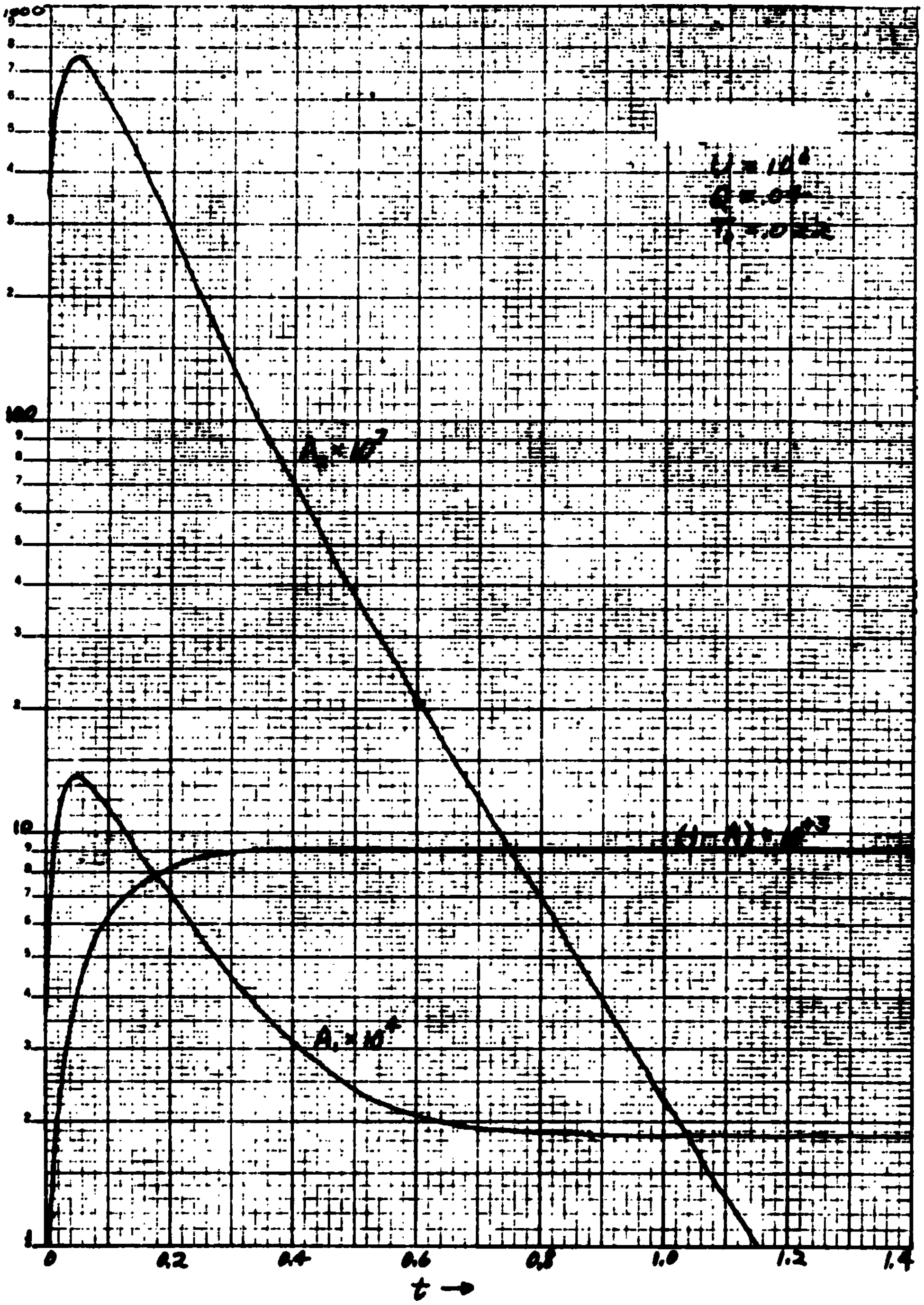
1000
100
10
1
U = 10^6
Q = .04
T_1 = .022
A_2 × 10^2
(1 − A) × 10^3
A_1 × 10^4
0
0.2
0.4
0.6
0.8
1.0
1.2
1.4
t →

Figure 2

TABLE I

T_o	A	A_1	A_2	1-F
0.0075	0.999962	1.897×10^{-5}	4.422×10^{-9}	1.93×10^{-5}
0.008	0.999951	2.285×10^{-5}	5.286×10^{-9}	2.60×10^{-5}
0.02	0.994945	1.850×10^{-4}	3.572×10^{-8}	4.87×10^{-3}
0.022	0.990754	1.846×10^{-4}	3.465×10^{-8}	9.06×10^{-3}

Note then the following comparison. In the non-statistical treatment of Equation (7), it is necessary to go to an ambient temperature greater than 0.032 in order to achieve explosion. In the statistical single-point model, an ambient temperature as low as 0.02 gives a probability of 1/2 of 1 percent that an explosion will occur. Note also that an increase of ambient temperature to 0.022 is sufficient to increase the explosion probability by a factor of two.

IV. Concluding Remarks

The explosion probabilities listed in Table I may seem very small but it must be remembered that very many 'initiation sites' will be present in the sample and only one of them need be successful in order that an explosion result. In fact, the probabilities listed in Table I are almost surely much too large. More likely values are probably in the range 10^{-15} to 10^{-20}. The value of 1-F is very sensitive to the values chosen for Q, U and T_o and it is possible to achieve much smaller values of 1-F while still using reasonable values for the parameters Q, U and T_o.

In conclusion I would like to emphasize that I fully realize that the 'single-point' model is very crude. However, it is what I choose to call a 'conservative model'. By this I mean that if the 'single point' model indicates a need for a statistical treatment (which it clearly does) then a more realistic model would even more definitely require a statistical treatment.

THE SYNTHESIS AND PROPERTIES OF TETRAVALENT LEAD AZIDES

by

Eugene Lieber
Roosevelt University
Chicago, Illinois

Abstract

The investigations on the synthesis of tetravalent lead azides were prompted by the hypothesis (Lieber, ENG-3242) that the degradation of lead (II) azide, either thermal or radiant induced, proceeds by a disproportionation to lead (IV) azide (plus lead), followed by a sequence of steps leading back to lead (II) azide (plus nitrogen). Previous studies (Lieber, ENG-3728) indicated that if lead (IV) azide did, indeed, exist, its existence was transitory. In examining the disproportionation hypothesis, a similarity was observed between it and the disproportionation behavior of arylated lead in both the two and four oxidation states. Thus, diphenyl lead disproportionates to tetraphenyl lead (plus metallic lead). This suggested an experimental approach which has resulted in the preparation of lead (IV) azides. These compounds are organo-lead azides containing the phenyl group. Three members of the simplest series, triphenyl lead azide, diphenyl lead diazide and phenyl lead triazide have been the subject of this investigation. Details of the successful preparation of triphenyl lead azide and diphenyl lead diazide are presented. Attempts to synthesize phenyl lead triazide are also described. The properties of triphenyl lead azide and diphenyl lead diazide are presented.

INTRODUCTION

The hypothesis has been suggested by Lieber[1] (superscripts refer to section on Footnotes and References) that the discontinuities observed in the breakdown of divalent lead azide (PbN_6) and its photochemical yellowing could be explained on the basis that the azide of divalent lead is capable of disproportionation to the azide of tetravalent lead (PbN_{12}). The path suggested was as follows:

$$2\,PbN_6 \longrightarrow Pb + PbN_{12}$$

$$PbN_{12} \longrightarrow PbN_{10} + N_2$$

$$PbN_{10} \longrightarrow PbN_8 + N_2$$

$$PbN_8 \longrightarrow PbN_6 + N_2$$

the cycle then being repeated. A similar disproportionation reaction involving the formation of a tetravalent lead compound and metallic lead was suggested by Krause[2] as an intermediate in the preparation of organo-lead compounds by the reaction of Grignard reagents with lead dichloride according to the overall equation:

$$4\ RMgX + 2\ PbCl_2 \longrightarrow R_4Pb + Pb + 2\ MgX_2 + 2\ MgCl_2$$

The following stepwise reaction was suggested[2] as representing the overall reaction:

$$2\ RMgX + PbCl_2 \longrightarrow R_2Pb + MgX_2 + MgCl_2$$

$$3\ R_2Pb \longrightarrow 2\ R_3Pb + Pb$$

$$4\ R_3Pb \longrightarrow 3\ R_4Pb + Pb$$

Attempts[3] to show the existence of the R_3Pb species were inconclusive. Accordingly, the disproportionation may be represented by the sequence:

$$3\ R_2Pb \longrightarrow R_6Pb_2 + Pb$$

$$2\ R_6Pb_2 \longrightarrow 3\ R_4Pb + Pb$$

or by the single disproportionation step:

$$2\ R_2Pb \longrightarrow R_4Pb + Pb \quad (i)$$

The similarity between equation (i) and Lieber's[1] hypothesis for the disproportionation of lead (II) azide provided the experimental approach for a study of lead azide with lead in the tetravalent state. The series selected for examination are summarized in Table I. The successful preparation of two members of the tetravalent azide series, summarized in Table I, was accomplished by displacing the phenyl group by an azide group.

TABLE I
FAMILY OF PHENYLATED TETRAVALENT LEAD AZIDES

Substance	Formula	Structure
Lead (IV) azide	PbN_{12}	$Pb(N_3)_4$
Phenyl lead triazide	$C_6H_5N_9Pb$	$(C_6H_5)Pb(N_3)_3$
Diphenyl lead diazide	$C_{12}H_{10}N_6Pb$	$(C_6H_5)_2Pb(N_3)_2$
Triphenyl lead azide	$C_{18}H_{15}N_3Pb$	$(C_6H_5)_3Pb(N_3)$
Tetraphenyl lead	$C_{24}H_{20}Pb$	$(C_6H_5)_4Pb$

TETRAVALENT LEAD AZIDES

(A) Synthetic Studies

(1) Lead (IV) Azide, (PbN_{12}):

Previous attempts to synthesize lead (IV) azide, PbN_{12}, by Möller[4] and Lieber[5] served only to indicate the qualitative existence of the species PbN_{12} to which the structure (I):

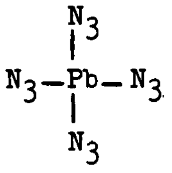

$$\begin{array}{c} N_3 \\ | \\ N_3-Pb-N_3 \\ | \\ N_3 \end{array}$$

I

can be assigned. Accordingly, while the preparation of divalent lead azide (PbN_6) is well characterized there is, as yet, no authentic isolation of PbN_{12}. However, it is interesting to note that "related" tetravalent lead compounds have been well described in the literature. The so-called "halogenoid" character of the azide group focuses attention on lead (IV) chloride, (II):

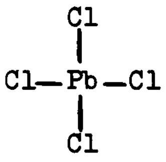

$$\begin{array}{c} Cl \\ | \\ Cl-Pb-Cl \\ | \\ Cl \end{array}$$

II

first isolated by Postinikov[6]. It is a yellow liquid, solidifying at -15°. Above +5° it decomposes, apparently, according to the reaction:

$$PbCl_4 \longrightarrow PbCl_2 + Cl_2$$

The tetra-bromide and -iodide of lead have not as yet been described. It is also important to note that, while lead (IV) chloride is unstable (above +5°), the halo ions show a marked increase in stability. Thus, ammonium hexachloroplumbate, $(NH_4)_2PbCl_6$, a white crystalline solid, is stable up to 120°. While it appears impossible to prepare lead (IV) fluoride (PbF_4), Hoppe[7] has recently (1957) described the preparation of barium hexafluoroplumbate, $BaPbF_6$. Standard methods are available[8] for the preparation of lead tetraacetate ($Pb(C_2H_3O_2)_4$), (III):

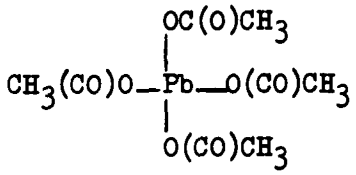

$$CH_3(CO)O-\overset{\displaystyle OC(O)CH_3}{\underset{\displaystyle O(CO)CH_3}{Pb}}-O(CO)CH_3$$

III

It crystallizes as colorless prisms stable up to 180°.

(2) Triphenyl Lead Azide, $(C_6H_5)_3Pb(N_3)$, (IV):

The preparation of triphenyl lead azide (IV)

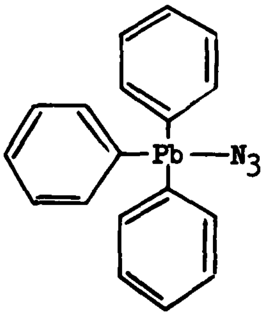

IV

was achieved essentially by the nucleophilic displacement of a phenyl group by the azide group:

$$(C_6H_5)_4Pb \quad + \quad HN_3 \longrightarrow (C_6H_5)_3PbN_3 \quad + \quad C_6H_6$$

However, in order to accomplish the substitution of one phenyl (C_6H_5) group for an azido-group, a series of reactions were required starting with tetraphenyl lead. These reactions are summarized in CHART I. This required as precursors the syntheses, respectively of:

(a)	Tetraphenyl lead	$(C_6H_5)_4Pb$	V (see Chart I)
(b)	Triphenyl lead chloride	$(C_6H_5)_3PbCl$	VI
(c)	Triphenyl lead hydroxide	$(C_6H_5)_3Pb(OH)$	VII

Tetraphenyl lead (V) was prepared, in 80 percent yield by a modification of the method of Gilman[9] summarized in CHART II. The tetraphenyl lead so obtained was converted to triphenyl lead chloride (see CHART I, structure VI), by the method of Gilman and Robinson[10] by treating tetraphenyl lead with dry hydrogen chloride. The yield

$$\underset{\mathrm{V}}{(C_6H_5)_4Pb} + HCl \longrightarrow \underset{\mathrm{VI}}{(C_6H_5)_3PbCl} + C_6H_6$$

$$(C_6H_5)_3PbCl + KOH \longrightarrow \underset{\mathrm{VII}}{(C_6H_5)_3Pb(OH)} + KCl$$

$$(C_6H_5)_3Pb(OH) + HN_3 \longrightarrow \underset{\mathrm{IV}}{(C_6H_5)_3Pb(N_3)} + H_2O$$

Chart I: Synthesis of Triphenyl Lead Azide

STEP (A) : $4\ C_6H_5Li + 2\ PbCl_2 \longrightarrow (C_6H_5)_4Pb + Pb + 4\ LiCl$

STEP (B) : $2\ C_6H_5I + Pb \longrightarrow (C_6H_5)_2PbI_2$

STEP (C) : $2\ C_6H_5Li + (C_6H_5)_2PbI_2 \longrightarrow (C_6H_5)_4Pb + 2\ LiI$

OVERALL REACTION:

$$3\ C_6H_5Li + PbCl_2 + C_6H_5I \longrightarrow (C_6H_5)_4Pb + 2\ LiCl + LiI$$

Chart II: Synthesis of Tetraphenyl Lead

TABLE II

ANALYSIS OF PRECURSORS OF TRIPHENYL LEAD AZIDE

Substance	Structure Given In Chart I	M.P. °C	Formula	Carbon		Hydrogen	
				Calcd.	Found	Calcd.	Found
Tetraphenyl lead	V	229-230	$C_{24}H_{20}Pb$	55.90	55.91	4.07	3.92
Triphenyl lead chloride	VI	207	$C_{18}H_{15}PbCl$*	45.61	45.87	3.20	3.61
Triphenyl lead hydroxide	VII	**	$C_{18}H_{16}PbO$	47.43	47.49	3.55	3.63

Notes: * Calcd: Cl, 7.48; Found: Cl, 7.50

** The thermal properties have not been previously reported. In this study, melting was observed to take place at about 240-250°.

TABLE III
ANALYSIS OF TRIPHENYL LEAD AZIDE

$(C_6H_5)_3Pb(N_3)$

Preparation	Element	Analysis Calcd.*	Analysis Found
Third	C	44.98	44.77
	H	3.15	3.39
	N	8.75	8.80
Second	C	44.98	44.90
	H	3.15	3.21
	N	8.75	8.70
First	C	44.98	44.88
	H	3.15	3.54
	N	8.75	8.43

* For $C_{18}H_{15}N_3Pb$

of triphenyl lead chloride was about 80 percent. The triphenyl lead chloride, in turn, was converted to triphenyl lead hydroxide (Chart I, structure VII) by treatment with potassium hydroxide, in 90 to 95 percent yield, using the method of Krause[2]. The analyses for these precursors are summarized in Table II. The final step in the synthesis (CHART I) consisted in treating the triphenyl lead hydroxide (in dilute ethanolic solution) with a chloroform solution of hydrazoic acid (see CHART I). The conversion of triphenyl lead hydroxide (VII) to triphenyl lead azide was better than 90 percent. Table III summarizes the analytical values for a number of independent runs. The method is quite reproducible even in the hand of inexperienced students. The properties of triphenyl lead azide are described below.

(3) Diphenyl Lead Diazide, $(C_6H_5)_2Pb(N_3)_2$, (IX)

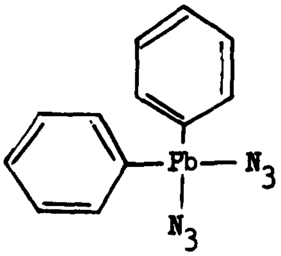

IX

$$\underset{\text{V}}{(C_6H_5)_4Pb} \quad + \quad HCl \longrightarrow \underset{\text{X}}{(C_6H_5)_2PbCl_2}$$

$$\underset{\text{X}}{(C_6H_5)_2PbCl_2} \quad + \quad 2\ KOH \longrightarrow \underset{\text{XI}}{(C_6H_5)_2Pb = O} \quad + \quad 2\ KCl + H_2O$$

$$\underset{\text{XI}}{(C_6H_5)_2Pb = O} \quad + \quad 2\ HN_3 \longrightarrow \underset{\text{IX}}{(C_6H_5)_2Pb(N_3)_2} \quad + \quad H_2O$$

Chart III: Synthesis of Diphenyl Lead Diazide

The synthesis of diphenyl lead diazide (IX) was achieved by a series of syntheses summarized in CHART III. Tetraphenyl lead was converted to diphenyl lead dichloride (X), in 97 percent yield, by treatment with dry hydrogen chloride by the method of Gilman and Robinson[10] (treatment of tetraphenyl lead with dry hydrogen chloride produces both triphenyl lead chloride and diphenyl lead dichloride). The diphenyl lead dichloride, so obtained, was converted to diphenyl lead oxide (XI) by treating a hot suspension of X in absolute ethanol with ethanolic potassium hydroxide to yield 90 percent of a white amorphous powder. The final reaction consists in treating XI with a chloroform solution of hydrazoic acid. The conversion of diphenyl lead oxide (XI) to diphenyl lead diazide (IX) is better

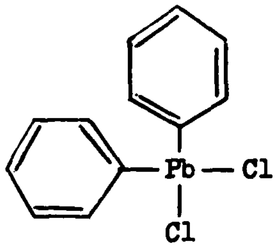

X

TABLE IV

ANALYSIS OF DIPHENYL LEAD DIAZIDE AND PRECURSORS

Substance	Structure Given In Chart III	M.P. °C	Formula	Carbon		Hydrogen	
				Calcd.	Found	Calcd.	Found
Diphenyl lead dichloride	X	283-286	$C_{12}H_{10}PbCl_2$[a]	33.34	33.39	2.33	2.24
Diphenyl lead oxide	XI	-	$C_{12}H_{10}PbO$	38.19	38.16	2.67	2.76
Diphenyl lead diazide[b]	IX	d	$C_{12}H_{10}PbN_6$[e]	32.35	32.61	2.26	2.46
Diphenyl lead diazide[c]	IX	d	$C_{12}H_{10}PbN_6$[f]	32.35	32.49	2.26	2.37

Notes: [a] Calcd: Cl, 16.40; Found: 16.55. [b] First preparation.
[c] Second preparation. [d] The thermal properties are described elsewhere.
[e] Calcd: N, 18.87; Found: 18.62. [f] Calcd: N, 18.87; Found: 18.43.

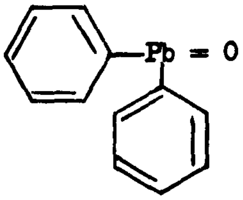

XI

than 95 percent yield. Table IV summarizes the analytical data obtained. The synthetic method described for diphenyl lead diazide is readily reproducible. The properties of diphenyl lead diazide are described below.

(4) Triphenyl Lead Triazide, (XII):

At the time of the writing of this report (September 8, 1961) the synthesis of phenyl lead triazide, XII:

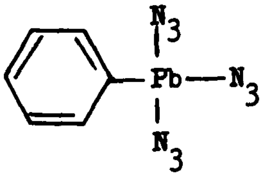

XII

has not as yet been achieved. However, the method of attack being studied in this investigation is summarized in CHART IV. Diphenyl lead oxide (a precursor used in the diphenyl lead diazide synthesis) is converted to diphenyl lead diacetate (XIII, CHART IV) by treatment with acetic acid. This latter product, in turn, is treated with mercuric acetate by the method of Panov[12] to produce phenyl lead triacetate (XIV). Two alternate routes leading from this precursor are being investigated and are shown in CHART IV. It is expected that the direct displacement of the acetate groups in XIV can be achieved by treatment with hydrazoic acid.

$$C_6H_5Pb(C_2H_3O_2)_3 \xrightarrow{HN_3} C_6H_5Pb(N_3)_3 \quad + \quad HC_2H_3O_2$$

XIV

The second route consists in converting phenyl lead triacetate (XIV) by treatment with dilute ammonium hydroxide to phenyl plumbonic acid (XV, CHART IV):

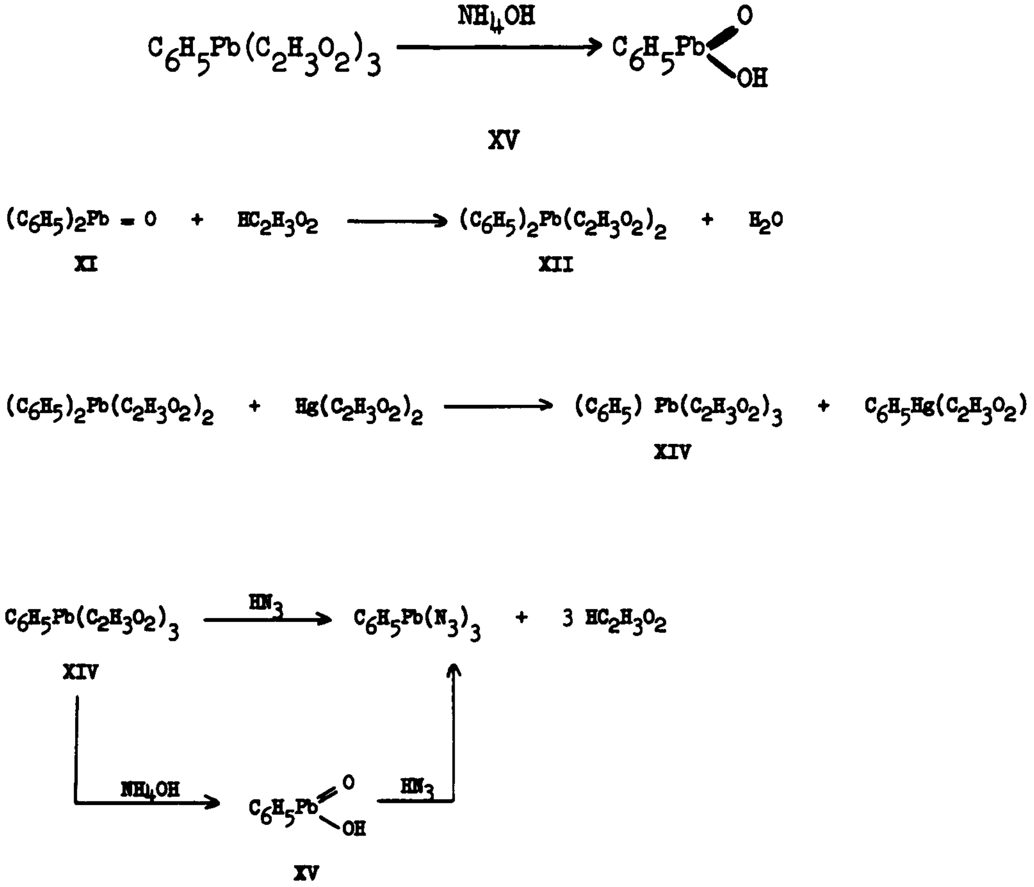

Chart IV: Projected Synthesis of Phenyl Lead Azide

Phenyl plumbonic acid on treatment with hydrazoic acid should yield the desired phenyl lead triazide:

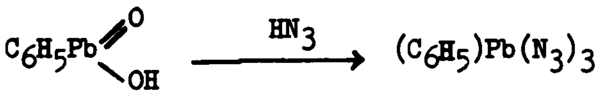

This phase of the investigation is still in progress and will be subsequently reported upon.

(B) Property Studies on Triphenyl Lead Azide and Diphenyl Lead Diazide.

(1) Appearance

(a) Triphenyl lead azide

Triphenyl lead azide crystallizes from the cooled ethanolic solution medium in the form of a small transparent acicular crystal habit.

(b) Diphenyl lead azide

Diphenyl lead diazide is obtained in the form of small crystals from the reaction mixture of acicular habit but of smaller size than triphenyl lead azide. As yet no suitable recrystallizing solvent has been found.

(2) Density

The densities of triphenyl lead azide and diphenyl lead diazide were determined by immersion in liquids at 30° and found to be 1.77 and 1.69 grams/cubic centimeter, respectively. The method of equivalent volume displacement of a solid on immersion in an insoluble liquid was used. Ethanol (95 percent) was found to be a suitable medium (see below on solubility studies).

(3) Solubility

Quantitative measurements of the solubilities of triphenyl lead azide and diphenyl lead diazide were determined at 30° for water, 95 percent ethanol and anhydrous ethyl ether, respectively. The data obtained are summarized in Table V. Qualitative estimates of solubility were also performed. Triphenyl lead azide was found soluble in bromoform, dimethylformamide and pyridine. Diphenyl lead diazide was found to have slight solubility in dimethylformamide and pyridine. However, in these later solvents decomposition takes place when recoveries of both substances are attempted.

(4) Thermal Behavior

(a) Qualitative Flame Tests

Qualitative ignition flame tests on triphenyl lead azide and diphenyl lead diazide, respectively, were conducted in the flame of a Bunsen burner on the tip of a porcelain spatula. Triphenyl lead azide shows no explosive properties but rather ignites quietly and at once burns rapidly with a bright yellow flame depositing what appears to be metallic lead. Similarly, diphenyl lead

TABLE V

SOLUBILITY OF TRIPHENYL LEAD AZIDE ($\emptyset_3PbN_3$) and DIPHENYL LEAD DIAZIDE ($\emptyset_2PbN_6$) at 30°

Solvent	grams/100 ml solution $\emptyset_3PbN_3$	 $\emptyset_2PbN_6$
Water	Insol	Insol
Ethanol (95)	1.39	Insol
Ethyl Ether (anhyd)	0.12	Insol

diazide showed no explosive properties but ignited immediately, however, burning with a "cracking" sound accompanied by weak flashes of light. On cooling the spatula, a deposit similar to that obtained previously was observed. The test specimen comprised approximately 2 mg of material.

(b) Transition Points

(i) Triphenyl lead azide

Triphenyl lead azide was found to have no thermodynamic melting point but to decompose upon heating. Small crystals (approximate length of longest face was 40 microns) were observed with a polarizing microscope when heated on a hot stage at the rate of 4-5°/minute. Loss of birefringence was observed at 159°-164°. A 2 mg sample was heated on a Fisher-Johns Melt Point Block at the rate of 4°-5° per minute. Table VI summarizes the observations. The initial point of gas evolution was obtained by heating a small sample under silicone oil. Gas evolution was observed at 192°. The decompositions were repeated in a manometric apparatus over the temperature range of 26-200° and a gas sample collected for mass spectrometric analysis. A vigorous pressure change was observed at 180°. The mass spectrometric analysis showed 88 percent nitrogen and 12 percent benzene. The stoichiometric relationship between substrate and gas evolution will be determined in subsequent work. Differential thermal analysis studies are in progress and these studies will also be subsequently reported upon. It, however, can be reported that two different types of apparatus confirm the presence of an endotherm between approximately 180°-190° coinciding with the appearance of a liquid phase between 186°-187° (Table VI) and the initiation of gas evolution.

TABLE VI

THERMAL CHARACTERISTICS* OF TRIPHENYL LEAD AZIDE

Temp. °C	Observation
123	Point pores formed in the mass
179	Semi opalescence observed in the mass
186-187	Phase change with liquid appearing
190	Yellow color apparent as temperature increases color darkens until reddish colored mass results with liquid phase also present
219	Partial melting of red mass Surface of liquid shows disturbance
280-300	Gradual darkening of red mass to black

* Two mg heated at rate of 4°-5°/minute.

TABLE VII

THERMAL CHARACTERISTICS* OF DIPHENYL LEAD DIAZIDE

Temp. °C	Observations
204	The white material began to show a light brown coloration
228	Wet appearance on the brown material
234	The solid phase is completely brown
280-290	Brown changes to black

* Two mg heated at rate of 5°-6°/minute.

(ii) Diphenyl lead diazide

Diphenyl lead diazide on heating was found to decompose without melting. Table VII summarizes the observations obtained. The initiation of gas evolution, determined under silicone oil, was found to be 145° with maximum rate of gas evolution between 190°-205° and ceasing at about 250°. Manometric decompositions have been initiated and will be subsequently reported upon. However, the experimental difficulties appear to be greater than with a triphenyl lead azide since a preliminary experiment resulted in a vigorous explosion (0.5 gram sample) at 197° demolishing the apparatus. These studies, however, will be continued as well as differential thermal analyses which will be subsequently reported upon.

(5) Infrared Absorption Spectrophotometry

The infrared absorption spectra in potassium bromide pellets were determined for triphenyl lead azide and diphenyl lead diazide. Figures No. 1 and No. 2 present the spectral curves obtained.

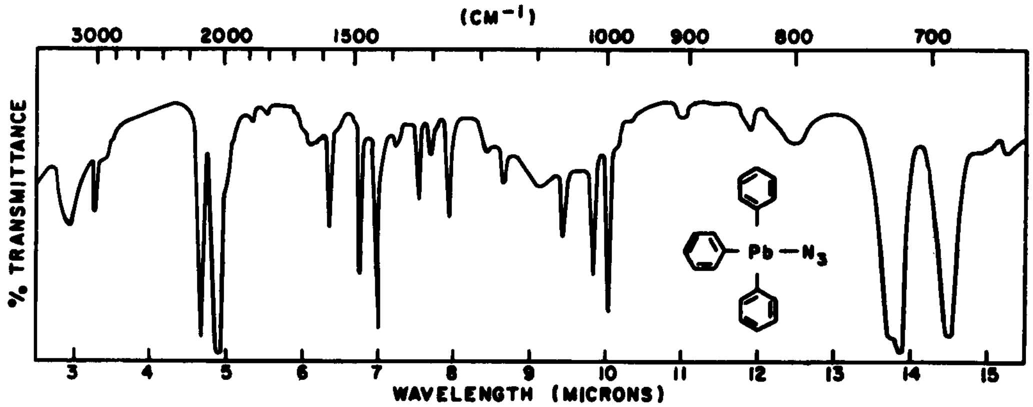

Figure 1. Infrared spectral curve for triphenyl lead azide, 1.5 mg in potassium bromide disc (vacuum compression at 12.25 tons gauge pressure).

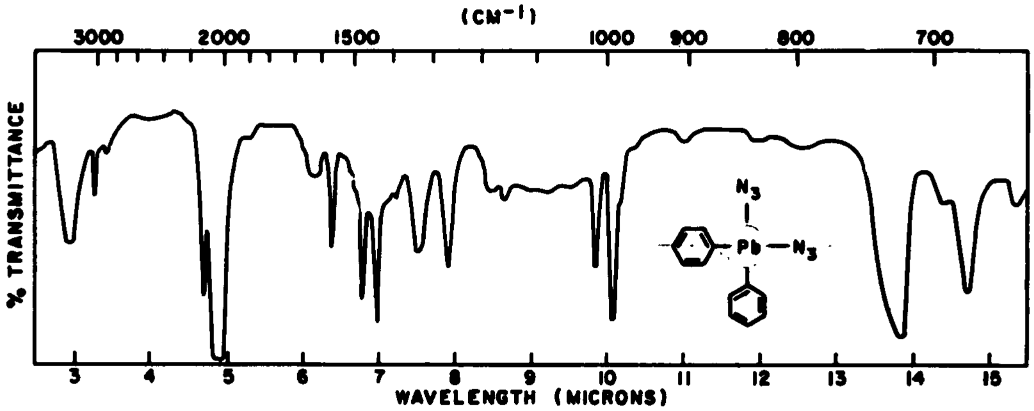

Figure 2. Infrared spectral curve for diphenyl lead diazide, 1.5 mg in potassium bromide disc (vacuum compression at 12.25 tons gauge pressure).

The splitting of the asymmetric stretching N_3 frequency to doublets (in the region of 2020 cm^{-1}) is noteworthy of attention and will be commented upon in a separate paper from Roosevelt University. Similar doublets of the asymmetric stretching frequency were also observed in mull studies. Infrared absorption spectra data are being obtained for tetraphenyl lead, triphenyl lead chloride, triphenyl lead hydroxide, diphenyl lead dichloride and diphenyl lead oxide, respectively. These data will be subsequently reported upon at which time all of the frequencies will be studied and commented upon.

FOOTNOTES AND REFERENCES

1. E. Lieber, Final Technical Report, ENG-3242 (1959).

2. Krause, E., VonGrosse A., Die Chemie der Metall-Organischen Verbindungen" (1937).

3. Leeper, R. W., Summers, L., and Gilman, H., Chem. Revs., 54, 101 (1954).

4. H. Möller, Z. Anorg. Chemie, 260, 249 (1949); C. A., 44, 5750 (1950).

5. E. Lieber, Final Technical Report, ENG-3728.

6. V. F. Postinikov and Speranskii, A. I., J. Gen. Chem., U.S.S.R., 10 1328 (1940).

7. Hoppe and Blinn, Z. Anorg.u.allgem. Chem., 293, 251 (1957).

8. H. S. Booth, Inorganic Synthesis, McGraw-Hill Book Co., New York, 1939,page 47.

9. H. Gilman, L. Summers and R. W. Leeper, J. Org. Chem., 17, 630 (1952).

10. H. Gilman and J. Robinson, J. Am. Chem. Soc., 51, 3112 (1929).

11. Micro-analyses were carried out by Dr. Weiler and Dr. Strauss, Oxford, England.

12. Panov, E. M. and Kochestov, K. A., Doklady Akad. Nauk. S.S.S.R., 85, 1037 (1952).

ACKNOWLEDGMENT

It is a pleasure to gratefully acknowledge the assistance of my students, Mr. Frank Keane, Mr. Laszlo Pollak, Mr. Jan Teetsov and Mr. Joseph Kawalko in the prosecution of these studies. I am especially indebted to Dr. Walter McCrone, of McCrone Associates, and Professor Carl Moore, of Loyola University, for permitting my students practically free access to their instrument laboratories. The assistance of Mr. John Reffner, of the McCrone Associates Laboratory, was particularly helpful. Without the kind help of the Ceramics Laboratory, of the Armour Research Foundation, and the Laboratory of the U. S. Naval Ordnance Test Station, China Lake, California, the preliminary differential thermal analysis studies would not have been possible. It is a pleasure to acknowledge their assistance.

BASIC RARE EARTH AZIDES

by

Hyman Rosenwasser
U. S. Army Engineer Research and Development Laboratories
Fort Belvoir, Virginia

Introduction

The only reference to the preparation and isolation of rare earth azides is that by Curtius and Darapsky (1) in 1900. Lanthanum and cerous hydroxides, and didymium carbonate, were respectively reacted with aqueous hydrazoic acid and explosive residues were recovered by evaporation of the resulting solutions in vacuo. Analysis for metal and nitrogen content gave a ratio of 1 to 6, a representative formula being $Ln(OH)(N_3)_2 \cdot 1\text{-}1/2\ H_2O$. Another link between rare earths and azides is found in the studies of Ant-Vuorinen (2). The individual rare earths in a mixture were selectively precipitated as hydroxides by boiling the rare earth nitrate solution after addition of sodium azide. The method was later modified by dissolving a rare earth hydroxide mixture in hydrazoic acid and performing the hydrolytic separation by electrolysis (3).

The current availability of "pure" rare earth oxides makes possible a more extensive investigation of the preparation and properties of the lanthanon azides.

Preparation

The reaction between hydrazoic acid and the respective sesquioxides of Nd and La, as well as Pr_6O_{11}, was used to prepare the rare earth azides. A 10 percent aqueous solution of commercial sodium azide was passed through a column containing Amberlite IR-120(H) ion exchange resin. The HN_3 eluate was allowed to react with the oxide powder in an Erlenmeyer flask. Reaction proceeds slowly and was generally continued overnight for completion. A neutral solution then remains since the acid which has not been used up in the reaction has volatilized away. After filtering off any unreacted oxide, the azide is obtained by precipitating out with acetone. The azide residues obtained by filtering on a Buchner funnel have a glassy appearance. These residues were found in an agate mortar prior tc further study.

Properties

The colors of the La, Nd, and Pr azides are white, rose, and green, respectively. Positive tests for the azide ion in these compounds were obtained with ferric chloride solution (formation of red ferric azide complex) and with ceric ammonium sulfate solution (gas evolution). The powder X-ray diffraction patterns and the infrared spectra of these azides show them to have the same structure. They are all soluble with decomposition in the common acids, but are insoluble in common organic solvents, formamide, or liquid ammonia. On heating them in a Bunsen flame deflagration takes place.

A number of possibilities was at first considered for the formula of these isomorphous azides. These were the normal azide LnN_9, the oxyazide $LnON_3$, the hydroxyazide $Ln(OH)N_6$, and the oxoazide Ln_2ON_{12}. The oxoazide would be an unexpected product but a Nd oxoacetate has been reported to form from degradation of the polymeric sesquioxide in anhydrous acetic acid (4).

Analysis

The simplest method for the analysis of the lanthanon azides is based on the thermal decomposition in air to the corresponding oxide. In the oxidation to Pr_6O_{11}, however, the possible production of nonstoichiometric oxides or of PrO_2 are complicating factors. Samples of the Nd azide heated at 1000 degrees C. for several hours gave azide to oxide ratios closest to that from the oxoazide, an experimental value of 1.395 compared to 1.404. This corresponds to a Nd composition of 62.2 percent. At this point the normal azide and oxyazide could be eliminated as possibilities. A spectrophotometric determination of a hydrochloric acid solution of the azide at 5730 A. gave a Nd content of 60.7 percent. The method used was to take the HCl solution to dryness and make to volume with distilled water. Similar solutions made from Nd_2O_3 were used as standards to prepare the calibration curve.

A volumetric determination of the azide ion content was made by adding excess ceric ammonium nitrate solution (standardized against sodium oxalate) to the Nd azide powder the backtitrating the excess with ferrous ammonium sulfate (standardized against potassium permanganate). A recrystallized sample of sodium azide analyzed in the same manner showed a purity of 99.25 percent, which appears reasonable. Calculations showed that the nitrogen content of the Nd azide was 18.3 percent. This value is well below that required for the oxoazide or hydroxyazide and it became necessary to consider a metal to nitrogen ratio of 1 to 3. The dihydroxyazide monohydrate, $Nd(OH)_2N_3 \cdot H_2O$ best fits the analytical data (60.5 percent Nd, 17.6 percent N).

Infrared Spectra

A typical infrared spectrum of the basic rare earth azide in a KBr pellet is shown in Figure 1. A sharp medium strength band at

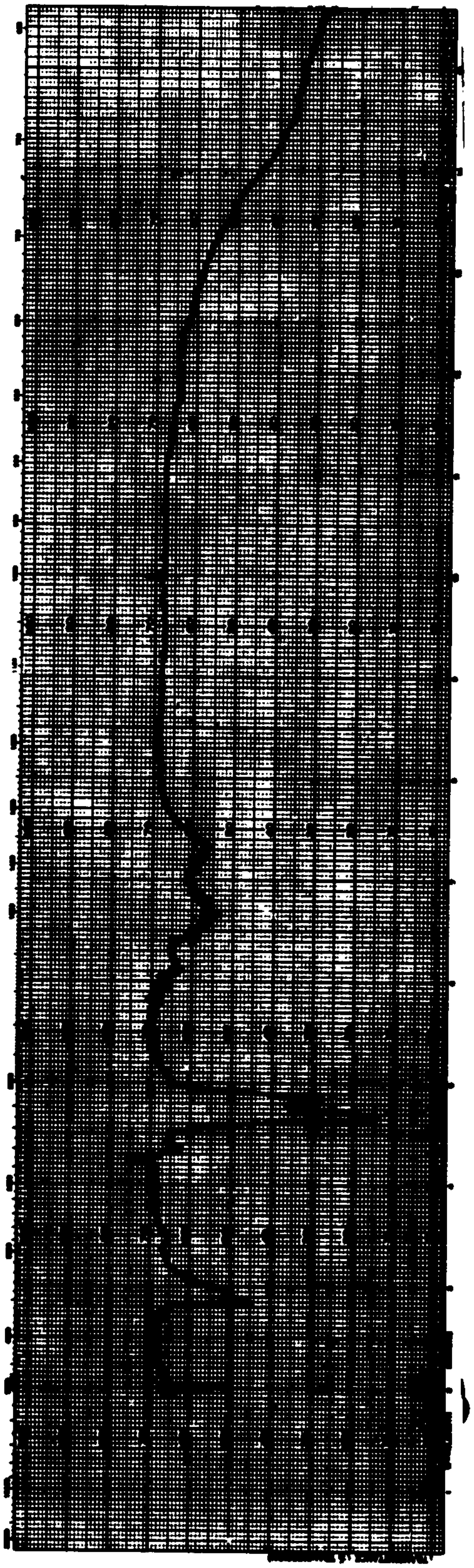

Figure 1. Infrared spectrum of basic Pr azide.

2.85 microns is assigned as the stretching fundamental of the free (no H-bonding) hydroxyl group. The bands at 2.95 and 6.15 microns are attributed to water of hydration. Bands in the 4.7-4.9 micron region are due to asymmetric stretching frequency of the azide ion. Such splitting would result if the site symmetries for azide ions in the crystal were not spatially identical. The bands about 6.6, 7.8, and 11.8 microns result from the presence of carbonate ion, which is a likely impurity caused by aging of the azide samples in air. Assignments for water of hydration and carbonate ion are supported by comparison with the infrared spectrum of $Pr_2(CO_3)_3 \cdot 8\ H_2O$ by Faeth and Clifford (5).

Conclusion

Neglecting the water of hydration, a generalized formula for rare earth azide compounds prepared from aqueous solution would be $Ln(OH)_x(N_3)_{3-x}$. At a pH of 8 or higher the hydroxide (or hydrous oxide) would be expected to precipitate (x=3). In our experiment the results approximate x=2 at a pH of 7. It is assumed that the hydroxyazide prepared by Curtius and Darapsky was isolated from an acid medium (x=1). It is likely that under certain conditions x would not be an integer, as has been observed with the aging of hydroxy chlorides in contact with the solution (6).

References

1. Curtius and Darapsky: J. prakt. Chem. (2), 61, 408 (1900).
2. Ant-Vuorinen: Teknillinen Aikakauslenti, Nos. 7-8, 365 (1931).
3. Ant-Vuorinen: Suomen Kemistilehti B30, 1 (1940).
4. Seaton, Sherif, and Audrieth: J. Inorg. Nucl. Chem. 9, 222, (1959).
5. Faeth and Clifford: Second Rare Earth Conference, Glenwood Springs, Colorado (Aug. 1961).
6. Aksel'rud: Zhur. Priklad. Khim. 34, 776 (1961); C.A. 55, 17179.

DISTRIBUTION LIST FOR PROCEEDINGS OF THE 10TH BASIC RESEARCH CONTRACTORS CONFERENCE AND SYMPOSIUM

ADDRESSEE	REPORT
Government Agencies	
Technical Library Office, Assistant Secretary of Defense Washington 25, D. C.	1
Army Research Office Arlington Hall Station Arlington 12, Virginia ATTN: Dr. R. Weiss	1
U. S. Army R&D Liaison Group Europe (9851) APO 757 New York, New York ATTN: Dr. Bernard Stein	1
U. S. Army Chemical Warfare Laboratories Army Chemical Center, Maryland ATTN: Technical Library (1) G. Clift (1)	2
Chief of Engineers Department of the Army Washington 25, D. C. ATTN: ENGRD-P	1
Director, USAERDL	1
Military Department, USAERDL	1
Basic Research Group, USAERDL	50
Mine Warfare Branch, USAERDL	1
Dr. George W. Hickox, USAERDL	1
Information Resources Branch, USAERDL	1
R&D Project Case File, USAERDL	1
Technical Documents Center, USAERDL	2
Office of Counsel, USAERDL	1

ADDRESSEE	REPORT
British Liaison Officer, USAERDL	6
Canadian Liaison Officer, USAERDL	5
Transportation Corps Liaison Officer, USAERDL	1
Office, Chief of Ordnance Department of the Army Washington 25, D. C. ATTN: ORDTX-AR	1
Commanding General Frankford Arsenal Pitman-Dunn Laboratory Group Philadelphia 37, Pennsylvania ATTN: Library (1) H. Kirshner, 1331 (1) Jack Radell (1) M. S. Silverstein (1)	4
Commanding Officer Ordnance Materials Research Office Watertown Arsenal Watertown 72, Massachusetts	1
Commanding General Aberdeen Proving Ground Aberdeen Proving Ground, Maryland ATTN: Ballistic Research Laboratory	1
Commanding Officer Office of Ordnance Research Box CM, Duke Station Durham, N. C.	1
Commanding Officer Picatinny Arsenal Dover, N. J. ATTN: Library (1) L. H. Eriksen (2) Dr. J. V. R. Kaufman (1)	4
Chief of Naval Research Reports Branch (Code 530) Department of the Navy Washington 25, D. C.	1

ADDRESSEE	REPORT
Commander U. S. Naval Ordnance Lab White Oak, Silver Spring, Maryland ATTN: Library (1) Dr. James E. Ablard (1)	2
Commander U. S. Naval Ordnance Test Station China Lake, California ATTN: Technical Library Branch (1) Dr. H. D. Mallory (1) Dr. T. B. Joyner (1)	3
Research and Development Department Naval Propellant Plant Indian Head, Maryland ATTN: Library (1) Dr. M. Fauth (1) Dr. Marguerite Chang (1) Mr. George Roecker (1)	4
Air Force Office of Scientific Research Solid State Sciences Division Washington 25, D. C. ATTN: M. Swerdlow	1
Brookhaven National Lab Upton, New York ATTN: Dr. George J. Dienes (1) Dr. Paul W. Levy (1) Dr. D. Rosenblatt (1) J. E. Mapes (1)	4
National Bureau of Standards Washington 25, D. C. ATTN: Dr. V. Dibeler (1) Dr. Olen Kraus (1)	2
National Academy of Sciences 2101 Constitution Avenue, N.W. Washington 25, D. C. ATTN: Dr. J. H. Probus	1
National Aeronautics & Space Administration 1520 H Street, N.W. Washington 25, D. C. ATTN: A. S. Bass	1

ADDRESSEE	REPORT
Diamond Ordnance Fuze Laboratory Connecticut Ave. and Van Ness St., N.W. Washington 25, D. C. ATTN: Library (2) Mr. Lipnick (1)	3
Lawrence Radiation Laboratory Livermore, California ATTN: Dr. Roger Anderson	1
U. S. Army Research Office (Durham) Durham, North Carolina ATTN: Dr. Robert G. Ghirardelli (1) Dr. G. Wyman (1)	2
Chief of Engineers ATTN: Dr. Gilford G. Quarles Rm 1310, Gravelly Point	1
Office, Chief of Research & Development Department of the Army Washington 25, D. C. ATTN: Dr. H. C. Weber	1
U. S. Naval Weapons Station Yorktown, Virginia ATTN: Ernest Mason	1
U. S. Naval Weapons Laboratory Dahlgren, Virginia ATTN: Peter Altman	1
Others	
Stanford Research Institute Palo Alto, California ATTN: Dr. Charles Cook (1) Dr. W. J. Fredericks (1)	2
Roosevelt University 430 S. Michigan Avenue Chicago 5, Illinois ATTN: Dr. Eugene Lieber (1) Jack G. Dodd (1)	2
McCrone Associates 501 East 32nd Street Chicago 16, Illinois	1

ADDRESSEE	REPORT
PEC Corporation 1001 Mapleton Avenue Boulder, Colorado ATTN: Dr. D. G. Burkhard (2) Dr. D. S. Ling (1)	3
Dr. R. Rollefson University of Wisconsin Madison, Wisconsin	1
Armour Research Foundation Illinois Institute of Technology 10 West 35th Street Chicago 16, Illinois ATTN: Dr. Sam Marshall (1) Dr. Dickron Mergerian (1) Dr. Irvine Solomon (1)	3
Sandia Corporation, Sandia Base Albuquerque, New Mexico ATTN: Frank A. Goss (1) Bill Meikle (1)	2
Howard University Chemistry Department Washington, D. C. ATTN: Dr. G. C. Turrell (1) James S. Burton (1)	2
Dr. C. R. Naeser George Washington University Chemistry Department Washington, D. C.	1
Dr. Roman Smoluchowski School of Engineering Princeton University Princeton, New Jersey	1
Dr. F. C. Tompkins Department of Chemistry Imperial College Imperial Institute Road London S. W. 7, England	2

ADDRESSEE	REPORT
The Catholic University of America Washington 17, D. C. ATTN: Dr. Karl F. Herzfeld (1) Dr. Basil Darwent (1)	2
Dr. John H. Anderson Department of Physics University of Pittsburgh Pittsburgh, Pa.	1
Dr. J. H. Boyer American Chemical Society Washington 6, D. C.	1
University of Utah Salt Lake City, Utah ATTN: Dr. Melvin A. Cook (1) Dr. R. T. Keyes (1) Dr. C. H. Pitt (1)	3
Dr. D. E. Davenport Stanford Research Institute Menlo Park, California	1
Mr. Howard Fisher Aerojet General Corp. Downey, California	1
Dr. A. G. MacDiarmid University of Pennsylvania Philadelphia, Pa.	1
University of Connecticut Storrs, Connecticut ATTN: Dr. O. R. Gilliam (1) Mr. Fred Otto (1)	2